Design and Tailoring A- and B-site of Fe-based perovskites as novel Oxygen Carriers for Hydrogen Production in Chemical Looping Processes

Alex Martínez Martín

A thesis submitted for the degree of Doctor of Philosophy (PhD) in Chemical Engineering at Newcastle University

School of Engineering

Abstract

The pursuit for sustainable hydrogen (H_2) production whilst minimising by-products formation has led to the development of new technologies such as chemical looping (CL). Chemical looping water-gas shift (CLWGS) allows for clean H_2 production from steam whilst producing carbon dioxide (CO_2) from carbon monoxide (CO) in the following gas stream, facilitating a route for CO_2 capture. This process requires CO as feedstock, currently derived from methane (CH_4). Chemical looping steam reforming of methane (CLSRM) generates syngas (H_2 + CO), serving this CO as a reactant in the subsequent process of CLWGS, achieving up to 4 moles of H_2 per mole of CH_4 fed in the overall process.

This thesis focuses on the design, synthesis, and characterisation of novel oxygen carrier materials (OCM) for H_2 production via CLWGS and CLSRM. Initial results of this project were based on $Pr_{0.5}Ba_{0.5}FeO_{3-\delta}$ and $Sm_{0.5}Ba_{0.5}FeO_{3-\delta}$ as OCM. These materials exhibited higher oxygen capacity than established benchmark materials. Under CLWGS conditions, $Pr_{0.5}Ba_{0.5}FeO_{3-\delta}$ showcased a sustained higher H_2 production and a steam conversion rate of around 40% for 400 cycles.

Further study involved the subsequent tailoring of $Pr_{0.5}Ba_{0.5}FeO_{3-\delta}$ for CLSRM, consisting of Ni-doping to promote CH_4 activation and A-site deficiency to facilitate exsolution of nanoparticles, yielding $(Pr_{0.5}Ba_{0.5})_{0.9}Fe_{0.9}Ni_{0.1}O_{3-\delta}$. This OCM resulted in high stability and high syngas selectivity towards syngas due to the formation of a FeNi alloy. The formation of this alloy was monitored via *operando* Powder X-Ray Diffraction at ESRF. OCM were tested in CLSRM over 400 cycles, underscoring their high stability and suitability for sustained H_2 production.

Moreover, the initially designed materials and their Ni-doped analogues were effective in the catalytic process of reverse WGS. The Ni-doped OCM displayed high CO selectivity even at low temperatures, underscoring their suitability for high-selectivity catalytic applications.

The proposed materials not only are of interest for sustained clean H_2 in CL process but also possess remarkable catalytic reverse Water-Gas Shift capabilities.

Acknowledgements

This PhD journey has been a challenging and rewarding experience, filled with moments of doubts, discovery, and development. Many thanks to the Royal Academy of Engineering for funding this research and making it possible.

I would like to thank the team that supported me throughout the PhD. To Prof. Ian Metcalfe for his consistent and valuable support. I acknowledge Dr Wenting Hu, whose input has contributed to my personal growth. I would like to thank Dr Dragos Neagu for his valuable contributions to this work. Finally, to Dr Kelly Kousi for her unconditional support and for trusting in my capabilities.

I would also like to thank the members of the MatCoRE group, with whom I closely worked during these years. In particular many thanks to Dr Reinaldo Juan Lee Pereira for his continuous help with all the computer-based tasks, to Dr Deblina Majumder for her emotional support, to Dr Leonidas Bekris for his help as a colleague but mostly for his continuous presence and support outside the lab, as a friend. Finally, to Dr Daniel Telford for all the insightful discussions, contribution and priceless help throughout these years, especially during the campaign at ESRF. This synchrotron experience could have not happened without his presence.

Related to the ESRF campaign, thanks to all the people that made it possible. Thanks to Dr Evangelos Papaioannou for helping with the heavy duty of driving down to Grenoble and his help with the experiments. To Shailza Saini for her generous decision to be present during this time and her help during these years. To Dr Catherine Dejoie, for all her help and support during the campaign. Finally, to Prof John Evans, for his selfless contribution to the analysis while being on site taking care of data analysis and for the post-processing.

I would like to mention the continuous and unvaluable assistance of the technical and admin team in Newcastle University, especially Kevin Brown for his thorough and full support, and his willingness to help.

A special thanks goes to Dr Francisco Garcia-Garcia and his group for generously offering his facilities to host me in The University of Edinburgh when our lab in the university flooded and was not accessible for an extended period of time. I would also like to thank

the University of Surrey for giving me the opportunity to use their microscopy facilities and for making me welcome during my stay.

Thanks to my family for their continuous support. Thanks for giving me all the opportunities that have made me become the confident person I am today. To my friends back in Spain, which I feel very close to me despite the distance.

To my friends in Newcastle, my UK family. The ones that came and left and the ones that came and stayed. Thanks for making everyday a little bit better. Adrián, Salvo, Leo, Greg, Maria, James, Tom, Tere, Pepe, Eva, Chris, Andri. Thank you. To Domenico Balsamo, *grazie per esserci sempre stato*. Ari, *moltes gràcies per il·luminar els nostres dias amb el teu riure*. Soon-to-be Dr Sergio Serrano Blanco, *desde el primer día hasta el último*. *Sin duda, de quien más aprendizaje y momentos me llevo de este largo e intenso viaje. Gracias por dejarme aprender de ti, por entenderme y por venir a mí cuando lo necesitabas. Por decirme que "no" cuando el momento lo requería. Gracias por ser ese pilar que hacía falta para que este viaje mantuviese su rumbo.*

And lastly, Giulia. *Le parole non possono spiegare l'importanza che hai nella mia vita. Ciò che per molti è uno sforzo, per te è genuinamente un piacere. Tu solevi dire che "non sarebbe stato lo stesso senza di te". Ora io dico che "senza di te non sarebbe stato". Grazie per esserti assicurata che, come dicevamo sempre, tutto andasse bene.*

To everyone, *gracias por tanto y perdón por tan poco*.

Table of Contents

Abstract ii

Acknowledgements iii

Table of Contents v

List of Figures viii

List of Tables xiv

List of Publications xv

Additional Lists xvi

Chapter 1 Introduction 1

1.1. Hydrogen as an energy carrier, use and transport 1

1.2. H_2 production 2

1.2.1. Overview 2

1.2.2. Steam Reforming of Methane 2

1.2.3. Partial Oxidation of Hydrocarbons 4

1.2.4. Coal Gasification 5

1.2.5. H_2 from renewable sources 5

1.3. Chemical Looping for H_2 production 5

1.3.1. Concept and applications 5

1.3.2. Chemical Looping Water-Gas Shift 7

1.3.3. Chemical Looping Steam Reforming Methane 8

1.4. Oxygen Carrier Materials 10

1.4.1. Choice of OCM 10

1.4.1.a. Iron oxide 12

1.4.1.b. Nickel oxide 14

1.4.1.c. Other Metal / Metal Oxide systems 15

1.4.1.d. Perovskite oxides 16

1.4.1.e. Fe-based perovskites 20

1.4.2. Exsolution 22

1.5. Thesis aims and objectives 26

1.6. Thesis outline 27
Chapter 2 Experimental methods 29
2.1. Synthesis of materials 29
2.2. Exsolution of nanoparticles 29
2.3. Powder X-ray diffraction 30
2.4. Synchrotron *in* situ and *operando* PXRD 31
2.5. Scanning Electron Microscopy 33
2.6. Thermogravimetric Analysis 34
2.6.1 Oxygen Storage Capacity measurements 35
2.6.2 Preliminary studies for suitability of OCM for CL processes 35
2.7. Iodometric titration 36
2.8. Experimental set-up 37
2.8.1 Temperature Programmed Reductions 38
2.8.2 Temperature Programmed Oxidations 39
2.9. Reactor for Chemical Looping Cycling Experiments 39
2.9.1 System Flow 39
2.9.2 Gas Analysis 40
Chapter 3 Design and Characterisation of Carrier Materials for CLWGS 43
3.1. Introduction 43
3.2. Materials characterisation 45
3.3. Initial oxygen vacancies and OCM stability 48
3.4. Study of non-stoichiometry 52
3.5. Cell lattice modification and material stability 55
3.6. Application in Chemical Looping Water-Gas Shift 60
3.6.1 Temperature optimisation 60
3.6.2 Half cycle duration 60
3.6.3 Sustained activity in CLWGS 64
3.6.3.a SBFO 64
3.6.3.b PBFO 68
3.6.4 Normalised H_2 production in the long term and OCM stability 72
3.7. Advantages and limitations of PBFO and SBFO over other OCM 76
3.8. Heat Balance and Thermodynamics of PBFO and SBFO in CLWGS 77
3.8.1. *Step 1 – CO oxidation half cycle* 77

3.8.2. *Step 2 – H_2O reduction half cycle* 78
3.8.3. *Step 3 – Oxygen vacancies formation and oxygen release* 78
3.8.4. *Step 4 – Overall energy balance* 78
3.9. Summary of Chapter 3 79
Chapter 4 Development and investigation of the as-designed carrier materials for CH_4 activation 81
4.1. Introduction 81
4.2.Developing OCM with enhanced CH_4 reactivity towards syngas – Partial Oxidation of CH_4 82
4.3. Preliminary tests 83
4.4. Finding the adequate exsolution conditions 85
4.5. *Operando* CH_4 activation using *as sintered* 0.1 A-site deficient PBFNO 90
4.6. *Operando* re-oxidation of exsolved nanoparticles 97
4.7. *Operando* CH_4 activation using PBFNO after undergoing exsolution and reoxidation 101
4.8. Oxygen capacity of the studied systems 106
4.9. Summary of Chapter 4 107
Chapter 5 Testing exsolved OCM in CLSMR 109
5.1. Introduction 109
5.2. Finding conditions for CLSMR 110
5.2.1 Temperature of the cycles 111
5.2.2 Half cycle duration 112
5.2.3 Long term application of the exsolved system as OCM for CH_4 conversion in CLSRM 116
5.3. Summary of Chapter 5 123
Chapter 6 Further applications of the designed OCM 125
6.1. Introduction 125
6.2. Experimental 127
6.3. Materials design principles 129
6.4. Synthesising Fe-based perovskites tailored at the A and B site; crystal structure, oxygen content and microstructure 129
6.5. Reducing the as synthesised materials; exsolution 131
6.6. Catalytic activity of the new catalysts in rWGS 133
6.7. Replenishing the oxygen lattice 135

6.8. Summary of Chapter 6 137
Chapter 7 Conclusions and Future work.....139
7.1. Summary of the thesis 139
7.2. Possible future work 142
References 144

List of Figures

Figure 1.1 Simplified scheme of a conventional SMR process. *HDS* corresponds to hydrodesulfurization unit. *HTS* and *LTS* refers to high and low temperature shift, respectively. Image courtesy of Go et al (2009). 3
Figure 1.2. General schematic for a CL H_2 production process. OCM acronym corresponds to *oxygen carrier material*. 6
Figure 1.3. Gibbs free Energy vs Temperature (Ellingham diagram) for iron oxide systems and carbon monoxide as reactant. Image taken from Mondal et al. (2004). 8
Figure 1.4. Schematic representation for the CLSRM process for H_2 and syngas production, with **a**. two reactors, and **b**. three reactors, where the Air-Reactor has been included. Image courtesy of Luo et al. (2018). 10
Figure 1.5. Ideal perovskite structure (ABO_3). Image courtesy of (Xu *et al.*, 2010). 16
Figure 1.6. Exemplification of the types of non-stoichiometry present in a perovskite via $SrTiO_3$. Image courtesy of Neagu (2012), where $n \geq 1$ for the super-stoichiometric perovskites. 18
Figure 1.7. Surface morphology of exsolved metallic nanoparticles. **a**. SEM image of A-site deficient material. **b**. SEM image of stoichiometric material. Both images were published by (Neagu *et al.*, 2013). **c**. SEM image displaying the anticoking behaviour of exsolved Ni-nanoparticles. Nanoparticles presented exhibit a low rate of carbon nanofibers formed. Image published by (Neagu *et al.*, 2015). **d**. Illustrated morphology of exsolved nanoparticles compared to impregnated particles suggested by different authors. 25

Figure 2.1. High resolution power diffractometer, equipped with its fast spinner, 13 channels multi-analyser stage and pixel detector. Image courtesy of (Fitch et al., 2023)(Fitch et al., 2023). 32
Figure 2.2. Reactor system set-up: Diffractometer-left side image, Furnace-centre, Gas Flow System-Bottom right. Mass spectrometer for gas analysis was placed behind the set up and cannot be displayed in the picture. 33
Figure 2.3. Different signals that can be generated when an electron beam hit the sample in the Scanning Electron Microscope. Different regions where these signals are originated are marked with lines separating different textures within the image (Zhou et al., 2007)(Zhou et al., 2007). 34
Figure 2.4. Flow diagram of the system used for Temperature Programmed Reactions .. 38

Figure 2.5. Flow diagram of the CL rig set-up. MFC corresponds to “mass flow controller” 40
Figure 2.6. Schematic depiction of the internal structure of the mass spectrometer. Image courtesy of the company.....41

Figure 3.1. CO to CO_2 and H_2O to H_2 theoretical conversions as a function of log pO_2 at T = 820 ºC. Image courtesy of Ungut (2022). 44
Figure 3.2. a. Synchrotron PXRD diffractograms of as sintered PBFO and SBFO, sintered at two different temperatures (1000ºC and 1400ºC) during 14h. hkl indices are attributed to the top pattern and apply to all the displayed diffractograms. Macrostructure images with different magnifications of PBFO sintered at different temperatures, done by SEM. **b.** PBFO-1400 ºC with different magnifications. **c**. PBFO-1000 ºC. 47
Figure 3.3. OCM behaviour during redox cycles at high temperature and potent redox agents. **a**. Oxygen vacancies (3-δ) of the designed materials after undergoing redox cycles. Cycles plotted: 1st, 5th, 10th, 15^{th,} and 20th. **b**. SBFO, **c**. PBFO. PXRD patterns of the as sintered and tested OCM: SBFO, left; PBFO, right. Rietveld refinement of the OCM after undergoing 20 TGA cycles, **d**. SBFO after test, **e**. PBFO after test.....51
Figure 3.4. Oxygen vacancies (3-δ) as function of pO_2. values obtained at 820 ºC for same OCM sintered at different temperatures (1400 ºC and 1000 ºC), **a**, SBFO. **b**, PBFO. 3-δ values at different temperatures (820 ºC and 720 ºC) as function of pO_2, for materials sintered at 1000 ºC during 10 h, **c**, SBFO, **d**, PBFO. 54
Figure 3.5.**a**. Example of PXRD patterns of PBFO after undergoing subsequent oxidoreductions under different buffer gases. Data collected from capillaries at room temperature, at ESRF. **b**. Zoomed area of the PXRD pattern to observe peak shifting. 56
Figure 3.6. Diagram representing the three types of unit cells reflected in this chapter. Symmetry decreases from cubic to orthorhombic. Ionic disorder is increased with the lower symmetry, increasing ionic tilting. Ideal and distorted perovskites are represented with their pseudocubic unit cell underneath each name. Image borrowed from Neagu (2012)(2012). 57
Figure 3.7. Pseudo-cubic unit cell parameters calculated by *ex situ* capillaries at ESRF at room temperature. The samples examined were collected at room temperature after undergoing reduction under different buffer gases at 820 ºC. **a**, SBFO. Some error bars are smaller than the symbols containing them. **b**, PBFO. Error bars in the y axis for data provided by synchrotron wavelength is smaller than the symbol designing the value.....59
Figure 3.8.**a**. Conversion of CO (blue) and H_2O (orange) as a function of cycle number. 1 mmol of OCM was placed in the reactor and reactive gases were 5% CO and 6.5% H_2O, both balanced in He. 3 regions can be identified: Cycles 1-15, half cycles of 60 s each. Cycles 16-30, half cycles of 48 s. Cycles 31-45, half cycles of 120 s; all of them at 820ºC. **b**. Moles of H_2 produced per mole of OCM used in the reactor bed. 62
Figure 3.9. Molar fraction at the outlet of the reactor as a function of time. Three cycles representing the different time duration applied, **a**. 60 s half cycle, **b**. 48 s half cycle, **c**. 120 s half cycle.....63

Figure 3.10. CO (blue) and H_2O (orange) conversion of SBFO in CLWGS vs time, represented as cycle number, for 400 cycles. Half cycle duration of 60 s, gas feeds were 5% mol CO and 6.5% mol H_2O, 100 mL / min. 65
Figure 3.11. Outlet composition vs time for the long-term experiment for SBFO. **a**. 1st cycle, **b**. 70th cycle, **c**, 150th cycle, **d**. 225th cycle **e**. 300th cycle, **f**. 400th cycle. Gas flow used: 5% CO and 5% H_2O, both balanced in He. 67
Figure 3.12. CO (blue) and H_2O (orange) conversion of PBFO in CLWGS vs time, represented as cycle number, for 400 cycles. Half cycle duration of 60 s, gas feeds were 5% mol CO and 5% mol H_2O, 100 mL / min. 68
Figure 3.13. Outlet composition vs time for the long-term experiment for PBFO. **A**. 1st cycle, **b**. 70th cycle, **c**, 150th cycle, **d**. 225th cycle **e**. 300th cycle, **f**. 400th cycle. Gas flow used: 5% CO and 6.5% H_2O, both balanced in He. 71
Figure 3.14. Normalised H_2 production (mmol H_2 produced per g of OCM) after 400 cycles of 1 min half-cycle duration. 73
Figure 3.15. Crystallographic patterns obtained by PXRD comparing the OCM as sintered and the OCM after undergoing 400 CLWGS cycles, **a**. SBFO, **b**. PBFO. In **a** and **b**, two patterns are presented. Patterns below (dark green for SBFO and brown for PBFO) correspond to the initial materials, as sintered. Patterns above (light green for SBFO and yellow for PBFO) correspond to the materials after undergoing CLWGS. Zoomed patterns to observe secondary phases and peaks observation between 20-40º **c**. SBFO, **d**. PBFO. Minor formation of secondary phases has been appreciated in both patterns, but the quality of the spectra does not allow to identify them. 76

Figure 4.1. CH_4 conversion vs pO_2 for **a**. syngas production and **b**. CH_4 combustion at two different temperatures commonly used in CL processes. The area between those two temperatures corresponds to all the temperature range comprised between the two displayed in which the process is thermodynamically favourable. 82
Figure 4.2.**a**. Temperature Programmed Reaction profile of CH4 activation for PBFO. Ramp rate 10 ºC / min until reaching ~820 ºC, keeping isothermal conditions for 30 min. **b**. Temperature Programmed Reaction profile of CH_4 activation for PBFNO. Ramp rate 10 ºC / min until reaching ~820 ºC, keeping isothermal conditions for 30 min. **c**. X-Ray diffractograms of PBFO as sintered (yellow) and after undergoing CH_4-TPR (green). Intensity is expressed in normalised square root. **d**. PXRD diffractograms of PBFNO as sintered (dark blue) and after undergoing CH_4-TPR (light blue). Patterns for the Ni-doped OCM were not recorded at ESRF, hence they appear at Cu wavelength. 84
Figure 4.3. X-Ray pattern of **a**. as sintered 0.1 A-site deficient PBFNO. hkl indices for the main cubic phase are shown in brackets. **b**. Stack PXRD patterns of the A-site deficient PBFNO reduced at different temperature and time conditions. Secondary phases (▲) and metallic nanoparticles (●) have been identified. SEM images of surface PBFNO systems after exsolution at 600ºC for different times, **c**-**d**, 10 h. **e**, 20 h. **f**. Particle size distribution for the exsolved PBFNO at different conditions (600 ^oC for 10 h, 600 ^oC for 20 h and 700 ^oC for 1h), **g**. Population density of exsolved nanoparticles at different time durations (600 ^oC for 10 h, 600 ^oC for 20 h and 700 ^oC for 1h). 86

Figure 4.4. PXRD pattern of reduced and reoxidised materials **a**. PBFNO-600(10).Miller indices have been indicated for both structures whilst characteristic peaks relative to each structure have been assigned with the adequate colour for each pattern. **b**. PXRD pattern of PBFNO-600(20) reduced and reoxidised. Miller indices for the reduced samples correspond to the same ones as in the left image. No peak assignation could be done for the reoxidised pattern. Reoxidised materials share the colour code, as they were expected to be identical. 88
Figure 4.5. Temperature Programme Profiles of CH_4 activation **a.** PBFNO-600(10). **b.** PBFNO-600(20). Same reaction conditions apply for both materials. Ramp rates 10 ºC / min for both reactions until reaching ~820 ºC, keeping isothermal conditions for 30 min, when T profile was stopped and was not recorded any longer. SEM images of both materials after undergoing CH_4 activation. **c.** PBFNO-600(10), **d**. PBFNO-600(20). 89
Figure 4.6. Results of the 1% CH_4 – TPR with 0.350 g of *as sintered* PBFNO, conducted at ESRF. **a**. Gas outlet vs time. Molar fraction of gases (left) and temperature (right). **b**. Metallic phase (named as *fcc Ni wt.%*, left) and metallic phase cell size (*fcc Ni cell size*, measured in Å, right) variation with time. **c.** NiO phase (named as *NiO wt.%*, left) and NiO phase unit cell variation (*NiO cell size*, measured in Å, right) All the parameters plotted share the X-axis (Time, min). Figures have been plotted together to facilitate the visualisation of the *operando* experiment. X-axis (Time) is shared for all of them. 91
Figure 4.7.**a**. Fe-Ni phase diagram originally elaborated from experimental data (Swartzendruber, Itkin and Alcock, 1991). **b**. fcc Ni cell expansion calculated from the literature (orange) vs Temperature. Experimental fcc Ni value (green) has been added to the graph. 93
Figure 4.8. Zoomed of obtained *in situ* PXRD pattern (8.5º < 2θ < 10.5º) where the transition from NiO (9.7º) to fcc Ni (9.8º), or alloy is observed. **a.** Front view. **b.** View from above. Images correspond to superposition of PXRD patterns collected at ESRF. The colour map displays the variation of the PXRD patterns and peak positions with temperature. Images directly taken from TOPAS Academic v7 after conducting Rietveld refinement. 95
Figure 4.9. Different phases percentage variation (left) for 0.350 g of the *as sintered* 0.1 deficient A-site PBFNO reduction under CH_4-TPR. Results extracted from Rietveld refinement, and main perovskite unit cell variation (right) vs Time. Results give an approximate variation of the different weight fraction of the species found in the PXRD spectra. As highlighted before, NiO wt.% was dismissed after the 35^{th} min. 95
Figure 4.10. Zoomed area in **a**, 2θ for the peak corresponding to metallic fcc Ni angle. **b**. Peak deconvolution of the PXRD peak presented in a, translated into Particle size (nm). Images courtesy of Kousi, Neagu, Bekris, Papaioannou, et al. (2020)(2020)(2020)(2020)(2020)(2020). **c**. PXRD pattern obtained at ESRF for further peak deconvolution at the angle of metallic fcc Ni. 97
Figure 4.11. Results of the in situ 3%-TPO of 0.083 g of PBFNO-600(10) after conducting Rietveld refinement of the PXRD patterns obtained at ESRF. **a**. Main perovskite percentage phase (left y-axis) and temperature (right y-axis) vs Time (h). **b**. FeNi alloy and secondary phase percentages (left y-axis), PBFNO unit cell variation (right y-axis) vs Time (h). Graphs **a** and **b** are sharing x-axis. Error bars not displayed given the large amount of points as they would hide the visibility of the actual graph line. 99

Figure 4.12. Results of the 1% CH_4 – TPR with 0.094 g of PBFNO-600(10), conducted at ESRF. **a**. Gas outlet composition obtained by MS, represented by molar fraction of gases (left) and temperature (right). **b**. Metallic phase (named as fcc Ni wt.%, left) and metallic phase cell size (right) variation with time. Data obtained as result of PXRD peaks refinement. **c**. NiO phase wt.% (left) and NiO cell size (right). All the parameters plotted share the X-axis, Time (min), only displayed at the bottom graph. 102
Figure 4.13. Different identified and refined phases percentage (left) when conducting a 1% CH_4-TPR for 0.093 g of reoxidised 0.1 deficient A-site PBFNO. Right axis displays PBFNO unit cell variation vs Time (min). All the plotted features were obtained via Rietveld refinement. As stated previously, the weight fraction from NiO was discarded after the 60th min of reaction, as its presence lacked chemical implication..... 104
Figure 4.14. Zoomed PXRD pattern (6.8º < 2θ < 10.5º) where the transition from NiO (9.7º) to fcc Ni (9.8º), or alloy is observed. **a**. Front view (above image). **b**. View from above (bottom image). Images correspond to superposition of PXRD patterns collected at ESRF, images taken from TOPAS Academic v7 after conducting Rietveld refinement. ... 105
Figure 4.15. Comparison of the oxygen released (left axis) by the OCM after undergoing CH_4 reduction at 600 ºC. Oxygen released measured with the different oxygen-containing gases (O_2, CO and CO_2) in the outlet during the CH_4-TPR conducted at ESRF..... 106

Figure 5.1. CLSRM experiments to find the optimal temperature for the process while using 0.23 g PBFNO-600(10). Each temperature was kept for 15 cycles, gas flows were of 80 mL / min of each reactant gas (5% CH_4 and 6.5% H_2O). First 15 cycles were carried at 730 ºC and temperature was incremented 20 ºC every 15 cycles until reaching 790 ºC. **a**. Gas conversion versus cycle number as a function of cycle number, over 60 cycles. **b**. CH_4 conversion and CO, CO_2 selectivity values as a function of cycle number. 111
Figure 5.2. CH_4 and H_2O conversion variation for the half cycle duration time optimisation of CLSRM. Cycles were conducted at isothermal conditions (790 ^oC). Gas flows were of 80 mL / min per reactant gas (5% CH_4 and 6.5% H_2O). Cycle duration was modified every 15 cycles. Three zones are identified in the graphs: forty-five redox cycles were undertaken at isothermal conditions varying the time every fifteen cycles: left region, 60 s, middle region, 48 s, right region, 120 s. 113
Figure 5.3. Selectivity variation for the half cycle duration time optimisation in CLSRM. Cycles were conducted at isothermal conditions (790 ^oC). Gas flows were of 80 mL / min per reactant gas (5% CH_4 and 6.5% H_2O). Cycle duration was modified every 15 cycles. Three zones are identified in the graphs: forty-five redox cycles were undertaken at isothermal conditions varying the time every fifteen cycles: left region, 60 s, middle region, 48 s, right region, 120 s. **a**. Syngas (H_2:CO) ratio versus cycle number for each CH_4 half-reduction cycle. **b**. Product selectivity corresponding to the OCM reduction (CH_4 to CO and CO_2). 115
Figure 5.4. Representative shape of CH_4 conversion half-cycle CH_4. **a**, 60 s. **b**, 48 s and **c**, 120 s. 116
Figure 5.5. CH_4 (red) and H_2O (beige) conversion of reoxidised PBFNO-600(10) in CLSRM vs time, represented as cycle number, for 400 cycles. Half cycle duration of 60 s, gas feeds were 5% mol CH_4 and 6.5% mol H_2O, 100 mL / min. 118

Figure 5.6. Half cycle duration time optimisation for CLSRM. **a**. Syngas (H_2:CO) ratio versus cycle number for each half-reduction cycle. **b**. Product selectivity corresponding to the OCM reduction (CH_4 to CO and CO_2).....119
Figure 5.7. Outlet composition vs time for the long-term experiment for PBFO. **a**. 5th cycle, **b**. 100th cycle, **c**, 200th cycle, **d**. 300th cycle **e**. 400th cycle. Gas flow used: 5% CH_4 and 6.5% H_2O, both balanced in He. 121

Figure 6.1. Characterisation of A-site tailored ferrites. a) Schematic of the crystal structure $Sm_{0.5}Ba_{0.5}FeO_3$ (SBFO, top) and $Pr_{0.5}Ba_{0.5}FeO_3$ (PBFO, bottom). Visible difference in cationic size is represented by green (smaller, Sm) and purple (larger, Pr) cations. **b)** Synchrotron X-Ray patterns of the *as sintered* PXRD patterns of the *as sintered* samples. hkl indexing corresponding to the perovskite phase on top of each peak. **c)** Example of Rietveld refinement of a single-phase perovskite. **d)** Oxygen non-stoichiometry of *as sintered* SBFO and PBFO, calculated by iodometric titration. Microstructure, by SEM images of *as sintered* SBFO, **e)** and PBFO, **f)**. 130
Figure 6.2. Characterisation of B-site Ni-doped ferrites. **a.** Schematic depicting the substitution of both the A and B-site in a $BaFeO_{3-\delta}$. Visible difference in cationic size is represented by green (smaller, Sm) and purple (larger, Pr) cations. **b.** Synchrotron X-ray patterns of the *as sintered* samples. hkl indexing corresponding to the perovskite cubic phase on top of each peak. Superposition of SBFO and SBFNO for observation of peaks shape variation, **c**. Catalysts microstructure, represented by SEM images of as-sintered SBFO, **d.** and PBFO, **e**. 131
Figure 6.3. Reducing the as-synthesised materials SEM images of catalysts after being reduced at 900 ºC for 10 h. In order, *r*-SBFO, *r*-SBFNO, *r*-PBFO, *r*-PBFNO **a-d**. Particle distribution size for Ni-doped catalysts SBFNO, **e**, PBNFO, **f**. XPS survey spectra of *r*-SBFO and *r*-SBFNO **g,** *r*-PBFO and *r*-PBFNO catalysts. **i**. Fe 2p of Sm-based catalysts **j.** Fe 2p of Pr-based catalysts and Ni 2p, **k** and **l** for both reduced samples. 132
Figure 6.4. Employing the newly prepared ferrites in rWGS. CO_2 conversion with temperature for reduced SBFO and PBFO **a.** and reduced Ni-doped counterparts **b**. Both graphs display an equilibrium curve for the tested temperatures. Products selectivity at different temperature for reduced SBFO and PBFO **c.** and reduced Ni-doped counterparts **d**. CO selectivity is represented with square (■) and CH_4 selectivity is represented with triangle (▲), **e.** Schematic representation of the concept presented here. 135
Figure 6.5. Catalytic testing of the reactivated materials. CO_2 conversion with temperature for reduced (●) and reactivated (◌) SBFO and PBFO **a**. and Ni-doped counterparts **b**. Both graphs display an equilibrium curve for the tested temperatures. Products selectivity at different temperatures for reduced (●) and reactivated (◌) SBFO and PBFO **c**. and reduced Ni-doped counterparts **d**. CO selectivity is represented with a square (■) and CH_4 selectivity is represented with a triangle (▲). Selectivity values are identical for the reactivated samples hence they might not be visible in the graphs. 136
Figure 6.6. Characterisation of reactivated materials SEM images of catalysts after being reduced at 600ºC for 1 h after undergoing exsolution at 900ºC for 10h, subsequent reoxidation at 600ºC for 30 min. In order: ra-SBFO, ra-SBFNO, ra-PBFO, ra-PBFNO, **a-d**.137

List of Tables

Table 1.1. Different oxidation states and names different phases receive for Fe-based system (Jeong, Lee and Bae, 2015). 13
Table 1.2. Summary of the main types of materials used in CL processes for H_2 and syngas production in the literature. 22

Table 3.1. Structural properties obtained by PXRD and Rietveld refinement of the prepared materials, PBFO and SBFO. 46
Table 3.2. Oxygen vacancies values, δ, and corresponding B-site valence of OCM in the as sintered state and after undergoing one 5% H_2 reduction at 875 ºC during 1 h. As sintered values cannot be obtained via TGA. 49
Table 3.3. Buffer gases ratio ($CO:CO_2$) and the flowing order through the system 53
Table 3.4. Oxygen balance for representative cycles selected between the 400 cycles conducted for SBFO. 66
Table 3.5. Oxygen balance for representative cycles selected between the 400 cycles conducted with PBFO 69

Table 5.1. Amount of each product quantity, calculated at the outlet of the stream..... 115

List of Publications

Part of the results of this thesis have been published in the following:

Conference Article. Martinez Martin, A, Kousi, K., Neagu, D., Hu, W., Metcalfe, I. "$Ln_{0.5}Ba_{0.5}FeO_{3-\delta}$ (Ln = Pr, Sm) as novel Oxygen Carrier Materials for Chemical Looping Water-Gas Shift". *6th International Conference on Chemical Looping*, **2022**.

Research Article. Alex Martinez Martin, Shailza Saini, Dragos Neagu, Wenting Hu, Ian S. Metcalfe, Kalliopi Kousi. "Tailoring the A and B site of Fe-based perovskites for high selectivity in the reverse Water-Gas Shift reaction." *Journal of CO_2 Utilisation*, **2024**, *83*, 102784.

Whilst conducting this PhD I have actively participated in collaborative research projects, although not related to my primary research focus, have resulted in significant publications. These contributions merit acknowledgment:

Research Article. Atta ul Haq, Fiorenza Fanelli, Leonidas Bekris, Alex Martinez Martin, Steve Lee, Hessan Khalid, Cristian D Savaniu, Kalliopi Kousi, Ian S Metcalfe, John TS Irvine, Paul Maguire, Evangelos I Papaioannou, Davide Mariotti. "Dielectric barrier plasma discharge exsolution of nanoparticles at room temperature and atmospheric pressure." *Adv. Sci.*, **2024**. 2402235.

Research Article. Antonio Hernandez-Manas, Alex Martinez Martin, Johan Madignier, Pascal Fongarland, Frederique Bertaud, Lea Vilcocq, Laurent Djakovitch. "Copper Catalyzed Alkaline Aerobic lignin depolymerization: Effect of botanical origin and industrial extraction process on reactivity supported through characterizations." *RSC Sustainability*, **2024**. Manuscript under revisions.

Research Article. Daniel M. Telford, Alex Martínez Martín, Matthew D. Guy, Paul F. Henry, Martin O. Jones, Wenting Hu , Ian S. Metcalfe , John S.O. Evans. "Super-equilibrium hydrogen production: spatially-resolved operando neutron diffraction studies of a non-conventional reactor." *Nature Chemical Engineering,* **2024**. Manuscript under revision.

Additional Lists

List of Conference Contributions

Oral Presentations

- Sept. 2022 **6th International Conference on Chemical Looping**
  Zaragoza, Spain
  '$Ln_{0.5}Ba_{0.5}FeO_{3-\delta}$ (Ln = Pr, Sm) as novel Oxygen Carrier Materials for Chemical Looping Water-Gas Shift'
  A. Martinez Martin, K.Kousi, D. Neagu, W. Hu, I. Metcalfe
- Jan. 2023 **UK Catalysis Conference 2023**
  Holywell Park, Loughborough, UK
  '*Lanthanide-based ferrites for CO_2 valorisation*'
  A. Martinez Martin, S. Saini, K.Kousi, D. Neagu, W. Hu, I. Metcalfe

Poster Presentations

- Aug. 2023 **Europacat 2023**
  Prague, Czech Republic
  '*Lanthanide-based ferrites perovskites for catalytic rWGS*'
  A. Martinez Martin, S. Saini, D. Neagu, W. Hu, I. Metcalfe, K.Kousi

Contributions

- Sept. 2023 **3rd International Conference on Applied Science and Engineering**
  Paris, France
  Oral Presentation contribution to '*Selective Oxygen Carrier for Low-Carbon Ethylene Oxide Production via Chemical Looping*'
  D. Majumder, A. Martinez Martin, K. Kousi, I. Metcalfe, E. Papaioannou
- Jun. 2023 **Symposium Royal Society of Chemistry**
  London, UK
  Poster contribution to *'Lanthanide-based ferrites perovskites for catalytic rWGS'*
  S. Saini A. Martinez Martin, D. Neagu, W. Hu, I. Metcalfe, K.Kousi

Summer School & Public Engagement Events

- Jul. 2022 **Catalysis: Fundamentals and Practice Summer School 2022**
  University of Liverpool, Liverpool, UK

Chapter 1 Introduction

1.1. Hydrogen as an energy carrier, use and transport

Considered as the energy vector of the future, hydrogen (H_2) is expected to replace fossil fuels within the next decades as an energy carrier. H_2 can be obtained from clean and renewable sources. H_2 combustion generates only H_2O as product and the high exothermicity of the process makes H_2 the best candidate for the energetic transition and to target the Net Zero economic objectives. Thanks to the energy generated in its combustion (see Eq 1.1), 1 g of H_2 produces the same amount of energy as 2.8 g of gasoline, H_2 can be used in internal combustion engines in the automotive industry (Farias *et al.*, 2022).

$$H_2 + 0.5O_2 \rightleftharpoons H_2O, \Delta H_{298\,K} = -286\ kJ\ /\ mol \qquad \text{Eq 1.1}$$

For instance, H_2 is used in the ammonia (NH_3) production, in the Haber-Bosch process. Generation of NH_3 consumes 50% of the total H_2 produced (Abdalla *et al.*, 2018). NH_3 is a key compound not only in the production of fertilisers and food, but also in other industrial processes, such as the production of nitric acid, nylon, pharmaceutical or even the production of explosive materials (Ghavam *et al.*, 2021). In several chemical industries, H_2 is used as reduction agent in large scale, such as in the saturation of oils in the food industry or in the conversion of sugars to polyols (Abdalla *et al.*, 2018). Other uses of H_2 comprise the production of methanol, considered a building block in industries such as the pharmaceutical industry, or its use in electronics or the aerospace industry (Abdalla *et al.*, 2018).

However, the requirements for H_2 transport and storage vary from those for H_2 use. According to Allendorf et al. (2022), the slow pace of infrastructure development is among the major barriers for H_2 transport and storage. Associated to these challenges, there is the generation of low-carbon H_2. Hydrogen-rich molecules can act as H_2 reservoirs, as it is the case of metal hydrides, NH_3 or liquid hydrocarbons. On the other hand, Liquid Organic Hydrogen Carriers (LOHC, such as aromatic hydrocarbons), which offer reversible (de)-hydrogenation, can be adapted to the existent infrastructures and can avoid carbon emissions in the production of H_2. The challenge associated with them is to find a suitable catalyst that carries out both processes.

1.2. H_2 production

1.2.1. Overview

H_2 can be obtained from several different processes and can be classified into multiple categories according to the production process, the feedstock, etc. No classification is intended here and only the main industrial methods will be explained. Several reviews concerning the types of H_2 obtention have been recently published regarding that purpose (Dawood, Anda and Shafiullah, 2020; Huang, Balcombe and Feng, 2023). The focus of this thesis is on the generation of blue H_2, which consists of the obtention of H_2 from H_2O or fossil fuels without emission of CO_2 to the atmosphere (AlHumaidan *et al.*, 2023). However, different methods should be mentioned in order to provide a wider approach of the possibilities of producing H_2.

Still today, 96% of the total H_2 is produced through thermochemical processes (Xu, Zhou and Yu, 2022). Most of the H_2 industrially produced worldwide is linked with large carbon emissions, as it relies on carbon-based fuels. Therefore, efforts are done in the scientific community to switch towards greener ways of generating it.

NH_3 decomposition into its elements is another source of H_2. However the use of NH_3 as source of H_2 is not commercially spread (Cha *et al.*, 2021). Other methods of H_2 production involve the use of electricity via the use of fuel cells and membranes or the use of light as feedstock, although the latter is still in early stages of development. Finally, biological methods are an alternative way of producing H_2, among which, dark fermentation has gained relevance in the last years for clean H_2 production (Jain *et al.*, 2022).

1.2.2. Steam Reforming of Methane

50% of all the H_2 produced worldwide comes from natural gas via different processes such as steam reforming of methane process (SRM), partial oxidation and autothermal reforming (Iulianelli *et al.*, 2016). SRM is a long catalytic process with many steps involved (see Figure 1.1). Firstly, CH_4 and H_2O undergo a desulphurisation step to remove impurities from the gas feed before they poison the catalyst. Secondly, this gas feed reacts at high temperatures and pressure (typically 700 ºC < T < 1450 ºC and 14-20 bar, (Levalley, Richard

and Fan, 2014; Meloni, Martino and Palma, 2020), given the endothermic nature of the reaction to generate syngas ($CO + 3H_2$).

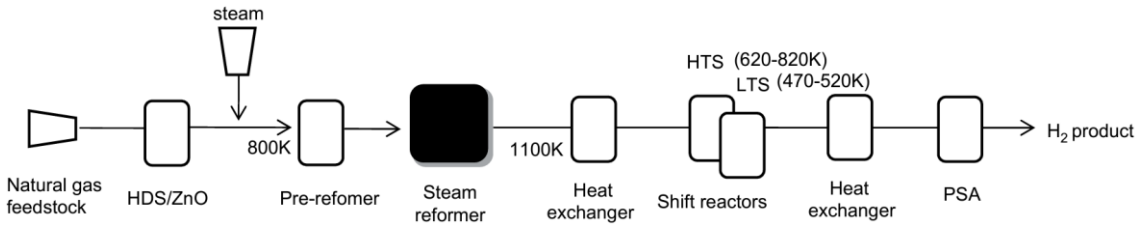

Figure 1.1 Simplified scheme of a conventional SMR process. *HDS* corresponds to hydrodesulfurization unit. *HTS* and *LTS* refers to high and low temperature shift, respectively. Image courtesy of Go et al (2009).

Typically, Ni-based catalysts are the ones mostly used in the process to activate CH_4 (Meloni, Martino and Palma, 2020). The products are subsequently cooled down to 200 ºC – 500 ºC, and CO is further oxidised in the water-gas shift (WGS) process (Eq 1.3). This CO oxidation generates CO_2 and H_2, increasing the H_2 to carbon ratio. A final separation process is required to purify the obtained H_2, known as pressure swing adsorption (PSA).

$$CH_4 + H_2O \rightleftharpoons 3H_2 + CO, \Delta H_{298\,K} = 206.3\ kJ\ /\ mol \qquad \text{Eq 1.2}$$

$$CO + H_2O \rightleftharpoons H_2 + CO_2, \Delta H_{298\,K} = -41\ kJ\ /\ mol \qquad \text{Eq 1.3}$$

Generally, SRM generates a high H_2 to carbon ratio, 4 mol of H_2 per 1 mol of CH_4, but many drawbacks are related to the process. It is considered an energy intensive process, given all the required steps to obtain pure H_2. Pure H_2 production is associated with large CO_2 emissions and the challenging task of capturing of the CO_2 generated. Secondary reactions, such as CH_4 cracking and the Boudouard reaction (Eq 1.4 and Eq 1.5, respectively), are present in the process, decreasing the overall efficiency (Damaskinos *et al.*, 2019). Ni-based catalysts are the most used materials in SMR. However, they tend to quickly deactivate. Park et al. (2017) defined the reason for this quick deactivation: carbon deposition onto the catalyst's surface (caused by CH_4 cracking and Boudouard reaction), sulphur poisoning, and particle sintering (caused by the high temperatures involved in the process). Another associated problem to SRM is the high process cost, such as the high temperature (typically T > 750 ºC), or the use of PSA for product separation and higher H_2 purity. Moreover, by implementing Carbon Capture and Storage (CCS) systems, it is estimated that H_2 production costs increase more than 20% (Luo *et al.*, 2018).

$$2CO \rightarrow C + CO_2 \qquad \text{Eq 1.4}$$

$$CH_4 \rightarrow C + 2H_2 \qquad \text{Eq 1.5}$$

After all the reactions and separation processes have taken place, the overall reaction for the SRM process is as follows in Eq 1.6:

$$CH_4 + 2H_2O \rightleftharpoons 4H_2 + CO_2, \Delta H_{298\,K} = -165.3\ kJ\ /\ mol \qquad \text{Eq 1.6}$$

The high energy demand of this process and the low process stability are among the main drawbacks of SRM, which is installed as a mature technology (Chen *et al.*, 2020), but efforts are yet to be made to achieve high CO selectivity and catalysts that avoid carbon deposition.

1.2.3. Partial Oxidation of Hydrocarbons

Considered a faster method than SMR (Chaubey *et al.*, 2013), partial oxidation of hydrocarbons (POX) requires a lower amount of oxygen for the combustion of C_nH_m species to generate H_2 and CO (see the general formula, Eq 1.7). Hydrocarbons used as feedstock can be short carbon chains (C1) up to naphtha (C_n).

$$C_nH_m + (0.5m)O_2 \rightarrow (0.5m)H_2 + nCO \qquad \text{Eq 1.7}$$

This reaction can be non-catalytic (usually T > 1000 ºC) or catalytic (650 ºC < T < 1000 ºC), generally using Ni-based catalysts. To increase the overall H_2 formation additional steps are also involved, such as the WGS reaction to transform CO to CO_2 by reducing H_2O to H_2, with its consequent undesired emissions. As in SRM, separation processes are involved, increasing the energy demand of the process and, thereby, its overall cost.

Generally, Ni tends to be the most used catalysts, although some other transition metals (Fe, Co) with high selectivity towards H_2 are also used (Sengodan *et al.*, 2018). However, these catalysts tend to suffer from the same issues as stated before: carbon deposition and they are prone to sintering . Although noble metals may avoid these issues, their use is less recommended given the high environmental and cost impact they entail (Vieira *et al.*, 2023).

1.2.4. Coal Gasification

Coal gasification involves the thermo-chemical conversion of carbon-based materials to produce H_2 and other added-value products, such as syngas. It allows the conversion of different raw materials, going from coal to car tyres, that generate higher quality products and yield, compared to other traditional methods (Midilli *et al.*, 2021). Nonetheless, it is challenging to achieve optimal H_2 production, due to the high temperatures required ($T > 1000\ ^oC$), according to Dai et al. (2023), generating CO_2 as byproduct. Consequently, separation steps are needed, contributing to the increased cost of the process.

1.2.5. H_2 from renewable sources

A method that gained popularity recently is H_2O electrolysis, in which the H_2O can be dissociated into gaseous H_2 and O_2 in a process known as water splitting via the transfer of electrons to a metal/electrolyte that carries out this reaction (Grigoriev *et al.*, 2020). According to these authors, commercially available electrolysers operate between room temperature (RT) and 100 ºC. Among the different possible electrolysers, three are the most mature technologies: alkaline water electrolyte (AWE), the proton exchange membrane (PEM), and the solid oxide electrolysis cells (SOEC).

However, these methods suffer from different drawbacks. In their review, Emam et al. (2024) state that AWE electrocatalysts are yet underdeveloped and the best results are still obtained with noble metals instead of transition metals, increasing thus costs and environmental impact. PEM anodes possess stability issues and cathodes without noble metals have reduced activity when compared to cathodes that are loaded with noble metals. PEM cell lifetimes are still short and capital costs are higher-than-average (Simoes *et al.*, 2021). SOEC entail rapid degradation of the material in short times and require elevated temperatures.

1.3. Chemical Looping for H_2 production

1.3.1. Concept and applications

In the context of looking for alternative processes capable of overcome certain issues highlighted in the traditional methods for H2 production, chemical looping (CL) has gained

interest in recent times. While CL can be used for various processes, this thesis focuses on the obtention of H_2. Other CL processes, such as CL combustion, lay out of this scope.

Fan (2011) described CL as a reaction split into sub-reactions separated in time by a chemical intermediate. Different types of CL reactions can be identified but the primary research focus will be the Type I, as it is the one implemented in the processes described in the following chapters. Typically, Type I looping systems occur at high temperatures where redox reactions take place in one (Figure 1.2) or more than one separate reactors, that are the reducer and the oxidiser/combustor. The reducer carries out the material reduction by transforming the reactant into its oxidised forms. This is achieved by depleting the material from its available oxygen, leading to the production of added-value chemicals, liquid fuels and electricity (Gupta *et al.*, 2011). Subsequently, the material replenishes its structure with oxygen provided by the oxidising agent. This cycle can be repeated multiple times over a period of time. These materials that release and regain oxygen receive the name of Oxygen Carrier Materials (OCM), whose study and characteristics will comprise a further study within this introduction chapter. In CL there is no contact between the gas streams and the oxygen exchange between the streams is via the OCM, eliminating possible side reactions.

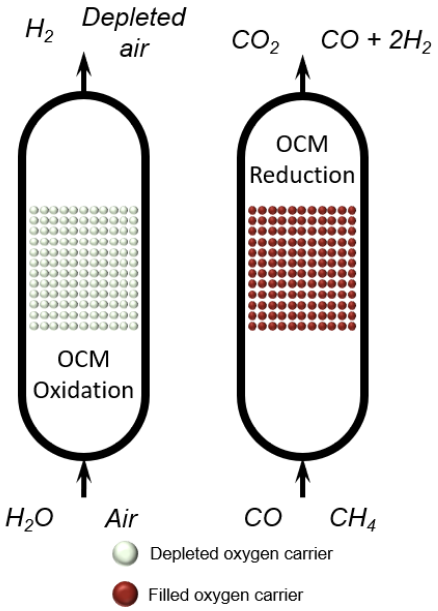

Figure 1.2. General schematic for a CL H_2 production process. OCM acronym corresponds to *oxygen carrier material*.

Using CL reactors results in avoiding energy-intensive and high-cost separation steps, such as PSA, defined previously for SMR to separate the added-value H_2 from byproducts such

as CO_2. Consequently, thanks to the lack of separation steps, high purity H_2 is yielded, operational costs are significantly reduced, also facilitating the capture of already pure CO_2 from the reactor outlet. Moreover, CL allows for higher conversions than conventional catalytic processes (Metcalfe *et al.*, 2019). Typically, CL processes can generate H_2 in different ways: by oxidising the OCM with H_2O and by partial oxidation of hydrocarbons and subsequent generation of syngas, etc. Two processes are the primary research of this study: Chemical Looping Water-Gas Shift (CLWGS) and Chemical Looping Steam Methane Reforming (CLSRM).

Even though the term 'chemical looping' was coined in 1987, similar processes were already used in 1903 by Howard Lane (Bayham *et al.*, 2016). However, this technology is yet to be developed and implemented on larger scale, with only few facilities developing CL processes at pilot scales (Lyngfelt *et al.*, 2019). In the last years, only one recent successful CL application in the UK has been the Cranfield's 25 kWth calcium looping pilot plant (Anthony and Patchigolla, no date).

1.3.2. Chemical Looping Water-Gas Shift

In Chemical Looping Water-Gas Shift (CLWGS), a carbon monoxide (CO) stream enters the reactor, depleting the OCM from the available oxygen and producing pure CO_2. This step is known as CO oxidation (Eq 1.8). H_2O is the oxidising agent and is transformed into H_2 by providing oxygen to the now oxygen depleted OCM. This step is known as Chemical Looping Water Splitting (Eq 1.9).

$$CO + O[OCM] \rightleftharpoons CO_2 + [OCM] \qquad \text{Eq 1.8}$$

$$H_2O + [OCM] \rightleftharpoons H_2 + O[OCM] \qquad \text{Eq 1.9}$$

CO is used as reducing agent to maximise CO_2 yield, given its low tendency towards carbon deposition at high temperatures ($\Delta G > 0$, see Figure 1.3). Therefore, selectivity issues are reduced. However, using CO as reducing agent is not a realistic scenario, since CO needs to be generated from another source, generally from CH_4, and undergo further separation processes.

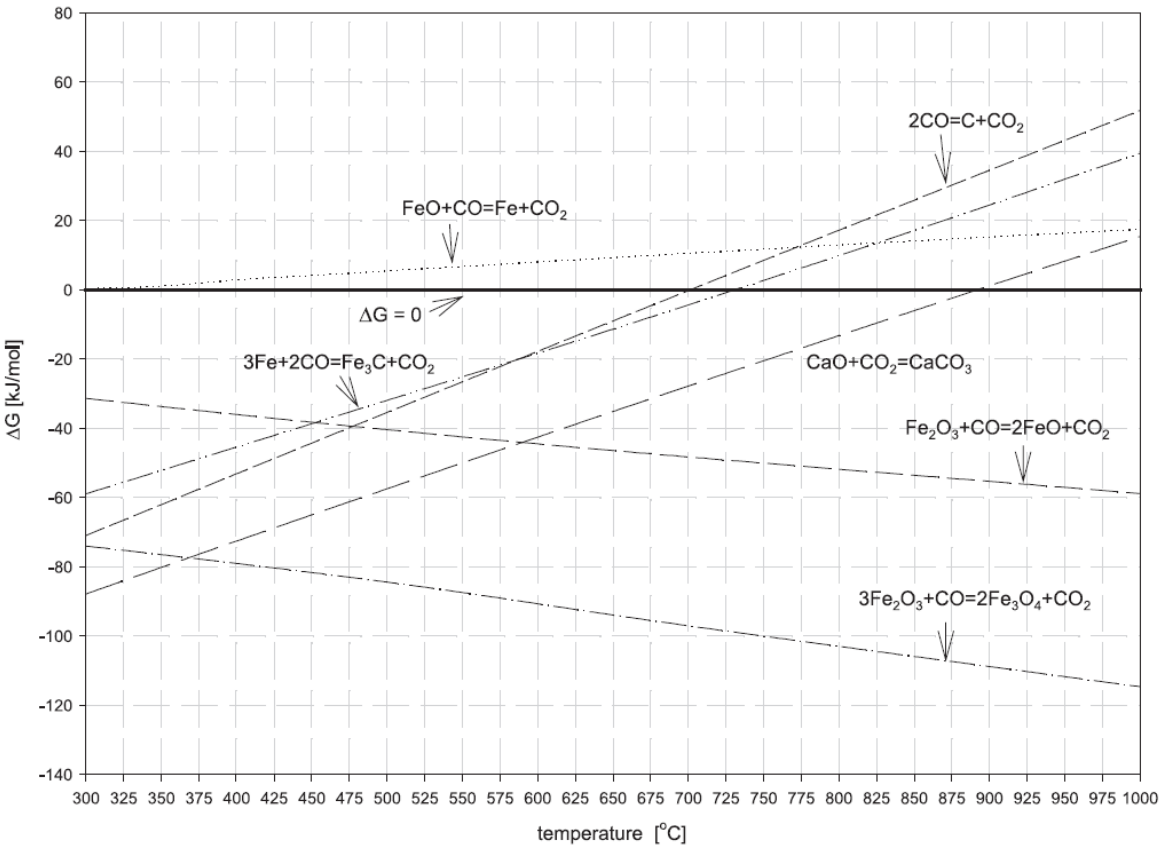

Figure 1.3. Gibbs free Energy vs Temperature (Ellingham diagram) for iron oxide systems and carbon monoxide as reactant. Image taken from Mondal et al. (2004).

1.3.3. Chemical Looping Steam Reforming Methane

Chemical Looping Steam Reforming of Methane (CLSRM) becomes a more attractive technology since two added-value chemicals are generated in the same process: syngas and pure H_2. The CO generated as part of the syngas product can be separated from the H_2 and be transformed into CO_2 via WGS, generating a larger amount of H_2 (4 mol of H_2 per 1 mol of CH_4 used as reactant), as previously explained in the conventional SMR. Generally, in CLSRM, CH_4 is partially reduced by the OCM, yielding syngas (Eq 1.10). Subsequently, the OCM is reoxidised by H_2O in the steam reactor (Figure 1.4.a), generating H_2 (Eq 1.11), easy to separate from the unreacted H_2O by simple condensation. However, an additional Air reactor can be added to the system to achieve full OCM oxidation (Figure 1.4.b). Thereby, the overall process is as shown below:

$$O_x[OCM] + \delta_2 CH_4 \rightarrow O_{x-\delta_1-\delta_2}[OCM] + \delta_2(H_2 + CO) \qquad \text{Eq 1.10}$$

$$O_{x-\delta_1-\delta_2}[OCM] + \delta_2 H_2O \rightarrow O_{x-\delta_1}[OCM] + \delta_2 H_2 \qquad \text{Eq 1.11}$$

$$O_{x-\delta_1}[OCM] + \frac{\delta_2}{2} O_2 \rightarrow M_y O_x \qquad \text{Eq 1.12}$$

where O[OCM] is the oxygen carrier material, $M_yO_{x-\delta_1}$ and $M_yO_{x-\delta_1-\delta_2}$ correspond to the reduced oxygen carrier material at different reduction degrees (δ_1 and δ_2). An air reactor is eventually added if the OCM requires further reoxidation (Eq 1.12). This way, by avoiding mixing streams, purification steps are avoided. However, even though the process is simplified compared to the conventional SMR, secondary reactions are possible to take place. If conducting CLSRM at T > 800 ºC, Boudouard reaction displays a low equilibrium conversion, and it is therefore unlikely to occur. However, carbon deposition is not thermodynamically limited (Murugan, Thursfield and Metcalfe, 2011). If carbon deposition occurs, it would be eliminated upon reoxidation with the steam flow. In this case, the oxidation stream would yield impurities, incurring extra costs, as the produced H_2 would be mixed with the carbonaceous products. It is therefore necessary to operate with highly carbon deposition resistant OCM that avoid this undesired side reaction.

Initially presented by Mattisson & Lyngfelt (2001), CH_4 as reducing agent entails the drawback of poor selectivity and tendency to create carbon deposition. However, this selectivity towards CO_2 or CO can be tailored depending on the available oxygen in the carrier material – or its equivalent in oxygen partial pressure (pO_2): high pO_2 will favour the combustion of CH_4 and generate CO_2 (Eq 1.13), whilst a more reducing environment (i.e., lower pO_2) will favour the partial oxidation of CH_4 and form CO (Eq 1.14). The latter is desired given the high economic value in the chemical industry. By promoting partial oxidation of CH_4, the OCM would not undergo total reduction, limiting the amount of H_2 generated, even though this can be increased via WS in the oxidation step.

The lack of a WGS reactor step and a CO_2 separation step, as side reactions are avoided, and the lack of H_2 purification step, are among the main benefits of CLSMR. Furthermore, the introduction of the air reactor allows for elimination of any possible contaminants beyond carbon deposition, such as sulphur, and can help increase the conversion of the fuels in the next steps by fully re-oxidising the OCM.

$$CH_4 + 2O_2 \rightarrow CO_2 + 2H_2O \quad \text{Eq 1.13}$$

$$CH_4 + 0.5O_2 \rightarrow CO + 2H_2 \quad \text{Eq 1.14}$$

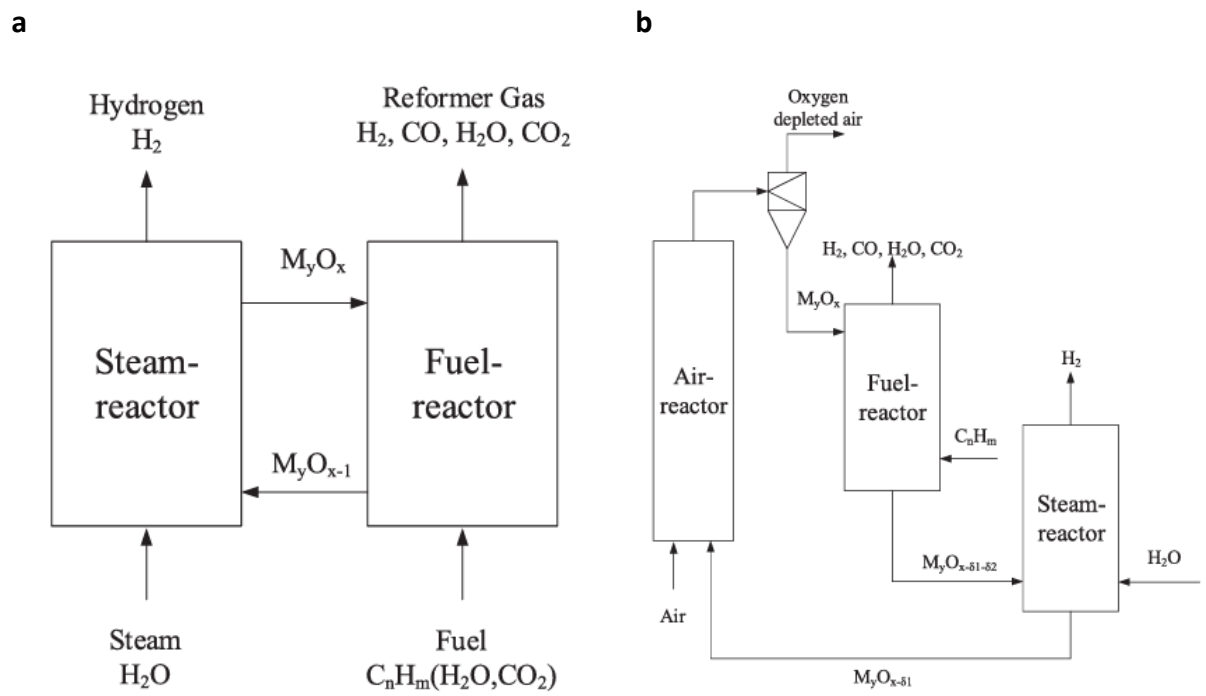

Figure 1.4. Schematic representation for the CLSRM process for H_2 and syngas production, with **a**. two reactors, and **b**. three reactors, where the Air-Reactor has been included. Image courtesy of Luo et al. (2018).

1.4. Oxygen Carrier Materials

This section provides a review of all the characteristics associated to the choice of a suitable OCM for a CL process. In this chapter, a breakdown of the requirements of potential OCM is accounted for. In this chapter, a breakdown of the requirements an OCM needs to possess as a potential material for a CL process will be accounted for. A summary of the most used metals/metallic oxides systems for CLWGS and CLSRM will be done, which are the processes of interest for this thesis. In CL, most of the studied reactions are gas-solid and consequently all the literature review and subsequent chapters will only emphasise this type of reaction, excluding liquid-solid and solid-solid processes.

1.4.1. Choice of OCM

OCM are materials with the ability of exchanging oxygen with the reactants. It functions as an intermediate to provide oxygen atoms between the two reactants: it gives oxygen to the fuel (reducing agent) and, in the following reaction, incorporates oxygen within its lattice by taking it from an oxidising agent.

The choice of a suitable OCM for CL purposes is of paramount importance for the overall process to be scaled up . In previous reviews, different authors such as Voitic & Hacker (2016), or Das et al. (2022) have gathered different features an OCM should embody:

- It should possess the ability to release and gain oxygen during several cycles.
- It should have a large oxygen storage capacity (OSC) and be capable of acting as an oxygen reservoir.
- Favourable thermodynamics and reactivity at the working oxygen partial pressure (pO_2).
- High reactivity when oxidising fuels (for instance, high reactivity towards CH_4 in CLSRM)
- Structural stability and constant conversion values extended in time.
- Low tendance to carbon deposition, and resistance to sintering, attrition, and other deactivation processes.
- Ideally, OCM synthesis is an economic and environmentally friendly synthetic process, and widely available raw materials as precursors for its synthesis.

These are the overall requirements an OCM should typically gather for a general CL process. However, depending on the reaction type, or the reactor used, specific requirements might apply. In recirculating fluidised bed reactors, the residence time of the flowed gas is longer than in other systems. Therefore, OCM require an enhanced resistance to deactivation (Sharma, Delebarre and Alappat, 2014), beyond other mechanical aspects that exceed the scope of this thesis. When using packed bed reactors, the appropriate particle size is needed to avoid pressure drops. In this case, the scope of the thesis is the development of a novel OCM suitable for CLWGS and CLSRM in a packed bed reactor. Other possible factors affecting fluidised bed reactors have not been taken into consideration. Furthermore, the small amounts of solid used (and consequently the short material bed length) were not expected to have a meaningful impact on the cycles in the long term.

In the case of the two CL processes pictured in this work, both share the same OCM half-oxidation reaction, being this CLWS. CLWS is kinetically limited (Z. Zhao et al., 2016a)(Z. Zhao et al., 2016), and the total production of H_2 is determined by this step. Thereby finding an OCM capable of overcoming this chemical challenge whilst maintaining its activity towards the reducing agent is of utmost importance. When donating oxygen (and incorporating it) at different pO_2, OCM undergo phase changes. It is thereby expected that a suggested OCM for a CL is able to reversibly undergo phase changes covering the whole pO_2 in which the process takes place. These phase changes are accompanied by a change

in the oxidation state of the active metal. Higher oxygen transfer potential is achieved with higher number of transitions between oxidation states the metal can undergo. Nevertheless, larger transitions due to constant reductions and changes in the oxidation state imply that the lattice parameters of the cell would change, stressing the material and eventually, fragmenting it.

Given their larger abundance compared to other metals (X. P. Li *et al.*, 2021), such as elements from the Pt group, focus is put on the metals from fourth period. Metals from following periods are not as active, as abundant or their use is intended to be minimised, as it is the case of noble metals. With a focus on developing greener materials, studies involving the use of noble metals have been sidelined, despite acknowledging their efficacy in CL applications (Zhu *et al.*, 2020).

1.4.1.a. Iron oxide

Iron-based (Fe-based) oxygen carrier materials are among the best candidates for H_2 production from H_2O (Zacharias, Bock and Hacker, 2020). Fe appears as the most abundant metal on earth's surface, and it is relatively cheap compared to all the other metallic ores. Fe/Fe-oxide systems can display multiple oxidation states, depicted in Table 1.1. Haematite (Fe_2O_3) is the most oxidised Fe-based system, in which the oxidation state is +3. Another phase called magnetite (Fe_3O_4) is created when Fe atoms form a mixed oxide where both +2 and +3 oxidation states coexist. However, the oxidation of magnetite to haematite with only steam is thermodynamically impossible and it requires from an air reactor to recover this oxidation state (Bleeker, Kersten and Veringa, 2007). The most reduced iron oxide is called wüstite, where Fe oxidation state is +2. Finally, the most reduced oxidation state is metallic iron, Fe. Complete reduction to Fe promotes carbon deposition and therefore OCM deactivation (M. Zhu *et al.*, 2018). Furthermore, H_2O reoxidises the carbon deposited to CO and/or CO_2, creating a contaminated H_2 stream. An alternative to this would be the implementation of a third step (air-reactor). After partial reoxidation with H_2O in the OCM oxidation, in which concentrated oxygen is supplied and fully reoxidises the OCM, burning any possible trace of carbon deposition. On the other hand, reactivity towards CH_4 is lower as compared to H_2 or CO (Adanez *et al.*, 2012). Showed by Das et al. (2022), Fe_2O_3 promoted both coking (carbon deposition) during CH_4 oxidation and sintering due the high temperatures used in CL after repeated cycles, thus decreasing H_2 yield. Therefore, Fe-

based OCM might seem like good candidates for CL processes for H_2 production, even though many challenges are associated to them in the long-term.

Table 1.1. Different oxidation states and names different phases receive for Fe-based system (Jeong, Lee and Bae, 2015).

Oxidation state	Formula	Phase name
0	Fe	Metallic iron
+2	FeO	Wüstite
+2, +3, mixed valence	Fe_3O_4	Magnetite
+3	Fe_2O_3	Haematite

Aiming at overcoming these issues, Fe-based OCM have been modified by different authors. These modifications are focused on enhancing the structural stability and reactivity of the material. Aiming at enhancing the material life by reducing its reduction temperature and improving reaction rates, a thorough study was conducted by adding small doping of different compounds to Fe_2O_3 (Otsuka *et al.*, 2003). Al_2O_3, CeO_2, TiO_2, V_2O_5, NiO, Cr_2O_3, CuO were used, among other compounds. Species that preserved constant activity whilst able to decrease the reduction temperature were Ce, Al, and Mo.

Fe_2O_3 supported on different species has resulted in yield improvements in CL. Aluminium-based supports are the most widely supports used for Fe-based OCM (Adanez *et al.*, 2012). High efficiency and no deactivation signs were detected when using 60 wt.% Fe_2O_3 and Al_2O_3 after 40 h of continuous activity (Abad *et al.*, 2007). By confining in an Al-based structure the active Fe, the OCM designed for CH_4 reforming maintained its activity while ensuring an optimal syngas as product during 3000 cycles with no signs of OCM degradation (Chung *et al.*, 2017). CeO_2 as support for Fe-based OCM has proven to increase the number of oxygen vacancies and an intensification of the oxygen mobility, being able to constantly produce syngas in CLSRM (Zhu *et al.*, 2014). Adding ZrO_2 to this previous system also resulted in an enhancement, given the oxygen mobility provided by Zr^{4+}, facilitating the migration of oxygen atoms and higher reactivity (Zhu *et al.*, 2011). Sole ZrO_2 as support of Fe_2O_3 as OCM resulted in high-purity H_2 (> 99.9%) in the steam reactor (Cho *et al.*, 2014) when undergoing CLSRM. In general, supported Fe-based OCM increased yields, especially in CLWGS. One Fe-based system, using SiO_2 as support, did not however show that increase. Fe_2O_3 supported on SiO_2 exhibited a drastic decrease in conversion after only 10 cycles (Zafar, Mattisson and Gevert, 2005) due to the formation of unreactive Fe_2SiO_4.

Existing and current reports indicate that Fe-based OCM are suitable for H_2 production in the reaction of Water Splitting. The reduction of H_2O is however thermodynamically limited, requiring from Fe to be as reduced as possible, while oxidising the system beyond Fe_3O_4 after cycles without the help of an air reactor is difficult (Tang, Xu and Fan, 2015).

1.4.1.b. Nickel oxide

Unlike Fe-based systems, nickel (Ni) can only be found in two forms, Ni and NiO. This fact limits the oxidation states of this OCM and its oxygen capacity (Murugan, Thursfield and Metcalfe, 2011) for CLWGS. Compared to Fe-based systems, Ni-based OCM have been found to have decreased reactivity towards H_2O for H_2 production (Kuo *et al.*, 2013; Zhao *et al.*, 2021). Besides, Ni-based OCM are prone to sulphur poisoning when using CO streams, even at low sulphur concentrations (García-Labiano *et al.*, 2009). When combining a low Ni-doping and Fe systems, high H_2 production is achieved, while maintaining reversible reoxidation capacity (Wei et al., 2014a; Medeiros et al., 2017)(Wei et al., 2014a; Medeiros et al., 2017).

On the other hand, Ni-based OCM are the most extensively investigated material for CH_4 reforming in CL, on account of their high reactivity at high temperatures. However, despite their activity towards CH_4, their selectivity towards syngas is poor: they suffer from quick deactivation, they are toxic and expensive (Tang, Xu and Fan, 2015; Protasova and Snijkers, 2016)(Tang, Xu and Fan, 2015; Protasova and Snijkers, 2016). To overcome the challenges of deactivation and desired syngas selectivity, Ni-based supported OCM have been tested by different authors. These supports could affect the dispersion of the active Ni/NiO through the material, alleviating the issues occurred by sintering or decrease carbon formation on the material. The supports would also affect the oxygen mobility and, similarly to Fe-based OCM, decrease the reduction temperatures, therefore enhancing the OCM lifetime (Tang, Xu and Fan, 2015).

High reactivity, sintering and carbon deposition were avoided when supporting NiO on Al_2O_3 (Tang, Xu and Fan, 2015). A comparison between NiO/$NiAl_2O_4$ and NiO/$MgAl_2O_4$ was done by Johansson et al. (2008), highlighting that the first OCM exhibited less reactivity. However, Al_2O_3 as support partially inhibits reduction of NiO to Ni, by forming a low-reactive $NiAl_2O_4$ spinel (Dueso *et al.*, 2012). Unlike with Fe_2O_3, in this case, the use of SiO_2 resulted in elevated CH_4 conversion and high H_2 selectivity (Zafar, Mattisson and Gevert,

2005). NiO supported on ZrO_2 maintained constant CH_4 conversion during 20 cycles displaying minimal deterioration as compared to NiO supported on Al_2O_3 (Silvester *et al.*, 2015).

The positive outcomes obtained by using Ni-based OCM in CLSRM and CL combustion in different studies indicate that Ni is an adequate candidate for this process. Despite the drawbacks associated to its toxicity, elevated cost and tendency to deactivation, there are enough works to continue the modification of these OCM for CL involving CH_4 reforming and H_2 production from steam.

1.4.1.c. Other Metal / Metal Oxide systems

Fe- and Ni-based materials are the most widely investigated materials for H_2 in CL processes. However, other metallic systems involving other transition metals such as Cu-, Mn- or W-based OCM have been previously reported (Adanez *et al.*, 2012; Protasova and Snijkers, 2016; Luo *et al.*, 2018; Zhao *et al.*, 2021). Less toxic and cheaper than Ni-based OCM, Cu-based OCM show higher initial reactivity for H_2 production, although these Cu/CuO systems tend to agglomerate due to their low melting point Qasim et al., 2021). Addition of dopants such as Al_2O_3 also leaded to the formation of the spinel $CuAl_2O_4$ which, in this case, does not decrease its activity (Cao, Sit and Pan, 2014). The use of Al_2O_3 as support has also shown improvements in CH_4 reactivity, as previously reported by Son, Go and Kim (2009).

Mn-based carriers are cheap, environmentally friendly and their ability to exist within a large range of oxidation states (from 0 to +7) suggests a high OSC. However, at CL operating temperatures, it only exists as Mn_3O_4 (Zafar *et al.*, 2007). Thus, the only feasible transition is $Mn_3O_4 \rightarrow MnO$, limiting the available oxygen capacity. Qasim et al. (2021) also underlined the low oxygen transport capacity between this pair of Mn-based oxides and its tendency to attrition after CL cycles.

Tungsten possesses four oxidation states besides metallic tungsten (WO_2, $WO_{2.72}$, $WO_{2.96}$ and WO_3). WO_3 is thermodynamically favoured in both reduction by CH_4 and oxidation by H_2O (Zhao *et al.*, 2021). It was determined by Khan and Shamim (2017) that T > 1000 ºC are needed to produce high H_2 yield even though the redox processes are thermodynamically feasible. Previous studies involving the pair WO_3/W system for production of solar fuels

found out that W carbides and carbon deposition were formed when using CH_4 as reducing agent (Villafán-Vidales *et al.*, 2017). All these features led the scientific community to discard tungsten as a possible OCM for H_2 production in CL in the long-term.

1.4.1.d. Perovskite oxides

If compared to single metals, the preparation of mixed oxides as OCM serves multiple purposes. Firstly, it seeks to increase initial reactivity by improving the oxygen properties or reducing the activation energy. Secondly, it enhances stability in the long term by mitigating different forms of deactivation processes (either physical such as sintering or attrition, or chemical such as carbon deposition). Ultimately, this approach aims at incorporating toxic metals in reduced quantities, such as Ni.

Perovskites are a family of ABX_3 materials, where 'A' and 'B' are cations and 'X' is an anion. In this thesis, 'X' will always be 'O', oxide. Cubic is the ideal perovskite-type structure for these oxides. In a cubic perovskite, the A cation is 12-fold coordinated while the B cation, smaller than A, is 6-fold coordinated (Peña and Fierro, 2001)(Peña and Fierro, 2001). B-site cations have a structural role forming strong bonds with the oxygen, generating an octahedra, BO_6, and the A-site cations are in the centre of the cuboctahedra (see Figure 1.5).

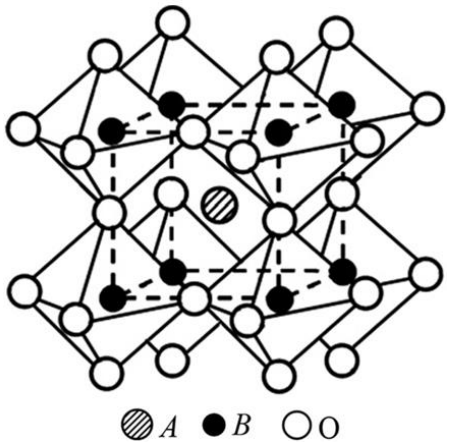

Figure 1.5. Ideal perovskite structure (ABO_3). Image courtesy of (Xu *et al.*, 2010).

The stability of the perovskite is defined by the tolerance factor, *t* (Goldschmidt, 1926), defined by the relationship between the radii of the different ions in Eq 1.15:

$$t = \frac{r_A + r_O}{\sqrt{2}(r_B + r_O)}$$ Eq 1.15

where r_A, r_B and r_O correspond to the ionic radii of A, B and O, respectively. The tolerance factor predicts the formation of a perovskite by studying the obtained value in the equation (Travis *et al.*, 2016; X. Li *et al.*, 2021): a perfect fit corresponds to t = 1. If $0.8 \leq t \leq 1$, perovskites are generally formed, even though distortion might appear at the lower values, occasioned by tilting and symmetry decrease of the BO_6 octahedra. If $t > 1$, the A-site cation is too big for the structure, often avoiding the formation of the perovskite. When $t < 0.8$, A-site cation size is not big enough to fit within the perovskite structure. This formation range accommodates a vast number of metallic elements, highlighting the high tailorability of this structure. Therefore, perovskites can host different metallic species in both A- and B-sites, allowing for potential diverse mixed oxides and thus to attain certain properties specific for CL applications. By doping or partially substituting the A- and/or the B-site, perovskites would possess the general formula $A_{1-x}A'_xB_{1-y}B'_yO_3$. This tailorability by substitution can alleviate the values of the tolerance factor that are off the ideal range and form then a stable perovskite (Goodenough, 2004). The incorporation of different elements can lead to an overall charge imbalance in the perovskite, which will ultimately generate vacancies (Zaidi, de Leeuwe and Spallina, 2024). It is worth mentioning that the tolerance factor is adapted to the substitution. Ionic radii will be a weighted average of the elements used in the A- and B-site.

Perovskites are materials that can easily accommodate defects within their lattice to tune certain physical-chemical properties, such as OSC or ionic mobility. These defects can be accommodated by size, deficiency or excess. Deficiency or excess defects are known as non-stoichiometry, and can apply to the three sites, even though B-site defects are less common and less studied since BO_6 octahedra constitute the building block of the whole perovskite structure (Neagu, 2012). Size defects will induce octahedra deviations from the ideal structure, reflected by atoms tilting and appearance of different symmetry groups rather than the ideal cubic. Deficiency and excess defects were gathered by the author and shown in Figure 1.6, exemplified with a typical perovskite, $SrTiO_3$.

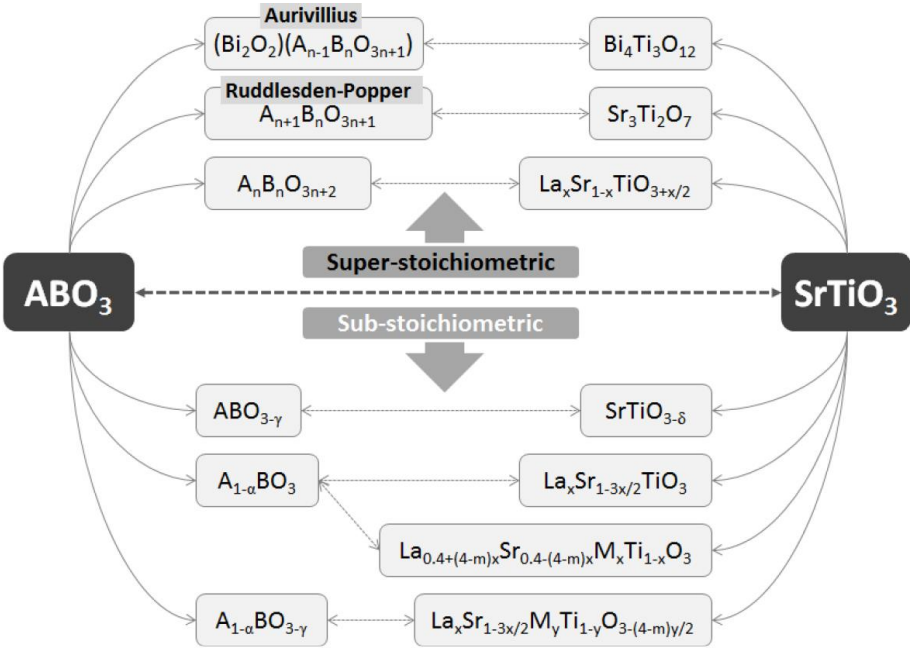

Figure 1.6. Exemplification of the types of non-stoichiometry present in a perovskite via $SrTiO_3$. Image courtesy of Neagu (2012), where n ≥ 1 for the super-stoichiometric perovskites.

A general classification for non-stoichiometric perovskites was established by the author: sub-stoichiometric and super-stoichiometric perovskites. An excess of A-site cation needs to be compensated with oxygen excess, creating an oxygen-rich structure, called Ruddlesden-Popper. This phase differs from the ideal perovskite phase. By partially substituting Sr^{2+} with La^{3+}, an oxygen compensation can occur to balance the electrical imbalance, resulting in the following $La_xSr_{1-x}TiO_{3+x/2}$ and creating thus an oxygen excess perovskite. Alternatively, this compensation can happen by forming A-site vacancies and therefore the structure formed would be $La_xSr_{1-3x/2}TiO_3$, keeping an oxygen stoichiometric perovskite. Finally, the last type of compensation that can occur is via partial reduction of the oxidation state from the B-site, $La_xSr_{1-x}Ti_x^{3+}Ti_{1-x}^{4+}O_{3+x/2}$. B-site cation can also occur with a metal M^{m+}, being in this case m ≠ 4+, as 4+ is Ti oxidation state. Two scenarios can happen here that will generate either oxygen vacancies or oxygen intergrowth. If m < 4+, the first scenario will happen and if m > 4+, the second scenario will take place. M^{m+} doping would produce the following stoichiometry, $SrTi_xM_{1-x}O_{3-(4-m)x/2}$. The latest case brings interest because it consists of creating deficiency in both A-site and O-site, creating higher distortion of the perovskite structure, and generating $La_xSr_{1-3x/2}M_yTi_{1-y}O_{3-(4-m)\cdot y/2}$, if the overall deficiency is small.

Thanks to their tailorability and adaptation to different scenarios, perovskites can be used in a wide range of processes (Irvine *et al.*, 2021). Different authors have gathered the results of the application of perovskite-based materials in different processes: photovoltaics and photocatalysis (Yin *et al.*, 2019), electrocatalysis (Zhang *et al.*, 2021), Li-Oxygen batteries (Tan *et al.*, 2017), solid oxide fuel cells (Biswas *et al.*, 2023), heterogeneous catalysis (Bian *et al.*, 2020) and chemical looping (Luo *et al.*, 2018).

Thanks to their ability to maintain their structure while hosting large number of oxygen vacancies (Kim *et al.*, 2022), non-stoichiometric perovskites have been considered in the recent years for CL processes. Most common defects are due to oxygen deficiency, modifying the general perovskite formula to $ABO_{3-\delta}$, where δ refers the oxygen deficiency (Rydén *et al.*, 2008). As explained before, the introduction of dopants can positively affect the ionic mobility by forming oxygen vacancies (Xu *et al.*, 2010), ultimately causing mixed valence state in the B-site. Metcalfe et al. (2019) explained that the WGS equilibrium constraint can be overcome with the use of non-stoichiometric perovskites. Perovskites, unlike single metal/metal oxide systems, can undergo multiple phase changes by continuously varying the oxygen content at different pO_2.

Perovskites' chemical versatility and the flexibility of their crystalline structure allow to enhance OCM properties. Resistance to sintering, durability with time, oxygen intake/release at certain pO_2, etc., can be tailored with the addition of dopants or partial substitution of certain elements. For instance, it is widely known that rare-earth metals in the A-site provide perovskites of an excellent thermal stability and redox properties (Zeng *et al.*, 2020) or provide the perovskite with large oxygen mobility and capacity (Nalbandian, Evdou and Zaspalis, 2011; Tang, Xu and Fan, 2015; Zhao *et al.*, 2016). Alkaline-earth elements reduce coking formation and promote Ni reactivity when activating CH_4 (Zhang, Sun and Hu, 2021) and promote the creation of oxygen vacancies (Song, Ning and Bouwmeester, 2020). Different transition metals are used to activate different reactions. Fe-based perovskites are promising and widely used in CLWS, where steam acts as OCM oxidising agent (Voitic and Hacker, 2016; Zhao *et al.*, 2021), even though they lack of continuous H_2 production in time due to material deactivation. On the other hand, Ni-based perovskites are the most studied carrier materials for CL processes when aiming for syngas as product (Ranganathan *et al.*, 2019), displaying enhanced oxygen transport (Q.

Jiang *et al.*, 2020). Perovskites have also been used as support for other OCM in CL H_2 production (Liang, 2015).

1.4.1.e. Fe-based perovskites

Identified as potential candidate for CLSRM, $LaFeO_3$ has been identified for nearly pure syngas production (Mihai, Chen and Holmen, 2012; L. Zhang *et al.*, 2020). Excellent results have been reported when dopants were added to this OCM: 10% doping of CeO_2 resulted in high syngas and pure H_2 yields and no carbon deposition (Zheng *et al.*, 2017). When partially substituting La for Ce in the A-site ($La_{0.5}Ce_{0.5}FeO_3$), syngas yield was 3 times higher than undoped $LaFeO_3$ for CLSRM. This was due to a major lattice distortion, allowing for a larger amount of oxygen vacancies (X. Zhang, Pei, *et al.*, 2020). Using alkaline-earth oxides (MgO and CaO) as supports of $LaFeO_3$ has resulted in carbon deposition avoidance and good material regeneration (Zhao *et al.*, 2016). The doping of the A-site with Sr^{2+} has been proven to enhance the quantity of oxygen adsorbed and avoid CH_4 decomposition. Sr^{2+}, with a lower valence than La^{3+} will create more oxygen vacancies (Protasova and Snijkers, 2016).

Regarding CLWGS, several authors have identified strontium lanthanum iron-based perovskites ($La_{1-x}Sr_xFeO_3$, LSF) as potential candidates for this CL process. LSF is among the most investigated materials for CLWGS (Murugan, Thursfield and Metcalfe, 2011; Nalbandian, Evdou and Zaspalis, 2011; Dueso, Thompson and Metcalfe, 2015). LSF allows for a larger operational pO_2 range than Fe_2O_3 (10^{-23} bar < pO_2 < 10^2 bar for LSF compared to 10^{-20} bar < pO_2 < 10^0 for Fe_2O_3), enabling larger gas conversions (Kim *et al.*, 2022). Over 100 redox cycles, $La_{0.7}Sr_{0.3}FeO_3$ (LSF731) achieved steady production of H_2 with no signs of material degradation (Murugan, Thursfield and Metcalfe, 2011). Other studies using $La_{0.6}Sr_{0.4}FeO_3$, LSF641, have reported steady conversion values after 1100 cycles of 92% and 85% for H_2O and CO, respectively (de Leeuwe, Hu, Evans, *et al.*, 2021). The interest in this material is relatively recent for CL applications but it has been studied in the past due to its oxygen properties. Several authors have studied the thermodynamics of the oxygen non-stoichiometry of the LSF 641 system at intermediate temperatures (Søgaard, Vang Hendriksen and Mogensen, 2007; Kuhn *et al.*, 2011). Secondary phases appeared as result of decomposition at pO_2 < 10^{-20} bar and not a OSC as high as expected, even though the material displayed high thermochemical stability.

By B-site doping ferrite perovskites, the material might exhibit desirable properties not displayed previously. Mn-doping increases the oxygen content and oxygen mobility (Markov *et al.*, 2016), the reactivity towards steam is improved and the reaction temperature is decreased (Luciani *et al.*, 2018). Co-doping of LSF enhances the material reducibility beyond the previous pO_2 described (10^{-20} bar), with no decomposition (Kuhn, Fukuda, *et al.*, 2013). In the $LaFe_{1-y}Ni_yO_3$ system, small Ni presence promoted both CH_4 dissociation and the OCM reactivity. However, the high amount of Ni-doping led to CH_4 decomposition and, therefore, coke formation. An optimal Ni content was found to be y = 0.1, without compromising the material stability or the CH_4 conversion (Shen *et al.*, 2019). In a recent study, authors investigated a calcium ferrite perovskite and the effects of Ni-doping in the B-site (Shah *et al.*, 2021). It was found that Ni-doped OCM increased their reactivity in the temperature range of CLSRM and CLWGS.

Table 1.2. below represents a brief summary of different OCM used in the last years for Chemical Looping processes.

Table 1.2. Summary of the main types of materials used in CL processes for H_2 and syngas production in the literature.

Material type	Key properties	Durability / Performance in CL
Fe-based oxides	High OSC and transport	Stable across multiple cycles, but they are very dependent on the support as it is prone to agglomeration.
Ni-based oxides	High thermal stability and reactivity towards CH_4 and CO for syngas production, not as suitable for CLWGS.	Prone to sintering at high T. Promote carbon deposition in CH_4-based processes.
Mn-based oxides	Broad range of oxidation states (from 0 to +7), suitable for high OSC materials. Reactive for CLWS. Larger OSC with dopants (Ca).	Prone to sintering. Limited OSC under CL conditions Longer durability if stabilised with Al_2O_3, ZrO_2, etc.
Ce-based oxides	Remarkable oxygen mobility and OSC.	Good durability, enhanced with dopants such as Zr.
Mixed Metal-Oxides (e.g. Fe, Ni, Cu, Mn-oxides)	Tailorable for targeted reactivity, selectivity, etc.	Long-term activity limited by segregation and sintering. Fe-Ni systems have better durability on CeO_2 supports.
Fe-based perovskites	High OSC and oxygen mobility suitable for CLWS due to multi-valent Fe ion. Examples are $LaFeO_3$, $La_{1-x}Sr_xFeO_3$.	Even though it is stable at high temperatures, it tends to sinter and therefore, deactivate. Alkaline-earth doping avoids carbon deposition and enhances product selectivity
FeNi-based perovskites	Higher stability and yields than mixed Fe-Ni oxides if A-site is a rare-earth metal.	High syngas yield but prone to sintering.

1.4.2. Exsolution

Most of the research conducted thus far has been focused on the challenges related to materials deterioration, such as sintering or carbon deposition, which ultimately result in material deactivation. However, the concept changed when Nishihata et al. (2002) introduced the concept of *self-regenerative* materials. The authors stated that the drawbacks associated with material deterioration could be addressed by reversible continuous redox processes in which a metal from the B-site (Pd, in this case) would emerge on the surface as metallic nanoparticles when reducing conditions were applied and re-dissolve upon material oxidation, which was demonstrated via X-Ray Diffraction.

This process is known today as *exsolution of nanoparticles*. The studied material was a full stoichiometric (i.e. A/B ratio ~ 1) $LaFe_{0.57}Co_{0.38}Pd_{0.05}O_3$, and higher activity than the Pd supported on the traditional Al_2O_3 was reported. They attributed this enhanced activity to the avoidance of sintering as the particles redissolved and re-emerged continuously within the lattice. Sulphur tolerance was later demonstrated (Tanaka *et al.*, 2004) and the concept was also proven for other noble metals such as Rh or Pt (Tanaka, Taniguchi, *et al.*, 2006) with application for emissions control. Further studies on the mechanism of the processes reported that the redissolution did not occur to a full extent within the lattice but only to some nm below the surface (Katz *et al.*, 2011). Later on, this process was also conducted with transition metals, such as Ni^{2+}, with application in fuel cells (Madsen *et al.*, 2007).

This 'self-regenerative' method has gained interest in the last decade. Compared to other traditional synthetic methods, such as impregnation of materials in which several steps are required for the preparation of the material, widely used in the chemical industry, the preparation of the presented materials is a single step process. However, this method was understood as a bulk process, rendering the nanoparticles inaccessible and thus decreasing the effectiveness of the process in the long term (Neagu *et al.*, 2013). Thanks to the ease to tailor perovskites and their versatility, these authors found that by creating A-site deficient perovskites (i.e., A/B < 1) B-site surface exsolution cations would be triggered. This would promote higher particle population and enhanced distribution. Ultimately, this would create higher active metals on the surface, achieving higher reactivity rates. This was suggested as A-site oxides (AO) were observed when exsolving metals from the B-site (Eq 1.16).

$$ABO_{3-\delta} \xrightarrow{Exsolution} (1-\alpha)ABO_{3-\delta}, + \alpha B + \alpha AO \qquad \text{Eq 1.16}$$

$$A_{1-\alpha}BO_{3-\delta} \xrightarrow{Exsolution} (1-\alpha)ABO_{3-\delta}, + \alpha B \qquad \text{Eq 1.17}$$

Using the archetypal perovskite $SrTiO_3$, La^{3+} partially substituted Sr^{2+}, the excess of charge can be compensated by A-site deficiency $La_xSr_{1-3x/2}TiO_3$. Ni^{2+} was selected as dopant in the B-site thus creating oxygen vacancies and destabilising the perovskite, being $La_{0.52}Sr_{0.28}Ni_{0.06}Ti_{0.94}O_{3-\gamma}$ the final material. To compare, stoichiometric $La_{0.3}Sr_{0.7}Ni_{0.06}Ti_{0.94}O_{3.09}$ was prepared. When reducing conditions were applied, the A-site deficient material displayed uniformly distributed Ni nanoparticles on the surface whilst the latter did not display any particle growth, indicating the higher reducibility to form

surface metallic nanoparticles (Figure 1.7.a, b). It was later proved that through this process of redox exsolution, metallic nanoparticles emerge to the surface of the oxide support (perovskite in this case) and come embedded to the lattice under oxidising conditions (Neagu *et al.*, 2015). This method, similarly to other synthetic methods such as deposition or impregnation, aims at forming active particles deposited onto the surface of the material. The materials presented by the authors were brought into comparison with impregnated ones when applied in catalytic testing involving Ni as active metal. The exsolved catalysts displayed better stability and lower carbon deposition (Figure 1.7.c). These features were attributed to a stronger metal-oxide interaction, allowing the authors to suggest a morphology for the exsolved nanoparticles (Figure 1.7.d). On the illustrated morphology, exsolved particles appear socketed within the surface (left-side of the image) and partially submerged on the oxide host. This socketed nature of the particles within the host suggests a deep anchorage of the particle with a strong interaction between metallic nanoparticle-oxide. Therefore, limited expansion and contact with adjacent particles is expected.

Several works implementing exsolved materials have been conducted (Neagu *et al.*, 2023). Exsolved materials have demonstrated higher reactivity in catalytic CH_4 activation (Otto *et al.*, 2019) and enhanced selectivity (Carrillo *et al.*, 2021) than other traditional catalysts. They have been implemented in electrocatalytic processes (Fu *et al.*, 2023), in the synthesis of NH_3 via fuel cells (Zhong *et al.*, 2023). Exsolved nanoparticles have also been used with CL applications (Carrillo *et al.*, 2020; Kousi, Neagu, Bekris, Papaioannou, *et al.*, 2020).

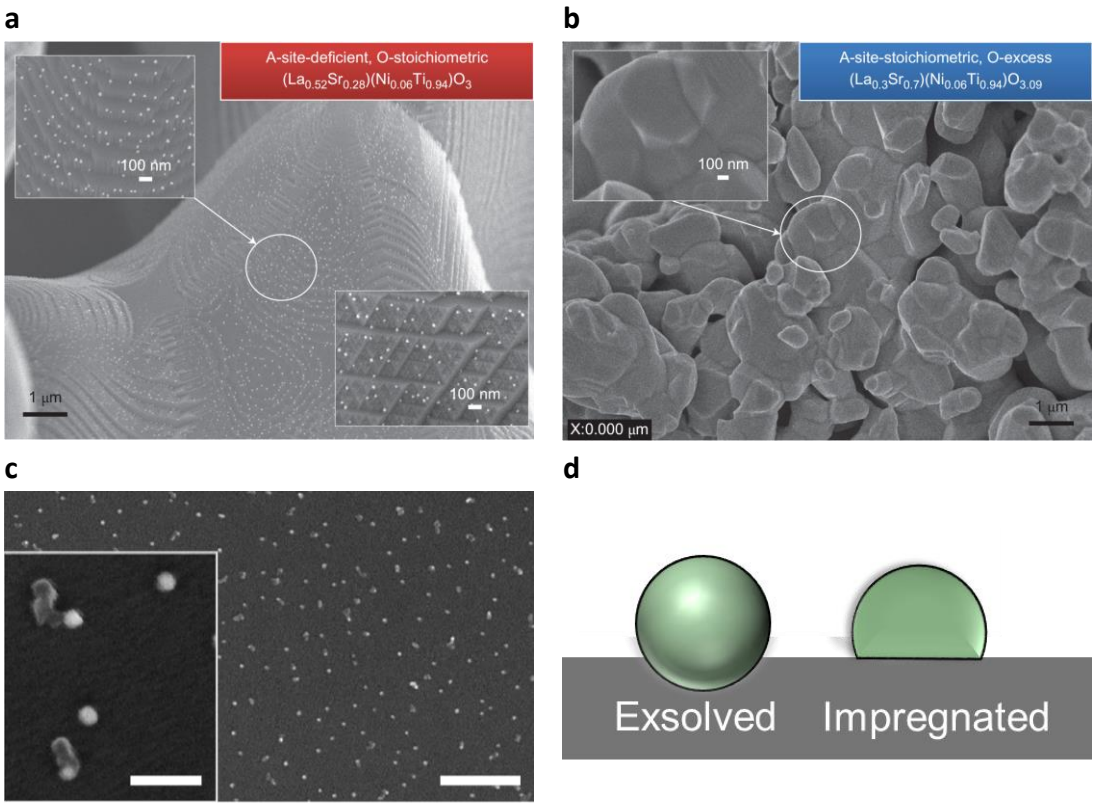

Figure 1.7. Surface morphology of exsolved metallic nanoparticles. **a**. SEM image of A-site deficient material. **b**. SEM image of stoichiometric material. Both images were published by (Neagu *et al.*, 2013). **c**. SEM image displaying the anticoking behaviour of exsolved Ni-nanoparticles. Nanoparticles presented exhibit a low rate of carbon nanofibers formed. Image published by (Neagu *et al.*, 2015). **d**. Illustrated morphology of exsolved nanoparticles compared to impregnated particles suggested by different authors.

Even though exsolved nanoparticles have been largely implemented using one or more exsolvable metals and most reviews focus on their applications, there exists a gap in its mechanism. Delving into this is still needed to fully understand and fully implement this method. However, in recent years, formation of a socketed particle followed by nucleation mechanism has aroused as the most plausible (Neagu *et al.*, 2019; Y. H. Kim *et al.*, 2023) mechanism. Furthermore, Calì et al. (2023) recently observed via microscopy the formation of iridium nanoparticles exsolved from a $SrTiO_3$ perovskite matrix.

On the other hand, not all the B-site cations are likely to exsolve. Kousi et al. (2021) presented the energy (ΔG^0) associated to the exsolution of metallic atoms of the most common cations used in perovskites. Exsolution of noble metals such as Rh or Pd is thermodynamically favourable. Exsolution of transition metals such as Ni or Cu is also favoured. ΔG (Fe) is close to 0 under typical temperature and pO_2 exsolution conditions (around 900 ºC and H_2). Nonetheless, some species less likely to exsolve such as Fe (if it is

the sole B-site cation), can exsolve together with another metal possessing a lower ΔG, such as Co or Ni (Ding *et al.*, 2020). The mechanism is yet to be explored, even though the "surface alloy formation" is believed to happen, given the favourable ΔG of the process (Tang *et al.*, 2021). In this case, Fe segregation energy was calculated to be positive, whereas co-segregation energy becomes negative with Ni-doping. Exsolved Fe-Ni bimetallic systems (i.e., FeNi alloys) have been frequently used as cathodes for CO_2 electrolysis or WS (Tang *et al.*, 2021). Their increased number of vacancies helped to reduce more CO_2 than other conventional materials. They are considered promising materials due to their proven resistance to carbon deposition and reaction conditions. Exsolved FeNi alloys have also been reported as catalytic materials for CO (Papaioannou *et al.*, 2019) and CH_4 reforming, resulting in enhanced CH_4 conversion (Papargyriou, Miller and Irvine, 2019) with nearly 100% selectivity towards syngas when used as a catalytic membrane (K. Jiang *et al.*, 2020).

Bimetallic exsolution systems have been less reported for CL applications in recent years as compared to single metal exsolution. High CH_4 conversion was reported whilst the operating temperature was decreased 200 ºC when an exsolved NiRh alloy was used for CLSMR (Kousi, Neagu and Metcalfe, 2020). CaFeO, CaFeNiO and CaFeCuO systems were evaluated and compared for H_2 production in CL CH_4 reforming (Hosseini *et al.*, 2019). Although a FeNi alloy was observed, exhibiting higher H_2 yield than the undoped CaFeO system, sintering and deactivation were reported. Conversely, the CaFeCuO system demonstrated more stability and improved CH_4 activation. However, Cu nanoparticles did not form an alloy with Fe. Cu was not reincorporated within the perovskite lattice under CO_2 as oxidising stream, necessitating thus an additional air oxidation step.

1.5. Thesis aims and objectives

CLSRM is regarded as a more thorough process for H_2 production than CLWGS, primarily due to the lack of availability of CO as feedstock. CO needs to be generated from another source to be further used as reactant. The *in situ* obtention of CO via CLSRM and its ulterior use in CLWGS can be transformed into high H_2 outputs using a sole material, thus decreasing overall costs whilst optimising the outcome. However, current materials often lack the required properties of OSC, syngas selectivity, final H_2 yield, and OCM stability to be implemented in CLSRM and subsequently CLWGS.

This thesis aims to bridge this research gap of developing these OCM with enhanced properties than benchmarked OCM. Since CO is a product generated in different processes and not a raw material, understanding its role in CLSRM and CLWGS becomes essential. Therefore, CLWGS is conceived in this thesis not only as a pathway to produce H_2 but also as a critical step in CLSRM. The conception, preparation, and characterisation of materials able to execute these processes is the ultimate goal of this thesis.

To accomplish of these broad objectives, different aims are outlined:

- To design and synthesise a set of Fe-based OCM with similar structure and morphology with high oxygen capacity suitable for CLWGS. These materials are expected to be stable and durable in the long term.
- To determine the oxygen capacity of the proposed materials. To do so, the oxygen release and intake under CL conditions has been conducted. To understand behaviour and chemistry modifications of the developed OCM under these conditions: thermal resistance, cell parameters modification, structural changes, etc. To establish a solid comparison with state-of-the-art OCM by contrasting their OSC and H_2 production under CL conditions.
- From the OCM showcasing best results combining all oxygen capacity, yield, durability and resistance, a further implementation in CLSRM. Adapt the composition with dopants and to attempt the exsolution concept in the selected material.
- To contribute to the understanding of the mechanism of exsolution of bimetallic systems.
- To conduct real CLSRM conditions for H_2 production in small-scale reactors with the final proposed OCM.

1.6. Thesis outline

Chapter 1 – Introduction. Here, the different H_2 production methods and challenges associated to its production are deconvoluted. Alternative paths for its generation are presented, accompanied from a short review of the current status. The end of the chapter is oriented towards the work that will be conducted, with a higher focus on the material's science for H_2 production.

Chapter 2 – Experimental. This chapter summarises all the techniques employed for the preparation, characterisation and testing of the designed materials. There are also included the machinery employed for that and the facilities in where these materials have been studied.

Chapter 3 – Design and characterisation of Oxygen Carrier Materials for CLWGS. The designed and synthesised OCM are characterised. A thorough study of their oxygen capacity is established. The variation in their chemical properties is also studied via *ex situ* X-ray Diffraction conducted at the synchrotron facilities, located in ESRF (Grenoble, France). Once the characterisation is elaborated, the activity of these two systems is observed in a packed bed reactor and running CLWGS conditions.

Chapter 4 – Development and investigation of designed OCM for Methane Activation. This chapter encompasses a description of the required conditions for CH_4 activation. It has a focus on the activation of CH_4 and the continuous modifications of one of the designed OCM to be suitable for CH_4 activation. Exsolution conditions are eventually applied and thanks to the *in-situ* powder X-ray Diffraction conducted at ESRF, a more thorough understanding is given on how the exsolution of an alloy occurs.

Chapter 5 – Testing exsolved OCM in Chemical Looping Steam Methane Reforming. Intended as a proof of concept for the suitability of the designed material, this chapter is solely focused on the activity of the OCM for CLSRM. A study of the half-reactions time and temperature conditions of the process are carried out before final test under CLSRM.

Chapter 6 – Further application of the presented OCM. These materials underwent catalytic testing for reverse WGS. Here, these designed materials are now used as catalysts. Materials structure is presented through a more thorough characterisation. New exsolution conditions have been applied and their catalytic activity has been studied.

Chapter 7 – Conclusions and future work. This shorter chapter will encompass a general conclusion from the conducted work and what can be expected from the obtained results in the near future.

Chapter 2 Experimental methods

2.1. Synthesis of materials

Two synthesis methods, modified Pechini method and solid-state were explained by (de Leeuwe, Hu, Neagu, *et al.*, 2021) and (Neagu and Irvine, 2011), respectively. Both were tested being only the latter the one used throughout the whole project, given the better results in terms of sample impurities, examined by PXRD.

Oxygen carrier materials ($(Ln_{0.5}Ba_{0.5})_xFe_{1-y}Ni_yO_{3-\delta}$, being Ln = Pr, Sm; x = 0.9, 1 and y = 0, 0.1) were prepared via solid-state method. Batches were of maximum 7 g of final product. In this method, oxide precursors (Pr_6O_{11}, Sm_2O_3) are dried at 400ºC during 3h to remove hydroxides and moisture, then cooled down to 250^{o}C and weighed while hot. Once all the hot precursors were weighed and reached room temperature, other precursors were weighed as needed ($Fe(NO_3)_3{\cdot}9H_2O$, $BaCO_3$, $Ni(NO_3)_2{\cdot}6H_2O$). A small amount of acetone (20-50 mL) and dispersant (Hypermer KD1, 10-20 mg) was added to the beaker. The mixture undergoes sonication, varying frequency, and intensity, to break down the agglomerates until obtention of a homogeneous and dispersed mixture. Sonication of the mixture was done to produce a fine and more stable dispersion. The acetone was then evaporated at 50 ºC, followed by the calcination of the mixture.

Calcination was done in alumina crucibles and calcined in air at 1000 ºC for 12 h (ramp rate of 2 ºC / min up to 600 ^{o}C, and then a faster ramp of 5 ^{o}C / min). The calcined powder was transferred into the cups of a planetary ball mill. Acetone (15-20 mL) and zirconia balls (5-15 mm diameter) were added to the jar. The planetary mill operated at ~ 400 rpm for 2 h. The acetone was then evaporated.

The resulting powder was then pressed into pellets and placed into an alumina boat, to be fired under air at the desired temperature (two temperatures were used for the OCM presented for further comparison, 1000 ºC and 1400 ºC, ramp rate of 5 ºC / min) during 14 h. The resulting powder was then sieved to 80-160 µm particle size.

2.2. Exsolution of nanoparticles

In order to produce perovskites with exsolved nanoparticles, around 400 mg of the sieved fraction was weighted and reduced under 5% H_2 / Ar balance, at different temperatures and various time durations (500-800 ºC, 1-20 h) in a controlled atmosphere tubular furnace. The chosen ramp was 5 ºC / min. Reducing gas was flowed to the furnace at 100-

125 mL / min, adjusted with a manual flow meter. Prior to entering the furnace, a moisture trap was placed so no residual water enters the furnace while operating.

Before testing the reduced powders, these were oxidised under air at 600ºC for 4h (5 ºC / min) to promote oxygen lattice replenishment.

2.3. Powder X-ray diffraction

Powder X-Ray diffraction (PXRD) is a widely used non-destructive technique used to study the atomic and molecular structure of crystal phases. It provides valuable information about the material, such as phase composition, crystal structure, crystallite size, etc.

X-rays formation and fundamentals were explained by (Epp, 2016): sealed tubes, rotating anodes, or synchrotron radiation sources generate the X-rays. Under vacuum, a tungsten filament is heated, generating electrons that are accelerated towards a target by a high potential field, generating X-rays. X-rays hit the studied powder at a certain angle (ϑ) and are scattered elastically. Elastic scatter implies that no change in wavelength between incident beam and scattered beam is produced. These scattered X-rays are reflected in specific directions, referred to as "reflection waves". When these waves are in phase, they create a constructive interference, determined by Bragg's Law (Eq 2.1), thus creating a pattern at a specific angle, 2θ. The method records the scattered intensity as a function of angle, displaying the pattern of the material.

$$n\lambda = 2d \cdot sin\theta \qquad \text{Eq 2.1}$$

Where *n* is the order of diffraction, λ is the wavelength of the X-Ray source (unit, nm), *d* is the lattice spacing or distance between planes (units, nm) and ϑ is the angle of the diffraction beam (units, ^{o}). *D* spacing is unique for every crystalline structure, therefore by comparing the obtained pattern with known patterns from databases, it is possible to identify the crystalline structure and the structure of the material studied.

Fine powder was prepared by manual grinding the pellets resulting from the sintering process. Rutinary phase composition and phase identification were done by room temperature PXRD by using PANalytical X'Pert Pro Multipurpose X-ray diffractometer, operating at 40 kV, 40 mA; with two characteristic wavelengths: $K_{\alpha1}$ and $K_{\alpha2}$, values were 1.5406 Å and 1.5444 Å, as a result of the emission of Cu atoms. The scan range used was 20º < 2θ < 90º, step size of 0.0167º, 6 s per step.

The patterns obtained were compared with the Inorganic Crystal Structure Database (ICSD), within the software HighScore Plus, to proceed with phase identification. Rietveld refinement was conducted for in-depth study of the crystallographic parameters. Rietveld refinement allows to build and fit a theoretical pattern in one obtained experimentally by combining and refining multiple variables, minimising the difference between the built model and the actual crystal structure.

Rietveld refinement was performed using TOPAS v7 Academic. The refined parameters include scale factors, background polynomial parameters, unit cell parameters, atomic positions, cationic site occupancies and temperature parameters. Weighted profile residual (R_{wp}, measured in %) was used as an indicator of the quality of the fit compared to the experimental data (Moltineri, 2007). The lower the value of R_{wp}, the better the fit.

2.4. Synchrotron *in* situ and *operando* PXRD

Aiming to gaining further information about materials reactivity and structural changes when they undergo oxidoreduction and thermal processes, *in situ* and *operando* PXRD experiments were conducted in ID22, at the European Synchrotron Radiation Facility (ESRF, Grenoble, France). Several *in situ* and *operando* experiments were conducted and over 70 capillaries were run in this facility.

In ID22, the X-rays are produced by an in-vacuum undulator located in a curve of the 844 m circumference of the particle accelerator in ESRF, that operates at 6GeV. ID22 can convert the entire energy range provided by the synchrotron from 6 keV to 80 keV (ESRF, no date) (2.07 Å to 0.15 Å in wavelength). The generated beam is monochromated and passes unperturbed to the sample. The diffractometer consists of 13 Si 111 analyser crystals, with channels 2º apart between them, mounted onto a rotating stage capable of recording peaks in the range of -40º < 2θ < 140º. The Eiger detector has replaced the previous $LaBr_3$ scintillator (the system can be appreciated in Figure 2.1, (Fitch *et al.*, 2023). The beamline was calibrated for 35 keV (wavelength of 0.3542818 Å).

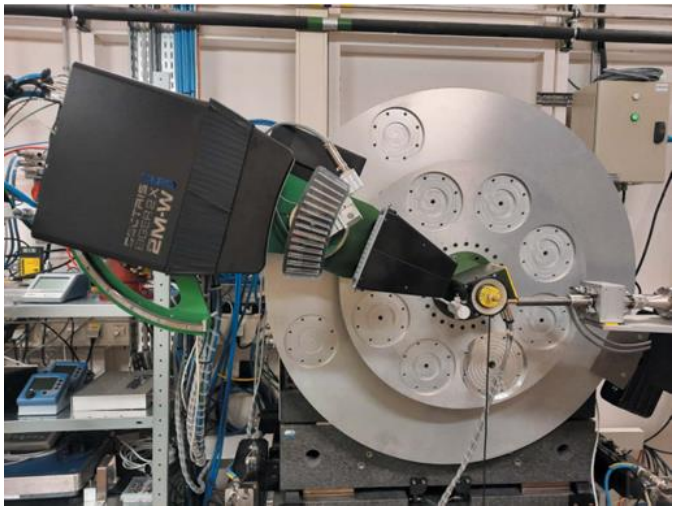

Figure 2.1. High resolution power diffractometer, equipped with its fast spinner, 13 channels multi-analyser stage and pixel detector. Image courtesy of (Fitch *et al.*, 2023).

Ex situ samples were scanned at room temperature by loading powders in 0.5 mm width capillaries and scanned in the range 0º < 2θ < 40º, with an average acquisition time of 10 min. The *in situ* and *operando* studies carried out in this expedition to ESRF were partially focused on the reactivity and evolution of $Pr_{0.5}Ba_{0.5}Fe_{0.9}Ni_{0.1}O_{3-\delta}$ under different atmospheres and conditions. Scan time was of 30 s, covering 0º < 2θ < 20º.

PXRD patterns presented in this thesis are presented using two different wavelengths, as not all the samples could be run at ID22. Different wavelengths result in different 2θ reflections, allowing to easily distinguish the source of each pattern displayed once plotted.

The furnace used during the synchrotron campaign, capable of reaching 1100 ºC, possessed an isothermal section no longer than 5 cm, suitable for small-scale reactions. To conduct *in situ* PXRD, the furnace had a hollow aperture, both entry and exit, large enough to allow X-rays to penetrate avoiding interferences but small enough to minimise the heat loses. A novel model of furnace was employed towards the conclusion of my doctoral period and the team of the expedition was unfamiliar with the controls and the difference between actual and set values, alongside the possible heat losses due to the hollow aperture. Consequently, the calibration of this furnace was not as precise as preferred. Therefore, the achieved temperature values might differ from the originally intended.

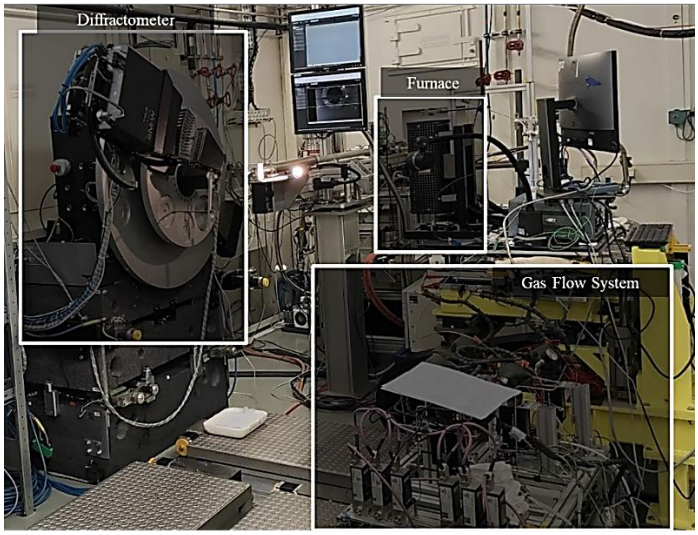

Figure 2.2. Reactor system set-up: Diffractometer-left side image, Furnace-centre, Gas Flow System-Bottom right. Mass spectrometer for gas analysis was placed behind the set up and cannot be displayed in the picture.

2.5. Scanning Electron Microscopy

Scanning Electron Microscopy (SEM) is a technique commonly used to imaging the studied specimen and to get information about the surface morphology microstructure of the material. A beam of electrons reaches the sample, and this interacts with the electrons in different ways: elastically or inelastically. With negligible energy loss after the collision and with a scattered electron wider than 90º, these electrons are called backscattered electrons, resulting in useful images. On the other hand, electrons from the beam can interact with the atoms and electrons from the sample, increasing its energy and therefore, exciting the electrons and ionising the atoms, leading to secondary electrons (SE), that can be used for sample analysis, i.e., surface visualisation, texture, etc. A secondary signal electron can provide high-resolution imaging at surfaces with a precision of 10 nm or finer (Zhou *et al.*, 2007). Some other signals are producing upon striking a sample with an electron beam (X-Rays, Auger, etc).

SEM analysis was carried out in University of Surrey , with a Thermo Scientific Apreo SEM as instrument to investigate the macrostructure of the OCM and the potential existence of exsolved nanoparticles. It operates under high vacuum with a voltage going from 1 to 30 kV. Fe-based samples exhibit charging effects, leading to image distortion, therefore, to mitigate this effect, they were scanned in Secondary electrons (SE) mode to determine microstructure, particle size and population using the voltage 1-2kV and 6.3 pA current. The samples were mounted on SEM holders using carbon adhesive tabs. Conductive silver

paint was used on the edges of the adhesive to minimise sample charging. Particle distribution and particle size were calculated using the image analysis software ImageJ.

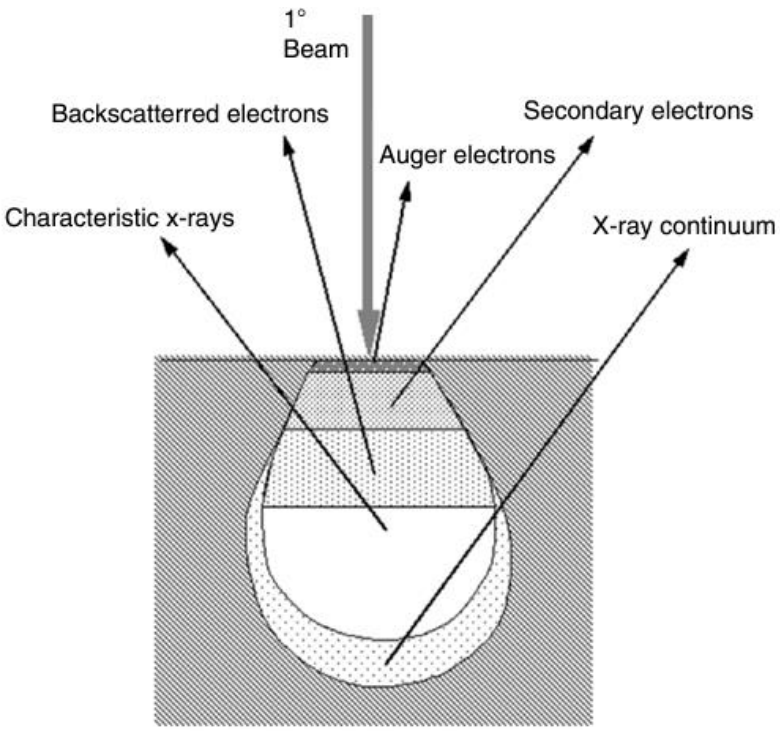

Figure 2.3. Different signals that can be generated when an electron beam hit the sample in the Scanning Electron Microscope. Different regions where these signals are originated are marked with lines separating different textures within the image (Zhou et al., 2007)(Zhou et al., 2007).

2.6. Thermogravimetric Analysis

Thermogravimetric Analysis (TGA) is a technique that records, with high precision, the mass loss (due to a reduction or drying of the material) or mass gain (oxidation, gas adsorption, etc). These changes are recorded against time and temperature under the desired atmosphere. Commonly used in the field for redox and thermal stability, oxygen capacity of carrier materials and reaction kinetics.

A TGA unit (Rubotherm dynTHERM system) with 4 gas unit inlets was used to carry out the study of stability under strong oxidoreduction and high temperature conditions. The TGA consisted of a balance with high sensitivity (0.1 μg). An alumina crucible was suspended from this balance with a Pt hook, inside an isolated furnace.

The study of investigations into the oxygen content of OCMs at different pO_2 values was conducted at The University of Edinburgh using a METTLER TOLEDO thermogravimetric analyser. The experimental procedure was as follows:

2.6.1 Oxygen Storage Capacity measurements

Approximately 1 mmol of sample was placed in the TGA crucible, and the gas flow was fixed to 200 mL / min. Gases connected to the inlets were: Compressed air, CO:CO_2 buffer gases with varying ratios (1:100, 1:10, 1:1, 10:1, 100:1) to record data within a wide pO_2 range, going from 10^{-13} to 10^{-26} bar, depending on the working temperature. An initial air ramp was done up to the desired temperature (720 ºC – 820 ºC). Once the target temperature was reached, the gas changed to the most reducing buffer gas at isothermal conditions and flowed until mass stabilisation. The gas was subsequently swapped by the second most reducing buffer gas and was flowed until mass stabilisation. The program continued until all the buffer gases were flowed. The sample was then cooled down under air.

The mass loss or gained was then converted into oxygen loss or oxygen recovery, allowing to study the non-stoichiometry (Δδ) variation, expressed as follows:

$$\Delta\delta = \frac{M(OCM)}{M(O)} \cdot \frac{\Delta m_{OCM}}{\Delta m_{initial\ OCM}} \qquad \text{Eq 2.2}$$

being *M* the molar, or molecular, mass of the said species and *Δm*, the mass variation of the said species.

2.6.2 Preliminary studies for suitability of OCM for CL processes

These experiments were done to study whether the materials released and regained oxygen under conditions more reducing and oxidising than CLWGS or CL Methane Reforming, in terms of pO_2. To achieve it, 5%H_2 and 20%O_2, both balanced in Ar, were flowed.

Around 1 mmol of OCM were placed in the TGA crucible, a ramp of 5 ºC / min under Ar was done until reaching 820 ºC (this is the temperature for optimal conditions as previously calculated (Metcalfe *et al.*, 2019). Once the temperature was stable, gas was changed to H_2 and run for 1h, switched to Ar for gas purge for 10 min and switched to O_2, for reoxidation. This cycle was repeated 20 times with an Ar purge in between every cycle.

2.7. Iodometric titration

Whereas TGA can provide information about the variation of oxygen vacancies, iodometric titrations are generally used to study the absolute oxygen content of the OCM of interest. Originally known as the Wrinkler method, described by (Carpenter, 1965), the method used for these OCM has suffered numerous variations, such as the addition of inert gases (Ar, N_2) or the use of HCl to dissolve the solid, carried out by (Carvalho *et al.*, 2006).

A three necked round bottom flask was filled with 50 mL HCl (3 M) and purged with Ar, to create an oxygen-free environment. Once purged, perovskite samples (20 – 50 mg) were dissolved under continuous stirring in approximately 30 min. The solution was vented to a second Erlenmeyer containing an excess of KI (around 3 g) dissolved in deionised H_2O and allowed a few minutes upon completion of React. 1 and React. 2. All the I_2 formed reacted with the I^- in excess to be converted into triiodide ions, remaining in the solution (React. 3):

$$Fe^{4+} + 2I^- \rightarrow Fe^{2+} + I_2 \qquad \text{React. 1}$$

$$2Fe^{3+} + 2I^- \rightarrow 2Fe^{2+} + I_2 \qquad \text{React. 2}$$

$$I_2 + I^- \rightarrow I_3^- \qquad \text{React. 3}$$

A titration was subsequently done using 0.02 M $Na_2S_2O_3$ and starch as indicator. The moles used of thiosulphate react with triiodide. This allows to calculate the moles of iodine produced following Reaction React. 4*)*:

$$I_3^- + 2S_2O_3^{2-} \rightarrow 3I^- + S_4O_6^{2-} \qquad \text{React. 4}$$

The second vessel was titrated in the case a colour change had taken place. This colour change is produced by the reduction of chlorine (formed by the reaction of Fe^{4+} with Cl^-, React. 5) to chloride (React. 6)), forming I_2 and following the consequent reactions as explained before:

$$Fe^{4+} + 2Cl^- \rightarrow Cl_2 + Fe^{2+} \qquad \text{React. 5}$$

$$Cl_2 + 2I^- \rightarrow I_2 + Cl^- \qquad \text{React. 6}$$

To calculate the oxidation state of the B-site, *Z*, Fe in this case:

$$\frac{n_{Na_2S_2O_3}}{\mathrm{Z}-2} = \frac{m_{OCM}}{M_{OCM}} \qquad \text{Eq 2.3}$$

Where $n_{Na_2S_2O_3}$ was the amount of moles of sodium thiosulphate needed to reduce all the triiodide, m_{OCM} is the mass of carrier material dissolved and M_{OCM} is the molar weight of the carrier material. From the molar weight, M_{OCM}, the number of oxygen vacancies for the given materials was obtained, with the following expression:

$$M_{OCM} = 0.5 \cdot M_{Ln} + 0.5 \cdot M_{Ba} + M_{Fe} + (3-\delta)M_O \qquad \text{Eq 2.4}$$

Where M_X is the corresponding atomic weight of the atoms (X) present in the OCM. Assuming the following oxidation states, +3 for Sm and Pr, +2 for Ba and -2 for O:

$$3 \cdot (1-x) + 2x + Z = 2 \cdot (3-\delta) \qquad \text{Eq 2.5}$$

Therefore, the number of oxygen vacancies was obtained via simplification of the equation:

$$\delta = \frac{3 + x - Z}{2} \qquad \text{Eq 2.6}$$

2.8. Experimental set-up

Temperature Programmed Reduction (TPR), Temperature Programmed Oxidation (TPO) were conducted as screening or activation experiments, aiming to explore the materials' reactivity to methane or carbon monoxide.

The system (Figure 2.4) consists of a series of mass flow controllers and pipes connected via 3- and 4-way valves, a furnace, reaching up to 1000 ºC, a quartz reactor tube and a mass spectrometer (MS). If needed, the system also possessed a steam entrance but was never needed.

The conversion from a fully manual to a semi-automated mass flow control system, which I carried out, addressed the potential for pressure losses inherent in the previous setup. This transformation, now controlled by PC, thanks to the connection of the now installed mass flow controllers, Brooks Instruments, whose flow is adjusted via IGI Systems software, also rectified inaccuracies associated with the previous manual control system. The reactor, measuring 30 cm in length, was fitted with a quartz frit of no. 2 porosity and has an outer diameter of 3/8". It was linked to the system using a sequence of Swagelok Ultra-Torr vacuum fittings within a vertical furnace setup. Ultra-Torr fittings were equipped with hollow ends to adapt the insertion of a 3 mm outer diameter and 2 mm inner diameter

quartz tube. This thin quartz was placed in the centre of the powder bed, facilitating temperature measurements through the utilisation of a K-type thermocouple inserted into tube.

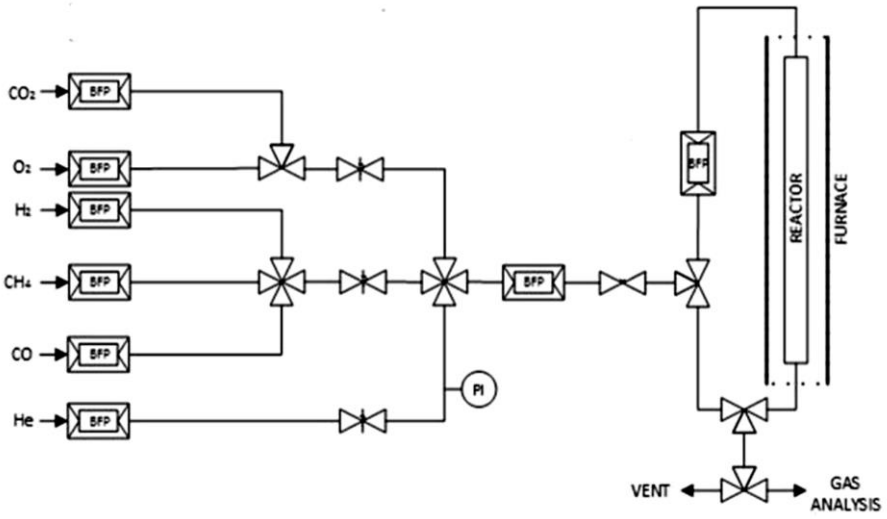

Figure 2.4. Flow diagram of the system used for Temperature Programmed Reactions

2.8.1 Temperature Programmed Reductions

Firstly, a calibration was done while bypassing the gases. While the calibration was taking place, approximately 230 mg of OCM (~1 mmol) were loaded in the reactor. Following the termination of the calibration, a reactor purge with inert gas (He in this case) was carried out until all the remanent H_2O from the air is dissipated from the MS. Temperature was generally recorded with PICOLOG. The TPR profile was generally done with a temperature ramp of 10 ºC / min until reaching the target temperature while flowing 100 mL / min 5% H_2 to emulate the exsolution conditions used in the tubular reactor, or 80 mL / min when flowing 5% CH_4. Once the system was cooled down, the sample was taken to PXRD to monitor structural changes.

Reaction results were generally presented as molar fraction (χ_{gas}) or gas conversion (expressed as %, Eq 2.7). To calculate the latter, the expression is as follows:

$$Gas\ conversion\ (\%) = \frac{[Gas]_{in} - [Gas]_{out}}{[Gas]_{out}} \qquad \text{Eq 2.7}$$

2.8.2 Temperature Programmed Oxidations

Temperature Programmed Oxidations (TPO) were generally done to monitor the carbon deposition after CH_4 activation experiments or to observe the oxygen intake by the reincorporation of the metals materials that had previously been exsolved. Carbon deposition studies were conducted after CH_4 activation; therefore, no calibration was needed. Approximately the same amount (1 mmol) of used sample as weighted for CH_4 activation was loaded in the reactor after undergoing PXRD study. Temperature was increased until 800 ºC at 10 ºC / min, under 5% O_2. Only O_2, CO and CO_2 signals were recorded. Carbon deposition was obtained by integrating the products signals (CO and CO_2).

2.9. Reactor for Chemical Looping Cycling Experiments

2.9.1 System Flow

Initially conceived as a catalytic system with a sole gas inlet and gas outlet, I took the responsibility of modifying the old rig to a newer rig. This new rig had the possibility of flowing gases counter-flow, as now both ends of the reactor could act as inlet or outlet. Therefore, this system could also be used at the synchrotron facilities for CL purposes.

The system was mainly comprised of a reactor, a vertical furnace, described in *2.4. Synchrotron in situ and operando PXRD*, a mass spectrometer (Hidden Analytical QGA, HAS-301-1291), six computer-controlled MFC, where three of them possessed solenoid valves to prevent the back flow, and a water delivery system. The water delivery system was formed by a liquid filled permeation tube, a furnace, and a set of two MFC which allows flowing water or inert gas through the perm tube. Heating lines were used to wrap the pipes through which the H_2O was circulating, ensuring the removal of cold spots, and preventing condensation of H_2O. This potential condensation entailed a risk of moisture in some specific areas of the piping, compromising the integrity of the results.

The flow system comprised five automated 4-way valves supplied by VICI (Valco Instruments Co. Inc.), enabling the alteration of gas flow directions. Flow of reactive and inert gases is continuous and gas direction to and from the reactor was orchestrated by manipulating three valves, operated via IGI software. Gas feed was regulated by the six MFC and the two MFC from the perm system and connected to high pressure cylinders. These MFC were connected to the PC and the flow rate was controlled there. Solenoids

following the MFC acted as an on/off valve, preventing the system continues to flow gases through that precise line, since the MFC did not possess the ability to act as such.

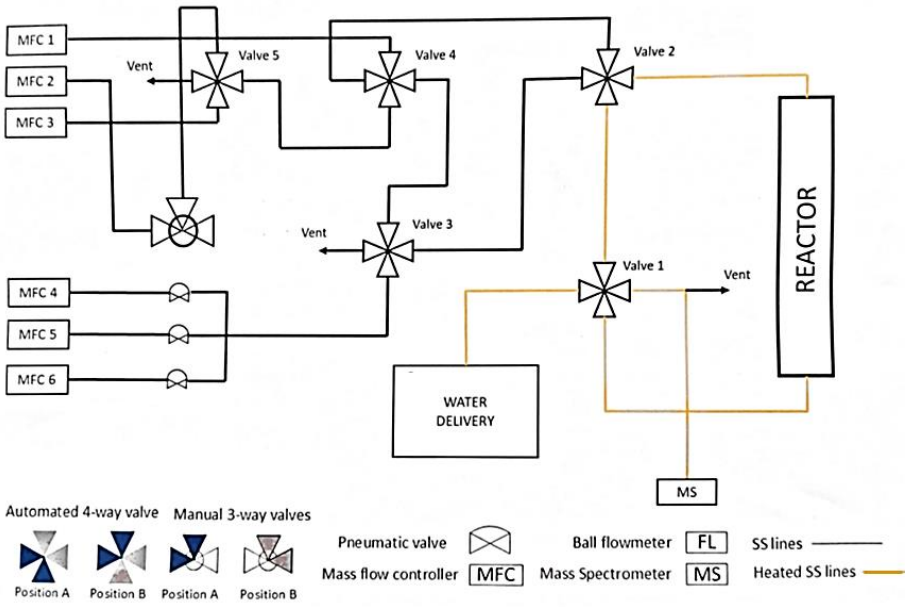

Figure 2.5. Flow diagram of the CL rig set-up. MFC corresponds to "mass flow controller"

The reactor was a 47.5 cm long quartz tube, with a 3/8" outer diameter, 3 mm wall thickness, quartz frit no. 2. It was connected to the system via two Ultra-Torr fittings, with hollow ends to allow the entrance of a thinner quartz tube (previously described) to allow the entrance of a K-type thermocouple that registers the system temperature. This thermocouple was placed on the top of the material bed, held by the quartz bed on the bottom.

2.9.2 Gas Analysis

Gas analysis for all the experiments was performed by Mass Spectrometry. To proceed, the group possessed a quadrupole MS working with electron impact ionisation, a quadrupole mass filter, and a secondary electron multiplier detector. The MS was connected to a scroll pump, as low pressure (working pressure was normally 10^{-6} – 10^{-7} bar) was needed for mass spectrometry analysis.

Mass spectrometry is a widely used technique as a method of detection and characterisation explained by (Dass, 2007). It is capable of accurately measuring molecular mass, provides ultrahigh detection sensitivity, it is applicable to every element can analyse a large range of molecules and compounds. Generally, a gas is ionised by electrons

bombarding at the ion source of the MS. They are separated according to their relation mass to charge (m/z) by being accelerating with a magnetic field. The last step is the detection of the ion current made from separated ions.

The outlet of the reactors is coupled, as specified before, to a MS, for real time quantitative gas data collection. It was configured for continuous analysis of gases and vapours. The MS was provided of a flexible 2 m capillary that provided fast response (less than 300 ms) and allowed a flow of 20 mL of gas / min. With a wide range of detected mass, the system was configured with a limit of detection lower than 100 ppb. Upon leaving the capillary at high velocity and low pressure (refer to Figure 2.6 for visualisation), the gas underwent a further reduction in pressure through an orifice, reaching 3 mbar approximately. It passes through an ultra-high vacuum (UHV) MS chamber, and from there, it was evacuated by a scroll pump.

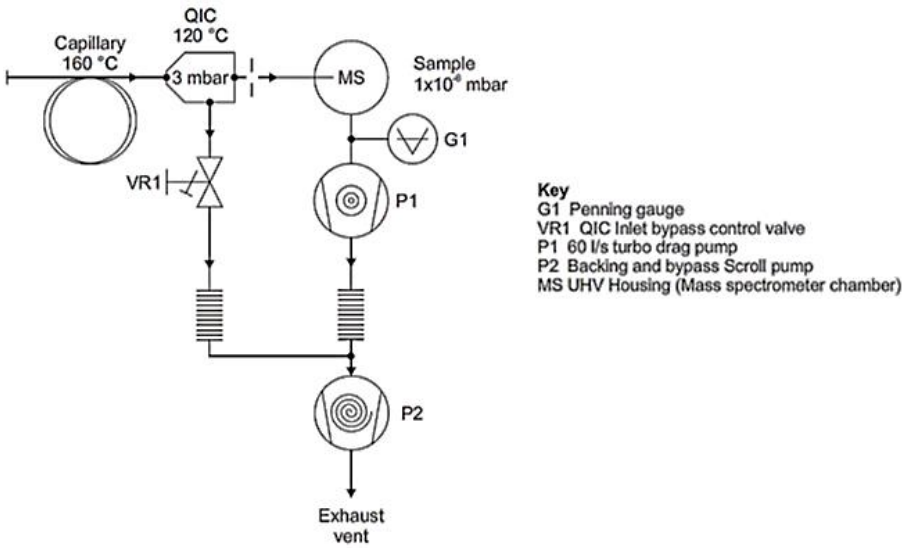

Figure 2.6. Schematic depiction of the internal structure of the mass spectrometer. Image courtesy of the company

The gases measured needed a Secondary Electron Multiplier (SEM) detector, given their small ion current, allowing to amplify the ion signals. During the experiments conducted, the monitored gases were, depending on the experiment carried out (in the m/z relation):

- H_2 (2), He (4), H_2O (18), CO (28), CO_2 (44), for Water-Gas Shift experiments
- H_2 (2), He (4), CH_4 (15) H_2O (18), CO (28), CO_2 (44) for Methane Activation

The m/z ratio was translated into gas concentrations via calibration. This calibration was conducted prior to every experiment or intermittently during long-duration experiments. For that, a known concentration of the reactant gases, balanced in He, and pure He, was fed to obtain the calibration factors, background and the splitting factors between CO and CO_2.

Molar fractions were determined by dividing the presence of each flowed gas by its calibration factor and the sum of all the gases recorded divided by their calibration factors, as follows:

$$y_n = \frac{\frac{I_n}{cal_n}}{\sum_1^n \frac{I_n}{cal_n}} \qquad \text{Eq 2.8}$$

Where y_n corresponded to the molar fraction of each gas, cal_n corresponded to the calibration factor of each gas. Following the molar fraction, the molar flowrate, $\dot{N}$ $(\mathrm{mol}\ /\ \mathrm{s})$, is then determined:

$$\dot{N} = \frac{y_n \cdot F}{60 \cdot 22400} \qquad \text{Eq 2.9}$$

Where F was the flowrate (mL / min) at standard conditions.

Chapter 3 Design and Characterisation of Carrier Materials for CLWGS

3.1. Introduction

OCM change their amount of available oxygen under different pO_2. Ideally, the oxygen exchange should be as large as possible for a given pO_2 range for a certain reaction. In WGS (Eq. 3.1), the equilibrium constant (K_{WGS}) is defined by (Eq. 3.2).

$$H_2O + CO \rightleftharpoons H_2 + CO_2 \quad \text{(Eq. 3.1)}$$

$$K_{WGS} = \frac{\frac{p_{CO_2}}{p_{CO}}}{\frac{p_{H_2O}}{p_{H_2}}} \quad \text{(Eq. 3.2)}$$

Each reaction is governed by the equilibrium constants (K_{ox} and K_{red}, for oxidation and reduction half reaction, respectively) of each redox couple:

$$K_{ox} = \frac{y_{H_2} \cdot p_{O_2}^{1/2}}{y_{H_2O}} \quad \text{(Eq. 3.3)}$$

$$K_{red} = \frac{y_{CO_2}}{p_{O_2}^{1/2} \cdot y_{CO}} \quad \text{(Eq. 3.4)}$$

At T ~ 820 ºC, the equilibrium constant of the process is equal to 1 (K_{WGS} = 1), meaning that K_{ox} = K_{red}. With a feed reactants ratio of 1:1, the maximum conversion achievable is 50%. That value has been previously determined by Wenzel, Rihko-Struckmann and Sundmacher (2017). The study published by Metcalfe *et al.* (2019) demonstrated an innovative approach. It proved that in a conventional catalytic WGS reaction at 820 ºC, feeding equimolar concentration of CO and H_2O and assuming fast kinetics, the equilibrium conditions reached at the outlet will contain 1:1:1:1 $CO:H_2O:CO_2:H_2$. The limitations presented above could be overcome by working with packed-bed reactor CL system. By counterflowing the reactants, the OCM bed created would possess multiple oxygen potentials. This multiple oxygen potential would maximise the conversions without the need of additional separation steps.

In a CLWGS process, the WGS reaction is split as follows:

$$H_2O \rightleftharpoons H_2 + \frac{1}{2}O_2 \quad \text{(Eq. 3.5)}$$

$$CO + \frac{1}{2}O_2 \rightleftharpoons CO_2 \quad \text{(Eq. 3.6)}$$

By operating at equilibrium conditions and considering reactants feed 1:1 (H_2O:CO) where conversions of H_2O to H_2 and CO to CO_2 are roughly the same ($X_{H_2O} = X_{CO_2}$, (Eq. 3.7) = (Eq. 3.8)), the oxygen lost or gained during the initial half reaction will be approximately the same amount of oxygen gained or lost during the other half reaction. This equal oxygen exchange ensures an optimal thermodynamical behaviour, and conversion of both half-reactions is high and equal throughout the process. Therefore, the pO_2 used throughout a CLWGS will be 10^{-23} bar when flowing CO (reduction) and 10^{-7} bar when flowing H_2O (oxidation), at 820 ºC. Consequently, the designed and conceived OCM ought to possess oxygen storage and transport capacity under the given pO_2.

$$X_{H_2O} = \frac{(y_{H_2O})_{outlet}}{(y_{H_2O})_{inlet} - (y_{H_2O})_{outlet}} \quad \text{(Eq. 3.7)}$$

$$X_{CO} = \frac{(y_{CO})_{outlet}}{(y_{CO})_{inlet} - (y_{CO})_{outlet}} \quad \text{(Eq. 3.8)}$$

Explained by Ungut (2022) and described in Figure 3.1, at mild oxidising conditions (or high pO_2, relative to CLWGS conditions) the conversion of CO to CO_2 is more favourable. On the other hand, at highly reducing conditions (low pO_2), the favoured process is the H_2O conversion to H_2.

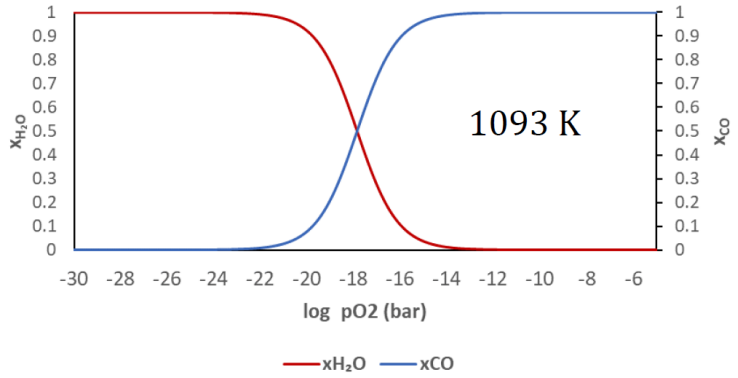

Figure 3.1. CO to CO_2 and H_2O to H_2 theoretical conversions as a function of log pO_2 at T = 820 ºC. Image courtesy of Ungut (2022).

As explained in the introductory chapter, in 1.4.1.d, the use of perovskites as OCM is widely established in CL processes. Their structure allows to tailor the stoichiometry between cations, their composition or the amount of oxygen vacancies desired. In the A-site, metals that promote ionic mobility are essential for CL processes, such as alkaline-earth elements, hence the choice of using barium (Ba), as demonstrated by Song, Ning and Bouwmeester (2020). To further ensure thermal stability and ionic mobility in the high-temperature

processes of CL and promote the formation of oxygen vacancies within the material, partial substitution of the Ba from the A-site was done, via the use of rare-earth metals (Zeng et al., 2020; Delgado-Galicia et al., 2024). Although lanthanum-based perovskites for CL applications are the subject of a vast majority of the publications in which perovskites are used, there is still little research done on alternate lanthanides. Because Pr and Sm have the ability to improve structural stability and encourage the creation of oxygen vacancies (Iihoshi, Goto and Shimakawa, 2024), both of which are essential for sustaining performance over prolonged CL operations, they were selected as A-site dopants in this work. In the B-site, the choice of active metals in the WGS is crucial, such as Fe, Cu, Ni or Co (Baraj, Ciahotný and Hlinčík, 2021). Following these properties, in this chapter, two lanthanide-based ferrite perovskites ($Pr_{0.5}Ba_{0.5}FeO_{3-\delta}$, and $Sm_{0.5}Ba_{0.5}FeO_{3-\delta}$) were selected as the oxygen carrier materials of choice to undergo the required characterisation for a CL process.

This study represents the first systematic investigation of $Pr_{0.5}Ba_{0.5}FeO_{3-\delta}$ (PBFO) and $Sm_{0.5}Ba_{0.5}FeO_{3-\delta}$ (SBFO) as oxygen carrier materials (OCM) for chemical looping water-gas shift (CLWGS) and chemical looping steam methane reforming (CLSRM). While simple oxides (i.e. Fe/CeO_2 systems, due to their ability to host high number of oxygen vacancies, Gao *et al*., 2022) and lanthanum-based perovskites have been extensively studied in CL applications, there is limited research on the use of alternative lanthanides, such as Pr and Sm, despite their well-documented ability to enhance structural stability and oxygen vacancy formation. This work explores their performance in CL conditions and their potential as superior OCM candidates.

Part of the described results of this chapter have been presented at the 6th International Conference in Chemical Looping, 2022, in Zaragoza, Spain, and disseminated via a conference article – *$Ln_{0.5}Ba_{0.5}FeO_{3-\delta}$ (Ln = Pr, Sm) as novel Oxygen Carrier Materials for Chemical Looping Water-Gas Shift*.

3.2. Materials characterisation

Patterns displayed in Figure 3.2.a illustrate the formation of high purity perovskites. A first comparison was done to study the structural differences in materials sintered under different conditions. The sharp peaks shown for the OCM sintered at 1400 ºC indicated also higher crystallinity than the OCM sintered at 1000 ºC, in which the peaks are broader.

To corroborate this affirmation, average crystal size was calculated (see Table 3.1) for the different prepared materials according to Scherrer's equation (Eq. 3.10):

$$D = \frac{K \cdot \lambda}{B \cdot \cos(\theta)} \quad \text{(Eq. 3.9)}$$

Where D is the average crystal size (nm), K is the Scherrer constant (kept at 0.94, assuming spherical shape), λ is the wavelength (0.354 Å, synchrotron wavelength), B corresponds to the full width at half maximum of the examined peak and θ corresponds to the diffraction angle of the peak. A remarkable difference between the average crystal size is observed between materials. PBFO and SBFO sintered at 1400 ^{o}C displayed an average crystallinity of 330 and 244 nm, respectively, whilst PBFO and SBFO sintered at 1000 ^{o}C possessed an average size of 17 and 15 nm, respectively.

Table 3.1. Structural properties obtained by PXRD and Rietveld refinement of the prepared materials, PBFO and SBFO.

Material	**Average crystal size, *nm***	**Main phase (Secondary phase)**	**Cell parameters Å Cell volume, Å^3**
PBFO-1000(14h)	17	Pm-3m	3.9337 Å 60.870 Å^3
PBFO-1400(14h)	330	Pm-3m	3.9362 Å 60.987 Å^3
SBFO-1000(14h)	15	Pm-3m (Pmmm)	3.9383 Å, 61.085 Å^3 (a=3.9655 Å,) (b=3.8989 Å,) (c=7.7733 Å) (120.185 Å^3)
SBFO-1400(14h)	244	Pm-3m	3.9383 Å 61.085 Å^3

Phase identification and Rietveld refinement confirmed cubic symmetry for all the patterns, belonging to the group *Pm-3m* with high accuracy (Rwp < 11) in all cases. No observable difference was found for the cell parameters of the cubic phases. PBFO presented similar lattice values, regardless the sintering temperature (3.9337 Å at 1000 ^{o}C sintering temperature vs. 3.9362 Å at 1400 ^{o}C). Similarly, SBFO presented close cell parameters in both materials (3.9384 Å sintered at 1000 ^{o}C and 3.9383 Å sintered at 1400 ^{o}C). No secondary phases were identified in PBFO, whilst minor peaks were detected at 5.8º, 7.7º, 11.9º, and 12.8º, for SBFO, suggesting the formation of secondary perovskite phases for the materials sintered at 1000 ^{o}C. These identified peaks and refined phases in

SBFO sintered at 1000 ºC corresponded to a *Pmmm* orthorhombic $SmFeO_3$ phase. This existence of secondary phases suggests that lower symmetry is achieved when sintering at lower temperatures, as single-phase cubic perovskites were at 1400 ºC.

Clear morphological differences are observed in the SEM images of the synthetised OCM. Figure 3.2.b corresponds to the sample sintered at 1400 ºC, showing a dense surface, whilst the samples sintered at lower temperatures (Figure 3.2.c) display a more porous structure. Thereby, samples sintered at higher temperature were expected to possess a lower specific surface area. It was determined that the lower crystal size was outweighed by the larger porosity. Therefore, the materials sintered at higher temperature were not further considered for future investigation.

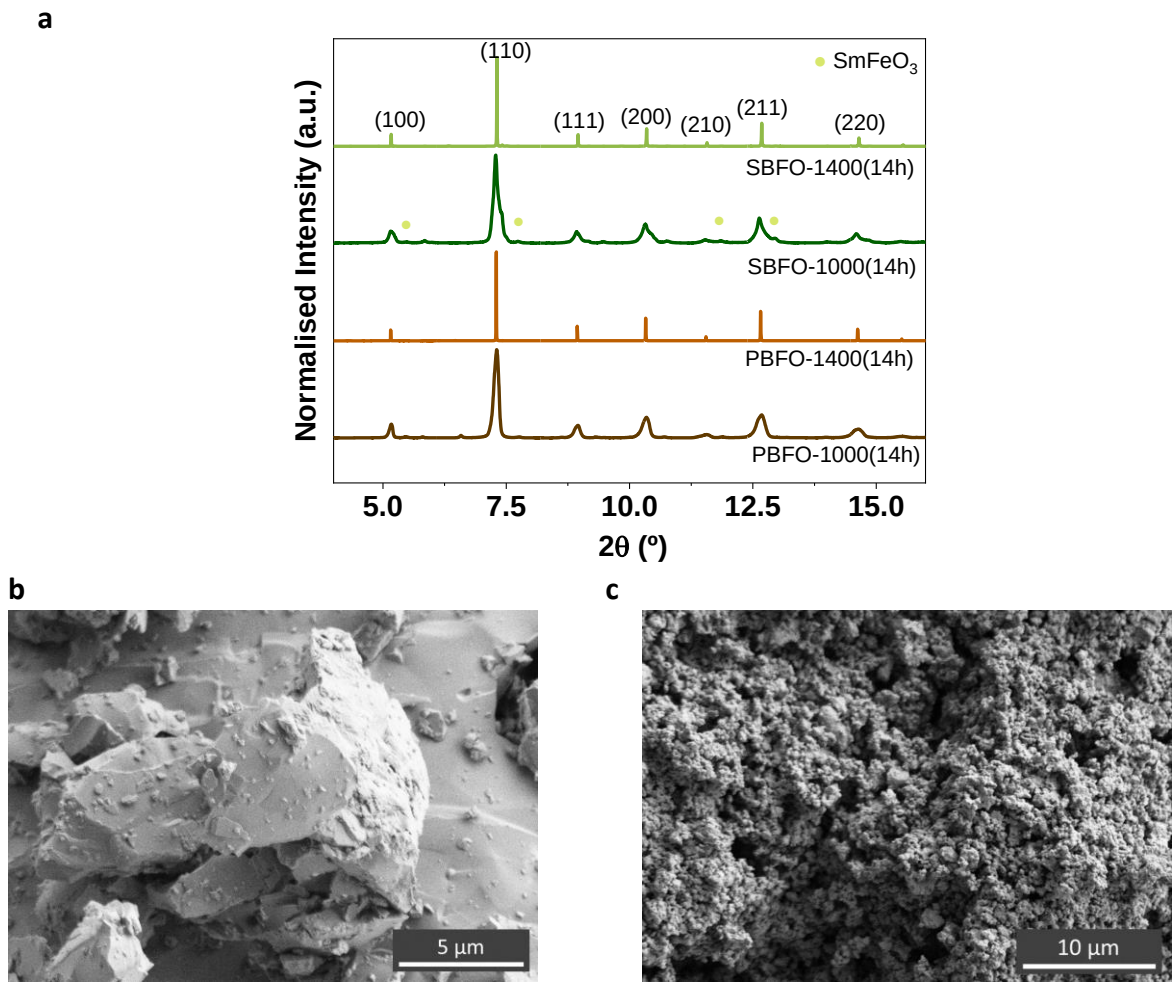

Figure 3.2. a. Synchrotron PXRD diffractograms of as sintered PBFO and SBFO, sintered at two different temperatures (1000ºC and 1400ºC) during 14h. hkl indices are attributed to the top pattern and apply to all the displayed diffractograms. Macrostructure images with different magnifications of PBFO sintered at different temperatures, done by SEM. **b.** PBFO-1400 ºC with different magnifications. **c**. PBFO-1000 ºC.

3.3. Initial oxygen vacancies and OCM stability

OCM were studied by iodometric titrations in the *as sintered* form and after reduction and at the end of a reduction cycle. Titrations showed values of δ = 0.13 ± 0.05 and δ = 0.18 ± 0.03 initial oxygen vacancies for both *as-sintered* (at 1000 ºC) PBFO and SBFO, respectively. Previous authors confirmed the existence of initial oxygen vacancies in this type of perovskites (Karen *et al.*, 2002; Karen, 2021). Even though small, this difference in δ_0 is attributed to the difference in cationic radii, ($r(Pr^{3+})$ = 1.179 Å and $r(Sm^{3+})$ = 1.079 Å, both in 9-fold coordination), as stated by Volkova et al. (2019). Rare-earth metals decrease their cationic radii when moving to the right in the periodic table. This property is partially explained by the relativistic effects (Das, et al., 2023)(Das, et al., 2023). Relativistic effects suggest that, by replenishing the electrons from the inner orbitals (4f and 5f), the effective nuclear charge is higher. This higher nuclear charge will provoke the atoms to experience a slight contraction, diminishing their radii. In the case of the atoms presented here, Pr and Sm will have the following electronic configurations: [Xe] $6s^2$ $4f^3$ for Pr and [Xe] $6s^2$ $4f^6$ for Sm. Consequently, $r(Pr^{3+})$ = 1.179 Å, is larger than $r(Sm^{3+})$ = 1.079 Å. This difference in size affects the bonding enthalpy of both Pr-O and Sm-O: $\Delta H_{f,Pr\text{-}O} < \Delta H_{f,Sm\text{-}O}$ (-147.7 kJ / mol vs -135.6 kJ / mol, respectively). These ΔH were taken from Volkova et al. 2019). Pr-O bond is therefore more stable than Sm-O, thus creating a larger number of initial oxygen vacancies in the latter structure, SBFO. Similar findings were observed in a recent study from Delgado-Galicia et al. (2024). In this study, larger lanthanide cations were however used in the perovskite matrix. These larger cations led to a lower amount of oxygen vacancies in the pristine materials.

When carrying out thermogravimetric analysis, the way the number of oxygen vacancies, δ, was calculated is as follows in (Eq. 3.10):

$$\delta = \frac{moles\ O\ released/gained}{molar\ mass\ OCM} \qquad \text{(Eq. 3.10)}$$

To confirm these number of vacancies, iodometric titrations were done. To do an estimation via iodometric titrations, an initial reduction of the OCM is done while the mass loss is recorded. The obtained value is attributed to oxygen released. These same samples are further titrated (as explained in the methods), obtaining another δ value. These values were gathered in Table 3.2 and finally compared.

Table 3.2. Oxygen vacancies values, δ, and corresponding B-site valence of OCM in the *as sintered* state and after undergoing one 5% H_2 reduction at 875 ºC during 1 h. *As sintered* values cannot be obtained via TGA.

Species	δ as sintered (titration)	Fe^{n+} as sintered (titration)	δ post reduction (TGA)	Fe^{n+} post reduction (TGA)	δ post reduction (titration)	Fe^{n+} post reduction (titration)
PBFO	0.13 ± 0.01	3.19	0.32	2.85	0.30 ± 0.01	2.90
SBFO	0.18 ± 0.02	3.13	0.36	2.78	0.36 ± 0.02	2.67

When reducing 1 mmol of these OCM under H_2 for 1h at 875ºC, they released 0.303 mmol O PBFO and 0.336 mmol O SBFO, equal to a relative δ of 0.32 and 0.36, respectively. 875 ^oC was the chosen temperature as a high extent of decomposition was observed at higher temperatures (T > 900 ^oC) in preliminary experiments. Relative δ was referred to the amount of oxygen lost as compared to the initial absolute value of oxygen vacancies, δ_0. These same samples were later analysed by iodometric titration. The calculated δ after the titration of these reduced samples were of 0.30 and 0.36, considering that the initial values were δ_0 = 0.13 and 0.18, respectively. These minor differences in values show a good agreement between the methods, helping therefore to confirm the presence of initial vacancies.

Iodometric titrations also provided information about the oxidation state of the B-site, Fe in this case. *As sintered* materials possessed a mixture of different Fe^{n+} species (average oxidation states of 3.13 for SBFO and 3.19 for PBFO). These oxidation states were considered to be a mixture of 13% of Fe^{4+} and 87% of Fe^{3+} for SBFO, and 19% of Fe^{4+} and 81% of Fe^{3+} for PBFO. Once reduced, as expected, Fe oxidation state decreased in both materials. OCM presenting initial oxygen vacancies suggested that Fe from the B-site would partially reduce its coordination number as Fe-O from 6 to 5, due to a smaller cationic size, creating a more reactive Fe (Ward *et al.*, 2021).

Stability of these materials was studied by conducting twenty redox cycles under elevated temperatures (875 ºC) and potent redox agents (5% H_2 for the reduction and 20% O_2 for the reoxidations). Parameters used during real CL conditions are not as potent as the conditions employed here, thereby the election of these conditions would determine whether the prepared OCM were suitable to be implemented in CLWGS. To carry out this, 1 mmol of OCM was used (0.25 g), with a temperature ramp of 5 ºC / min under Ar until reaching the target 875 ºC. 5% H_2 was conducted for 1 h followed by the reoxidation under

20% O_2, for 10 min. Figure 3.3.a shows the oxygen non-stoichiometry at different cycles for each OCM. Both OCM became more reducible over time, unlocking a higher oxygen potential with time. SBFO displayed a higher reducibility for the first cycles, indicating larger reducibility than its analogue PBFO in the early cycles, probably due to a larger amount of initial oxygen vacancies. This lower amount of initial vacancies would make SBFO more active and prone to be reduced. SBFO oxygen capacity did not increase after 10 cycles, suggesting the limitations of the material to accommodate more vacancies as number of cycles increases. Contrary to this, PBFO showed an increased reducibility throughout the cycles. The higher 3-δ value observed for PBFO in the first cycle of the experiment was due to an experimental error in which the gas inlet was not fully open, not allowing a proper gas flow, solved for the rest of cycles. Despite not possessing such initial high reducibility (see 5th cycle in Figure 3.3.a), PBFO showcased higher reducibility in the long term. This suggested that PBFO could achieve lower values of 3-δ, equal to a larger oxygen capacity and more activity towards reactants. Jiang et al. (2021) observed that decreasing the A-site cationic size affected the Fe-O covalency. Smaller cationic radius directly decreased the Fe-O covalency. These two parameters would directly determine the oxygen mobility and activity, eventually raising the formation energy of oxygen vacancies and generating less vacancies over time.

As the materials underwent continuous cycles to complete the program, PXRD patterns could not be captured after each individual half cycle and only after the entirety of the reaction conditions had ended. The examination of the PXRD patterns after 20 consecutive redox involving 5% H_2 – 20% O_2 cycles allowed for the study of any potential structural variation of the materials. From phase identification (Figure 3.3.b), it was noticed that the main perovskite phase was preserved in both SBFO and PBFO. SBFO presented however all the perovskite peaks separated. Refinement was conducted and fit was not good enough when applying a sole type of symmetry group (R_{wp} > 10), suggesting the coexistence of different perovskite phases for SBFO after reduction. Besides, no small adjacent peaks involving the decomposition of the perovskite into other structures were identified. On the other hand, PBFO only displayed peak enlargement, and no extra peaks appeared (Figure 3.3.c). The aggressive redox conditions used during this experiment led to a decrease in the crystallite size, displayed as peak in the PXRD pattern (Evans, 2018). PXRD patterns

indicated that OCM overall structure was maintained, highlighting the stability of the materials under these conditions.

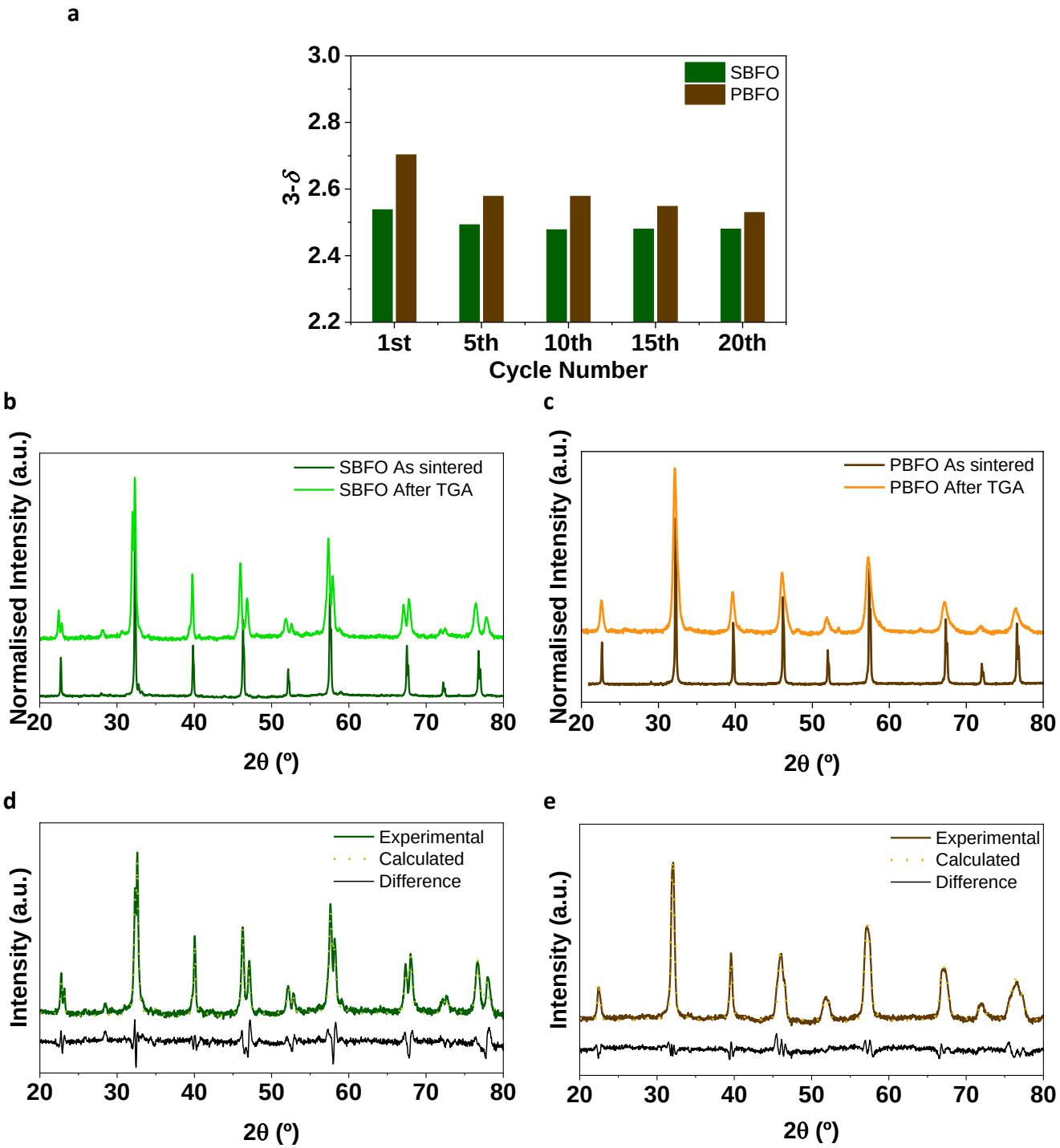

Figure 3.3. OCM behaviour during redox cycles at high temperature and potent redox agents. **a**. Oxygen vacancies (3-δ) of the designed materials after undergoing redox cycles. Cycles plotted: 1st, 5th, 10th, 15^{th,} and 20th. **b**. SBFO, **c**. PBFO. PXRD patterns of the as sintered and tested OCM: SBFO, left; PBFO, right. Rietveld refinement of the OCM after undergoing 20 TGA cycles, **d**. SBFO after test, **e**. PBFO after test.

Rietveld refinement analysis confirmed the transition to a tetragonal phase in both OCM, while the initial cubic phase was lost in both OCM (Figure 3.3.d-e). The transition was

associated to the formation of a larger amount of oxygen vacancies in the material, consistent with previous research (Karen et al., 2002). These results were confirmed by the titrations conducted after the OCM underwent reduction. The resolution of the patterns obtained did not allow to discern the cubic and tetragonal phases coexisting in SBFO. Regarding PBFO (Figure 3.3.e), the formation of other symmetry groups could not be stated, as only peak broadening occurred. This broadening hinders further peak deconvolution, not allowing to study the presence of other phases. Other structures, such as cubic or orthorhombic, were considered when carrying out the refinement, being ultimately the tetragonal phase the one that provided the best fit between model and experimental data. Other phases were included in the refinement, such as the Ruddlesden-Popper phase, but no agreement between the pattern and the model was obtained.

3.4. Study of non-stoichiometry

Previous works (Kuhn, Hashimoto, *et al.*, 2013; Araki, Miaolong and Arai, 2017; Zhao *et al.*, 2023) have reported oxygen non-stoichiometry dependency at intermediate pO_2's ($pO_2 > 10^{-10}$ bar). To simulate CL conditions, lower pO_2 are required (~10^{-22} bar). Other studies based on oxygen non-stoichiometry (Sengodan *et al.*, 2015) have done this analysis at the low pO_2 range by conducting coulometric titrations. However, only a few recent studies (de Leeuwe, Hu, Neagu, *et al.*, 2021) have determined δ values in the low pO_2 range by using TGA and buffer gases as the ones presented here.

Non-stoichiometry relative to the relevant CLWGS working pO_2 of the OCM was studied by TGA with a set of buffer gases. In order to observe the formation of oxygen vacancies under different pO_2 conditions, the study was carried out at different isotherms: 720 ºC and 820 ºC.

The gases would flow through the pipes system in the order shown in Table 3.3: 100 mL / min of air ramp (10 ºC / min) started until the target temperature was achieved. Once the target temperature was achieved, 100 mL / min of the buffer gases were flowed in decreasing order of reduction (1 was firstly flowed, 2 was the second gas flowed, etc) for a sufficient time to reach equilibrium. This equilibrium was understood when no mass change was recorded for a certain amount of time. Between each reduction gas, 100 mL / min of air were flowed for 5 min, to ensure the OCM were fully reoxidised after each half-cycle. Cool down took place under air.

Table 3.3. Buffer gases ratio (CO:CO_2) and the flowing order through the system

CO	CO_2	Flowing order
1	100	1
1	10	2
1	1	3
10	1	4
100	1	5

The 3-δ vs pO_2 dependence was determined by calculating the values of δ at different pO_2. Gases were flowed enough time until equilibrium was reached: this was observed by minimal mass variation in time while buffer gas was flowed (Δm ~ 1 mg after 5 min). For each measurement, around 0.25 g were placed into the crucible suspended from the TGA.

Changes in oxygen non-stoichiometry ($\Delta\delta$) were calculated from the weight change (Δw) observed in the sample after each half cycle:

$$\Delta\delta = \frac{M_S \cdot \Delta w}{M_O \cdot w} \qquad \text{(Eq. 3.11)}$$

where M_S corresponds to the molar weight of the sample, M_O corresponds to the molar weight of oxygen and w, to the initial measured weight.

Figure 3.4.a–d shows OCM gradual reduction using different CO:CO_2 buffer gases which provide different pO_2. The mass change was recorded and converted into oxygen non-stoichiometry values for the two materials studied in this chapter. The oxygen content was measured over a wide pO_2 range, going from beyond the upper limit of the oxidising pO_2 conditions for WGS (ambient pressure) until the pO_2 value was left out of the lower range of WGS conditions (down to 10^{-25} bar). The continuous oxygen loss at different pO_2 highlights the reducibility of the designed OCMs.

An initial comparison was done for OCM sintered at different temperatures. SBFO exhibited a similar behaviour regardless of the sintering temperature (Figure 3.4.a), unlike PBFO, which seemed to be more reducible and consequently, to possess a higher OSC when it was sintered at low temperatures (1000 ºC, Figure 3.4.b). The reason for this difference could be based on the macrostructure of the system observed by SEM: a higher gas-solid interaction due to the increased porosity caused by lower sintering temperatures. Given the similar results in terms of OSC between OCM synthetised at lower temperature, the

OCM sintered at lower temperature were the ones chosen for further OSC study at different pO_2 conditions.

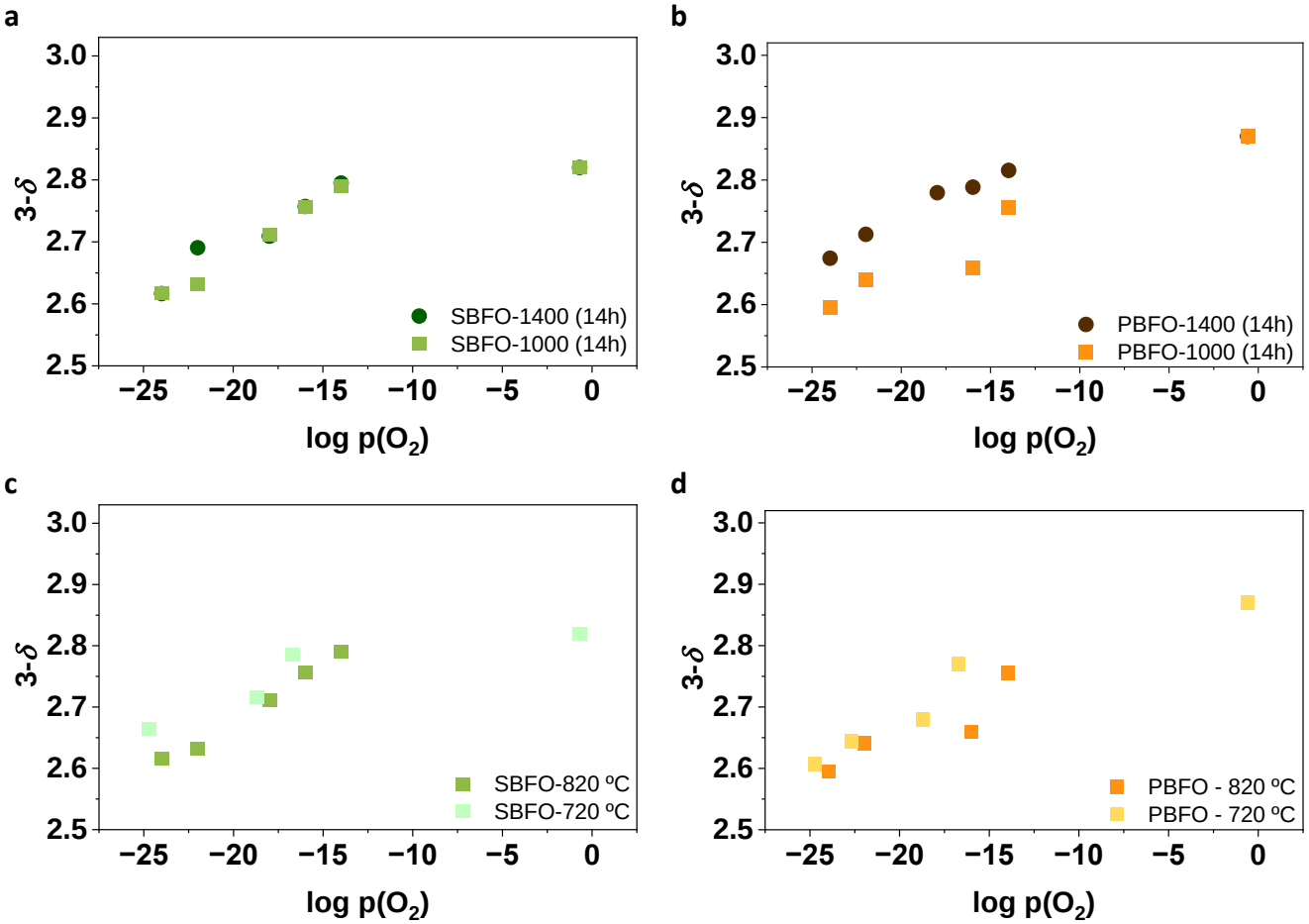

Figure 3.4. Oxygen vacancies (3-δ) as function of pO_2. values obtained at 820 ºC for same OCM sintered at different temperatures (1400 ºC and 1000 ºC), **a**, SBFO. **b**, PBFO. 3-δ values at different temperatures (820 ºC and 720 ºC) as function of pO_2, for materials sintered at 1000 ºC during 10 h, **c**, SBFO, **d**, PBFO.

Once OCM were chosen, SBFO and PBFO sintered at 1000 ºC for 14 h underwent the same process, but at 720 ºC, to establish a non-stoichiometry profile at different pO_2 for the two given temperatures. Following the trend from Kuhn, Fukuda, et al. (2013), the materials showed larger OSC at the lower temperatures (see Figure 3.7.c–d). At low pO_2, the risk of decomposition was higher, as previously stated by Kuhn, Hashimoto, et al. (2013). Given the reducing conditions, the studied perovskites (lanthanum strontium cobalt oxide, LSC, and lanthanum strontium iron oxide, LSF) underwent decomposition into spinel phases and single metal oxides (i.e., La_2O_3, CoO, etc). That decomposition was observed by a sharp drop in the 3-δ value at a certain pO_2, indicating decomposition. Contrarily to this, the studied OCM here showcased high stability, guaranteeing a smooth drop in the 3-δ value,

implying high stability. These OCM presented increasing reducibility throughout the whole pO_2 range, evidenced by a linear trend.

The lack of a sharp drop in the curve at the low range revealed that none of the materials decompose at any point of the reductions. This increased reducibility of these OCMs did not follow the profile previously observed for other materials, such as LSF641 or LSC641 (Sitte, Bucher and Preis, 2002; Kuhn, Hashimoto, *et al.*, 2013), which were materials used in CL processes. The profile of the materials reported showed a clear decomposition at $\delta > 0.25$ for intermediate pO_2, whereas the OCM presented in this chapter do not display the same trend, as no steep changes were observed in the curves presented in Figure 3.4.f-g. In this case, SBFO and PBFO only presented reversible decomposition of the perovskite phase at $\delta \sim 0.39$ and 0.41, respectively. Further investigation is therefore needed at low pO_2 to conclude on the limit of the OCM decomposition. Reversibility could be observed after these materials underwent several redox cycles as shown in Figure 3.3, in which they fully recovered their perovskite structure.

As predicted when carrying out the oxidoreduction cycles under strong temperature conditions and potent redox agents, PBFO eventually showcased a slightly larger δ, equal to a larger OSC and therefore oxygen mobility. Higher oxygen mobility would play a crucial role when testing the materials in real CL conditions (Li, Wang and Wei, 2013). The effect of this marginal difference between OCM will be looked into during the following sections of the chapter.

3.5. Cell lattice modification and material stability

The designed OCM were therefore proven stable after undergoing several cycles under strong redox conditions and high temperature (875 ºC and H_2 – O_2 cycles) and under CLWGS pO_2 conditions. Aiming at gaining further understanding about these OCM, PBFO and SBFO were taken for further analysis to synchrotron facilities to study *ex situ* their cell parameters under simulation of CLWGS conditions. The study of the materials' stability and lattice parameters allows to determine the modifications of the oxygen non-stoichiometry during cycling that will affect the material structure. In this case, the OCM underwent a singular reduction, the reducing gas run until equilibrium was reached and cooled down under the same buffer gas and the material was collected for further examination. This was repeated for all the buffer gases. Synchrotron PXRD patterns of the resulting materials

were collected from capillaries at room temperature. It is important to highlight that these values were taken at room temperature and *ex situ* conditions, hence it was not possible obtain thermal expansion values and apply them to real CLWGS operational conditions. All the values presented here are then referred to chemical expansion.

Rietveld refinement was conducted for all the patterns obtained. Only one pattern, corresponding to PBFO, is displayed in Figure 3.5.a,b. The exclusion of the pattern corresponding to SBFO is to avoid repetition as patterns look alike. An initial cubic phase was observed for the *as-sintered* OCM, as reported in previous sections of this chapter. After the first reduction under the less reducing gas, $CO:CO_2$ = 1:100 (pO_2 ~ 10^{-13}), a new phase was observed. This new phase, $P4/mmm$ tetragonal phase, coexisted with the original $Pm\bar{3}m$ cubic phase. This agreed with previous results (Karen and Woodward, 1999; Karen, 2021) for the said materials when the OCM. reached similar values of oxygen non-stoichiometry as the authors. To characterise the initial impurities and the perovskite decomposition, an orthorhombic model ($Pmmm$) was used. Both cubic and tetragonal phases coexisted in varying proportions, with relatively stable values observed, until the last buffer gas ($CO:CO_2$, 100:1) was flowed. At this stage, the material undergoes reversible decomposition, leading to the loss of the main structural configuration as a consequence of the high reducing potential used (pO_2 ~ 10^{-21}), but with a recovery of the tetragonal phase, as described when carrying out the 5% H_2 – 20% O_2 cycles.

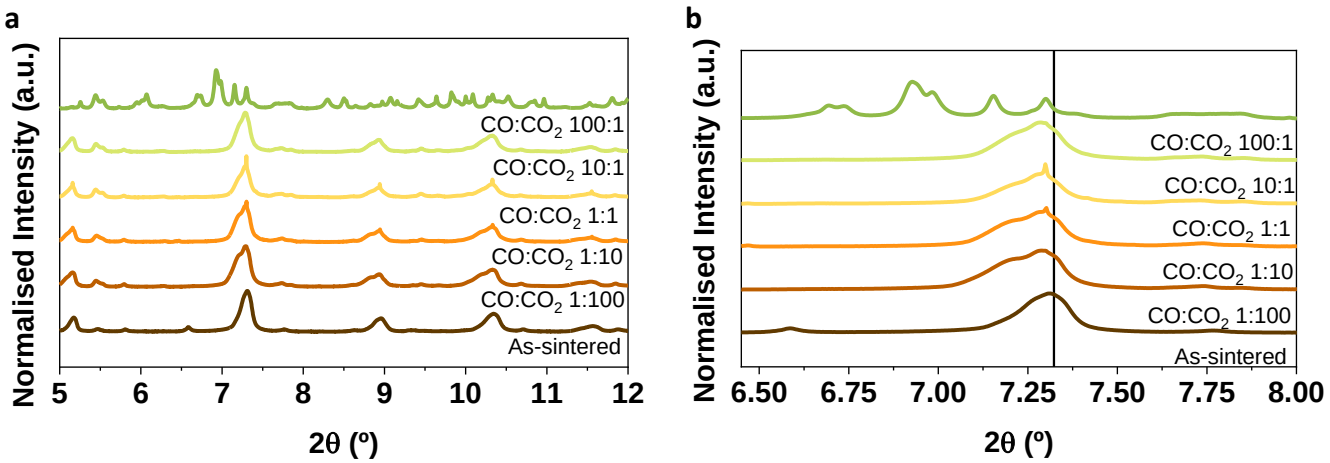

Figure 3.5.a. Example of PXRD patterns of PBFO after undergoing subsequent oxidoreductions under different buffer gases. Data collected from capillaries at room temperature, at ESRF. **b**. Zoomed area of the PXRD pattern to observe peak shifting.

Cubic symmetry directly provides the cell parameter, a_{cub}, but to obtain the pseudo-cubic cell parameter of the tetragonal symmetry group some further calculations are required:

tetragonal and orthorhombic lattice parameters are related to the primitive perovskite cell with the cell parameter, a_p, by ~ $\sqrt{2}a_p$ x $\sqrt{2}a_p$ x $2a_p$ and $2a_p$ x $2a_p$ x $2a_p$, respectively.

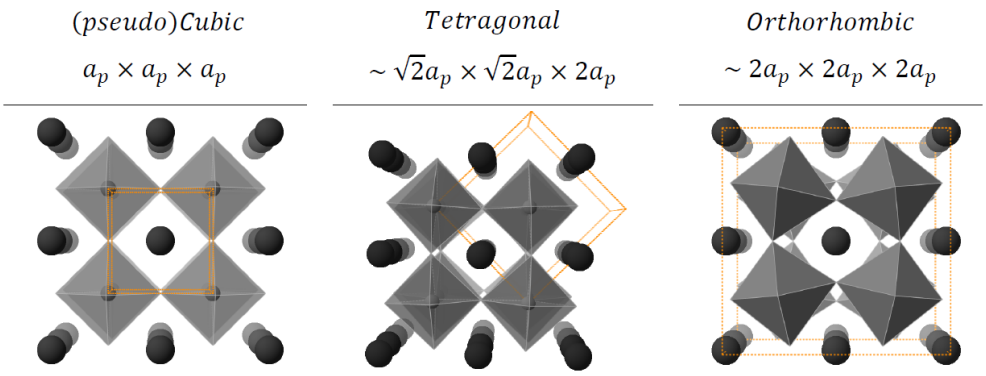

Figure 3.6. Diagram representing the three types of unit cells reflected in this chapter. Symmetry decreases from cubic to orthorhombic. Ionic disorder is increased with the lower symmetry, increasing ionic tilting. Ideal and distorted perovskites are represented with their pseudocubic unit cell underneath each name. Image borrowed from Neagu (2012)(2012).

Thereby, to obtain the pseudo-cubic cell parameter of non-cubic symmetry, the following expression is needed (Eq. 3.12):

$$a_p = \sqrt[3]{\frac{V_{unit\ cell}}{n_{unit\ cell}}} \qquad \text{(Eq. 3.12)}$$

Where $V_{unit\ cell}$ corresponds to the volume of the unit cell identified and $n_{unit\ cell}$ is the number of perovskite units contained in it (4- and 8-unit cells in tetragonal and orthorhombic, respectively, Neagu (2012)).

The reductions conducted with different buffer gases do not modify any oxidation number of the A-site. The redox processes involved in these experiments only modify the oxygen non-stoichiometry and the Fe oxidation state. By reducing the system, the oxidation state of Fe in the B-site decreased, increasing thus its cationic radius. As consequence of this reduction, the size of the unit cell expanded accordingly. Cell expansion originated a slight shifting towards the left in the PXRD Figure 3.5.b. A zoomed area corresponding to the largest peak of the perovskite phase (around 7.25º) was presented in Figure 3.5b. Lattice parameters were obtained from the Rietveld refinement conducted for the PXRD patterns along with their weight fraction contribution to the unit cell. For the core perovskite phase, cubic ($Pm\bar{3}m$) and tetragonal ($P4/mmm$) models were used (to see atomic distribution in the different symmetry group, observe Figure 3.6). OCM exhibited these two phases in

varying weight fractions. The *pseudo-cubic* cell parameters of the different phases corresponding to the main perovskite phase were investigated following (Eq. 3.12).

The results of the cell parameters modification are shown in Figure 3.7.a-b. Both structures initially present cubic symmetry. SBFO underwent several reductions and showed linear chemical expansivity until it reached the combination of both cubic and tetragonal regime ($\delta = 0.29$). Once this new regime was in place, the material showed cell expansion again. The refined value of the volume for the tetragonal phase was, at the beginning of the regime transition, of 118.73 $Å^3$. This value was close value 119.4 $Å^3$, previously reported by Karen et al. (2002), where the same material presented a similar oxygen deficiency. These close volume values indicated good agreement between the findings and the literature. However, instead of continuing increasing the cell size when entering the new regime, lattice parameters decreased. This value was transformed into pseudo-cubic cell parameter via the formula given in (Eq. 3.12). The jump in lattice expansion occurred once the OCM entered the cubic-tetragonal regime, suggesting a different chemical expansivity when $\delta < 0.29$ and when $\delta > 0.29$, as two symmetry groups were now detected. Similar findings were done by de Leeuwe (2019), where different chemical expansivities were detected within the same LSF641 structure ($\delta < 0.2$ and $\delta > 0.2$). The study conducted by the author involved further neutron scattering and *in situ* PXRD study in which the thermal expansion and the exact amount of oxygen vacancies could be observed while the buffer gas was flowed. The results presented in this chapter open the door for further understanding of the behaviour of SBFO and PBFO.

PBFO was proven stable within a wide δ range ($0 < \delta < 0.5$) when conducting coulometric titrations (Sengodan *et al.*, 2015) at lower temperatures than the working temperatures in CLWGS. When conducting the TGA for PBFO, it underwent a transition towards tetragonal symmetry before SBFO did. Whilst SBFO transitioned to a mix cubic-tetragonal regime at $\delta \sim 0.29$, PBFO did this transition at $\delta \sim 0.23$. Once this regime was reached, PBFO underwent cell expansion. No values could be refined at $\delta < 0.23$, as the experiment was not conducted with gases providing intermediate pO_2. Therefore, no lattice variation could be calculated.

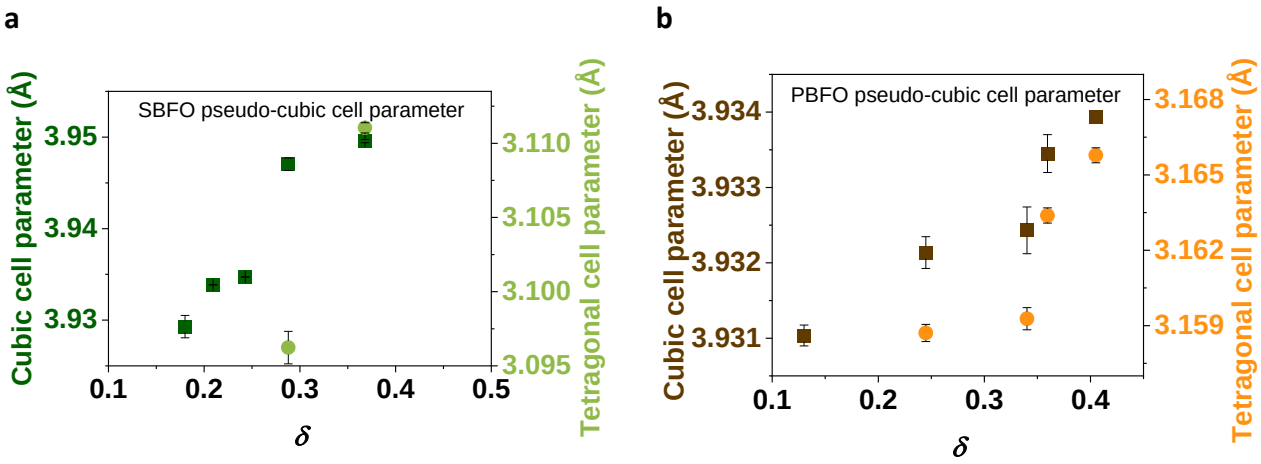

Figure 3.7. Pseudo-cubic unit cell parameters calculated by *ex situ* capillaries at ESRF at room temperature. The samples examined were collected at room temperature after undergoing reduction under different buffer gases at 820 ºC. **a**, SBFO. Some error bars are smaller than the symbols containing them. **b**, PBFO. Error bars in the y axis for data provided by synchrotron wavelength is smaller than the symbol designing the value.

In both cases, SBFO and PBFO remained as perovskites over a wide range of oxygen non-stoichiometry (10^{-19} < pO_2 < 10^{0} bar). When pO_2 < 10^{-19}, materials displayed a reversible loss of structure. After reductions at different pO_2, SBFO and PBFO did not undergo phase segregation, as previously revealed by the majority of patterns collected *ex situ* at the synchrotron (Figure 3.5.a). The most reducing $CO:CO_2$ buffer gas generated reversible partial decomposition of the main perovskite body. Nevertheless, both SBFO and PBFO preserved a perovskite structure over a wide range of oxygen non-stoichiometry.

These results overlook factors such as the formation of intermediate species during reduction, as the capillaries only provided information *ex situ*. No experimental data was available in the literature regarding this formation of secondary species when flowing buffer gases to this set of OCM. Consequently, they establish a precedent and open a new window of analysis by *in situ* PXRD to delve into the thermal and chemical expansion. Also, neutron diffraction is encouraged for an in-depth study of the Fe valence state and oxygen non-stoichiometry at the relevant pO_2. The structure at a precise pO_2 and temperature of an OCM is related to its oxygen content of non-stoichiometric and hence to its oxygen properties. A thorough understanding of these properties in these selected OCM will help overcoming the main challenges in H_2 production in CL. Another challenge is the presence of phase segregation in extended times of CL operation (Lein, Wiik and Grande, 2006). In CL, high temperatures are typically involved, and the risk of secondary phases or decomposition arises as reactions take place. The proposed neutron scattering and *in situ*

analysis would provide information about this oxygen content and possible secondary phases. The determination of the oxygen content and formation of these phases would eventually help deconvolute the design of the material and of the reactor to work under the desired CL conditions.

3.6. Application in Chemical Looping Water-Gas Shift

TGA showed that the materials continuously gained and released oxygen from the gas feed under the partial oxygen pressure conditions for CLWGS. PXRD confirmed that the tested OCM maintained the perovskite structure after these tests, highlighting that they did not undergo decomposition at CLWGS conditions. These features made the characterised materials suitable to be implemented in CLWGS.

3.6.1 Temperature optimisation

Temperature parameters were studied in the work carried out by de Leeuwe (2019). In this work, a large screening of temperature conditions was conducted. Experimental data and models indicated that, when the system operated near the equilibrium, at temperatures higher than $K_{eq} = 1$, product quality and yield were expected to worsen. Despite products yield would be enhanced when using higher temperature values at which $K_{eq} > 1$ ($T > 820$ ºC), the chosen working temperature value for these experiments was 820 ºC. This value was also studied by Metcalfe et al. (2019), as the system would be operating at the WGS equilibrium conditions. Setting up the process at 820 ºC allowed to determine, at small scale, whether the suggested OCM overcame the equilibrium limitations described for the conventional WGS reaction.

3.6.2 Half cycle duration

Following the study from Ungut (2022), an ideal OCM is the one displaying a large oxygen profile within the required pO_2. As presented in the previous section, both SBFO and PBFO showcased a large oxygen profile in the pO_2 relative to CLWGS.

Previous studies have displayed very different half reaction times: 25 cycles, going from 30 min (Dueso, Thompson and Metcalfe, 2015), with H_2 generated only during the first minutes of cycles. Other studies have only carried 60 s cycles (de Leeuwe, Hu, Evans, *et al.*, 2021), varying the amount of OCM used, going from few mg up to 20 g. The scope of this chapter is the characterisation and use of these materials so far unexplored in the realm of

CL. Following this principle, only small amounts of OCM short cycle times were tested at the said temperature (820 ^{o}C).

To study the optimal time duration of the half cycles, only PBFO was tested, given the structural similarities between SBFO and PBFO. This study was done by loading 1.25 g of OCM (~ 5 mmol) in the reactor and feeding reactant counter-current gases during different times: 60 s, 48 s, and 120 s. These experiments run under isothermal conditions (820 ºC). Gas flow was expected to be 5% CO and 5% H_2O. However, due to an experimental error with the calibration conducted with the hygrometer, the H_2O flow was set at 6.5%. In order to achieve steady state of gas conversion rates, each half cycle was repeated 15 times. The rig used for these CL experiments was not thought to be used for large amounts of material as the isothermal segment of the furnace had a measured length of 3 cm. The short length only allowed for low amounts of product in the reactor bed.

Figure 3.8.a shows the conversion results for the 45 cycles conducted to decide which duration each half cycle would have. Three areas were clearly differentiated, corresponding to the different gas feed durations. Higher conversions were shown for the shortest cycles, as expected, as the oxygen profile change is smaller. Overall, steady state was reached within the first two cycles, regardless of the cycle duration, meaning that the system would provide a quick answer to the redox changes.

In the first region, with feed gas time of 60 s, the first cycle displayed a higher conversion relative to the ones under the same conditions. The material was placed in the reactor bed as sintered, with its oxygen capacity at its maximum, allowing a higher oxygen content to react and convert a larger amount of CO to CO_2. The system showed an average CO and H_2O conversion of 43% and 20%, respectively.

When the feed gas time was switched to 48 s, the system reached steady state after two cycles. As predicted, CO conversion increased to 53%. On the other hand, H_2O conversion only showed a slight increase, going from 20% to 21%. A final H_2 balance confirmed a 6.5% H_2O flow concentration in the oxidising gas stream, instead of the 5% H_2O concentration originally intended. This could explain the low oxygen intake in the H_2O reduction half cycle, which would have been higher if the correct flow (5%) had been implemented. The error came from a wrong system calibration, detected upon experiments termination. This error suggested that, if a 5% flow rate had been used, as initially intended, H_2O conversion

might have resulted in an even higher conversion rate. The system displayed a high adaptability to achieve steady state under the new conditions despite not having shown a big increase in the reduction conversion values.

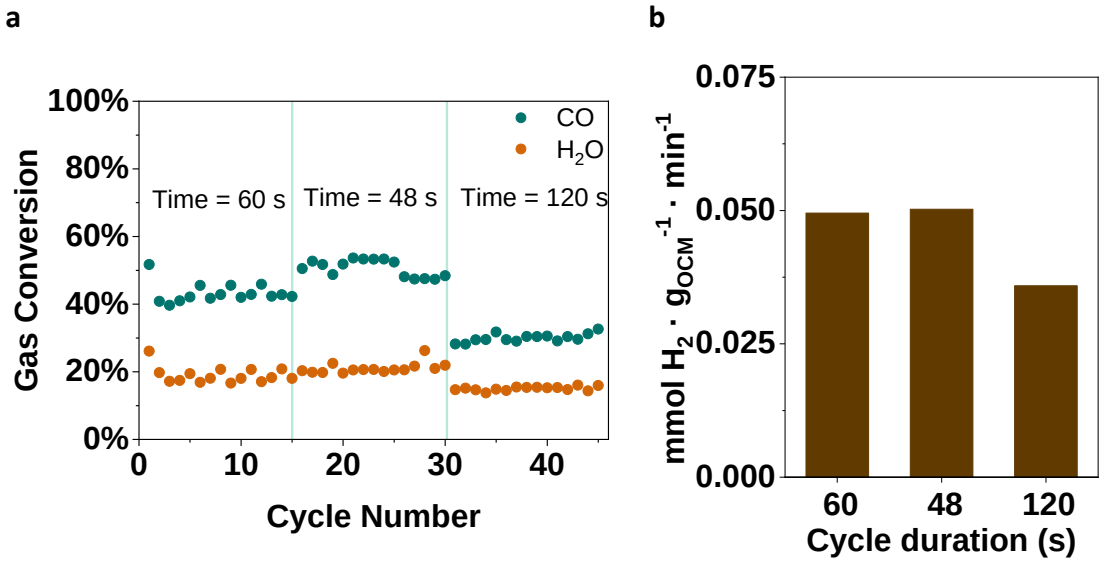

Figure 3.8.a. Conversion of CO (blue) and H_2O (orange) as a function of cycle number. 1 mmol of OCM was placed in the reactor and reactive gases were 5% CO and 6.5% H_2O, both balanced in He. 3 regions can be identified: Cycles 1-15, half cycles of 60 s each. Cycles 16-30, half cycles of 48 s. Cycles 31-45, half cycles of 120 s; all of them at 820ºC. **b**. Moles of H_2 produced per mole of OCM used in the reactor bed.

However, when switching to longer duration times, 120 s, both CO and H_2O conversions significantly decreased to 27% and 15% respectively, due to a higher depletion of the OSC, indicating a major change in the oxygen profile of the OCM (Metcalfe et al., 2019)(Metcalfe et al., 2019), lowering the reactants conversion. In all regions, lack of carbonaceous products outside the reduction cycle indicated that no carbon deposition was generated.

Figure 3.8.b shows the amount of H_2 produced per mole of OCM and unit of time. Half-cycles lasting 48 s displayed a higher conversion per unit of time, exhibiting a similar value to 60 s half-cycle duration (0.050 and 0.049 mmol $H_2 \cdot g_{OCM}^{-1} \cdot min^{-1}$, respectively). On the other hand, cycles of 120 s generated a significantly lower amount of H_2 per unit of time (0.036 mmol $H_2 \cdot g_{OCM}^{-1} \cdot min^{-1}$). CO and H_2O conversion substantially decreased for cycles lasting 120 s, indicating that the OSC of the material was exhausted when conducting longer cycles. This exhausted OSC would eventually turn out in a waste of unreacted gases, as the OCM was not capable of converting more amount.

Figure 3.9 shows each half cycle shape at different feed duration. A spike was observed for the CO flow at the end of every reduction cycle. Since no other species were observed and no other gas formation was noticed, the only possible explanation for this was a pressure drop when switching valves, indicating a difference in pressure between the gas lines. Pure CO_2 was generated at the beginning of each reduction, before undergoing quick CO breakthrough no more than 20 seconds later in the cycle. On the other hand, the quality of the H_2 in the oxidation reaction varied, depending on the feed duration. Cycles during 60 s and 120 s allowed the production of some pure H_2 followed by H_2O breakthrough, whereas the cycles during 48 s displayed an immediate H_2O breakthrough, diminishing the quality of the H_2 in the outlet. However, the low yields observed overall throughout the initial screening would suggest that the intake oxygen capacity of the *as designed* OCM was not as high as expected.

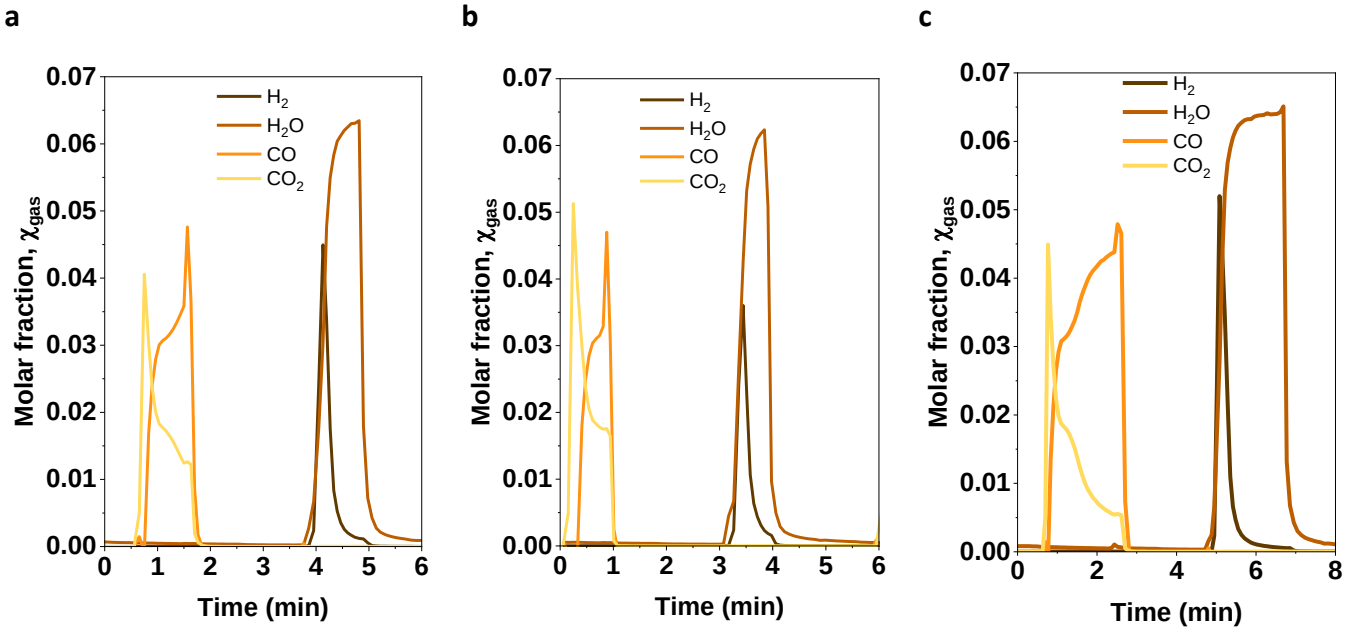

Figure 3.9. Molar fraction at the outlet of the reactor as a function of time. Three cycles representing the different time duration applied, **a**. 60 s half cycle, **b**. 48 s half cycle, **c**. 120 s half cycle.

Cycles of 60 s of feed duration seemed to produce a considerable amount of pure H_2 without inferring in a drop of gas streams conversion, compared to 48 s cycles, with a lower product quality. Expecting the system to unleash higher oxygen capacity and, therefore, higher conversion in the long term, 60 s was the decided duration for each half reaction.

3.6.3 Sustained activity in CLWGS

3.6.3.a SBFO

The durability and activity of the developed OCM was shown throughout 400 consecutive WGS cycles. Using OCM that keep constant levels of high CO_2 and H_2 production through time and that does not lead to an early deactivation is key for hypothetical scale-up and industrial approaches. If OCM deactivated faster than other classic OCM used in CLWGS, such as Fe_2O_3 or NiO (Murugan, Thursfield and Metcalfe, 2011), it might not be considered as candidate for further investigation, or indeed to be scaled-up.

5 mmol of material were introduced in a packed bed reactor with gas flow of 100 mL / min, 5% mol CO for the reduction half cycle and 6.5% mol H_2O for the oxidation half cycle, both gases balanced in He. Figure 3.10 displays the results for the CLWGS experiment for SBFO. It shows that the OCM rapidly achieved steady state after the first 3 cycles, sustaining a consistent conversion level along the time. Three unlikely conversion values appeared for CO conversion to CO_2. The points belonged to the 1^{st}, 125^{th} and 250^{th} cycle, corresponding to the beginning of relaunching the program, since the software only allowed to run 124 cycles per time/per launch. The OCM recovered its steady state of CO conversion to CO_2 at values around 70%. In the initial 249 cycles, H_2O exhibited a low conversion rate, reaching a steady value of 24%. Subsequently, an escalation in conversion was detected, reaching values up to 35% conversion. This wrong value was detected after all the experiments, as 5% was the theoretical value to be used. The increase in the H_2O conversion value leaded to think that more oxygen vacancies became available through cycles, allowing for higher reaction rates.

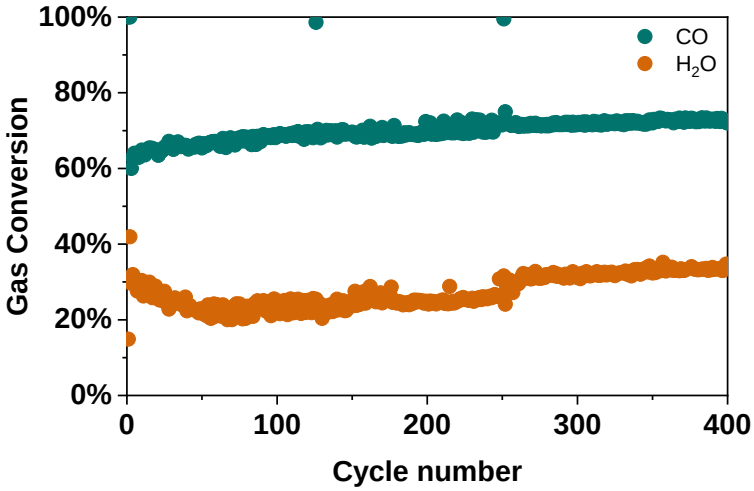

Figure 3.10. CO (blue) and H_2O (orange) conversion of SBFO in CLWGS vs time, represented as cycle number, for 400 cycles. Half cycle duration of 60 s, gas feeds were 5% mol CO and 6.5% mol H_2O, 100 mL / min.

Oxygen balance presented in Table 3.4 shows the oxygen amount exchanged during different cycles. The values were calculated assuming a 5% CO and 6.5% H_2O flow. An increasing trend in oxygen exchanged is observed during the cycles. CO conversion displayed a low but constant increase through the cycles, equal to a higher content of oxygen exchanged. H_2O also showed an increasing trend in the values of oxygen exchanged. The initial low H_2O conversion suggested a lower exchange of oxygen as compared to values from CO to CO_2 half reaction. For instance, in the 70th cycle the material released 0.134 mmol of O, whilst it only incorporated 0.060 mmol of oxygen from the H_2O stream as oxidising agent. These values became however closer as the number of cycles increased, indicating that the oxygen uptake capacity of the material increased with cycles. By the end of the 400 cycles, almost the same amount of oxygen released when oxidising CO (0.147 mmol of O) was gained in the subsequent OCM oxidation (0.134 mmol of O), when flowing H_2O.

As observed in Table 3.4, the oxygen loss is always higher than the oxygen uptake. However, it can be as well observed that across the cycles, the oxygen intake increases whilst the release remained constant. This creates an imbalance in the available oxygen in the OCM, hence making this material more prone to incorporate oxygen within its lattice through the cycles. As a matter of fact, literature does not suggest perovskites (ABO_3) and double perovskites ($A_2B_2O_6$) with an oxygen content lower than *3-δ* = 2.5 or *6-δ* = 5, respectively. One would understand that a perovskite's oxygen content below these

thresholds would decompose into its corresponding metallic oxides. For 5 mmol of SBFO used in the process, when possessing a δ_0 = 0.18, the maximum amount of labile oxygen the system can release is 1.6 mmol oxygen, assuming that the amount of oxides has to be equal or larger than 2.5 to not decompose, i.e., $ABO_{2.5}$. When analysing Table 3.4, it can be observed that the oxygen intake during the first 225 cycles was approximately half of the oxygen released, suggesting that the OCM loses a total of 0.070 mmol O per cycle, equal to 4.3% of its total usable OSC, each cycle. As indicated, after the 225th cycle, an increasing trend in oxygen intake was recorded, reducing thus the oxygen release/intake disparity observed initially. The high OSC previously exhibited by SBFO enabled the material to remain stable throughout cycles despite showing a negative oxygen balance. By reducing this unevenness in values, the OCM displays a stable OSC that allowed it to maintain its activity throughout an extended period of time. Although the OCM did not achieve a steady H_2O conversion state upon termination of the experiment explained by the increasing trend, it suggested potential for higher yields in future experiments.

Table 3.4. Oxygen balance for representative cycles selected between the 400 cycles conducted for SBFO.

Cycle number	Oxygen loss (mmol O)	Oxygen uptake (mmol O)
1	0.204	0.044
70	0.134	0.060
150	0.142	0.071
225	0.142	0.076
300	0.146	0.093
400	0.147	0.103

Figure 3.11.a–f displays the gas outlet profile at the cycles presented in Table 3.4. In the first cycle, the OCM, being in a fully oxidised state, had a larger amount of labile oxygen to react with CO in comparison to the rest of the cycles (de Leeuwe, 2019). In the rest of the half reduction cycles, the OCM was not expected to be fully oxidised, as the oxidising agent H_2O does not possess enough oxidising potential to fully reoxidised the material. Through the following cycles, the system presented a stable conversion value for both gas feeds. This suggested that the system shifted the oxygen potential to a stable state between the two working pO_2 (Ungut, 2022). CO breakthrough was observed after 30 seconds within the half-cycle. No carbonaceous products were observed beyond the OCM reduction reaction (CO to CO_2), implying that no carbon deposition occurred. For further confirmation, a carbon balance was conducted by adding the carbonaceous products,

displaying an average value of 4.95%, giving confidence to confirm that minimal or no carbon deposition took place. In the case of H_2O, an early breakthrough is noticeable. This was due to the previously indicated calibration error, in which H_2O was flowed at 6.5% instead of 5%. This higher flow exhausted faster than expected the oxygen vacancies of the material, generating an earlier H_2O breakthrough. During the first cycles, the breakthrough occurs within the first 20 seconds of reaction whilst in the graphs from Figure 3.11.e-f, a late breakthrough was observed, confirming the higher conversion and higher oxygen amount exchanged obtained by the end of the 400 cycles.

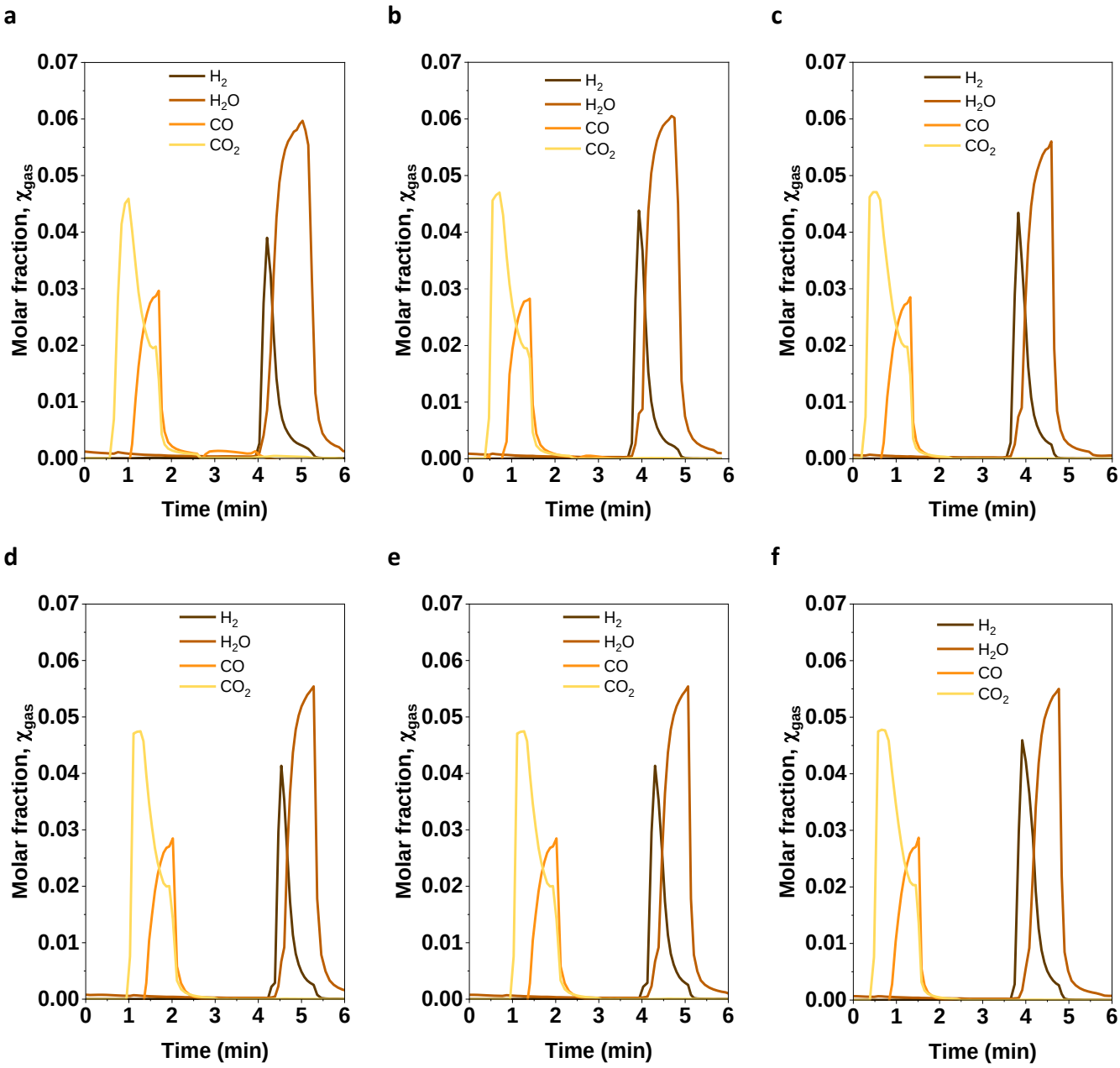

Figure 3.11. Outlet composition vs time for the long-term experiment for SBFO. **a**. 1st cycle, **b**. 70th cycle, **c**, 150th cycle, **d**. 225th cycle **e**. 300th cycle, **f**. 400th cycle. Gas flow used: 5% CO and 5% H_2O, both balanced in He.

After numerous cycles, it was expected a decay in products formation as a result of deactivation mechanisms. These mechanisms, as explained before, can occur by different factors: sintering of particles, decomposition of the main perovskite phase, complete depletion of the oxygen capacity, etc. Contrary to this, the materials showed constant activity throughout 400 investigated cycles with no signs of decay in products formation. Moreover, following the upward conversion trend in both reactants, we are confident to confirm that a larger amount of products are generated with an increased number of cycles until a full equilibrium in total exchanged oxygen is achieved.

3.6.3.b PBFO

To compare durability and activity of both materials, the experiment was conducted under identical conditions as in the case SBFO for PBFO. 5 mmol of PBFO were loaded into a packed bed reactor, occupying an approximate length of 3.5 cm. Gas flow was of 100 mL / min, 5% CO flowed for 60 s for the reduction half cycle and 6.5% mol H_2O flowed for 60 s for the oxidation half cycle. Both gases were balanced in He.

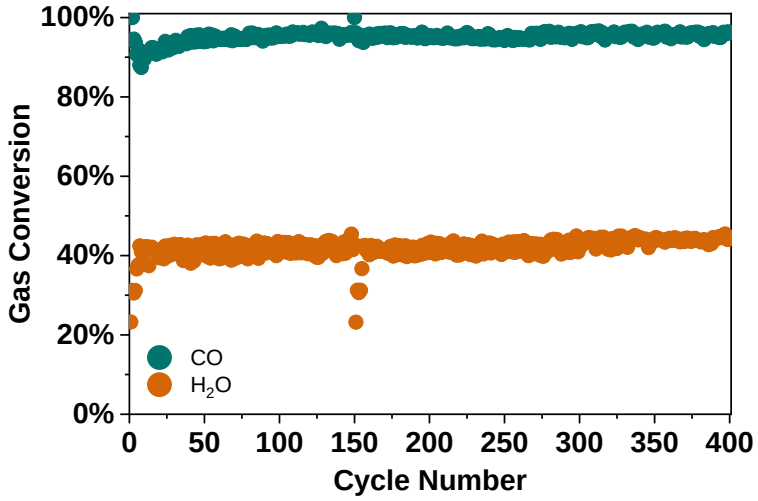

Figure 3.12. CO (blue) and H_2O (orange) conversion of PBFO in CLWGS vs time, represented as cycle number, for 400 cycles. Half cycle duration of 60 s, gas feeds were 5% mol CO and 5% mol H_2O, 100 mL / min.

Figure 3.12 illustrates the results of conversion for the OCM used these conditions. Like SBFO, 100% conversion was initially achieved. As discussed in the previous results, the material was initially fully oxidised, resulting in a larger amount of labile oxygen available. This facilitated the conversion of CO to CO_2 during the first cycles, while maintaining a lower-than-expected H_2O conversion to H_2 during those cycles. This lower H_2O is explained because the material had oxygen retained in its lattice to keep reacting with CO, therefore,

it did not uptake as much oxygen as expected from the H_2O stream. This trend was also observed in previous works from de Leeuwe, Hu, Evans, et al. (2021). The OCM achieved a steady CO conversion value of 96% after the first 40 cycles, maintaining that steady conversion value throughout the whole process. H_2O conversion achieved a steady value of 46% conversion after the first cycles and an increasing trend was observed during the last 100 cycles, reaching a steady value of 53%. Similarly to SBFO, H_2O flow was of 6.5% instead of the expected 5%, resulting in a lower conversion. Therefore, the oxygen vacancies from the OCM got replenished faster given the higher H_2O flow and smaller conversion than expected was achieved. Upon initial comparison between the two carrier materials, PBFO exhibited significant higher reduction conversion values than SBFO (96% vs 70% CO conversion and 24% vs 50%, respectively). In this case, PBFO seemed to convert more amount of reactant gases than SBFO. The production of H_2 will be further examined in following sections of this chapter.

Table 3.5. Oxygen balance for representative cycles selected between the 400 cycles conducted with PBFO.

Cycle number	Oxygen loss (mmol O)	Oxygen uptake (mmol O)
1	0.205	0.042
70	0.197	0.143
150	0.197	0.157
225	0.195	0.144
300	0.196	0.151
400	0.197	0.157

The amount of oxygen used during different redox cycles was summarised in Table 3.5. An oxygen disparity was noticed for the oxygen lost in the CO oxidation and the oxygen gained when flowing H_2O, being the latter lower than the initial. This meant that more oxygen was released than gained, creating more oxygen vacancies that were not replenished by the oxidising agent (H_2O). Despite the oxygen imbalance, which might eventually lead to decomposition, the material did not suffer from this deactivation, as the activity rate remained constant. Similarly to SBFO, this was attributed to the high OSC of the OCM, which allowed the material to gradually lose labile oxygen at the end of every cycle without losing its structure. Considering the initial amount of oxygen vacancies of PBFO, 3-δ = 2.88, for 5 mmol of OCM used in the process, the OCM could afford losing a maximum of 1.9 mmol O, following the principle stated before for perovskites (assuming a maximum oxygen deficiency of 0.5 mol of O per mole of perovskite, $ABO_{2.5}$). The OCM lost an average of 0.050 mmol O every complete cycle during the first, which accounted approximately for 2.6% of the total oxygen capacity. This continuous loss of oxygen enabled the material to undergo this process for even higher number of cycles as compared to SBFO. This indicated that a larger part of the OCM had gradually been brought to an equilibrium more suitable for the WGS pO_2 *(de Leeuwe, Hu, Evans,* et al*., 2021)*. A similar difference in oxygen consumption and uptake was also observed by Gao et al. (2022), showcasing increasing oxygen vacancy formation among all the Fe_2O_3 samples tested. Also, after 400 cycles with this constant oxygen release, the OCM would be expected to decompose, as it would have surpassed the 3-δ = 2.5 for oxygen vacancies. However, this did not occur, indicating that under the material could stay in equilibrium with this controlled CLWGS pO_2 atmosphere, without losing its structure, as proven later in the chapter by PXRD.

An increasing trend in oxygen gained by the OCM was noticeable, indicating enhanced activation of H_2O, demonstrated in Figure 3.12 and Table 3.5. This trend was linked to a larger presence of oxygen vacancies created via oxygen donation to CO. This larger amount of oxygen vacancies facilitated higher H_2O conversion rates. Consequently, despite the oxygen imbalance between half-reactions, PBFO succeeded in maintaining a sustained conversion without deactivation, underscoring its high OSC and material stability.

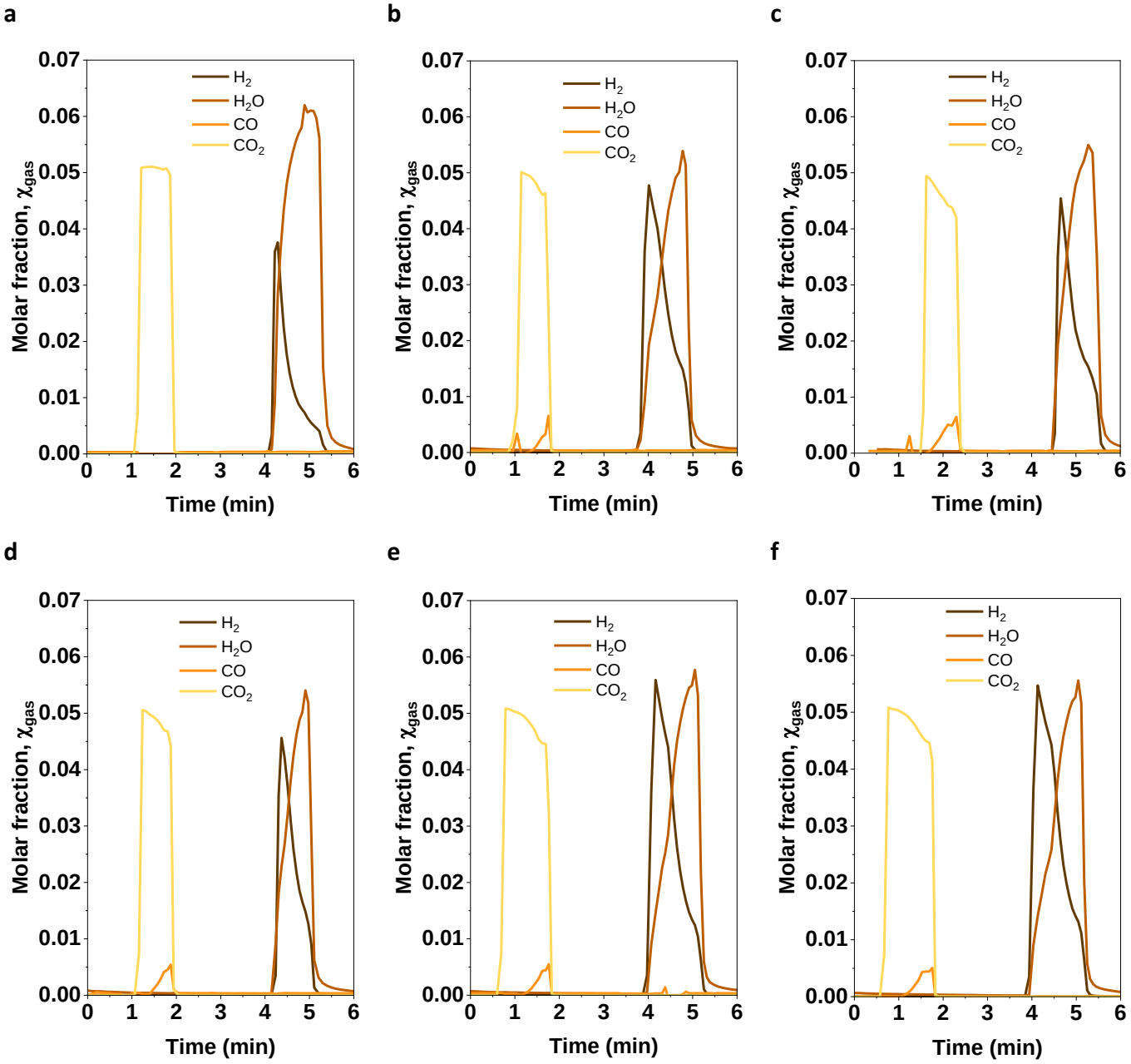

Figure 3.13. Outlet composition vs time for the long-term experiment for PBFO. **A**. 1st cycle, **b**. 70th cycle, **c**, 150th cycle, **d**. 225th cycle **e**. 300th cycle, **f**. 400th cycle. Gas flow used: 5% CO and 6.5% H_2O, both balanced in He.

Figure 3.13.a–f illustrates the gas outlet profile at the same cycles number presented in Table 3.5. During the first cycle, full CO and low H_2O conversion were achieved. This was previously justified by the available oxygen lattice in the fresh state of the material, which enabled higher CO conversion. Subsequent cycles demonstrate high CO conversion (values going from 96% to 100%). No CO breakthrough was observed when CO conversion was lower than 100%, implying an additional cost in the process, as CO and CO_2 appear as mixed gases at the final stage of the OCM reduction. Similar to SBFO, no carbon deposition took place. The only carbonaceous products observed in the gas outlets corresponded to the

OCM reduction half-cycle. Furthermore, carbon balance closed at values of approximately 4.95%, which, considering the inherent error of the equipment, confirmed the absence of carbonaceous deposits.

In this case, larger amounts of H_2O were converted to H_2. Analogue conversion profiles of H_2O to H_2 as compared to SBFO were observed. The H_2O breakthrough was observed halfway through the cycle. In PBFO case, this H_2O breakthrough occurred later than for SBFO, indicating larger amounts of pure H_2 formed.

A remarkable feature of this OCM is that not only it maintained high conversion of reactants, but it also increased the conversion of both CO and H_2O with time, and this could be extended during more cycles. This leads to confirm that the OCM did not deactivate with cycles and continue generating added-value products.

3.6.4 Normalised H_2 production in the long term and OCM stability

One of the aims of this chapter was the investigation of H_2 formation by these two OCM in CLWGS. OCM efficiency over an extended period of time is crucial for further study and scaling-up. Diagram presented in Figure 3.14 shows normalised H_2 production (H_2 produced per amount of sample loaded in the reactor). Despite both species seemed to increase the H_2 through repeated cycling, the diagram clearly demonstrates that PBFO generated more H_2 across the 400-cycle research, albeit with slight performance drops (continuous production of ~ 0.120 mmol $H_2 \cdot g_{OCM}^{-1} \cdot min^{-1}$ for PBFO against 0.075 mmol $H_2 \cdot g_{OCM}^{-1} \cdot min^{-1}$ for SBFO, during the last cycles). Moreover, as it was observed in previous images (Figure 3.8 and Figure 3.11), H_2O breakthrough occurred later for PBFO than for SBFO, resulting in a higher amount of pure H_2 in the outlet stream, equal to a higher H_2 selectivity. For better understanding of the tendencies, a detailed examination of the curves and normalised H_2 production over time is provided here and trying to identify the possible rate-limiting step.

The cumulative H_2 production profiles demonstrate a steep rise in productivity at first, which is followed by a slow stabilisation. This stabilization suggests the establishment of equilibrium conditions where the kinetic and structural limitations of the OCM become more apparent. The general form of the production curves is consistent with patterns seen for other perovskite-based OCMs (Ungut, 2022; de Leeuwe, 2019, Zhao Z. et al. 2016) when compared to comparable research in the literature, which provides additional evidence for the existence of kinetic and material limits.However, other authors such as Gao et al. (2022) have observed higher H_2 production rates (up to 0.8 mmol $H_2 \cdot g_{OCM}^{-1} \cdot min^{-1}$ using Fe_2O_3 supported on modified CeO_2, even though they conducted 40 cycles instead of 400, as done here. Using a La-based perovskite, with Mn in the B-site, Xu, Bhawe and Davis (2012) obtained values close to the ones in this study (0.2 mmol $H_2 \cdot g_{OCM}^{-1} \cdot min^{-1}$ vs 0.13 mmol $H_2 \cdot g_{OCM}^{-1} \cdot min^{-1}$, respectively).

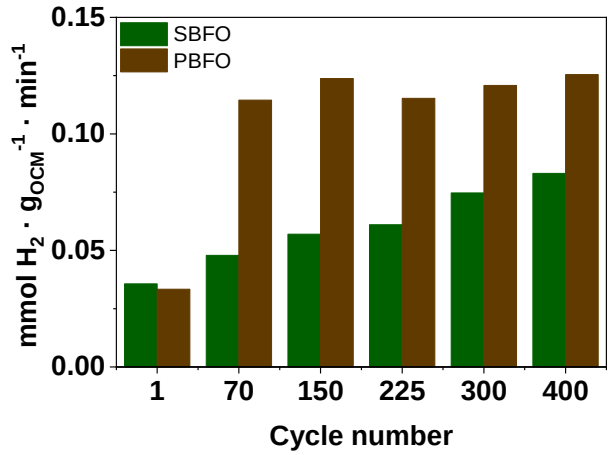

Figure 3.14. Normalised H_2 production (mmol H_2 produced per g of OCM) after 400 cycles of 1 min half-cycle duration.

To identify the rate-limiting step, a more thorough analysis of the H_2 production data is required. As highlighted by the literature (Z. Zhao et al., 2016; Xu et al., 2021), the conversion of H_2O to H_2 is limited by the H_2O dissociation step. Efficient interaction between material and gaseous H_2O molecules is necessary for this step. This step might not be carried out at the best rate throughout the cycles, according to observations of plateaus in the H_2 production curve. This finding is aligned with Z. Zhao et al., 2016, who claimed that the non-stoichiometry (δ) of the OCM directly affects the water splitting rates. This non-stoichiometry regulates the concentration of oxygen vacancies and consequently, the reaction kinetics. In the case of SBFO and PBFO, Fe in the B-site provides the perovskite with high oxygen capacity, but over extended number of cycles, slight lattice distortions

identified via PXRD might reduce the efficiency of the oxygen vacancies replenishment. This replenishment could occur by reduced oxygen diffusion rates over time or by partial blockage of the active sites, limiting the oxygen availability. Enhancing the OCM's capacity to maintain large amount of oxygen vacancies along cycles could help mitigating these limitations. Lastly, even though mass transfer limitations were minimised via the optimisation of the conditions, this effect cannot be ruled out. Although the porous properties of these OCM facilitate gas-solid interactions, diffusion resistance may be further decreased, especially with prolonged operation, by optimising the pore size distribution.

This H_2 production was compared with previous works under similar CLWGS conditions. Gao et al. (2022) conducted 40 cycles using Fe_2O_3 on various supports at different temperatures, being their maximum H_2 production rate of 0.8 mmol $H_2 \cdot g_{OCM}^{-1} \cdot min^{-1}$. Scheffe et al. (2011) conducted 7 CL cycles using atomic layer deposition as synthesis method for Fe_2O_3 and Co-doped Fe-based OCM. Average values of 2.02 and 2.34 mmol $H_2 \cdot g^{-1} \cdot min^{-1}$ were obtained. Zaidi et al. (2024) reported 0.236 mmol $H_2 \cdot g_{OCM}^{-1} \cdot min^{-1}$. The values of H_2 production obtained by using the designed materials are yet to be improved, as they did not match the ones from the literature. Beyond possessing sustained activity, the conversion rates remain lower than expected. In the described preliminary experiments, the OCM have shown to possess higher oxygen properties than the ones displayed in real CLWGS conditions.

PXRD diffractograms were collected after testing the samples in CLWGS conditions, after 400 cycles. The patterns depicted in Figure 3.15.a-b indicate that the main perovskite structure was preserved for both OCMs. Peaks of the pattern collected after testing show peak shifting towards the left (see zoomed area in Figure 3.15.c,d), indicating a reduction of the system. One would think that as the last half cycle was a reoxidation, the final OCM state should be as fully reoxidised. Even though the material was reoxidised, it was not reoxidised under air but under H_2O, meaning pO_2 ~10^{-13} bar instead of pO_2 ~ 0.2 bar as it would be under air.

PBFO exhibited a significantly lower formation of secondary structures compared to SBFO. While a single small peak emerged for PBFO (see peak at ~45º in Figure 3.15.b), several low-intensity peaks indicative of slight decomposition were detected for SBFO (e.g., the

peak at ~69º in Fig. 3.15.a). Despite multiple refinements considering possible phases such as $BaCO_3$, Sm_2O_3, BaO, and various iron oxides, none of these yielded additional accuracy. The low intensity of these peaks likely hindered their precise identification.

As this chapter presents the first implementation of these materials in CLWGS, no literature is available for direct comparison of these peaks. For clarity, the region between 20º and 40º has been magnified (Figure 3.15.c) to highlight secondary phase formation. It can be observed that SBFO exhibited a minor secondary peak at ~27º, whereas PBFO appeared largely unmodified. These results underscore the higher stability of PBFO under prolonged chemical looping conditions, further supporting its potential as a robust oxygen carrier material.

These materials have demonstrated long-term stability and robustness as potential OCM for CLWGS. However, the rate-limiting step – likely linked to kinetics of H_2O splitting or oxygen vacancies replenishment over time – will need further enhancement for higher efficiencies. These hypotheses have been contrasted with existing literature, offering context and understanding for these findings.

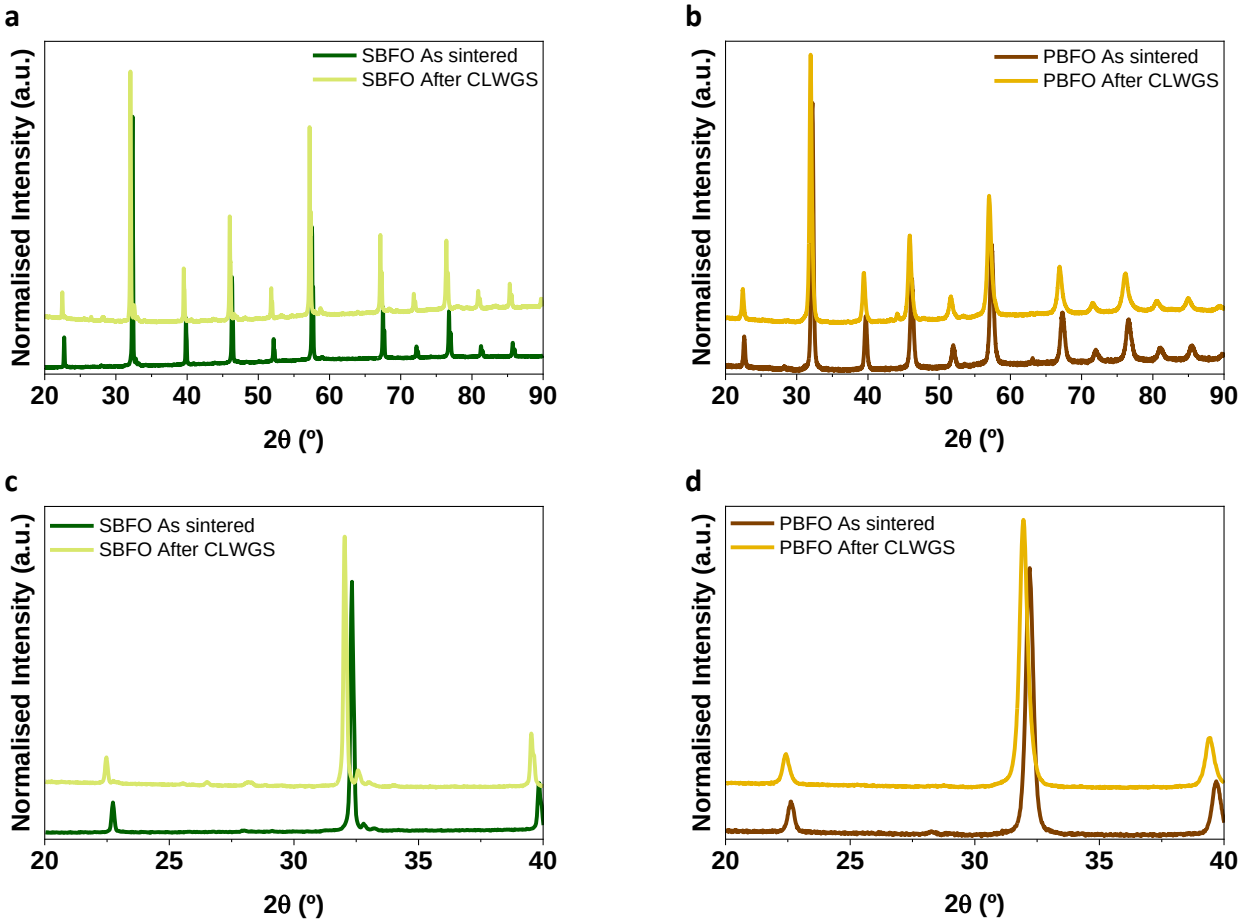

Figure 3.15. XRD patterns comparing the OCM as sintered and after undergoing 400 CLWGS cycles, **a**. SBFO, **b**. PBFO. In **a** and **b**, two patterns are presented. Patterns below (dark green for SBFO and brown for PBFO) correspond to the initial materials, *as sintered*. Patterns above (light green for SBFO and yellow for PBFO) correspond to the materials after undergoing CLWGS. Zoomed patterns to observe secondary phases and peaks observation between 20-40º **c**. SBFO, **d**. PBFO. Minor formation of secondary phases has been appreciated in both patterns, but the quality of the spectra does not allow to identify them.

3.7. Advantages and limitations of PBFO and SBFO over other OCM

The use of PBFO and SBFO in CLWGS introduces key advantages over conventional OCMs. Their enhanced oxygen storage capacity (OSC) allows for efficient redox cycling and stability over cycles. Additionally, Pr and Sm incorporation into the A-site has been shown to promote oxygen vacancies, which facilitates higher reactivity and prolonged stability over multiple redox cycles (Figure 3.10 and Figure 3.12).

Compared to traditional materials and perovskites, PBFO and SBFO exhibit:

- Higher OSC than similar compositions: $La_{0.6}Sr_{0.4}FeO_3$ (LSF641) oxygen capacity was measured by (Ungut, 2022) and both PBFO and SBFO showcased larger OSC than LSF641, also used in CLWGS for H_2 production (de Leeuwe, C., Hu, W., Evans, J., et al., 2021). Unlike

other materials such as the La-based perovskite investigated by Kuhn, Fukuda, et al., (2013), PBFO and SBFO presented here did not decompose at low pO2, showcasing their high stability under strong reducing conditions and ability to recover their original structure.

- Similar long-term stability to some state-of-the-art materials, such as LSF641 (de Leeuwe, 2019 Ungut, 2022): PBFO and SBFO sustained their original reactivity over 400 cycles, similarly to LSF641. On the other hand, other La-based systems have been used and reported higher normalised conversions, even though their long-term stability was not assessed. Additionally, PBFO and SBFO have been compared to other non-perovskite-based systems (i.e., modified CeO_2), resulting in an overall lower conversion.

However, limitations must also be considered. Minor phase decomposition was observed in SBFO after prolonged cycling, which could impact an even longer-term stability. Additionally, at lower operating temperatures (T < 820°C), these perovskites exhibit slightly reduced OSC compared to benchmark La-based perovskites (Kuhn, Fukuda, et al., 2013), which may limit their application in low-temperature CL processes. Further compositional tuning, such as additional dopant incorporation, may help address these challenges in the future.

3.8. Heat Balance and Thermodynamics of PBFO and SBFO in CLWGS

The thermodynamic properties of these reactions significantly influence the overall energy efficiency of the system. This section provides an analysis of the heat balance among the different steps of the redox cycle, including the impact of extrinsic oxygen vacancies on reaction enthalpies and process sustainability.

3.8.1. *Step 1 – CO oxidation half cycle*

CO transformation into CO_2 releases heat (ΔH_{ox} = -283 kJ / mol), contributing to the overall energy balance. CO concentration was of 5% in 100 mL / min during 1 min flow. For the calculations of the heat released in the half cycle, the conversion value is also taken into account. It has been decided to use the final conversion value at the 400th cycle for PBFO.

$$Q_{ox} = n_{CO} \cdot \Delta H_{ox} \cdot X_{CO} \quad \text{(Eq. 3.13)}$$

$$Q_{ox} = 0.2\ mmol \cdot -283 \frac{kJ}{mol} \cdot 0.96 = -0.056\ kJ \quad \text{(Eq. 3.14)}$$

3.8.2. *Step 2 – H_2O reduction half cycle*

H_2O transformation into H_2 absorbs heat (ΔH_{red} = 242 kJ / mol). In this case, due to the mistake in the gas flow, H_2O concentration was of 6.5% in 100 mL / min, during 1 min flow. For the calculations of the heat absorbed in the half cycle, the conversion value is also taken into account. It has been decided to use the final conversion value at the 400th cycle when using PBFO.

$$Q_{red} = n_{H_2} \cdot \Delta H_{red} \cdot X_{H_2O} \quad \text{(Eq. 3.15)}$$

$$Q_{red} = 0.27\ mmol \cdot 242 \frac{kJ}{mol} \cdot 0.53 = 0.034\ kJ \quad \text{(Eq. 3.16)}$$

3.8.3. *Step 3 – Oxygen vacancies formation and oxygen release*

Oxygen vacancies formation and oxygen release steps are continuously taking place. To calculate it, the oxygen vacancy formation value of a standard $LaFeO_3$ perovskite has been considered (Deml *et al.*, 2014), $\Delta H_{vacancy}$ = -2.6 eV / atom = -251 kJ / mol. To calculate the enthalpy, a balance has been done between the oxygen released and the oxygen taken (δ per cycle) in the 400th cycle.

$$Q_{vac} = \Delta n_{Oxygen} \cdot \Delta H_{vac} \quad \text{(Eq. 3.17)}$$

$$Q_{vac} = (-0.197 + 0.157)\ mmolO \cdot -251 \frac{kJ}{mol} = -0.01\ kJ \quad \text{(Eq. 3.18)}$$

This $\Delta H_{vacancy}$ value is an approximate value found on the literature in a similar matrix. For more accurate values, DFT analysis are encouraged.

3.8.4. *Step 4 – Overall energy balance*

Last approximation corresponds to the overall reaction heat calculation:

$$Q_{total} = Q_{ox} + Q_{red} + Q_{vacancies} \quad \text{(Eq. 3.19)}$$

$$Q_{total} = -0.056 + 0.034 - 0.01 = -0.122\ kJ \quad \text{(Eq. 3.20)}$$

-0.122 kJ is the result of the heat balance per complete redox cycle. This negative value indicates that the process is exothermic, meaning that the reactor can operate without additional heating. Additionally, the presence of oxygen vacancies contributes to the

energy demand of the oxidation step but remains within a tolerable range, ensuring material stability over multiple redox cycles.

The heat balance analysis confirms that the CLWGS cycle is energy-efficient and self-sustaining under typical operating conditions for the said materials. The formation of extrinsic oxygen vacancies contributes to the overall process efficiency. Future work could explore additional compositional tuning to further optimize heat management and enhance material performance.

3.9. Summary of Chapter 3

This chapter presents the design, synthesis, characterisation and testing of two oxygen carrier materials (OCM), namely $Sm_{0.5}Ba_{0.5}FeO_{3-\delta}$ and $Pr_{0.5}Ba_{0.5}FeO_{3-\delta}$ (SBFO and PBFO). These OCM gathered the required conditions to be implemented in CLWG such as initial oxygen vacancies, expected to contribute to the activation of the water-gas shift (WGS) reaction in CL. Moreover, they displayed reversible oxygen intake and release within the adequate pO_2 and showed structural stability at more reducing and oxidising conditions than the real CLWGS redox potential. PBFO showed a larger oxygen storage capacity (OSC) within the mentioned pO_2 range, even though SBFO possessed a larger initial amount of oxygen vacancies. Preliminary results were obtained for the study of the cell variation of the materials and the oxidation state of Fe along the reaction. *In situ* PXRD would provide the necessary data for a better understanding of these parameters, to observe the evolution of the OCM under CLWGS conditions.

Both materials were tested under the same reaction conditions for conversion and products selectivity evaluation, and notably, while none of them displayed signs of carbon depositions or phase decomposition, PBFO outperformed SBFO with better conversion results and slight better stability in the long term after running 400 CL cycles. This enabled the production of CO_2 with minimal CO in the outlet and an increased H_2 production. However, this achieved H_2 formation values still below the activity reported by previous authors.

TGA conducted under different buffer gases could promote carbonates formation due to CO_2 present in the atmosphere. However, upon concluding the (CL) cycles, no evidence of carbonation or other carbon-related processes was detected: the carbon balance

consistently closed within 5%—well within the experimental error—indicating that carbon deposition or related deactivation processes did not occur. This conclusion is further supported by the materials' stability and sustained activity throughout the cycles. Additionally, synchrotron XRD confirmed that the materials did not undergo decomposition or carbonation, highlighting their resilience under the operating conditions.

These findings serve as a proof-of-concept of the potential of the conceived materials. Further materials' modification to promote higher oxygen properties, characterisation, testing and half-cycle adjustments are necessary to fully understand these materials outcomes and optimise their H_2 production rates.

Chapter 4 Development and investigation of the as-designed carrier materials for CH_4 activation

The main focus of this chapter relies on the modification of one of the previous perovskites. The modification was done by promoting exsolution of nanoparticles for CH_4 activation towards syngas. Thanks to the high OSC and stability demonstrated by PBFO in Chapter 3, the reactivity of this designed OCM was studied and used as benchmark for the subsequent modifications that the OCM undergoes to target this reaction. Techniques used to monitor these results were PXRD, SEM, and gas analysis coupled to *operando* PXRD. The latter was conducted at ESRF (France).

4.1. Introduction

In the previous chapter it was studied how the Pr-based carrier material PBFO showcased better results relative to conversion, selectivity, and stability in the long term. Therefore, it was the material selected for further studies in CL processes involving CH_4 activation. The materials presented have been proven to work for the CLWGS. CLWGS is conceived, as stated previously, as the prior step for CLSRM. This is due to the lack of CO (used in CLWGS) as feedstock, instead it is generated, among others, in CLSRM. However, this material can undergo structural modifications to be then applied in more CL processes, not only CLWGS. In this way, these OCM can gain a major interest for CL processes involving H_2 production. Thanks to its ability to cleave the C–H bond (Li, Xu, Li, *et al.*, 2020), Ni has been widely used as an active metal to activate CH_4 in catalytic processes (Osman, 2020; Elbadawi *et al.*, 2021) and in CL processes (de Diego *et al.*, 2008; Protasova and Snijkers, 2016; Li, Xu, Li, *et al.*, 2020; Das *et al.*, 2022). It is however prone to quick deactivation by coke deposition and sintering due to the high temperatures involved. As it has been explained in the introduction chapter, besides possessing higher activity than other traditional synthetic methods, exsolved nanoparticles on the surface of materials are more durable and avoid these deactivation process that happens to traditional Ni-based catalysts. These exsolved nanoparticles are dispersed onto the surface of the host structure (perovskites, in this case) when applying reduction conditions (although other processes can induce the exsolution of nanoparticles, such as plasma (Kyriakou *et al.*, 2021). Exsolved systems have gained popularity in chemical looping (Hosseini *et al.*, 2019; Kousi, Neagu, Bekris, Papaioannou, *et al.*, 2020), catalytic processes (le Saché *et al.*, 2018; Padi *et al.*, 2020; Lindenthal *et al.*, 2021), electrochemical processes (Y. Zhu *et al.*, 2018; Opitz *et al.*, 2020), etc.

4.2.Developing OCM with enhanced CH_4 reactivity towards syngas – Partial Oxidation of CH_4

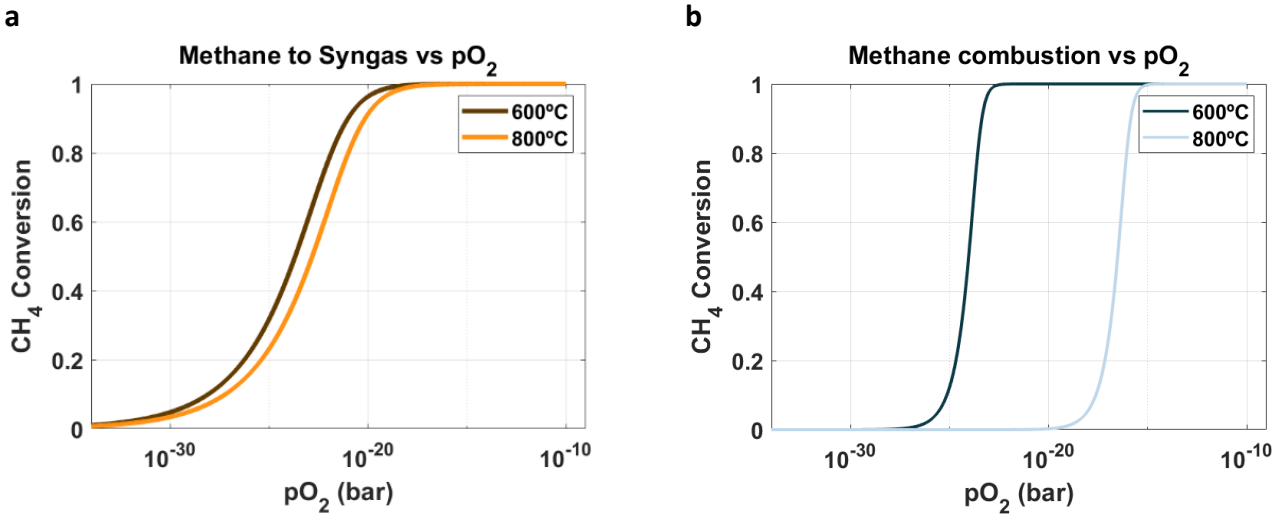

Figure 4.1. CH_4 conversion vs pO_2 for **a**. syngas production and **b**. CH_4 combustion at two different temperatures commonly used in CL processes. The area between those two temperatures corresponds to all the temperature range comprised between the two displayed in which the process is thermodynamically favourable.

The partial oxygen pressure (pO_2) to generate syngas is the first parameter to be examined when studying its production in CL. As displayed in Figure 4.1.a, CH_4 activation towards syngas is a temperature-dependant process. It generally takes place under low oxidising conditions and high temperatures. These conditions help overcoming kinetic and thermodynamic limitations, favouring the production of H_2 and CO, ideally with a H_2:CO ratio of 2:1, a useful ratio for intensive industrial processes (Elbadawi *et al.*, 2021). Emphasis needs to be put in controlling reducing environments with low pO_2. In contrast, CH_4 combustion also exhibits temperature dependence. It is more thermodynamically favourable than partial oxidation of methane (POM): ΔH^0 is -806 kJ / mol for combustion (Eq 4.1) vs -36 kJ / mol, for POM (Eq 4.2), according to Chen et al. (2010). Working at high temperatures and lower pO_2 levels is a way to ensure the desired syngas selectivity over combustion products. The narrow pO_2 window simplifies working conditions. By carefully tailoring the already designed OCM, which have shown to work under similar pO_2 conditions, reactivity and selectivity of the material could be enhanced.

$$CH_4 + 2O_2 \rightarrow CO_2 + 2H_2O, \qquad \Delta H^0_{298\,K} = -803\ kJ/mol \qquad \text{Eq 4.1}$$

$$CH_4 + 0.5O_2 \rightarrow CO + 2H_2, \qquad \Delta H^0_{298\,K} = -36\ kJ\ /\ mol \qquad \text{Eq 4.2}$$

For the creation of OCM with exsolved nanoparticles on the surface and active for methane activation, the core structure was kept as originally intended given the high selectivity of Fe-based OCM towards POM (Li, Xu, Li, *et al.*, 2020) and the stability at high temperatures. The B-site was initially doped with 2 wt.% Ni to create $Pr_{0.5}Ba_{0.5}Fe_{0.9}Ni_{0.1}O_3$, referred to as PBFNO. Zaidi et al. (2024) proved that the addition of Ni to Fe-based perovskites system increases the oxygen-carrying capacity of the material. It was subsequently tested for methane activation at the conditions indicated in the Experimental Section. To promote surface exsolution of Ni, 0.1 A-site deficiency was introduced (Neagu *et al.*, 2013), creating $(Pr_{0.5}Ba_{0.5})_{0.9}Fe_{0.9}Ni_{0.1}O_3$. Reductions were done under 5% H_2 / Ar balance in varying temperature and duration conditions. In previous works involving exsolution (Kousi, Neagu, Bekris, Calì, et al., 2020), surface and bulk exsolution was intended. To achieve that, the doping extent of exsolvable metals was larger, up to 10 wt.% in Ni.

The presented results here correspond to a thorough study of the reactivity of the designed OCM towards CH_4, their structural characterisation via PXRD and morphology via SEM.

4.3. Preliminary tests

Given their oxygen capacity stability at high temperatures, one of the designed and presented materials in the previous chapter (PBFO) was tested for CH_4 activation towards syngas (CO and H_2), as part of the process known as partial oxidation of methane (POM). For that, a temperature programmed reaction under CH_4 was conducted, at 10 ºC / min until achieving 800ºC. The temperature was kept for 30 min. Ideally, the ratio of products H_2:CO in CH_4 activation should be of 2:1.

CH_4 activation did not commence until the target temperature was reached (790 ^oC), and the conversion was not higher than 20% during the whole reaction time. The products maintained a constant ratio of ~2:1 during the first two thirds of the isothermal part. In the last third of the isothermal part, a spike in the H_2 stream was observed, probably due to CH_4 cracking. This phenomenon is understood as CH_4 cracking (Amin, Croiset and Epling, 2011), that led to material decomposition. This decomposition was seen in the PXRD pattern of the material post CH_4-TPR, depicted in Figure 4.2.a. The main perovskite phase, observed in the initial material, either undergoes complete disappearance after the

reaction or experiences a reduction in its presence to an extent that the identification or refinement of phases becomes unfeasible (Figure 4.2.c).

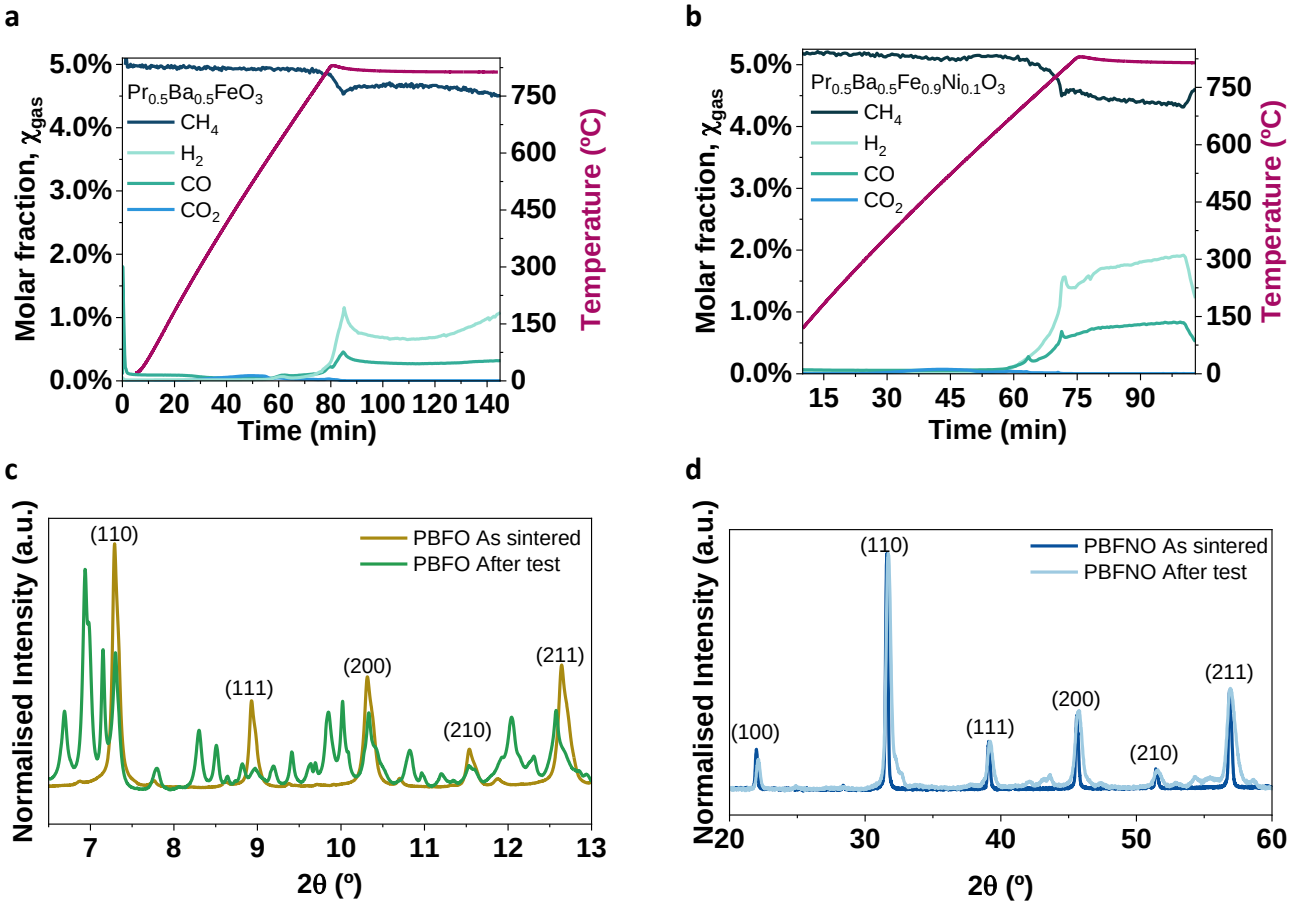

Figure 4.2.**a**. Temperature Programmed Reaction profile of CH4 activation for PBFO. Ramp rate 10 ºC / min until reaching ~820 ºC, keeping isothermal conditions for 30 min. **b**. Temperature Programmed Reaction profile of CH_4 activation for PBFNO. Ramp rate 10 ºC / min until reaching ~820 ºC, keeping isothermal conditions for 30 min. **c**. X-Ray diffractograms of PBFO as sintered (yellow) and after undergoing CH_4-TPR (green). Intensity is expressed in normalised square root. **d**. PXRD diffractograms of PBFNO as sintered (dark blue) and after undergoing CH_4-TPR (light blue). Patterns for the Ni-doped OCM were not recorded at ESRF, hence they appear at Cu wavelength.

Same experiment was carried out for the same material but Ni-doped in the B-site (Ni wt.% = 2%), now $Pr_{0.5}Ba_{0.5}Fe_{0.9}Ni_{0.1}O_{3-\delta}$, which preserved a cubic symmetry after the incorporation of Ni within the original matrix. The highly pure OCM displayed similar reactivity to PBFO, by producing an insignificant amount of CO_2 when temperature reached 400 ºC. However, conversion towards syngas commenced before than in the previously tested OCM. Activation was detected at 700 ºC with full selectivity towards the desired products. In the graph shown in Figure 4.2.b. it was observed a constant formation of syngas keeping a constant products ratio of 2:1 throughout the isothermal part of the reaction. $Pr_{0.5}Ba_{0.5}Fe_{0.9}Ni_{0.1}O_{3-\delta}$ achieved a similar conversion compared to its

corresponding non Ni-doped OCM (20% conversion), however it does not show any sign of methane cracking during the process, maintaining a constant 2:1 ratio of desired products during the whole isothermal part of the reaction. This absence of cracking is attributed to a higher stability of the FeNi active site of the OCM towards methane, which is in accordance with the conclusions from Theofanidis et al. (2019), who observed low carbon deposition when forming these FeNi alloys. The high stability of the new material could be observed by the pattern displayed after testing in Figure 4.2.d, where the main perovskite structure maintained its original phase.

4.4. Finding the adequate exsolution conditions

In this context, given the high stability and selectivity towards syngas, $Pr_{0.5}Ba_{0.5}Fe_{0.9}Ni_{0.1}O_3$ was chosen to further investigate its reactivity for this selected reaction. To promote exsolution and aiming to increase reaction rates (as explained in the introductory chapter), A-site deficiency was introduced while keeping the same ratio of A-site metals (1:1) and the same ratio of B-site metals (9:1), having now $(Pr_{0.5}Ba_{0.5})_{0.9}Fe_{0.9}Ni_{0.1}O_3$.

Results of applying different exsolution conditions have been collected in Figure 4.3. Initial PXRD (Figure 4.3.a) shows the *as synthesised* 0.1 A-site deficient PBFNO. A high purity material can be appreciated in the picture, where two main perovskites phases coexist. By applying a $Pm\bar{3}m$ cubic model to the refinement, the accuracy of this is of R_{wp} = 17.9, On the other hand, by applying a combination of $Pm\bar{3}m$ cubic (ICSD #23076) and $Pmmm$ orthorhombic (ICSD #135026) systems, the R_{wp} value decreases the value until reaching 13.5, implying higher accuracy of the suggested model. The presence of an orthorhombic perovskite contributes to explain the peak splitting occurring in the higher angles and the presence of shoulders at the right base of the peaks, corresponding to the (100), (110), (111), (200) and (210) peaks, in the Miller indices. Synchrotron PXRD pattern yield highly precise results. As a result, any drop in computed value during refinement is more significant than in standard diffractograms. There are however some peaks that remain unidentified (see peak at 6.4º), as no structure was found to match the peak. These peaks are 30 times smaller than the main perovskite peak (highlighted as 110 in hkl index). As they do not belong to the main phases studied in this chapter (Fe, FeNi alloys, NiO, spinels, etc), no major significance was attributed to them, and their identification was not continued. These peaks were not expected to possess a compelling contribution to the overall system, nor to affect the conversion of the reactants.

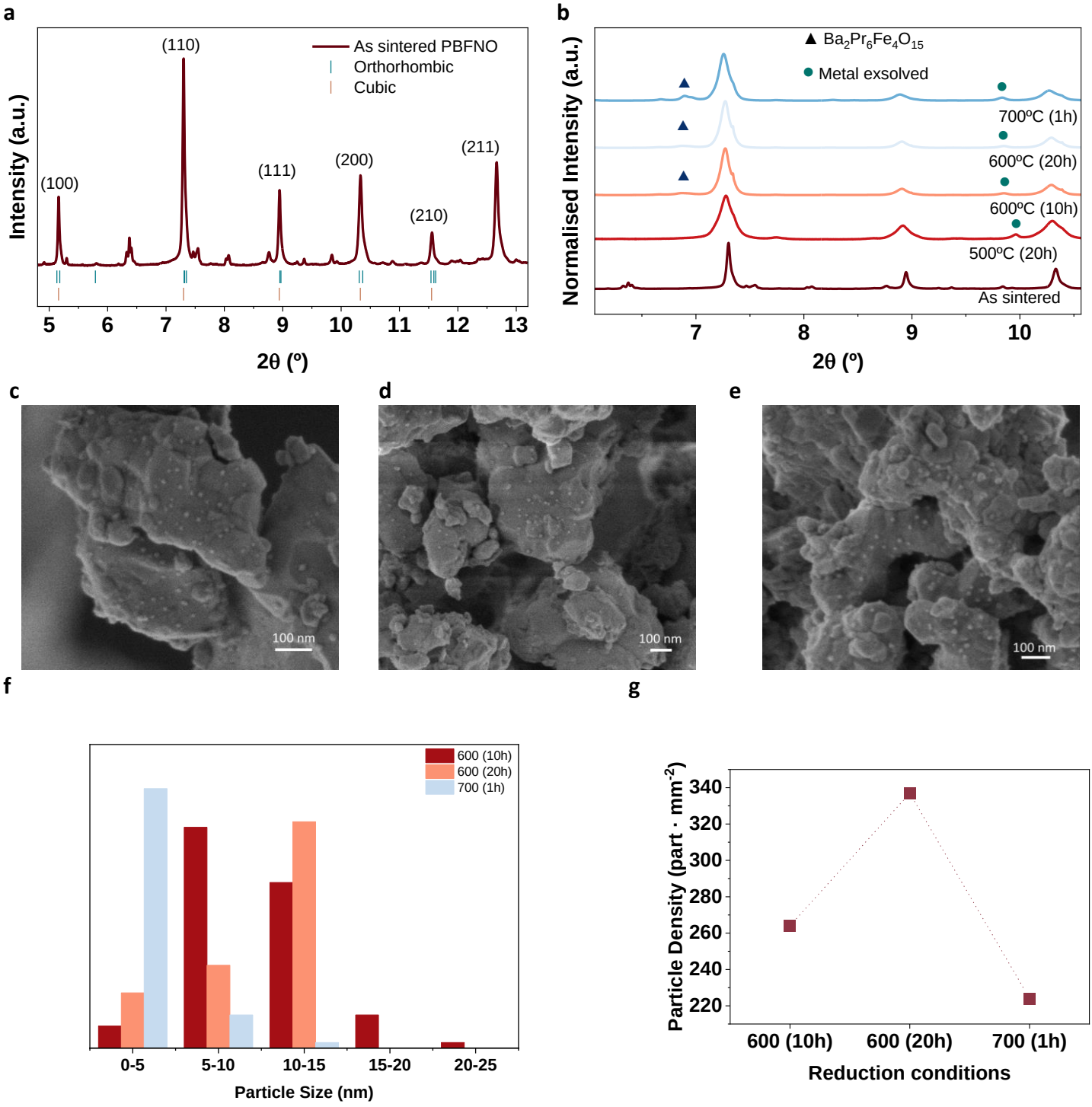

Figure 4.3. X-Ray pattern of **a**. as sintered 0.1 A-site deficient PBFNO. hkl indices for the main cubic phase are shown in brackets. **b**. Stack PXRD patterns of the A-site deficient PBFNO reduced at different temperature and time conditions. Secondary phases (▲) and metallic nanoparticles (●) have been identified. SEM images of surface PBFNO systems after exsolution at 600ºC for different times, **c**-**d**, 10 h. **e**, 20 h. **f**. Particle size distribution for the exsolved PBFNO at different conditions (600 ºC for 10 h, 600 ºC for 20 h and 700 ºC for 1h), **g**. Population density of exsolved nanoparticles at different time durations (600 ºC for 10 h, 600 ºC for 20 h and 700 ºC for 1h).

This new material, 0.1 A-site deficient PBFNO, underwent the following reducing conditions in order to promote exsolution: 5% H_2 balanced in Ar at different temperature

and time conditions to study the ones with better results for exsolution of Ni nanoparticles. The initial material had minor impurities that could only be observed at the synchrotron intensity (Figure 4.3.a). PXRD patterns of the OCM undergoing different reduction conditions can be observed in Figure 4.3.b. As expected, exsolved metallic nanoparticles were detected in the PXRD at 500 ºC after long time of reducing conditions (20 h). However, some impurities were still present after the reduction. Therefore, these materials were discarded for future investigation. Higher temperatures (600 ºC and 700 ºC) were also tested with the purpose of eliminating the initial secondary phases without losing the amount of exsolved metal. Exsolved metal nanoparticles were again observed, and the initial secondary phases had successfully disappeared from the pattern. This time, a new secondary phase was now detected at 7.3º in all the three materials reduced under different conditions: 600 ºC for 10 h, 600 ºC for 20 h and 700 ºC for 1 h. This new undesired phase was less pronounced when the reduction took place at 600 ºC for 10 h. This secondary structure possessed a structure of rhombohedral $Ba_2Pr_6Fe_4O_{15}$ (ICSD #24658, identified with the software *HighScore Plus*). According to Santaya et al. (2022), in exsolution, secondary phases are a consequence of the A-site segregation caused by an A-site enrichment after exsolving more B-site amount than the original deficiency (in this case, 0.1 mol deficiency).

SEM images of the materials undergoing reduction at 600 ºC for 10h and 20 h (Figure 4.3.c–e) showed a heterogeneous particle distribution, with areas presenting a higher population of nanoparticles than others. These images were further analysed with ImageJ for particle size and distribution study (Figure 4.3.f–g). Nanoparticles formed while reducing at 600 ºC for 10 h depicted a normal size distribution, covering a wider range of particles distribution ($0 < \text{diameter} < 25$ nm), being the range 5-15 the one with a larger number of particles. The material reduced at 600 ºC for 20 h experienced an increase in the average size of the exsolve nanoparticles (average diameter > 10 nm). This is explained by an increased growth of the particles with increased times of reduction (Neagu *et al.*, 2019). Most of the nanoparticles' size formed while reducing at 700 ºC for 1 h were below 5 nm diameter, and displayed a lower population density, indicating a lower extent of exsolution. This decreased size is also explained by the same principle as stated by Neagu et al (2019). Reduction at 600 ºC for 20 h promoted the exsolution of more nanoparticles than the

reduction at 600 ºC for 10 h and 700 ºC for 1 h (335 particles · mm^{-2}, 265 particles · mm^{-2} and 225 particles · mm^{-2}, respectively).

Given the lower extent of exsolution and the higher formation of secondary phases, the material reduced at 700 ºC for 1 h was not further studied. Before final decision of keeping investigating one of either material reduced for 10 or 20 h, a last experiment was required for final confirmation: CH_4 activation. From now on, these materials will be named PBFNO-600(10) and PBFNO-600(20), respectively. In this experiment, materials need to undergo mild oxidation to be able to oxidise the reactant gas. Therefore, before flowing CH_4, OCM were reoxidised under diluted O_2 (5% O_2) at 600 ºC for 30 min. Figure 4.4 shows the respective PXRD of these new reoxidised samples, depicting different features: whilst PBFNO-600(10) recovered its initial crystallographic structure (Figure 4.4.a), PBFNO-600(20) did not do so, showing clear signs of decomposition into multiple phases, unidentifiable by phase identification Figure 4.4.b. Consequently, this suggests that, although the latter did not demonstrate a substantial decomposition in the initial reduction, it underwent higher degradation, as evidenced in SEM from Figure 4.3.e and further confirmed after the reoxidation (Figure 4.4.b).

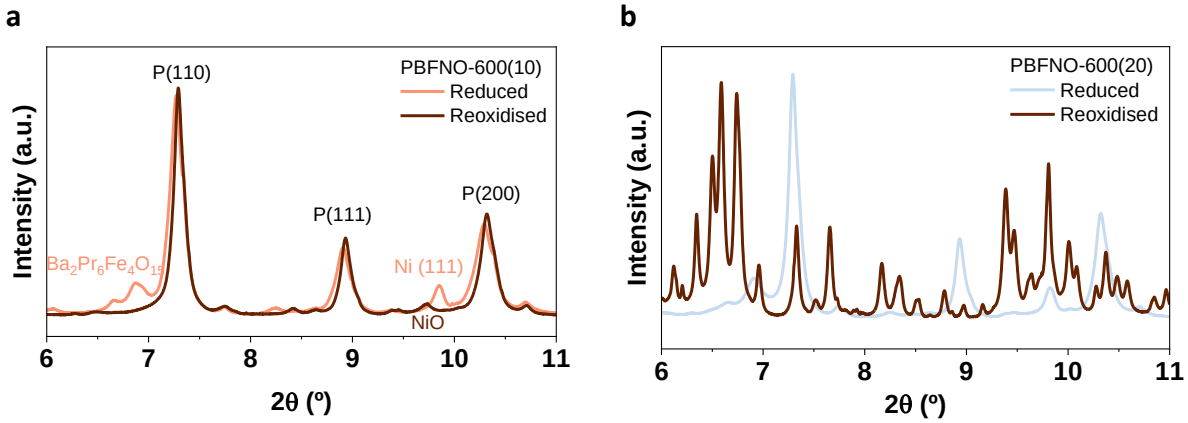

Figure 4.4. PXRD pattern of reduced and reoxidised materials **a**. PBFNO-600(10).Miller indices have been indicated for both structures whilst characteristic peaks relative to each structure have been assigned with the adequate colour for each pattern. **b**. PXRD pattern of PBFNO-600(20) reduced and reoxidised. Miller indices for the reduced samples correspond to the same ones as in the left image. No peak assignation could be done for the reoxidised pattern. Reoxidised materials share the colour code, as they were expected to be identical.

When conducting the CH_4-TPR, 80 mg of material (~ 0.3 mmol) were used. 5% CH_4 was flowed at 80 mL / min. Temperature ramp was of 10 ºC / min up to 800 ºC, and this value was held for 30 min. Results of these tests are illustrated in Figure 5.a-b. No reaction was

observed at low temperatures for any of the materials. As observed in Figure 4.5.a., PBFNO-600(10) activated the reaction with CH_4 at 720 ºC, increasing conversion as the temperature increased. The reaction products maintained a constant ratio of 2:1 (H_2:CO) during some minutes after the isothermal part of the reaction was reached (up to 80 min in the graph), increasing up to 32% conversion of CH_4. From that moment, it can be observed that H_2 begins an uncontrolled increase, and so did the desired ratio of products, indicating CH_4 cracking.

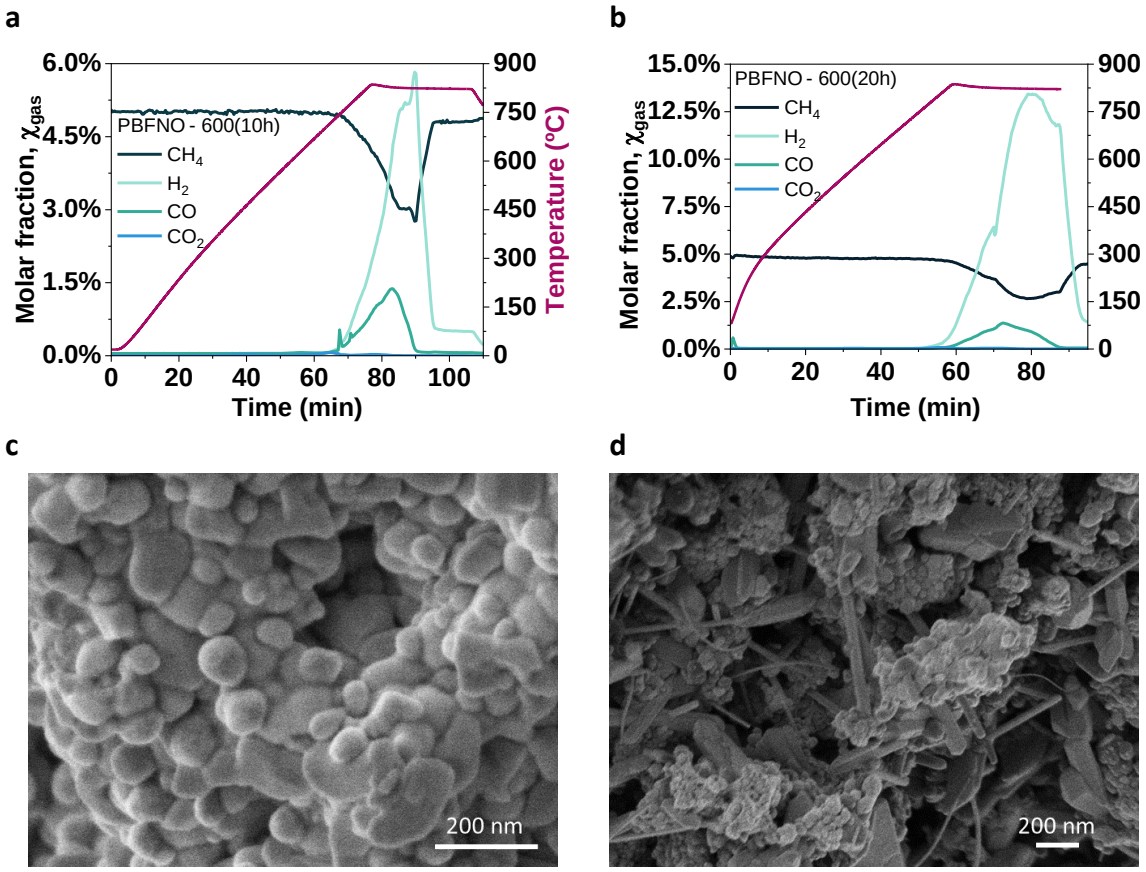

Figure 4.5. Temperature Programme Profiles of CH_4 activation **a.** PBFNO-600(10). **b.** PBFNO-600(20). Same reaction conditions apply for both materials. Ramp rates 10 ºC / min for both reactions until reaching ~820 ºC, keeping isothermal conditions for 30 min, when T profile was stopped and was not recorded any longer. SEM images of both materials after undergoing CH_4 activation. **c.** PBFNO-600(10), **d**. PBFNO-600(20).

Similar to PBFNO-600(10), with PBFNO-600(20) no products were observed at low temperature. PBFNO-600(20), which underwent severe decomposition after reoxidation, as depicted in Figure 4.5.b, activated the process at 780 ºC, which is 30 ºC higher than PBFNO-600(10). As highlighted before, PBFNO-600(20) displayed more secondary phases with a $Ba_2Pr_6Fe_4O_{15}$ structure hindering the formation of exsolved nanoparticles, explaining the later activation of this material. In this case , the ideal ratio is lost promptly, achieving

high levels of CH_4 conversion (up to 55%, as shown in Fig. 5.b), but with very poor selectivity towards the desired ratio of products, indicating that these exsolution conditions are not adequate to activate CH_4 towards partial oxidation purposes. Furthermore, this material promoted more coking formation than its analogue reduced during 10 h.

SEM images were taken after the described tests. Even though both materials produced undesired CH_4 cracking, significant differences could be observed between these two. Whilst PBFNO-600(10) (see Figure 4.5.b) generated less cracking and showed signs of decomposition by exhibiting enlarged exsolved particles and different morphology compared to the images in Figure 4.3.c,d, its analogue PBFNO-600(20) generated larger amounts of H_2 as a result of CH_4 cracking and showed clear signs of full phase decomposition. This material, that was believed to be partially decomposed after PXRD study from Figure 4.4.b, underwent absolute decomposition after the tests of CH_4 activation. Therefore PBFNO-600(20) was discarded as further part of the study and all the results presented hereinafter will correspond to the tests conducted with PBFNO or PBFNO-600(10).

4.5. *Operando* CH_4 activation using *as sintered* 0.1 A-site deficient PBFNO

To gain further understanding about the formation of the exsolved metallic nanoparticles and the reactivity of these designed materials, two similar operando experiments were conducted at the synchrotron facilities in ESRF. The first one consisted of carrying out a 1% CH_4-TPR with 0.350 g (1.5 mmol) of *as sintered* PBFNO (0.1 A-site deficient) as OCM. Ramp rate (10 ºC / min) was used until reaching 770ºC, since it was the temperature at which both systems started forming products.

PXRD of different capillaries did not provide enough information to confirm whether the exsolved nanoparticles correspond to metallic fcc Ni or a FeNi alloy, as Ni and Fe are the only exsolvable species from the system (Kousi *et al.*, 2021). As previously explained by Kousi et al., (2021), ΔG is lower for Ni in the exsolution process, thereby it would exsolve before the other metals included in this composition. However, metallic fcc Ni peaks fall under the same angle as FeNi alloys (9.8º and 11.2º, for fcc Ni #225, $FeNi_3$ #5116, fcc FeNi #103556). To identify the nature of these species, *operando* PXRD experiments were carried out at ESRF.

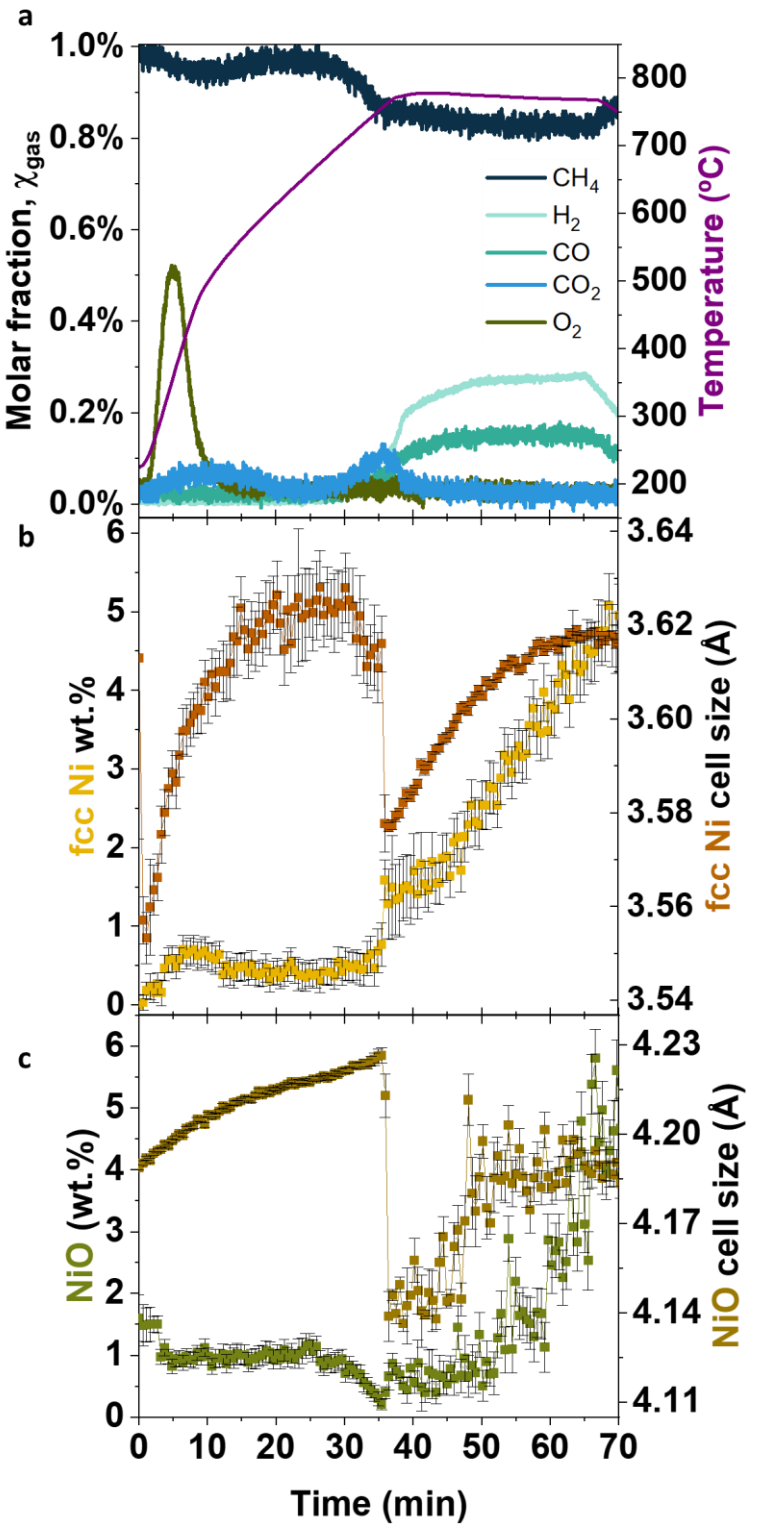

Figure 4.6. Results of the 1% CH_4 – TPR with 0.350 g of *as sintered* PBFNO, conducted at ESRF. **a**. Gas outlet vs time. Molar fraction of gases (left) and temperature (right). **b**. Metallic phase (named as *fcc Ni wt.%*, left) and metallic phase cell size (*fcc Ni cell size*, measured in Å, right) variation with time. **c.** NiO phase (named as *NiO wt.%*, left) and NiO phase unit cell variation (*NiO cell size*, measured in Å, right) All the parameters plotted share the X-axis (Time, min). Figures have been plotted together to facilitate the visualisation of the *operando* experiment. X-axis (Time) is shared for all of them.

The recording of diffractograms began at 240ºC, instead of room temperature. At this temperature, the orthorhombic contribution to the main perovskite phase had disappeared. At the initial temperature in which the *in situ* PXRD was collected (T = 224ºC), different phases were detected. Beyond the transition to a full cubic system by elimination of the orthorhombic phase, NiO peaks were identified. The peaks associated to NiO were 8.4º, 9.7º (Figure 4.4.a), and 13.8º. Cubic NiO (ICSD #9866) was the only phase identified falling under these angles. Rietveld refinement confirmed its low presence (~ 1.5 wt.%), as impurity.

A sharp O_2 peak was observed at 300 ºC (Figure 4.6.a), corresponding to 0.089 mmol of O desorbed · g_{OCM}^{-1}. This oxygen was equivalent to the amount of NiO transformed into Ni: NiO weight fraction went from 1.5 wt.% to 0.95 wt.%, which accounted for the formation of 0.5 wt.% of Ni. This weight fraction of Ni remained constant throughout the following 400 ºC. By carefully looking at the graphs in Figure 4.6.a-b, the formation of fcc Ni aligned closely with this oxygen peak. During this temperature ramp and due to the thermal expansion, NiO experienced an inherent cell expansion of $6.69 \cdot 10^{-5}$ Å / ºC (Figure 4.6.c), being this a close value compared to the literature ($7 \cdot 10^{-5}$ Å / ºC), determined by Konysheva et al. (2009). This value confirms the correct execution of the refinement conducted here. At that same temperature, 300 ºC, CH_4 activation began towards combustion products. As no weight fraction variation was observed in any of the identified phases, the origin of this reaction was attributed to the reaction between CH_4 and the labile oxygen from the perovskite.

Eventually, at T ≈ 680 ºC, the system reactivated, generating both combustion and POM. Upon temperature stabilisation, at approximately 760 ºC (50 ºC lower than the preliminary studies, at the beginning of the chapter), combustion ceased and CH_4 exhibited a conversion of 50% per g_{OCM}, with the desired ratio of H_2:CO of 2:1. The system continued yielding syngas at that ratio throughout the isothermal profile, devoid of any signs of cracking formation or carbon deposition. Upon increase of CH_4 conversion, at the 30^{th} min, the presence of NiO decreased (Figure 4.6.c) in exchange of the formation of fcc Ni (Figure 4.6.b) whilst combustion took place. Once syngas formation started, NiO weight fraction was close to 0% and fcc Ni weight fraction increased up to 1.5 wt.%, indicating a full transformation of NiO into fcc Ni. After this value, fcc Ni wt% gradually increased beyond

2 wt.% whilst maintaining syngas as a product. As this value was higher than the total Ni wt.% within the final composition, it was suggested that another species was exsolving along Ni. The other exsolvable species was Fe (Kousi *et al.*, 2021).

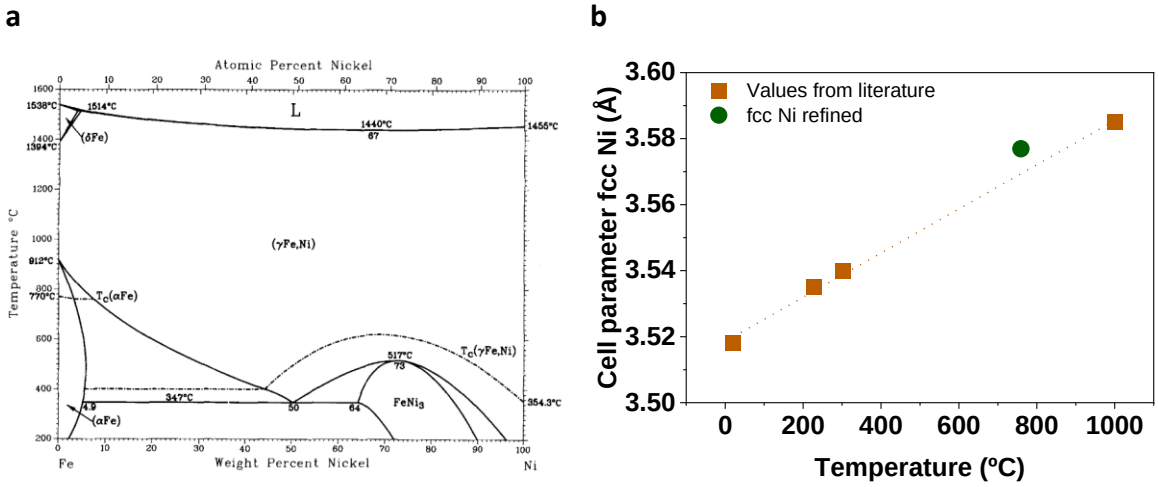

Figure 4.7.a. Fe-Ni phase diagram originally elaborated from experimental data (Swartzendruber, Itkin and Alcock, 1991). **b**. fcc Ni cell expansion calculated from the literature (orange) vs Temperature. Experimental fcc Ni value (green) has been added to the graph.

The investigation of the formation of fcc Ni during the isothermal phase of the reaction has gathered particular scrutiny. This was due to the possibility of being characterised as a FeNi alloy, as both species exhibit peaks at the same 2θ. The initial value of the fcc Ni cell parameter was compared to existing values (Figure 4.7.b), by applying Vegard's law. Explained by Denton & Ashcroft (1991), Vegard's law is an empirical rule, based on approximation, which holds that there exists a linear relation, at isothermal conditions, between the crystal lattice constant of an alloy and the concentrations of the constituent elements. The experimental cell pattern was 3.577(7) Å, whilst theoretical calculations indicated a value of 3.571(0) Å, both appearing at 750 ºC. The marginal difference between these values was not sufficient to discard the possibility of the exsolution of all the Ni, followed by the exsolution of Fe and the final formation of a metallic alloy (as suggested/proposed previously in this work). As reflected previously, ΔG exsolution for Ni is lower than for Fe (Kousi *et al.*, 2021), confirming that Ni exsolves first. However, despite exsolving first, the cell size of fcc Ni continued to expand along with the weight fraction, exceeding 2 wt.%. Exceeding this 2 wt.% deemed improbable considering that the initial Ni content in the synthesis never exceeded 2 wt.%. These observations strongly suggested the formation of a FeNi alloy (ICSD #103556). As indicated by the refinement, the fact that

Ni exsolved first, followed by Fe, strongly suggests the formation of a (*αFe)Ni* alloy, at the operational temperature (750 ºC), supported by the diagram presented in Figure 4.7.a. Previous authors, such as Najimu et al. (2023) achieved similar findings in which the exsolved nanoparticles were initially Ni-rich and formed FeNi alloy nanoparticles upon reduction time. However, the techniques they used (*in situ* XAS, EXAFS and XANES) were not available for the research conducted here, therefore the support we rely on for this investigation is diagram in Fig.4.7.a. To obtain more information about the alloy structure, further characterisation would have been required, such as TEM or TEM-EDS analysis (Jo et al. 2022)

Rietveld refinement revealed the consistent presence of NiO throughout the entire process, despite the disappearance of its characteristic peaks upon commencement of the isothermal period (see Figure 4.8). This suggested that the NiO phase followed two different trends: firstly, cell expansion occurred over 35 min, followed by its subsequent transformation into fcc Ni (Figure 4.6.c). This statement is further supported by Figure 4.8.a-b, which displayed initial NiO peaks (9.8º) disappearing and being transformed into fcc Ni (peaks at 9.9º).

However, this finding contradicted the conducted refinement, which fails to establish a discernible trend, yielding values lacking chemical coherence. According to the PXRD patterns displayed in Figure 4.8, NiO disappeared as result of the reduction (by observing the area at 9.8º in Figure 4.8.a-b), but the refinement affirmed it increased after the 35th min. This inconsistence was due to the impossibility of conducting two different sets of refinements for the same pattern. Different phases were provided to TOPAS (software for refinement) and it accounted for them all throughout the refinement without the possibility of refining until a certain time and change it afterwards. This was supported by the data exposed in Figure 4.6.c. Whilst there was coherence among the data refined before the 35th min (unit cell expansion, phase percentage decrease, etc.), no logic follows after the said time. Values for NiO experienced an undeliberated increase and scattering after the 35th min and the error bar accompanying them experienced the same dynamic. Therefore, the increase in NiO weight fraction and NiO cell size beyond the 35th min was dismissed.

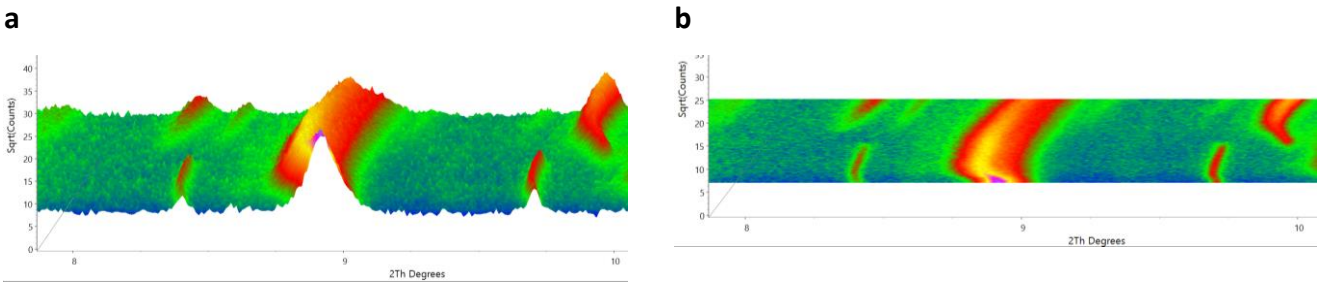

Figure 4.8. Zoomed of obtained *in situ* PXRD pattern (8.5º < 2θ < 10.5º) where the transition from NiO (9.7º) to fcc Ni (9.8º), or alloy is observed. **a.** Front view. **b.** View from above. Images correspond to superposition of PXRD patterns collected at ESRF. The colour map displays the variation of the PXRD patterns and peak positions with temperature. Images directly taken from TOPAS Academic v7 after conducting Rietveld refinement.

These observations in the formation of the exsolved FeNi alloy, alongside the results in syngas formation, led to confirm that exsolved particles supress or minimise coke formation when activating CH_4.

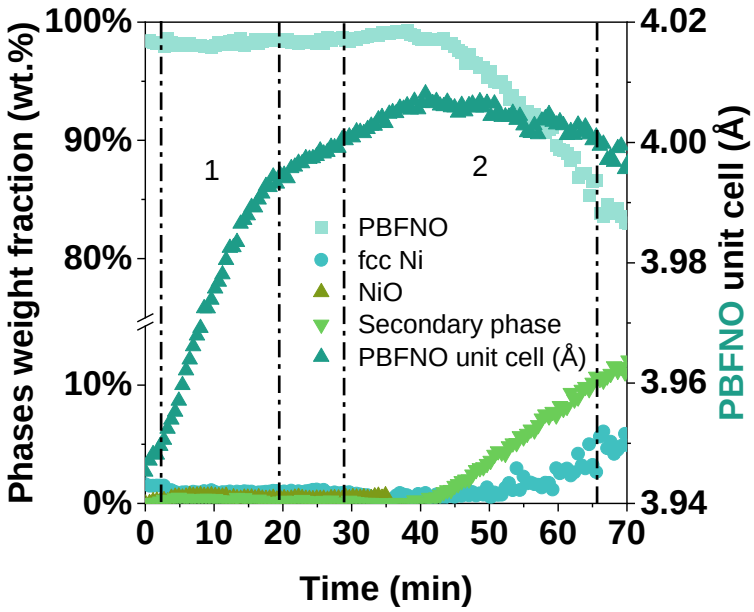

Figure 4.9. Different phases percentage variation (left) for 0.350 g of the *as sintered* 0.1 deficient A-site PBFNO reduction under CH_4-TPR. Results extracted from Rietveld refinement, and main perovskite unit cell variation (right) vs Time. Results give an approximate variation of the different weight fraction of the species found in the PXRD spectra. As highlighted before, NiO wt.% was dismissed after the 35th min.

The main PBFNO phase underwent cell expansion due to the temperature increase and the reduction caused by CH_4 combustion. Combustion range (CO_2 + H_2O as products) is within the area marked as "1" in Figure 4.9. Upon the end of the combustion, the slope became less pronounced. During the second stage of CH_4 conversion (marked as "2"), PBFNO cell size kept increasing, until the 40th min approximately. During the subsequent 5 min, the

perovskite weight fraction before experiencing a drop. At the moment this weight fraction began, the previously identified *sec-BPF*, rhombohedral $Ba_2Pr_6Fe_4O_{15}$, started forming. The presence of this structure intensified over time, experiencing a linear increase throughout the isothermal part, as result of the main phase decomposition into other phases. The complete exsolution of Ni (0.1 Ni in the B-site) followed by the partial exsolution of Fe could be attributed to the partial decomposition of the perovskite into *sec*-BPF. Here follows an explanation of the possible cause: $A_{0.9}Fe_{0.9}Ni_{0.1}O_3 \xrightarrow{H_2+\Delta} AFeO_3 + 0.1Ni$, would have been the final result of the reduction if Fe had not been exsolved, achieving an equilibrium between perovskite and exsolved Ni phase. However, as Fe was continuously being exsolved, the equation was now as follows – $AFe_{1-\alpha}O_3 + (0.1Ni)(\alpha Fe)$. This imbalance generated between A and B site could be the trigger for the perovskite to partially decompose into the rhombohedral identified perovskite phase in order to compensate for that Fe loss in the B-site.

Previous studies from Kousi, Neagu, Bekris, Papaioannou, et al. (2020) discussed the formation of Ni exsolved nanoparticles within the bulk and on the surface of the material studied. To achieve this, the authors designed a different material from the one presented here. Instead of Fe^{3+} in the B-site, the cation is Ti^{4+}. Titanates possess lower cation transport properties than ferrites (Ivanov *et al.*, 2022). The increased cation transport facilitates the migration of the exsolved cations to the surface. The presence of Ni in the B-site was 5 times higher than the amount of the materials presented here (10 wt.% vs 2 wt.%, respectively) and, finally, the temperatures used for exsolution were much higher than the ones that have been used here. This way, exsolution of bulk nanoparticles was achieved, which was observed via SEM. To study this formation of endo-/exo- nanoparticles, the deconvolution of peaks at 9.8º from the PXRD pattern was crucial. The peak possesses double contribution: a sharp large peak and a broad and small base. Two different particle sizes corresponding to endo and exo nanoparticles were corroborated by PXRD after splitting the peak at 9.9º into two different peaks (Figure 9.a). The presented peak does not look symmetrical: a left shoulder on the top third of the peak indicates the possible existence of two structures. By deconvoluting the peak obtained via PXRD, those two structures are confirmed and two different nanoparticles size can be appreciated (Figure 4.10.a-b), corresponding to endo-nanoparticles (smaller size 13 nm, due to the strain and

lower mobility from within the lattice) and exo-nanoparticles (larger size, 45 nm) (Kousi, Neagu, Bekris, Papaioannou, *et al.*, 2020).

In this case, the peak displayed for PBFNO undergoing exsolution appears as a symmetrical peak with no shoulders near the base of the peak (Figure 4.10.c), suggesting the existence of a sole exsolved species, in this case an FeNi alloy.

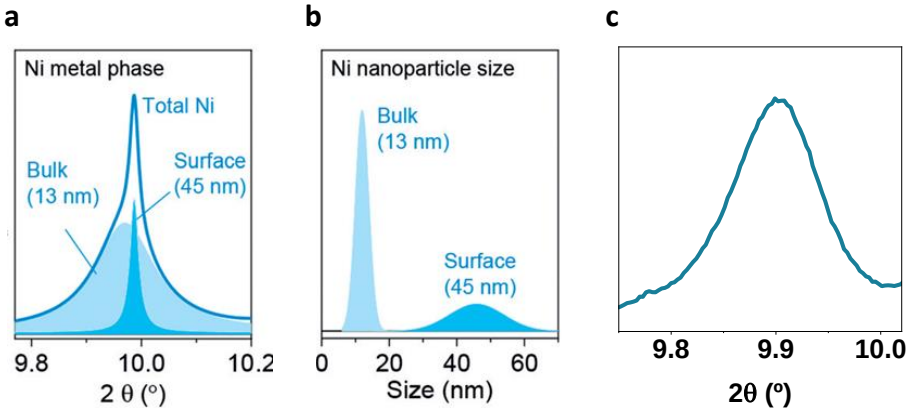

Figure 4.10. Zoomed area in **a**, 2θ for the peak corresponding to metallic fcc Ni angle. **b**. Peak deconvolution of the PXRD peak presented in a, translated into Particle size (nm). Images courtesy of Kousi, Neagu, Bekris, Papaioannou, et al. (2020)(2020)(2020)(2020)(2020)(2020). **c**. PXRD pattern obtained at ESRF for further peak deconvolution at the angle of metallic fcc Ni.

4.6. *Operando* re-oxidation of exsolved nanoparticles

For better understanding of the oxygen capacity, oxygen exchange and reversibility of the process in the said material, the OCM underwent *operando* reoxidation at ESRF, with 3% O_2 balanced in He for 4 hours. To proceed, 87 mg of PBFNO previously reduced at 550 ºC for 10 h was loaded in the reactor bed. Extra 25% of Y_2O_3 (25 mg) were loaded in the reactor. Y_2O_3 peaks do not interfere with the material's PXRD pattern, and it is inert under the oxidising conditions of the experiment. Refinement of Y_2O_3 has been widely investigated for Rietveld refinement. The study of Y_2O_3 is used to calculate the experiment temperature. Empirical equations calculated by Swamy et al. (1999) allowed to link the lattice parameters of Y_2O_3 and its thermal expansion with the temperature of the process.

The results of the material reoxidation are presented in Figure 4.11. As expected, initially the perovskite structure (ABO_3) is the main phase (Figure 4.11.a), with presence of FeNi alloy and the secondary phase sec-BPF, as result of the controlled decomposition (Figure 4.11.b) conducted previously at 600 ºC and 10 h. After 0.5 h of reoxidation, when

T ~ 150 ºC, the presence of the FeNi alloy started decreasing and PBFNO increased, and the secondary phase remained stable. This indicates that the exsolved nanoparticles of FeNi were redissolved within the lattice of the perovskite even at low temperature, corroborating the reversibility of the process, as previously stated by (Nishihata et al. (2002). Different stages can be discerned in the first moments of the alloy oxidation and incorporation within the lattice. The first one presented a soft decrease in the weight percentage, until temperature was ~260 ºC (1 h) and a steep decrease, going from 1.9 wt.% to a steady value 0.3 wt.%. This drop in value lasted until the isothermal conditions were reached (560 ºC). After 2 h of reoxidation, the value triples and is maintained steady during 1 h. After 3 h into the reoxidation, FeNi alloy wt.% reaches again the value of 0.3 wt.% for less than 30 min, tripling once more to a steady value of 0.9 wt.%. A similar behaviour is observed towards the end of the isothermal area, when Time ~ 5.2 h. Before establishing any conclusions, a simultaneous study of the main perovskite phase is required.

As stated previously, PBFNO (ABO_3) phase is the main phase, starting at approximately 93 wt.% (Figure 4.11). This value starts increasing at the same moment in which the first soft slope detected for the alloy began. This correspond to approximately 30 min of reoxidation and displays a constant increasing slope until the isothermal phase is reached. This constant value corresponded to 94.7 wt.%. In the case of PBFNO, values are not as steady, but an average was calculated. A slow increasing trend can be appreciated in the graph, reaching up to 95.2 wt.% upon termination of the isothermal area. PBFNO wt.% also displayed the same variations previously mentioned for the alloy at Time ~ 3 h and Time ~ 5.2 h. Both growths lasted the same amount of time. These variations in values are attributed to a possible experimental error due to a pressure drop. The variations observed are steep, instead of gradual changes. Furthermore, no NiO reduction was possible, as no reducing gases were flowed at any instant during the reoxidation. However, it is observed how NiO weight fraction dropped during the third hour of the reoxidation. This result lacks chemical coherence and supports the previous statement of the possible pressure drop during the experiment.

NiO had been included into the refinement model as it was likely to be formed during the reoxidation. It was initially detected in the pattern even though it was proven that no remnants of NiO were left in the material after reduction (Figure 4.4a). While the alloy

decreased its phase weight, the presence of NiO augmented from 0 to a steady value of 0.3 wt.% throughout the oxidation. NiO exhibited two abrupt increases in its phase fraction at the same time as the alloy underwent a sharp decrease, and the same perovskite displayed an increase (3 h and 5.2h). The presence of NiO during the reduction suggests that the alloy nanoparticles were not fully reincorporated within the perovskite lattice.

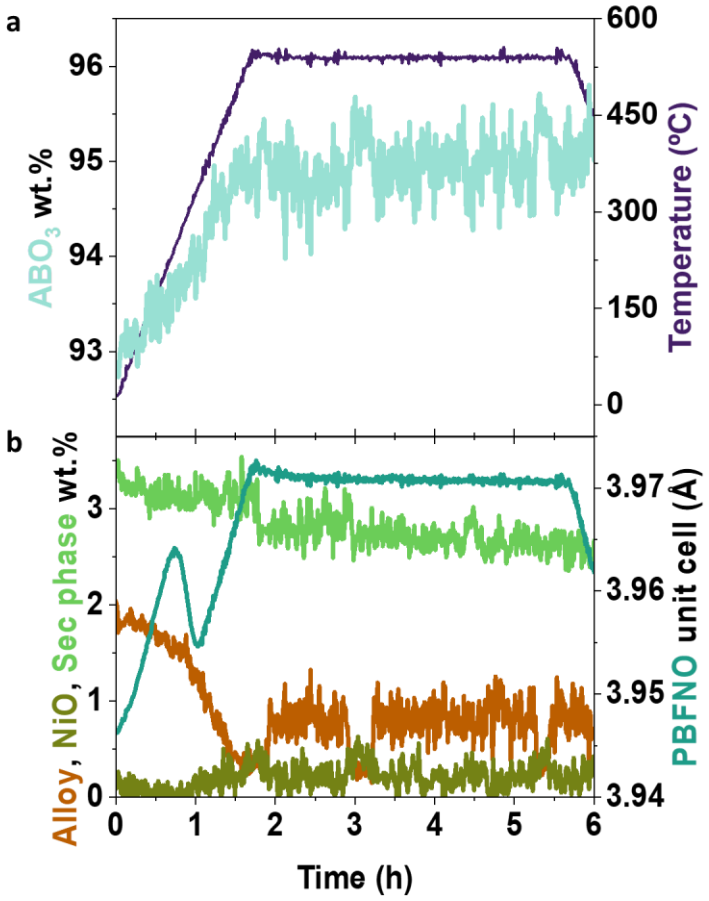

Figure 4.11. Results of the *in situ* 3%-TPO of 0.083 g of PBFNO-600(10) after conducting Rietveld refinement of the PXRD patterns obtained at ESRF. **a**. Main perovskite percentage phase (left y-axis) and temperature (right y-axis) vs Time (h). **b**. FeNi alloy and secondary phase percentages (left y-axis), PBFNO unit cell variation (right y-axis) vs Time (h). Graphs **a** and **b** are sharing x-axis. Error bars not displayed given the large amount of points as they would hide the visibility of the actual graph line.

On the other hand, as previously mentioned, a secondary phase ($Ba_2Pr_6Fe_4O_{15}$, sec-BPF) was identified in the starter material at the beginning of the reoxidation. This phase originated as result of the H_2 reduction at 600 ºC, identified previously. Upon the beginning of the isothermal conditions, at around 1.6 h, sec-BPF) experienced a decrease in its value, going from 3.4 wt.% to approximately 2.8 wt.%. After reaching this value of 2.8 wt.%, the secondary phase reduces its presence with a slow pattern, reaching down to 2.4 wt.% upon experiment termination. The gradual decrease is accompanied by a gradual increase of the

perovskite amount after reaching that isothermal value, indicating that part of the secondary phase is transformed into the original core perovskite. This underlines the reversibility of the exsolution process.

Unit cell of PBFNO underwent thermal expansion until Time ~ 0.75 h. Here, a decrease in the lattice value was observed, going from 3.964 Å to 3.955 Å in 0.25 h. This lattice contraction is due to the replenishment of the oxygen vacancies originated during the reduction. After this contraction, a new increase is observed, with an identical slope as the one observed initially, until it reached a stable lattice parameter when meeting the isothermal conditions. The value was kept constant until the cooling down process took place. The absence of any modification in the lattice parameters during the isothermal part is another indicator that the two steps mentioned earlier regarding the FeNi wt.% and ABO_3 wt.% correspond to a temporary experimental issue, not affecting the overall result.

However, despite being a reversible process, it cannot be stated that exsolved nanoparticles are fully reintegrated within the initial matrix. Here it is seen that not all the amount exsolved has undergone redissolution at the described conditions (3% O_2, 560 ºC and 4 h), as expected from the results presented previously in this chapter. Several authors have reported complete reincorporation of the metals into the lattice (Tanaka, Uenishi, *et al.*, 2006; Burnat *et al.*, 2016; Hosseini *et al.*, 2019). On the other hand, some authors have reported an incomplete redissolution of the surface nanoparticles within the lattice (Lai and Manthiram, 2018; T. Liu *et al.*, 2020) under smooth reoxidation conditions, which are closer to the conditions used in this *operando* experiment. Some other authors, such as Katz et al. (2011) underlined that the redissolution process is highly dependent on the conditions used and the material's surface crystallinity. Therefore, the incomplete redissolution of the FeNi nanoparticles presented here can be attributed to the smooth oxidising conditions used. However, the system has been proven to undergo full reoxidation and deploy the *self-regenerative* behaviour that authors such as Nishihata et al.(2002) or Shin et al. (2012) described.

The study conducted by Santaya et al. (2022) corroborates these findings. The authors found the existence of a FeNi alloy that increased the Fe content with longer reducing time and further A-site segregation caused by the B-site imbalance.

4.7. *Operando* CH_4 activation using PBFNO after undergoing exsolution and reoxidation

Same experiment than the one conducted for PBFNO *as sintered* was carried out for the material that underwent exsolution and further reactivation under air. The OCM was reduced at 600 ºC for 10 h and reoxidised at 600 ºC under air for 1 h, PBFNO-600(10). In this case, 0.093 g of material (0.4 mmol) were used. As in previous cases, all the oxygen loss and intake or conversion results are expressed in units per g of OCM, to get comparable results. In the graph depicted in Figure 4.12.a, at 315 ºC, an O_2 peak can be observed. This

O_2 peak was extended until reaching 485 ºC, due to thermal desorption from the labile oxygen of the OCM, corresponding to 0.213 mmol $O_{lost} \cdot g_{OCM}^{-1}$.

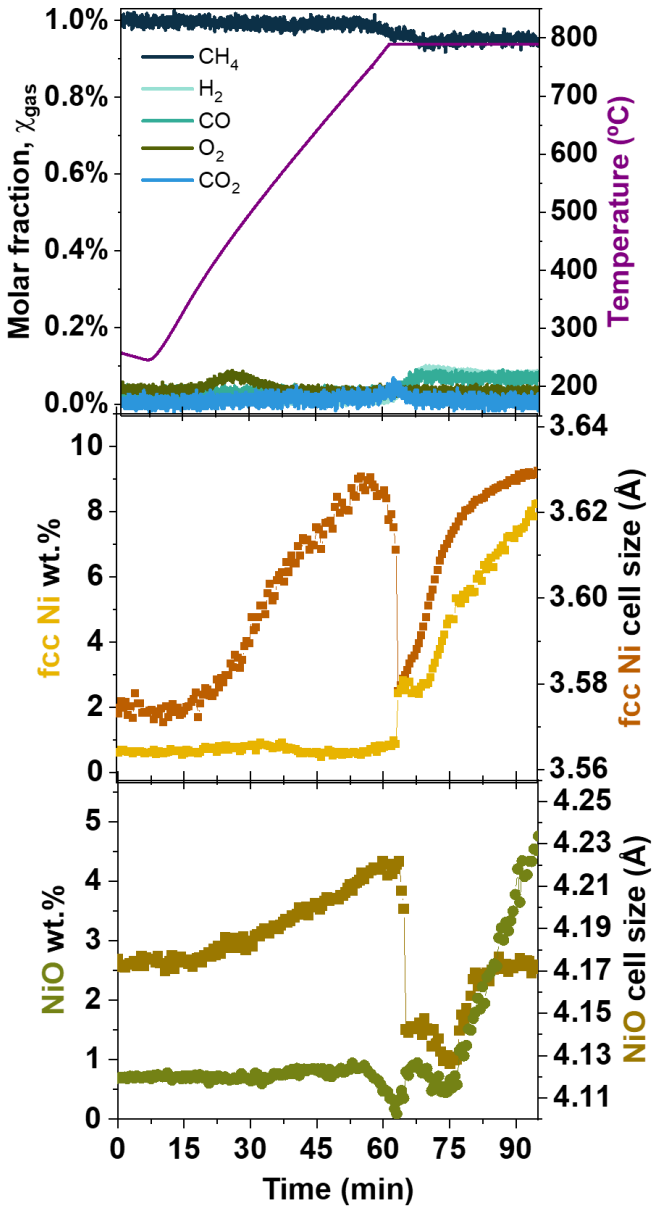

Figure 4.12. Results of the 1% CH_4 – TPR with 0.094 g of PBFNO-600(10), conducted at ESRF. **a**. Gas outlet composition obtained by MS, represented by molar fraction of gases (left) and temperature (right). **b**. Metallic phase (named as fcc Ni wt.%, left) and metallic phase cell size (right) variation with time. Data obtained as result of PXRD peaks refinement. **c**. NiO phase wt.% (left) and NiO cell size (right). All the parameters plotted share the X-axis, Time (min), only displayed at the bottom graph.

In this case, following the same dynamics from previous experiments and shown in Figure 4.5.a, no combustion was detected at low temperatures. CH_4 reactivity became evident only at 700 ºC (expected temperature to start reacting), with low syngas selectivity. Even though CH_4 combustion was initially observed, it quickly decayed upon reaching the isothermal point (800 ºC), highlighting that nearly all the selectivity was towards the

desired products (H_2:CO in a 2:1 ratio). CH_4 conversion rate was constant throughout the reaction, (60% conversion of CH_4 per 1 g of material) but the ratio was slightly lower than 2:1. This low ratio indicated the possibility of secondary reactions occurring during the process, such as reverse Water-Gas Shift, rWGS, (Eq 4.3). In a recent study, Siang et al (2020) explained that, at the conditions of temperature and pressure used in CH_4 activation (T > 700 ^oC and atmospheric pressure), rWGS is a dominant side reaction. These authors also stated that low oxygen-rich environments such as CH_4 towards syngas promote high CO yields, promoting other processes such as rWGS. In this reaction, the H_2 generated reacts with the residual CO_2 from the combustion. This secondary reaction helps explaining the quick drop of CO_2 as product in detriment of H_2 consumption and increase of H_2O. Unfortunately, H_2O could not be monitored during the experiment to further support this hypothesis.

$$CO_2 + H_2 \rightarrow CO + H_2O \qquad \text{Eq 4.3}$$

A minor proportion of NiO (2.5 wt.%) was initially detected, (Figure 4.12.c), indicating that not all the Ni had been reincorporated to the matrix upon reoxidation. This NiO content remained constant throughout the temperature ramp and begins declining once the combustion peak ceased (70th min). A possible explanation for this is that the CH_4 gets all the oxygen primarily from the NiO species rather than the perovskite matrix, reducing NiO to Ni. As explained previously during the first CH4-TPR, it would be logic for NiO to disappear from the refinement results after the 70th. However, the software did not allow to split the refinement and tried to fit the NiO phase in all the patterns, despite not finding it. Following the same trend as in section 4.5., the NiO wt.% was discarded after the 60th min, as it was not detected in the XRD spectra upon that minute. The results shown in

previous graphs display the same trends as in the previous section: uncontrolled increase in its weight fraction lacking chemical implications.

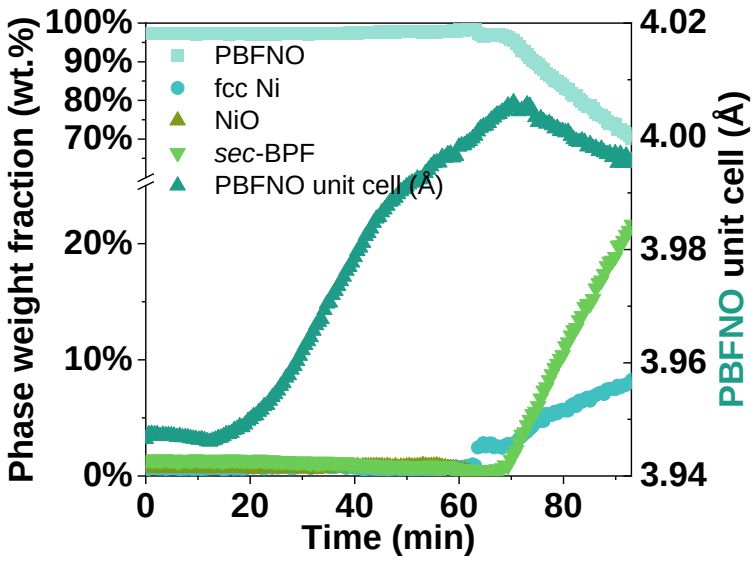

Figure 4.13. Different identified and refined phases percentage (left) when conducting a 1% CH_4-TPR for 0.093 g of reoxidised 0.1 deficient A-site PBFNO. Right axis displays PBFNO unit cell variation vs Time (min). All the plotted features were obtained via Rietveld refinement. As stated previously, the weight fraction from NiO was discarded after the 60th min of reaction, as its presence lacked chemical implication

Figure 4.13 shows the different phase percentage (expressed as wt.%) during the CH_4-TPR of PBFNO-600(10) after undergoing oxidation. Perovskite weight fraction remains constant until the 60th minute. After this, CH_4 started reducing the material and consequently being transformed into products. Perovskite reduction aligns with the concurrent exsolution metallic fcc Ni. Ni weight fraction remains stable at 2% until reaching the 70th min. At the 70th min, syngas products start forming and the perovskite weight fraction diminishes whilst fcc Ni fraction and the secondary phase sec-BPF increase accordingly. On the other hand, unit cell of PBFNO decreases once. By closely looking at the graph in Figure 4.13, the decrease of the unit cell value of the perovskite coincides with the increment in the fcc Ni wt.%. This fcc Ni increment corresponds to the formation of a FeNi, as demonstrated previously in this chapter. During a reduction, the unit cell of a material is expected to increase, as larger cations are being formed as result of their reduction. However, once the Ni was exsolved from the core material, this unit cell dropped its value. Upon full Ni exsolution (0.1 mol Ni), the material A-site deficiency (0.1) was compensated. Nevertheless, FeNi alloy was observed, indicating that part of the Fe was leaving the main perovskite phase. J. Kim et al. (2023) confirmed that, despite the reducing conditions, most

of the Fe from the perovskite remained as Fe^{3+}, which could explain the decrease in the cell size observed here.

After undergoing exsolution and further reoxidation, the main perovskite phase underwent higher decomposition than the non-exsolved homologue (20% and 12% sec-BPF formation, respectively). On the other hand, a larger extent of exsolution has occurred during the second exsolution: 7% of metallic alloy phase compared to the 5% of metallic FeNi alloy observed when reducing the *as sintered* PBFNO. The combination of these two results lead to confirm after the first exsolution, materials become more prone to decomposition, despite the reversible character of the exsolution process.

As explained previously, the refinement needed to be conducted with all the expected phases included in the TOPAS script, as the software did not allow to split according to time preferences. Moreover, the inclusion of NiO was needed to explain the initial peaks at 9.7º. The results display an augmentation of NiO phase fraction after the 60th minute. Even though the peak at 9.7º could be initially observed as depicted in Figure 4.14, it disappears as the reduction takes place. Therefore, NiO wt.% or cell parameters do not form part of the discussion after the 60th min of reduction.

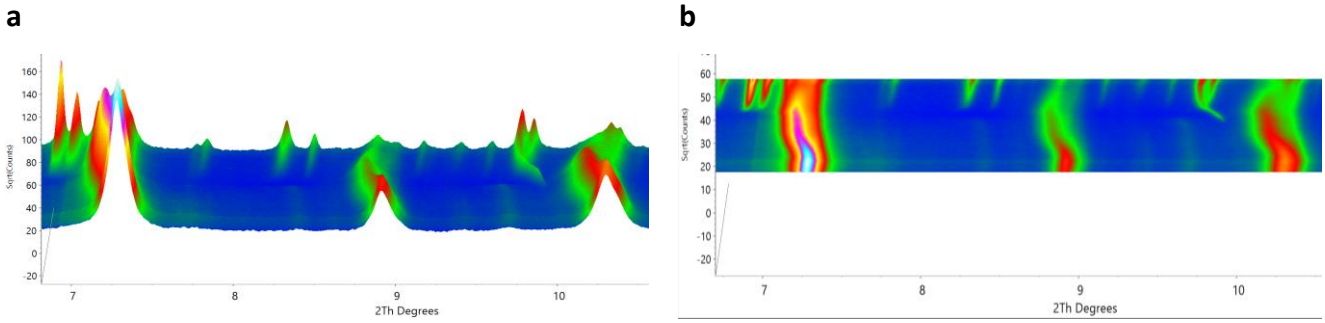

Figure 4.14. Zoomed PXRD pattern (6.8º < 2θ < 10.5º) where the transition from NiO (9.7º) to fcc Ni (9.8º), or alloy is observed. **a**. Front view (above image). **b**. View from above (bottom image). Images correspond to superposition of PXRD patterns collected at ESRF, images taken from TOPAS Academic v7 after conducting Rietveld refinement.

The study of fcc Ni regained significance. Comprehending the phases formed became crucial to understand why the reaction maintains such an effective selectivity throughout the process without undergoing OCM decomposition. At 800 ºC (60th min), Ni presence increased from 0% to 2% and remained constant for 5 min until it began increasing. The cell size value was of 3.57831 Å. At 800 ºC, fcc Ni presented a value corresponding to the determined value from the literature, 3.5746 Å. This indicates that initially only fcc Ni

exsolved initially. That value however increased at isothermal conditions, suggesting the formation of a (αFe),Ni alloy as previously presented for the *as sintered* PBFNO.

4.8. Oxygen capacity of the studied systems

The materials studied in this chapter are expected to be implemented in CL for H_2 production in CLWGS. Proven their ability to undergo reversible exsolution whilst maintaining their core structure, a final study in the oxygen capacity is required. The oxygen consumed and regained after reoxidation will determine what material is *a priori* more suitable for the process.

Oxygen atoms were released forming different species: O_2, CO, and CO_2. By measuring the amount of oxygen released by studying the different species formed, it is possible to study the oxygen capacity of the OCM. Results were normalised in order to obtain a more realistic approach of the oxygen loss; therefore, all the numbers are represented with respect to the amount of oxygen released per mass of OCM. After undergoing exsolution and reoxidation, the OCM undergoing exsolution and further reoxidation ended up liberating more amount of oxygen per mass unit of OCM involved in the process than its analogue *as sintered*. The OCM from the last study displayed a larger formation of exsolved nanoparticles, accompanied however by the formation into more secondary phases.

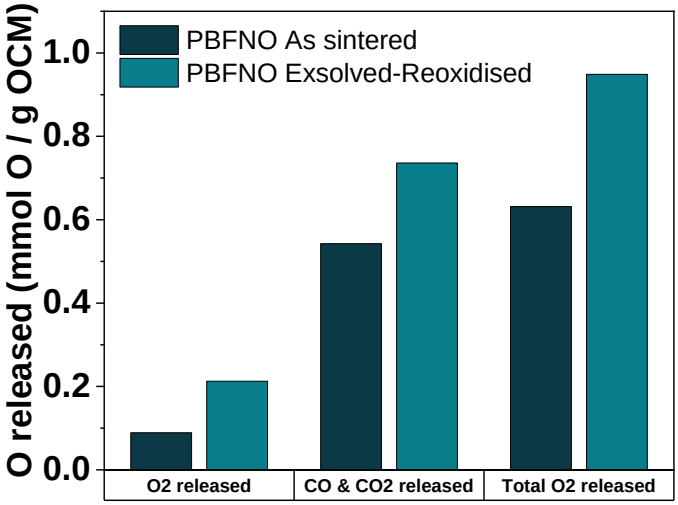

Figure 4.15. Comparison of the oxygen released (left axis) by the OCM after undergoing CH_4 reduction at 600 ºC. Oxygen released measured with the different oxygen-containing gases (O_2, CO and CO_2) in the outlet during the CH_4-TPR conducted at ESRF.

Contrary to expectations and despite displaying a larger oxygen capacity and higher CH_4 conversion for the said process, syngas ratio was very far from the ideal value expected

when using PBFNO-600(10) exsolved for a second time. Selectivity was believed to decrease because of the presence of the secondary reaction of rWGS. CO_2 activation towards rWGS was believed to occur in the oxygen vacancies from the materials lattice (Opitz *et al.*, 2020). In the vacancies, one of the oxygen atoms from the C=O bond is adsorbed, forming CO, and the oxygen replenishes the lattice of the material. H_2 formed during the activation of CH_4 therefore reacts with the labile oxygen from the material, forming H_2O (not recorded in the MS), decreasing the overall selectivity of syngas.

4.9. Summary of Chapter 4

This chapter presents the modifications done in the initial material that was chosen as benchmark (PBFO) for further implementation in subsequent CL processes involving H_2 production.

PBFO was initially chosen as material for further study and characterisation thanks to its higher CO and H_2O conversions compared to its analogue SBFO. It was tested for CH_4 activation, and the material initially presented decomposition. The incorporation of Ni (now the material was referred to as PBFNO) and the modification of the A-site of the material have resulted beneficial for higher yields and material durability. The introduction of A-site deficiency allowed for a preliminary study of exsolution conditions. It was decided that the optimal conditions for exsolution were 600 ºC and 10 h, after finding a balance between the amount of nanoparticles exsolved, their size, distribution and secondary phases generated.

The *as sintered* material was studied in depth at ESRF by *operando* experiments under a reducing CH_4 atmosphere with a temperature ramp in which we could directly observe the modifications the material underwent in these conditions. We observed the formation of a FeNi alloy in which the Ni is believed to exsolve first, followed by the Fe, as it requires higher energy. Reoxidation of the material previously reduced at 600 ºC and 10 h was also observed at ESRF and we observed the partial redissolution of the formed FeNi alloy. A final comparison between the activity towards CH_4 with the *as sintered* material and the one undergoing reduction (5% H_2, 600 ºC and 10 h) and further reoxidation (air, 600 ºC, 4 h) was conducted. The second OCM showcased higher CH_4 conversion values but poorer selectivity, because of the promotion of the undesired secondary reaction, rWGS. This

reaction was favoured due to a larger amount of oxygen vacancies that promoted the activation of CO_2, transforming it into CO, lowering down the ideal 2:1 H_2:CO ratio.

The reactivity towards CH_4 of the designed material was successfully tested and proven with high syngas selectivity for *as sintered* 0.1 A-site deficient PBFNO. Therefore, for the final test of real CLSRM conditions, 0.1 A-site deficient PBFNO is the chosen material to be studied.

Chapter 5 Testing exsolved OCM in CLSMR

Discussion of Chapter 3 was focused on the conception and development of a novel OCM for CL H_2 production in a packed bed reactor via the WGS reaction. The oxygen capacity, the lattice parameters and stability of the OCM were evaluated. Two materials, SBFO and PBFO, were initially prepared and underwent CLWGS conditions for H_2 production. After OSC and yield assessment, PBFO displayed larger OSC and higher conversion than its analogue SBFO. Nevertheless, both materials were stable and durable after 400 looping cycles.

Chapter 4 illustrated the modification of PBFO targeting H_2 production via another process, CH_4 activation. A continuous change and modification of the initially designed material are observed through this fourth chapter. This tailoring was achieved by doping the benchmark material with Ni in the B-site and inducing A-site deficiency. Exsolution of nanoparticles was eventually carried out at 600 ^oC to activate CH_4 with high selectivity towards syngas. To gain further understanding of the system and its reaction with CH_4, *operando* PXRD experiments were conducted during the reduction of the material. This experiment provided large insight about the formation of a FeNi alloy and its reactivity towards CH_4 with syngas selectivity for further implementation in processes involving CH_4 as reducing agent.

The purpose of this chapter was to experimentally prove that the modified material can be implemented as an OCM in CL steam methane reforming (SMR). Hereby, the activity of the new material (PBFNO-600(10)), its durability and stability after undergoing several cycles in CL methane reforming were studied.

5.1. Introduction

As explained in the introductory chapter, SRM is widely installed as a technology for H_2 production, even though the drawbacks it entails. SRM is a high-energy demand process and the catalysts required often suffer from deactivation. The main events of deactivation are sintering (due to the high temperatures needed to achieve high syngas selectivity) or poisoning (caused by carbon deposition or other species present in the natural gas stream (Chen *et al.*, 2020). On the other hand, this process is generally associated to a selectivity problem. CO_2 is generally generated as byproduct decreasing the overall selectivity of it.

Chemical Looping Steam Reforming of Methane (CLSRM) arises as an alternative to the traditional implemented technologies. As every CL process, the success of the technology relies on the implemented oxygen carrier and its conversion, in this case, CH_4 and H_2O conversion. By conducting the process at high temperatures (800-900 ºC), CLSRM is expected to minimise the CO selectivity issues, generating higher yields of syngas and to easily generate pure H_2.

5.2. Finding conditions for CLSMR

CLSRM is a process that is generally undertaken at a high temperature range, T > 850 ºC, (Li, Xu, Gu, *et al.*, 2020) and partial oxygen pressure falls under $10^{-19} < pO_2$ (bar) $< 10^{-13}$. These conditions narrow the initial CLWGS pO_2 range in which the experiments from Chapter 3 were conducted. For optimal CH_4 transformation to CO whilst avoiding competing with CO_2 production, pO_2 should be around 10^{-19} bar and temperature should be around 800 ºC, approximately. Nonetheless, high conversions can be also achieved at even lower pO_2 values, indicating that the designed OCM should be active in this range (Figure 3.1). Changes induced to the material presented in previous chapters (A-site deficiency and Ni-doping) were not expected to hugely affect the material's OSC. Therefore PBFO (now PBFNO) was maintained as OCM for the following studies. Initially developed OCM showed activity towards CH_4 with promising selectivity results (almost 100% syngas selectivity). Further Ni-doping suggested better conversion results and enhanced stability, as Ni is expected to increase the reactivity towards CH_4 (Wei *et al.*, 2014b; Yang *et al.*, 2023), keeping the desired selectivity. Otto et al. (2019) successfully developed Ni exsolved nanoparticles from a perovskite matrix, obtaining high syngas selectivity (>70%) in CLSRM at T ~ 600 ºC. Lastly, exsolution conditions were implemented to promote the reactivity and selectivity of the OCM, which resulted in an almost pure production of syngas when conducting CH_4 activation. These results suggested that these OCM could be implemented in real CL methane activation tests, using steam as oxidising agent, as high activity was reported in Chapter 3 when H_2O was used in CLWGS. This chapter shows how these OCM were tested in CLSRM, expecting relatively modest CH_4 conversion but with highly remarkable CO selectivity, totally avoiding CO_2 as byproduct. The purpose of this chapter is the attempt to exploit these designed and modified OCM under a lower-than-average working temperature range for CLSRM (T < 850 ºC). To do so, the adequate temperature

conditions and time duration need to be studied prior to be applied in several CLSRM cycles.

5.2.1 Temperature of the cycles

Previously, in Chapter 4, it was demonstrated that CH_4 could be activated at lower operational temperatures (680–700 ºC). The first purpose of this chapter was to find an optimal working temperature. As all the CL experiments carried out in this thesis were conducted at isothermal conditions, it is therefore needed to find a suitable temperature to operate the CLSMR cycles.

Briefly, an amount of 0.23 g of OCM (~ 1 mmol) were placed on the reactor bed. Particle size of the OCM was sieved to be between 80-160 µm. The OCM, PBFNO-600(10) was in an oxidised state after undergoing oxidation for 1 h at 600 ºC under air prior to the experiment, as it was observed that larger oxygen content was available after reoxidation. The material was expected to be further reduced as cycles progressed and thereby, to generate more exsolved nanoparticles on the surface, given the low oxidising potential of H_2O as compared to pure air. The OCM was cycled between 5% CH_4 and 5% H_2O with a flow of 80 mL / min, for 1 min each at a different set of temperatures ranging from 730 to 790 ºC, with 20 ºC jumps, maintaining each temperature for 15 cycles.

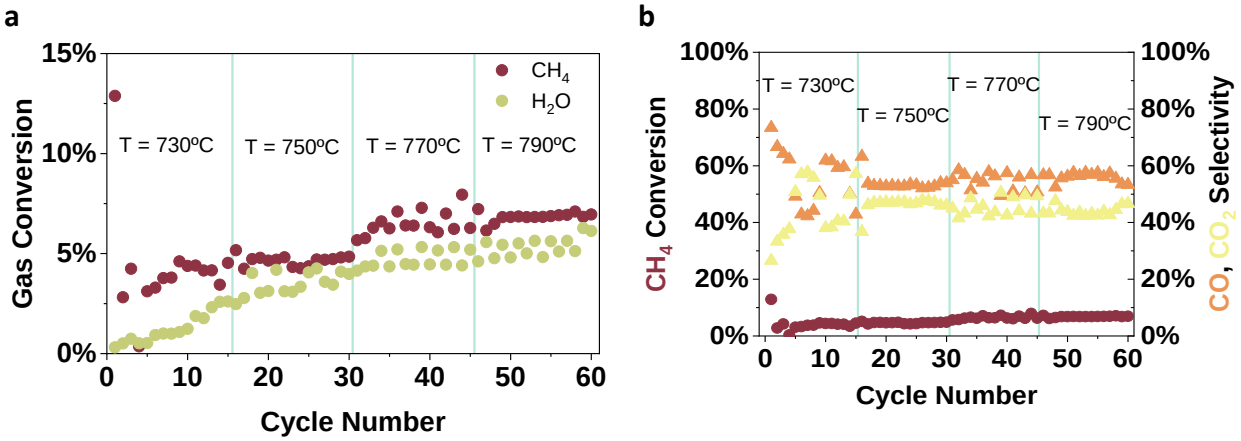

Figure 5.1. CLSRM experiments to find the optimal temperature for the process while using 0.23 g PBFNO-600(10). Each temperature was kept for 15 cycles, gas flows were of 80 mL / min of each reactant gas (5% CH_4 and 6.5% H_2O). First 15 cycles were carried at 730 ºC and temperature was incremented 20 ºC every 15 cycles until reaching 790 ºC. **a**. Gas conversion versus cycle number as a function of cycle number, over 60 cycles. **b**. CH_4 conversion and CO, CO_2 selectivity values as a function of cycle number.

Gas conversion and selectivity values of this experiments were illustrated in Figure 5.1. After undergoing reoxidation under air, the OCM had all its oxygen capacity replenished,

hence the initial CH_4 conversion value was higher than average (see Figure 5.1.a), until it reached steady state. H_2O conversion shows an increasing conversion which did not reach steady state, unlike CLWGS experiments had previously demonstrated, in Chapter 3. CH_4 conversion values remain close (4% and 5%, respectively) between the first two temperature values, 730 ºC and 750 ºC. In both cases, it remained at a steady state of 5%. Conversion values showed a small increase when temperature was incremented 20 ºC (770 ºC), reaching up to 7% CH_4 conversion and 4.5% H_2O conversion. Gas conversion values at 770 ^oC and 790 ^oC also displayed similar CH_4 and H_2O conversion values: at 770 ^oC, 7% and 4.5%, respectively; and at 790 ^oC, 7.5% and 5%, respectively.

Selectivity was however influenced by the working temperature, as shown in Figure 5.1.b. As expected in partial oxidation of CH_4, the material displayed a higher CO selectivity at the highest temperature values (almost 60% CO selectivity) On the other hand, at the lowest temperature value (730 ºC) a clear selectivity pattern could not be determined due to the competing reactions.

Contrarily to observations from the previous chapters, in which values of 20% CH_4 conversion when activating CH_4 and 46% H_2O conversion when carrying CLWGS cycles were achieved, the OCM did not exhibited these expected values. A possible explanation for this is that the operating temperatures employed here were still far from the classic temperatures in CLSRM, which are usually T > 850 ºC. However, prior to pencilling any conclusion, further research about the behaviour of these materials was required. Aiming at studying the optimal cycle time, 790 ºC was the chosen temperature to proceed with this. This temperature was chosen as higher conversion and selectivity were obtained among the temperatures used.

5.2.2 Half cycle duration

Duration of the reactions may significantly affect the overall yields of the process. For instance, (Zhao *et al.*, 2014; X. Zhang, Su, *et al.*, 2020) used long cycle durations – 30 and 33 min for the CH_4 reduction and 20 and 21 min for the WS step, respectively. CH_4 conversion dropped from 90% to 45% over ten cycles for the first and was kept around 90% for the latter. Other authors (Yin *et al.*, 2021) reduced the cycling times to 20 min but conversion decreased from ~100% to 0% after 2 min of CH_4. In this case, both material and

CH_4 decomposition were observed for some of the screened OCM. Other works (Zhao, Zheng, *et al.*, 2017) conducted the process at different half reduction times, going from 3 to 20 min, observing decrease in CH_4 conversion at cycles lasting longer than 15 min.

To determine the half reduction time, 1 g of OCM (~ 5 mmol of reoxidised PBFNO-600(10)) were loaded in the reactor, emulating real CL conditions. The sample was loaded in a packed bed reactor and, similarly to Chapter 3, 5% CH_4 and 5% H_2O (both balanced in He) were flowed counter-current during 15 continuous cycles at different half-cycle duration times. All the cycles were run at 790 ºC.

Results of these tests are depicted in Figure 5.2. Three regions can be identified and are separated by blue vertical lines. The first region corresponds to the first fifteen cycles, during 60 s each half redox cycle, the second fifteen cycles, in the middle zone, lasted 48 s and finally, the last fifteen cycles were of 120 s each half cycle.

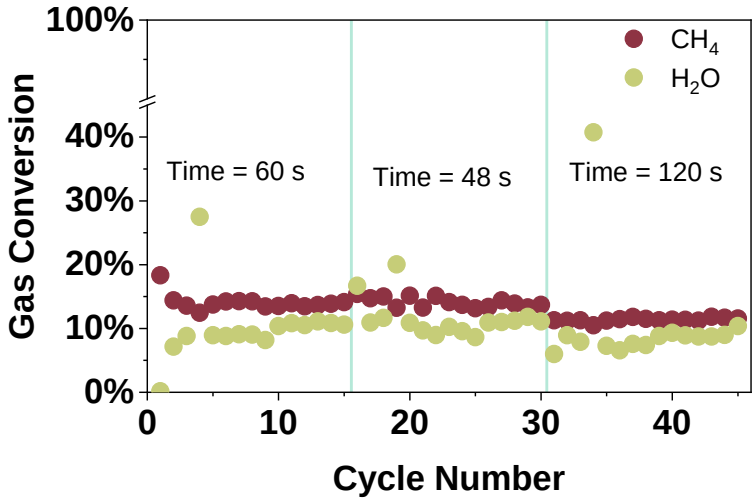

Figure 5.2. CH_4 and H_2O conversion variation for the half cycle duration time optimisation of CLSRM. Cycles were conducted at isothermal conditions (790 ºC). Gas flows were of 80 mL / min per reactant gas (5% CH_4 and 6.5% H_2O). Cycle duration was modified every 15 cycles. Three zones are identified in the graphs: forty-five redox cycles were undertaken at isothermal conditions varying the time every fifteen cycles: left region, 60 s, middle region, 48 s, right region, 120 s.

Slightly higher CH_4 and H_2O conversions (15% and 13.5%, respectively) were achieved at the second region, when half-cycles were of 48 s each. As the increment in values is very low, the increase was not considered relevant. Steady state was quickly reached in the system. Three unusual points were recorded for the H_2O conversion – one in the first region and two in the second region. These points were not attributed to the material activity but to a likely faulty of the system due to the possible presence of temporary cold spots in the

steam lines, which had to be at a constant temperature while the experiment takes place. An unexpected temperature drop while H_2O was circulated could create condensation flows. The other possible reason was the inconsistent He flow while collecting the steam from the water permeation tube prior to enter the system. This inconsistency in the He flow could be due to a higher pressure of the gas allowing for a lower than 6.5% H_2O (which is the value calibrated), therefore, less H_2O was circulated and eventually, converted, generating a higher conversion value.

Figure 5.2 illustrates how the system quickly reached steady conversion values after every cycle duration change, taking only one cycle to reach that state, indicating that the ends of the bed were in equilibrium with the feed. Approximately 12% of CH_4 and 13% of H_2O were transformed into products when half-cycle duration was of 60 s.

The short isothermal length of the furnace did not allow to load larger amounts of OCM in the reactor and eventually, increase the available oxygen. Therefore, as expected by the limited oxygen available, both CH_4 and H_2O conversion dropped when the half-cycle time was increased to 120 s. Steady state was also reached quickly, at the second cycle, as the conversion did not show any major variation throughout the 15 cycles.

Selectivity is yet another important factor to examine on CH_4 oxidation experiments. This selectivity was studied by both H_2:CO ratio (Figure 5.3.a) and syngas selectivity. The latter was studied by CO production (Figure 5.3.b). The used temperature was not high enough to promote CH_4 cracking, therefore it was assumed that all the consumed CH_4 was merely transformed either into CO or CO_2 with minimal carbon deposition. To further confirm this assertion, a carbon balance was calculated which closed at 4.95% ± 0.05 for carbonaceous products, thereby supporting this affirmation.

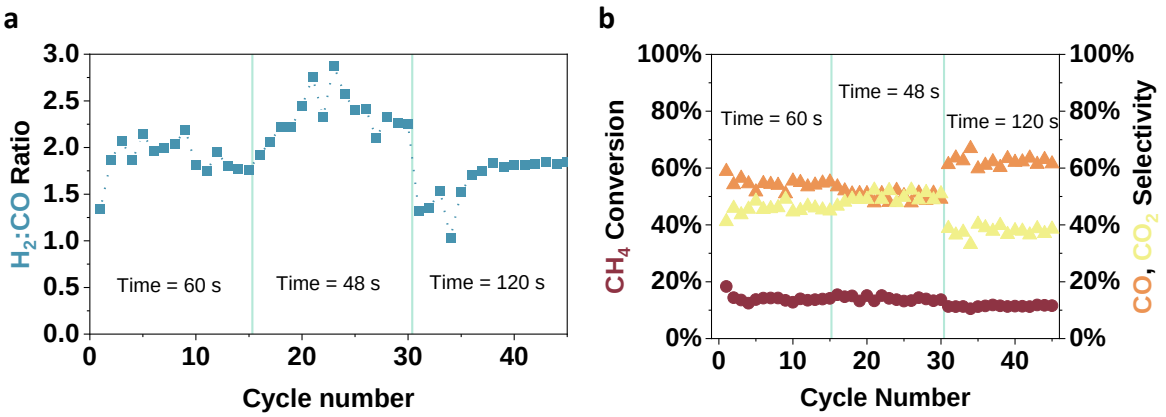

Figure 5.3. Selectivity variation for the half cycle duration time optimisation in CLSRM. Cycles were conducted at isothermal conditions (790 ºC). Gas flows were of 80 mL / min per reactant gas (5% CH_4 and 6.5% H_2O). Cycle duration was modified every 15 cycles. Three zones are identified in the graphs: forty-five redox cycles were undertaken at isothermal conditions varying the time every fifteen cycles: left region, 60 s, middle region, 48 s, right region, 120 s. **a**. Syngas (H_2:CO) ratio versus cycle number for each CH_4 half-reduction cycle. **b**. Product selectivity corresponding to the OCM reduction (CH_4 to CO and CO_2).

The first region of Figure 5.3.a (half cycle duration = 60 s) exhibited an average of 54% selectivity, higher value than the 50% average selectivity obtained when half cycle duration was of 48 s. However, two drawbacks arose. Even though shorter cycles produced more syngas per min, the purity of it was lower since it was highly mixed with combustion products (CO_2 and H_2O), see Figure 5.4.b. Secondly, upon values normalisation, there was a notable difference between the total amount of CO_2 generated during 60 s cycles and 48 s cycles: 0.011 · mmol CO_2 · g_{OCM}^{-1} · min^{-1} against 0.015 CO_2 · g_{OCM}^{-1} · min^{-1} per half cycle when the system reached steady state (see Table 5.1 for reference). Furthermore, shorter cycles meant lower syngas selectivity, as the combustion products were still in high concentration by the end of the cycles. On the other hand, while conducting cycles during 120 s, lower amounts of CO_2 per unit of time were produced, as the combustion products diminished their presence through time within the cycles, as observed in the image from Figure 5.4c. The overall amount of CO produced per half cycle showed a decrease, generating 0.010 mmol syngas · g^{-1} OCM · min^{-1}.

Table 5.1. Amount of each product quantity, calculated at the outlet of the stream.

Half-cycle duration (s)	mmol H_2/CO · g_{OCM}^{-1} · min^{-1}	mmol CO_2 · g_{OCM}^{-1} · min^{-1}	Syngas selectivity
60	0.038	0.011	54.5%
48	0.062	0.015	50.3%
120	0.010	0.005	62.3%

From Figure 5.4.a, it can be confirmed that, upon stabilisation, the cycles lasting 60 s were the ones providing a value of 1.93 ± 0.14, close to the ideal ratio of H_2:CO ~ 2.0. Cycles lasting 48 s provided a higher H_2 content, lowering the syngas quality, with a ratio of 2.34 ± 0.25 (Figure 5.4.b), higher than the ideal 2:1 ratio. Finally, the cycles conducted for 120 s initially yielded a lower-than-ideal syngas ratio (~1.5, see Figure 5.3.a) until stabilisation around an average value of approximately 1.81 ± 0.04, not as close to the ideal ratio as the cycles lasting 60 s. Figure 5.4.a-c illustrate how the products from the combustion (CO_2 and H_2O) disappear as the cycle is extended with time. Longer flow times would correspondingly result in enhanced selectivity whilst preserving a close-to-optimal syngas ratio. That said, the overall efficiency of the process would still not be high, as a large amount of CH_4 would remain unreacted. Thereby this time duration was not further considered for CLSRM application.

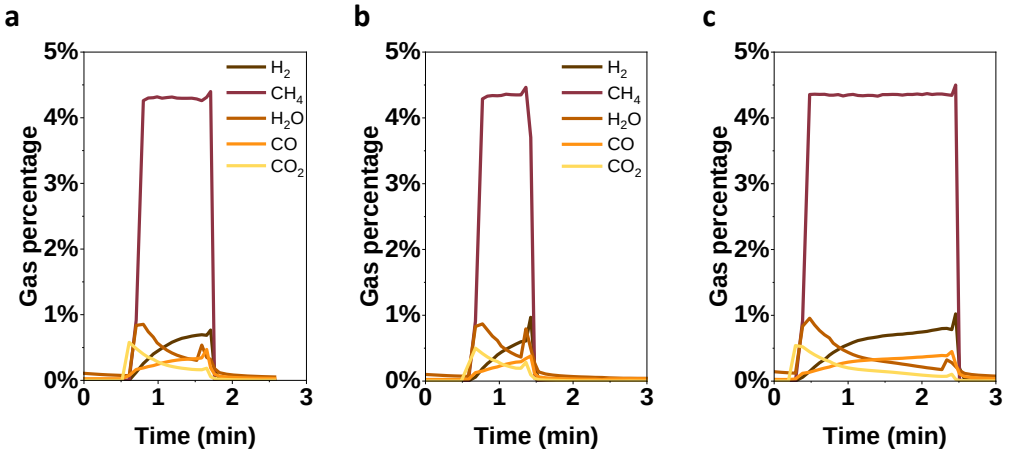

Figure 5.4. Representative shape of CH_4 conversion half-cycle CH_4. **a**, 60 s. **b**, 48 s and **c**, 120 s.

In order to achieve high purity syngas whilst minimising CO_2 production, cycles lasting 60 s were the ones providing the closest ratio (1.93 ± 0.14) to the ideal H_2:CO ratio of 2.0. Moreover, this cycle duration generated less byproducts than shorter cycles per unit of time without compromising the efficiency of the process. Therefore, half cycle duration was of 60 s for the implementation in CLSRM to study the activity and stability of the material in the long term.

5.2.3 Long term application of the exsolved system as OCM for CH_4 conversion in CLSRM

After studying the products yielded by the material during CH_4 activation in the previous chapter, the modified OCM seemed to activate the process at lower temperatures than

usual for CH_4 partial oxidation. Combustion was firstly detected at T ~ 690 ºC with a rapid formation of partial oxidation products whilst minimal combustion was observed: almost 100% syngas selectivity was observed after 10 min of reaction. Besides, selectivity seemed promising as no combustion was detected during the isothermal part of the CH_4-TPR (where T ~ 790 ºC). No carbon deposition was observed using 1% CH_4 in the early stages of the isothermal part whilst conducting the CH_4-TPR in ESRF. By using this low amount of gas, the OSC of the material was not depleted throughout the experiment.

Different scenario occurred when increasing CH_4 concentration from 1% to 5%. Temperature for CLSRM test was investigated and the conversion was not as high as exhibited for the CH_4 activation tests. It was decided to proceed at 820 ^oC. Temperatures up to 790 ºC were tested but, as CH_4 conversion was low (around 7.5%), the operational temperature was then changed, following works from Ortiz et al. (2012) or, more recently, Ding et al. (2018). Furthermore, as shown in Chapter 3, steam conversion up to 46% was achieved for the original PBFO. Short cycling times of 60 s each half cycle were chosen in this case. The aim of this test was to determine whether both high conversion and high syngas selectivity were initially achieved while conducting the experiment at temperatures lower than the state-of-the-art ones.

0.1 A-site deficient PBNFO was initially reduced for 10 h under 5% H_2 and further reoxidised under air at 600 ºC for 1 h to replenish the oxygen lattice while partially maintaining reoxidised nanoparticles on the surface. To test the OCM's stability in CLSRM, 1.29 g of this prepared material (5.6 mmol) were loaded in a packed bed reactor. Gas flow was 100 mL / min of 5% mol CH_4 and 6.5% mol H_2 both gases balanced in He.

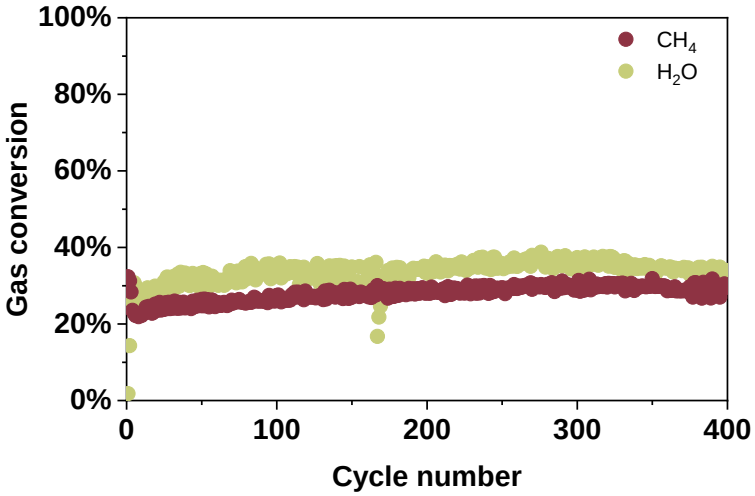

Figure 5.5. CH_4 (red) and H_2O (beige) conversion of reoxidised PBFNO-600(10) in CLSRM vs time, represented as cycle number, for 400 cycles. Half cycle duration of 60 s, gas feeds were 5% mol CH_4 and 6.5% mol H_2O, 100 mL / min.

Conversion results from the test are depicted in Figure 5.5. Initial low H_2O conversion is obtained. This is explained by the low initial OSC displayed by the material as it was replenished after the reoxidation at 600 ºC during 1 h. Later on, it achieved stable conversion values between 25% in the early cycles and 37.5% after 300 cycles. An average conversion of 33% was recorded by the end of the test. On the other hand, during the first cycles, CH_4 conversion was higher than in the rest of the test, starting at 40% until it stabilised at an overall conversion of 30%. This is due to the same reason as the low H_2O conversion – as the material had oxygen lattice replenished and NiO in the surface, it was more reactive towards CH_4 at the early stages of the cycles.

Syngas selectivity and syngas ratio were the other two parameters requiring special attention to study the efficiency of the process. Results relative to these parameters have been gathered in Figure 5.7. H_2:CO ratio is exhibited in Figure 5.7.a. Constant values close to 2.0 were shown throughout the first 300 cycles. Upon the 300th cycle, a slight increase in the value is observed. Ratio gradually shifted from 2.0 to values 2.2-2.3, with no signs of recovering the initial ideal ratio of 2. This could be attributed to CH_4 cracking (Wei et al., 2014; Hu et al., 2021). During cracking, CH_4 decomposes into solid carbon and forms higher amounts of H_2 explaining the increase in the ratio. The last reason for this could be due to an experimental issue, attributed to a pressure difference between the gas lines. This pressure difference generates gas spikes while switching valves which partially increment the gas presence at the outlet of the reactor. Further analysis of the gas outlet is required

to draw any final conclusion. Gas outlet of the 5th, 100th, 200th, 300th and 400th cycles were plotted in Figure 5.7.c-g.

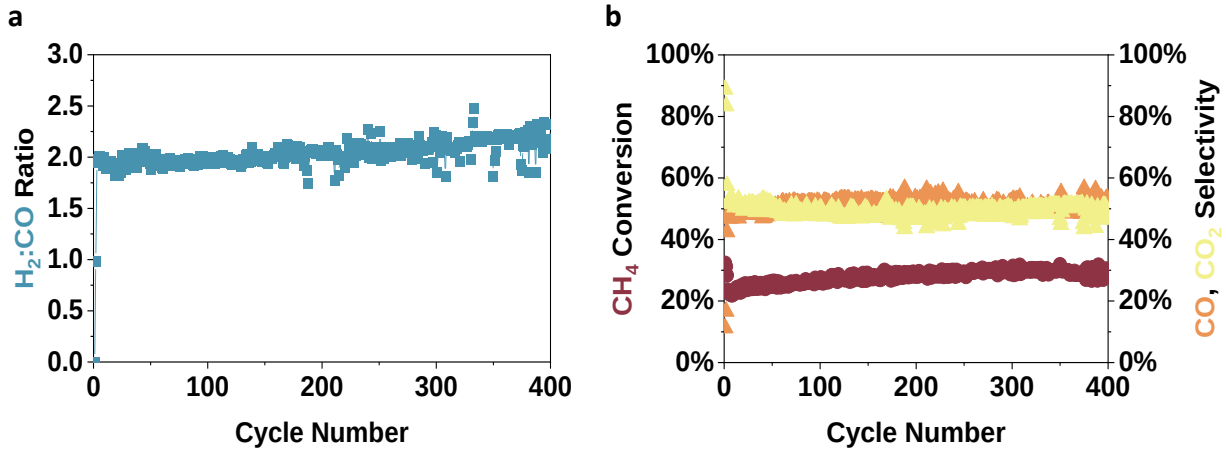

Figure 5.6. Half cycle duration time optimisation for CLSRM. **a**. Syngas (H_2:CO) ratio versus cycle number for each half-reduction cycle. **b**. Product selectivity corresponding to the OCM reduction (CH_4 to CO and CO_2).

Figure 5.7 show that the system is cyclable through a large number (400 cycles) of redox cycles and no signs of degradation are detected with cycles and time on stream at high temperatures. CH_4 reacted initially with the surface oxygen, promoting combustion (CO_2 + H_2O) (Zhao, Li, *et al.*, 2017). No CO_2 increase was noticeable, indicating that all the surface oxygen was consumed Secondly, no CO underwent the Boudouard reaction generating CO_2. CH_4 conversion was stable throughout the half cycle with no significant changes in the increasing trend of syngas formation. The last hypothesis is indeed the reason of the small increase in H_2:CO ratio. A pressure gas was created in the rig after several cycles, causing the gas spikes mentioned, being of higher intensity for H_2. The increase in H_2:CO ratio is therefore explained, and it can be read as a constant value of ~ 2.0. This gas spike was evidenced in Figure 5.7.c, upon the 200th cycle. The pressure difference between lines is attributed to the likely low amount of the CH_4 cylinder connected to the system, which generated gas fluctuations. On the other hand, an increasing conversion in the WS half-cycle is observed, as previously explained in Figure 5.5. This growth achieved a steady conversion value after the 200th cycle, where the H_2 molar fraction seems stable.

Gases followed the same conversion trend as the results from the previous chapter whilst activating CH_4: a small production of CO_2 and H_2O as result of the initial CH_4 combustion followed by the formation of CO and H_2O. Syngas formation increased as combustion products diminished their presence, without affecting at the total CH_4 conversion. CH_4

conversion remained constant, not higher than 32%, in the best of cases. This was evidenced by closely observing the shape of the CH_4 curve in Figure 5.7.a-e, with a constant molar fraction and no signs of decreasing by the end of the half-reaction. This was also unveiled by the curves of both H_2 and CO. They exhibited a steep growth until half of the reaction time (30 s) was consumed. Upon this instant, both curves flattened, indicating a slower syngas formation and no higher CH_4 conversion rates. Thus, based on these results and the ones from Chapter 4, there is no evidence that longer cycle times will generate higher CH_4 conversion. Longer half-cycle times will indeed enhance the selectivity, as the combustion products tends to zero, but not the conversion generated by these OCM. CO_2 will continuously be generated as it is generally favoured when large amounts of Fe are present within the system, according to Zhu et al. (2013).

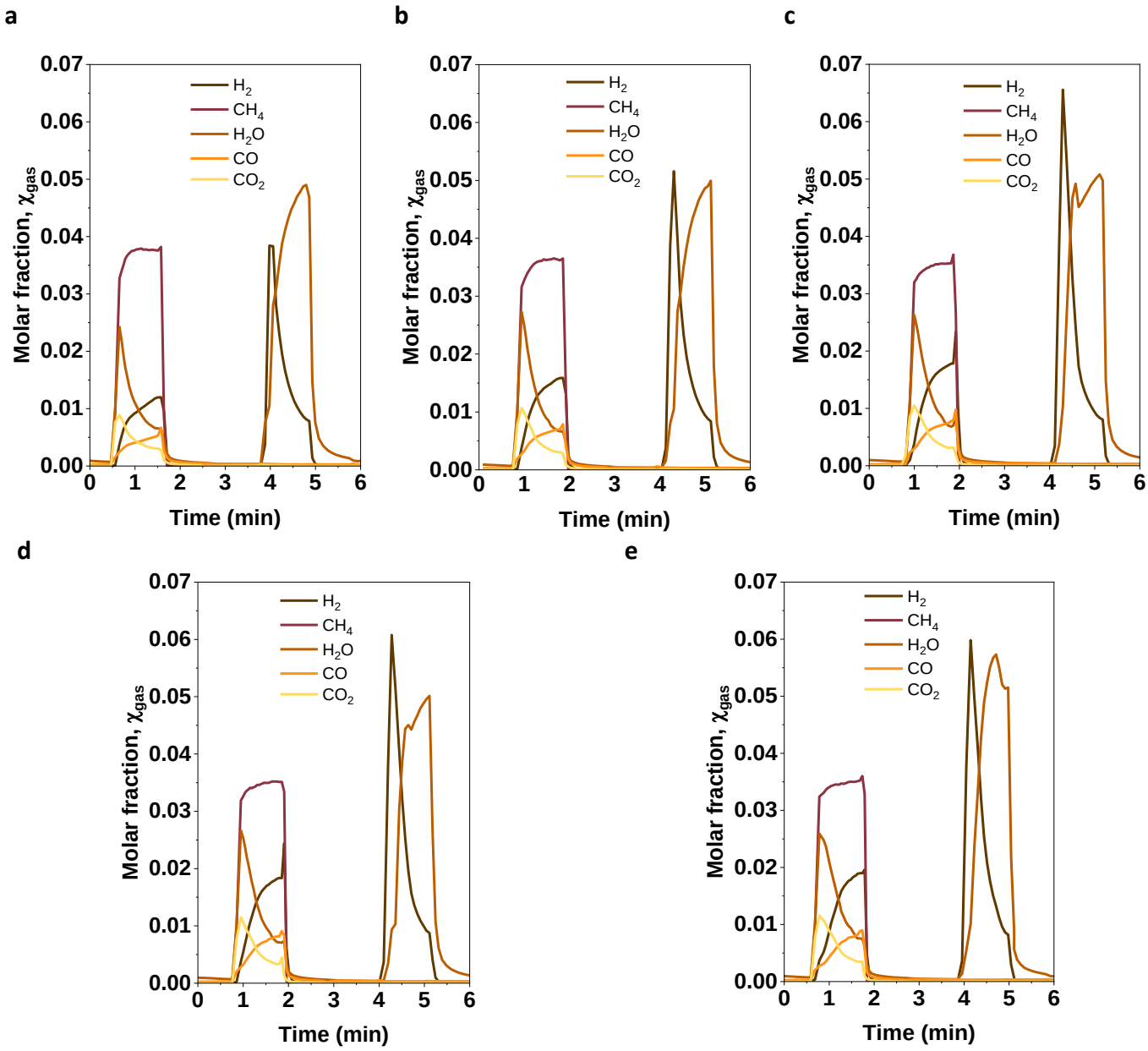

Figure 5.7. Outlet composition vs time for the long-term experiment for PBFO. **a**. 5th cycle, **b**. 100th cycle, **c**, 200th cycle, **d**. 300th cycle **e**. 400th cycle. Gas flow used: 5% CH_4 and 6.5% H_2O, both balanced in He.

At the steady conversion value at the 300th cycle, these OCM produced an average of 0.071 mmol syngas · g^{-1} OCM · min^{-1} while flowing 100 mL / min of 5% CH_4. Previous studies have reported high selective CH_4 activation towards syngas. For instance, Yang et al. (2024) used exsolved Fe from a LaSrFe(Al)O matrix with a 30 mL / min flow of 10% CH_4 and recently achieved 87% CH_4, almost 100% CO selectivity and a H_2:CO ratio of ~ 2.16 through the 20 cycles they performed. They reported an increasing H_2:CO slope as the looping cycles progressed, indicating this would represent CH_4 cracking for some of the Fe-based OCM they tested. In addition, they reported an average syngas ranging from 1.44 to 0.678 mmol syngas · g^{-1} OCM · min^{-1}, values up to 20 times higher than the ones obtained with PBFNO. In exchange, they observed partial decomposition of the used materials into other secondary phases which might have caused the CH_4 cracking. Kim et al. (2023) observed the effects of including Ir-doping and exsolution on $LaFeO_3$ for CLSRM, confirming the benefits of metal-doping Fe-based OCM for this process. They conducted cycles in a TGA and reported a 20% increase in conversion when Ir was used, whilst coking was reduced to a minimum extent at T ~ 750 ºC. Besides, they reported no combustion products formation and a H_2:CO ratio ~ 1.9, close to the ideal syngas ratio. Syngas production was of 2.03 mmol syngas · g_{OCM}^{-1} · min^{-1}, which is higher than the reported values in this chapter. The products obtained with PBFNO-600(10) fall under the range of values presented.

The low syngas yields can be explained by the lower-than-average temperature used here (790 ^{o}C during time optimisation and 820 ^{o}C during the experiments), as other authors such as Li, Xu, Gu, et al. (2020), reported temperatures higher than 850 for the same experiment with better yields. The low yield can also be explained by the role of the oxygen vacancies. A fully replenished oxygen lattice generates CO_2 as product when activating CH_4 (Cheng *et al.*, 2016). This CO_2 will eventually form oxygen vacancies in the material to promote syngas formation. A poor or depleted lattice oxygen during the CH_4 activation leads to favour syngas as product over combustion products (X. Zhang, Su, *et al.*, 2020) The reoxidation step, which has generated 0.22 mmol H_2 every half cycle in average, fully replenished the oxygen vacancies, continuously promoting the formation of CO_2. However, after observing the continuous low CH_4 conversion rates, it can be said that the OCM presented here possessed a lower OSC than expected whilst conducting the initial experiments of CH_4 activation in Chapter 4.

5.3. Summary of Chapter 5

Previous results unveiled CH_4 activation by the Ni-doped OCM after undergoing exsolution conditions, showcasing almost 100% syngas selectivity and maintaining a close to ideal H_2:CO ratio, at lower operational temperatures than the state-of-the-art ones (we observed activity at 690 ºC and high selectivity at T ~ 750 ºC, whilst temperatures are typically T > 800 ºC). Even though the OCM displayed activity, an initial test was conducted to decide on the operational temperature for real CLSRM conditions. Lower-than-average temperatures did not show high activity, with CH_4 conversion not higher than 8%. WS as OCM half-oxidation reaction did not show high conversion rates either, as it requires from higher temperatures, as we studied in Chapter 3. Therefore, it was decided to conduct the CL at 820 ºC, to ensure that the materials would display higher conversions.

A preliminary study was also undertaken regarding the half-cycle duration time. The obtained results suggested that a balanced yield was achieved at cycles lasting 60 s. Even though shorter cycles (48 s) generated larger amounts of syngas per unit of time, its purity was not as high as longer cycles.

Lastly, a similar test to the one conducted in Chapter 3 was carried out. In order to study the material's stability while efficiently generating syngas, the previously exsolved and further reoxidised OCM was loaded in the reactor. 400 cycles of 5% CH_4 and 6.5% H_2O, 1 min each half-cycle, were run at 820 ºC. CH_4 conversion values were similar to the ones recorded in previous results in Chapter 4, where CH_4 achieved up to 30-35% conversion. Syngas formation was constantly around the ideal value of 2.0, despite the low syngas formation, which was not as high as exhibited in preliminary tests. Lower selectivity was achieved, as the material's surface was constantly replenished with oxygen during the oxidation with H_2O. This surface oxygen typically promotes CO_2 formation when CH_4. This fact, combined to a high Fe content, lowers the selectivity towards CO formation and therefore, syngas as main product.

In conclusion, the developed and Ni-doped materials deployed good initial conversion in the process of CH_4 activation. As stated in the previous chapter, Ni-doping and exsolution proved a significant enhancement of the material. Over 400 CLSRM cycles, the OCM remained indeed stable, as it kept a continuous H_2:CO ratio and no signs of CH_4 or H_2O conversion decay. Furthermore, carbon deposition was not detected. On the other hand,

syngas selectivity was not as high as expected under CL conditions, maintaining a constant 50-55% syngas selectivity. The OCM does not possess the needed oxygen capacity, or the selectivity expected. As it will be further demonstrated, this low selectivity or oxygen capacity did not stop the development and application of the material in other processes.

Chapter 6 Further applications of the designed OCM

This thesis is mainly focused on the design and synthesis of oxygen-deficient OCM. Following their full characterisation, their reactivity was testing, highlighting their potential for efficient activity in CLWGS and effective CH_4 with high selectivity towards syngas at lower-than-average temperatures.

Building upon this foundation, this chapter aims to extend the scope of application of these materials by exploring their implementation in catalytic reverse Water-Gas Shift (rWGS). The objective was to enhance the selectivity and stability of catalysts applied in CO_2 hydrogenation for CO production. Oxygen-vacant tailored materials were used while exsolution conditions were applied to promote the said selectivity.

The results of this chapter were published in *Journal of CO_2 Utilisation*, co-authored by Alex Martinez Martin and Shailza Saini, where the sections corresponding to the collaborative work conducted by the latter at University of Surrey are quoted and explicitly attributed and referenced to maintain text integrity. All the images displayed in this chapter are courtesy of Martinez Martin et al.(2024).

The parts relative to the PXRD data analysis have been integrally conducted by myself whilst the parts relative to the XPS data analysis have been integrally by the other first author. The rest of the work has been reformulated as it corresponds to a joint work in which both authors have taken place.

6.1. Introduction

The conception of CO_2 as a precursor for production of fuels or its use in the food or pharmaceutical industries (Mikkelsen, Jørgensen and Krebs, 2010), rather than a byproduct from chemical processes could be the key to transform the energy and chemical sectors whilst contributing to the reduction of greenhouse gases emissions. CO_2 hydrogenation reactions, particularly rWGS (Eq 6.1) is of interest as CO generated as one of the products can be used as a building block to generate high-added- value chemicals, such as synthetic fuels or methanol (Wu *et al.*, 2021).

$$CO_2 + H_2 \rightleftharpoons CO + H_2O, \Delta H^0_{298} = 42.1\ kJ\ /\ mol \qquad \text{Eq 6.1}$$

Its endothermic nature results in the existence of side reactions, such as the formation of CH_4 and the conversion of CO_2 strongly depends on reaction conditions, such as high temperatures. Lower temperatures generally imply CH_4 formation and consequently, additional steps to separate products. According to Opitz et al. (2020), when designing catalysts, a balance between oxygen vacancies and metallic active sites is required. In particular, the amount of surface oxygen vacancies gain attention when seeking high CO selectivity. CO_2 activation is believed to occur in these oxygen lattice vacancies, as they serve as promoters of C=O bond dissociation from CO_2 and CO formation (González-Castaño, Dorneanu and Arellano-García, 2021), whilst active sites on the surface activate H_2 are required. The high temperatures needed to achieve high CO selectivity in the process often deteriorate the catalyst by contributing sintering and carbon deposition (Loiland *et al.*, 2016; González-Castaño, Dorneanu and Arellano-García, 2021; Pahija *et al.*, 2022). Current research in rWGS is focused on the design and preparation of scalable catalysts that provide high CO selectivity whilst avoiding deactivation processes. Even though they tend to be avoided given their high cost and low abundance (Vieira *et al.*, 2023), noble metals are an alternative solution thanks to the high reactivity they provide (Oshima *et al.*, 2014; Kattel *et al.*, 2016). Transition metals tend to be use instead, being the primary focus on Fe-based systems (Pastor-Pérez *et al.*, 2018; Sengupta *et al.*, 2019; Lindenthal *et al.*, 2021) and Cu-based systems (Jurković *et al.*, 2017; Zhang *et al.*, 2017; González-Castaño, Dorneanu and Arellano-García, 2021; Liu *et al.*, 2022). Other materials, such as Ni-based systems tend to be more stable than the previous ones mentioned even though they report higher CH_4 formation (Wang, Zhang and Liu, 2008; Wang *et al.*, 2013; F. M. Sun *et al.*, 2015).

As stated in previous chapters, perovskites have become of general interests thanks to their tailorability, as they can easily form oxygen vacancies and defects or adopt different metals in their lattice (Shin *et al.*, 2012; Lindenthal *et al.*, 2020). These adaptations can target different chemical processes. Perovskites also serve as the matrix for nanoparticles exsolution matrixes. Exsolution has emerged recently helping to overcome some of the challenges explained before. Exsolution has helped to generate highly stable and durable catalysts as reported by several authors (Kwon *et al.*, 2020; Islam *et al.*, 2021; Kousi *et al.*, 2021; Neagu *et al.*, 2023; Sun *et al.*, 2023). The exsolved nanoparticles are less prone to carbon formation and provide the material with higher thermal stability and/or activity for longer periods than other traditional synthesis methods (Zubenko, Singh and Rosen, 2017;

Otto *et al.*, 2019). Exsolution of nanoparticles has also been implemented previously in rWGS, where high CO selectivity through extended reaction time has been reported (Lindenthal *et al.*, 2021; Orsini *et al.*, 2023; Zhou *et al.*, 2023). However, this research is still in a very early stage and more investigation is needed in this area.

Here, a set of perovskites previously presented in Chapter 3 have been designed and used for the hydrogenation of CO_2 via rWGS. The partial substitution in the A-site (Pr and Sm), and Ni-dope have been done in an attempt to understand the formation and effect of oxygen vacancies in CO_2 hydrogenation. Exsolution has also been implemented to produce FeNi alloys that minimise the formation of by-products, leading to ideal selectivity. Different characterisation techniques have been used to fully characterise these materials. Some of them have been previously described, such as synchrotron PXRD, SEM or TGA. Other techniques, such as X-ray photoelectron spectroscopy (XPS) will be further explained.

6.2. Experimental

$Ln_{0.5}Ba_{0.5}Fe_{1-x}Ni_xO_3$ (Ln = Pr, Sm; and x = 0, 0.1) were prepared following the procedure described in Chapter 2. Final compounds were $Pr_{0.5}Ba_{0.5}FeO_{0.5}$ (PBFO) $Pr_{0.5}Ba_{0.5}Fe_{0.9}Ni_{0.1}O_{3-\delta}$ (PBFNO), $Sm_{0.5}Ba_{0.5}FeO_{3-\delta}$ (SBFO) and $Sm_{0.5}Ba_{0.5}Fe_{0.9}Ni_{0.1}O_{3-\delta}$ (SBFNO). To promote nanoparticles exsolution, the sintered powders were reduced under 100 mL / min of 5% H_2 balanced in Ar for 10 h at 900 ºC. The reduced catalysts are denoted as *r*-PBFO, *r*-PBFNO, *r*-SBFO and *r*-SBFNO. Following this reduction, catalysts were also reoxidised under air at 600 ºC for 1 h and reduced again under 5% H_2 balanced in Ar *in situ* for 30 min at 600 ºC. All the heating rates were set to 5 ºC / min. Catalysts undergone this pre-treatment are named as *ra*-PBFO, *ra*-PBFNO, *ra*-SBFO, *ra*-SBFNO.

Synchrotron PXRD was conducted to study the crystal structure and Rietveld refinement was carried out using TOPAS Academic v7. Parameters refined were background, thermal displacement, atomic coordinates, unit cell values and peak shapes. Atoms sum occupancies in the A- and B-site were set to unity, respectively. Iodometric titrations were conducted to study oxygen content. Surface properties of the catalysts was studied via SEM. Images were taken at low voltage, 2 kV, with a working distance of 4 mm and magnification ranging from 10000 to 50000. Images were analysed with Image J for particle size and distribution "XPS analyses were performed on a Thermo Fisher Scientific (East

Grinstead, UK) K-Alpha+ 127 spectrometer. XPS spectra were acquired using a monochromated Al Kα X-ray source (h = 1486.6128 eV). An X-ray spot of ~400 µm radius was employed. Survey spectra were acquired employing a Pass Energy of 200 eV. High resolution, core level spectra for all elements were acquired with a Pass Energy of 50 eV. All high-resolution core level spectra were charge referenced against the C1s peak at 285 eV to correct for charging effects during acquisition. Quantitative surface chemical analyses were calculated from the high resolution, core level spectra following the removal of a non-linear (Shirley) background. The manufacturers Avantage software was used which incorporates the appropriate sensitivity factors and corrects for the electron energy analyser transmission function." [1]

Catalytic tests were done by loading 1 mmol of catalyst in the middle of a fixed-bed reactor, with a powder length of 1 cm. After a thorough screening of different H_2:CO_2 ratio feeds ranging from 1:1 to 4:1, it was decided to proceed with 2:1 ratio as optimal selectivity was obtained. Temperatures varied from 400 and 750 ºC in 50 ºC increments holding each temperature until stabilisation. 1 atm was used as working pressure. Equations to calculate conversion and selectivity are provided below in Eq 6.2 to Eq 6.4:

$$CO_2\ conversion\ (\%) = \frac{[CO_2]_{in} - [CO_2]_{out}}{[CO_2]_{out}} \quad \text{Eq 6.2}$$

$$CO\ selectivity\ (\%) = \frac{[CO]_{out}}{[CO_2]_{in} - [CO_2]_{out}} \quad \text{Eq 6.3}$$

$$CH_4\ selectivity\ (\%) = \frac{[CH_4]_{out}}{[CO_2]_{in} - [CO_2]_{out}} \quad \text{Eq 6.4}$$

Initial CO_2 concentration was named as $[CO_2]_{in}$, whilst the unreacted CO_2, and CO and CH_4 as formed products were measured and denoted as $[CO_2]_{out}$, $[CO]_{out}$ and $[CH_4]_{out}$, respectively.

Lastly, the thermodynamic limits of rWGS were calculated and used as benchmark for further comparison with our experimental results. For this, the ChemCad software package from ChemStation was used. "The Soave-Redlich-Kwong equation of state was implemented in a Gibbs reactor, and the material flows were set to match those intended for the experimentation."

[1] Quoted text is integrally taken from the original manuscript published in *Journal of CO_2 Utilisation*. This distinction between reformulated and quoted text is intended to split the works conducted by myself at Newcastle University and Shailza Saini, co-author, at University of Surrey.

6.3. Materials design principles

Perovskite oxides generally possess an ABO_3 structure in which the A-site is typically occupied by a lanthanide (or rare-earth metal) or an alkaline-earth metal, providing resistance to the high temperatures (Lindenthal *et al.*, 2021; Liu *et al.*, 2022) and the oxygen vacancies for CO_2 activation (Ban *et al.*, 2014) and the B-site is usually occupied by a transition metal, which tends to be the active metal towards H_2 reactivity. The amount of oxygen vacancies in a perovskite relies on the cations' nature and their ratio in A-site and B-site positions. To understand this relationship, Pr^{3+} and Sm^{3+} were selected as partial substitutes of Ba^{2+} in the A-site (see Figure 6.1.a). Ba^{2+} is well known to provide oxygen mobility within the perovskite lattice (Song, Ning and Bouwmeester, 2020). The slightly smaller cationic radius of Sm^{3+} relative to Pr^{3+} (Volkova *et al.*, 2019), needs more energy to form the rare-earth metal-oxygen bond, possibly providing the catalyst with a larger amount of initial oxygen vacancies. Fe^{3+} is a typical transition metal used in rWGS due to its high activity for this catalytic process (Pastor-Pérez *et al.*, 2018) so it was therefore chosen as the main metal of the B-site. The incorporation of Ni as dopant in the B-site (Figure 6.1.b) was done to promote both the presence of oxygen vacancies due to its lower charge (2+) as compared to Fe (3+) and the expected formation of a FeNi alloy. FeNi alloys have positively impacted the selectivity in previous processes (Y. F. Sun *et al.*, 2015; Papargyriou, Miller and Irvine, 2019). Ultimately, the presence of Ni enhances the exsolution due to its higher segregation energy, according to Tang et al. (2021).

6.4. Synthesising Fe-based perovskites tailored at the A and B site; crystal structure, oxygen content and microstructure

The results of this PXRD were already presented in Chapter 3 (now in Figure 6.1.b), where only *Pm-3m* cubic phases were detected and the refinement (Figure 6.1.c) confirmed their presence. The difference between A-site cationic radii was previously explained in Chapter 3. However, the effects of the vacancies were not explained and attributed to the CO_2 reactivity. The Sm-based material exhibited a larger number of oxygen vacancies than the Pr-based (Figure 6.1.d) due to the smaller size of Sm^{3+}, as compared to Pr^{3+}. This difference implied that SBFO could exhibit higher CO_2 activation capabilities. When exploring the microstructure by SEM (Figure 6.1.e-f), PBFO showcases larger grain size and higher porosity than its Sm-based analogue, SBFO. The existence of smaller grain size and

therefore, higher surface area, supports the idea of SBFO as a better sample since higher exsolution extent could be achieved.

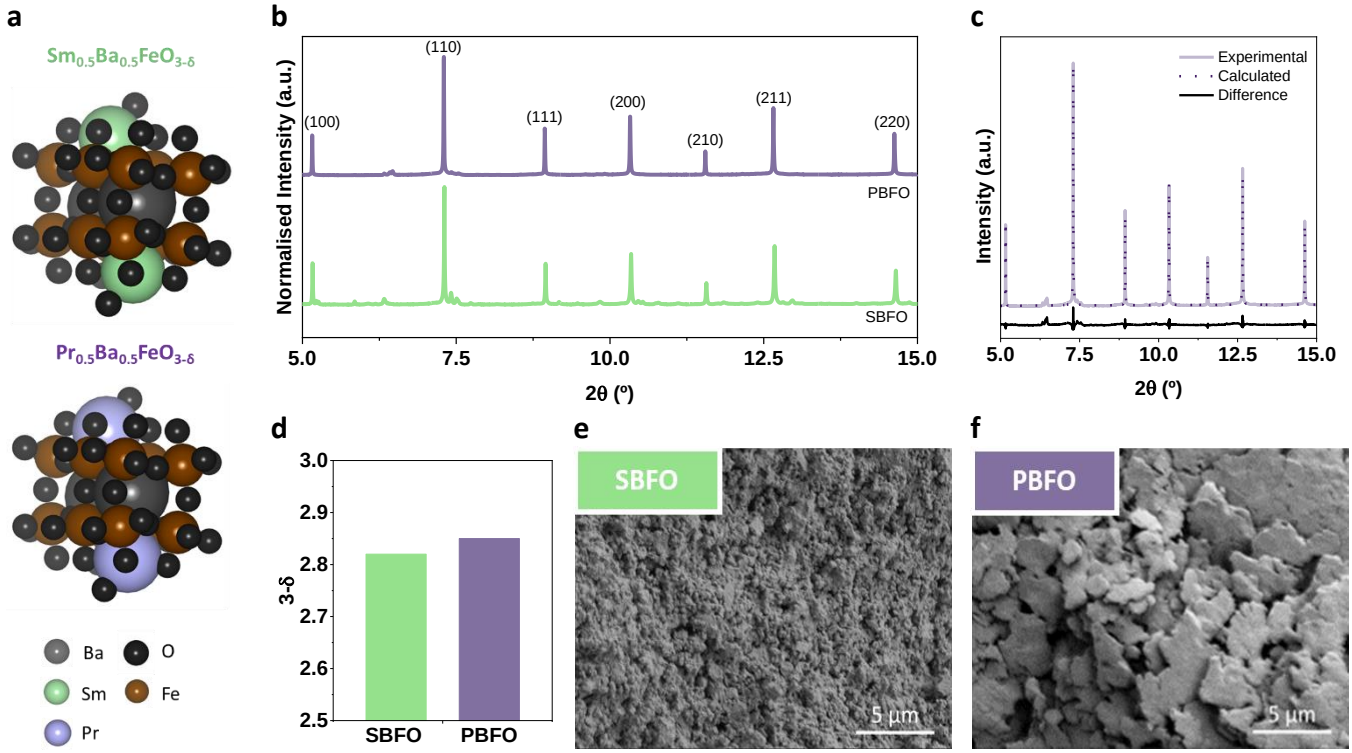

Figure 6.1. Characterisation of A-site tailored ferrites. a) Schematic of the crystal structure $Sm_{0.5}Ba_{0.5}FeO_3$ (SBFO, top) and $Pr_{0.5}Ba_{0.5}FeO_3$ (PBFO, bottom). Visible difference in cationic size is represented by green (smaller, Sm) and purple (larger, Pr) cations. **b)** Synchrotron X-Ray patterns of the *as sintered* PXRD patterns of the *as sintered* samples. hkl indexing corresponding to the perovskite phase on top of each peak. **c)** Example of Rietveld refinement of a single-phase perovskite. **d)** Oxygen non-stoichiometry of *as sintered* SBFO and PBFO, calculated by iodometric titration. Microstructure, by SEM images of *as sintered* SBFO, **e)** and PBFO, **f)**.

While only a *Pm-3m* cubic phase was detected for PBFNO, two symmetry groups coexisted however for SBFNO, confirmed by the lack of symmetric peaks displayed in Figure 6.2.c, beyond an additional secondary phase. These two SBFNO phases correspond to a *Pm-3m* cubic phase (69.0% of presence) and to a *P4/mmm* tetragonal phase (27.7% of presence). The additional secondary phase corresponds to a $SmFeO_3$ orthorhombic phase (3.3% of total contribution to the model). The calculations of the pseudo-cubic cell parameter of SBFNO (3.696 Å) also confirmed the existence of different symmetry groups, as compared to its non Ni-doped analogue (3.929 Å). This variation is attributed to the distortion caused by the combined effect of both the smaller size of Sm^{3+} compared to Pr^{3+} (1.079 Å and 1.179 Å, respectively) and the incorporation of Ni^{2+} within the B-site. Once all the PXRD pattern peaks have been attributed, the successful incorporation of Ni^{2+} into the lattice is confirmed. As the B-substitution is minimal and the cationic radii of Fe^{3+} and Ni^{2+} are

relatively close (0.645 Å and 0.69 Å, respectively), the overall distortion of the lattice results minimal, maintaining the cubic phase as main phase of the perovskite. Lastly, whilst a very similar microstructure is retained for SBFNO as compared to its non Ni-doped equivalent, the microstructure of PBFNO resembles now to SBFNO and SBFO rather than to PBFO.

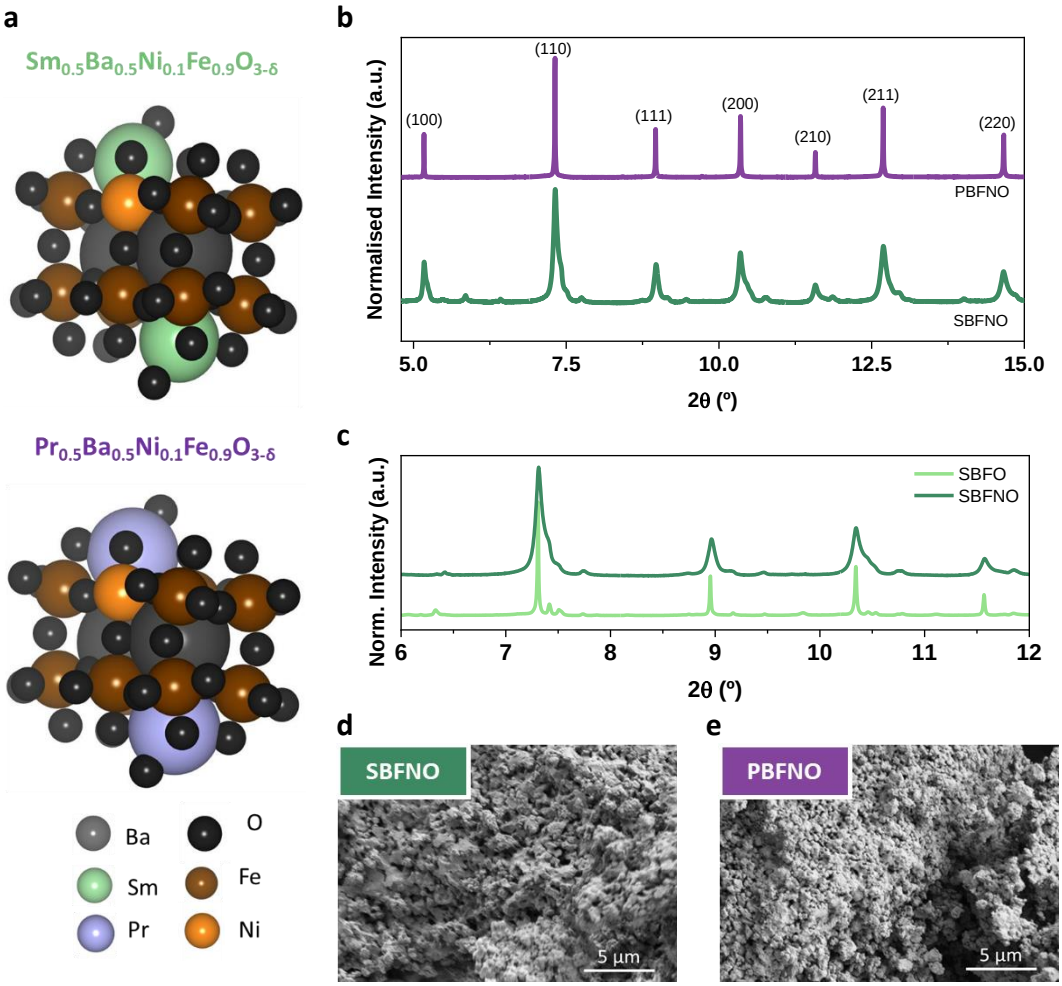

Figure 6.2. Characterisation of B-site Ni-doped ferrites. **a.** Schematic depicting the substitution of both the A and B-site in a $BaFeO_{3-\delta}$. Visible difference in cationic size is represented by green (smaller, Sm) and purple (larger, Pr) cations. **b.** Synchrotron X-ray patterns of the *as sintered* samples. hkl indexing corresponding to the perovskite cubic phase on top of each peak. Superposition of SBFO and SBFNO for observation of peaks shape variation, **c**. Catalysts microstructure, represented by SEM images of as-sintered SBFO, **d.** and PBFO, **e**.

6.5. Reducing the as synthesised materials; exsolution

Surface metallic active sites were achieved by reducing the materials under 5% H_2 during 10 h at 900 ºC. SEM images were taken and displayed in Figure 6.3.a-d, and are named as *r*-SBFO, *r*-SBFNO, *r*-PBFO, and *r*-PBFNO. Reduction at high temperature of non Ni-doped catalysts results in partial decomposition of the perovskites and uncontrolled segregation,

as exhibited in the SEM images of Figure 6.3.a,c. Particles segregation, with a particle size of ~ 200 nm is attributed to Fe. Uncontrolled segregation has been observed in exsolved Fe nanoparticles in previous studies (Jo *et al.*, 2022; Santaya *et al.*, 2023), instead of forming the typical "socketed" nanoparticle structure. XPS confirmed the presence of Fe particles, given in Figure 6.3.i-j.

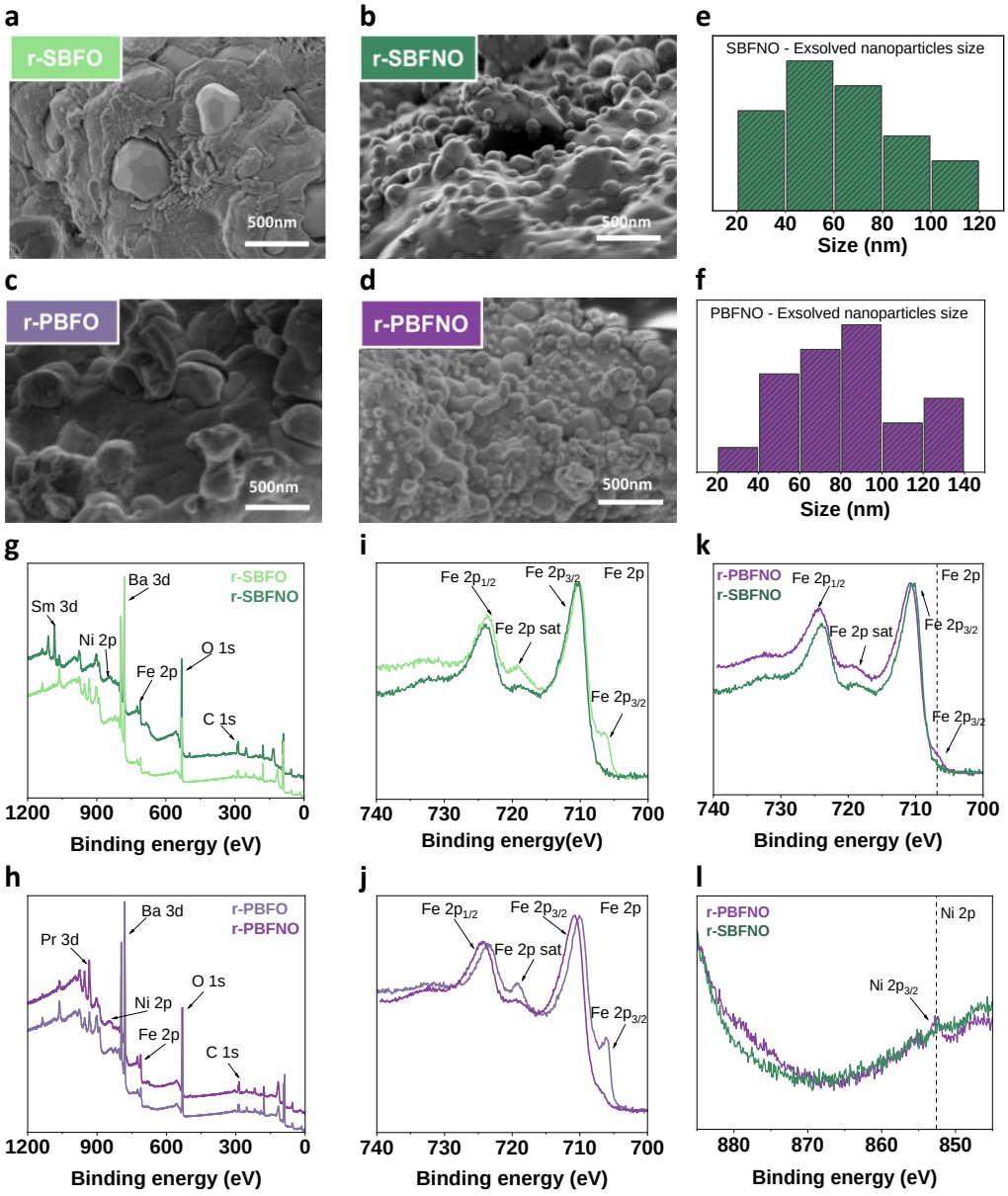

Figure 6.3. Reducing the as-synthesised materials SEM images of catalysts after being reduced at 900 ºC for 10 h. In order, *r*-SBFO, *r*-SBFNO, *r*-PBFO, *r*-PBFNO **a-d**. Particle distribution size for Ni-doped catalysts SBFNO, **e**, PBNFO, **f**. XPS survey spectra of *r*-SBFO and *r*-SBFNO **g,** *r*-PBFO and *r*-PBFNO catalysts. **i**. Fe 2p of Sm-based catalysts **j.** Fe 2p of Pr-based catalysts and Ni 2p, **k** and **l** for both reduced samples.

Contrarily to this uncontrolled Fe segregation, partial substitution of Fe with Ni (10 wt.%) generates a more controlled segregation of nanoparticles. Ni-doping causes lower

segregation energy, reducing the overall energy demand for cation exsolution, possibly promoting the Fe to exsolve alongside and form metallic nanoparticles (Ding *et al.*, 2020). These particles were believed to be FeNi alloys, as confirmed in Chapter 4, as Fe and Ni have been demonstrated previously to exsolve whilst forming this structure (Y. F. Sun *et al.*, 2015; Du *et al.*, 2016; Liu, Liu and Luo, 2016). "To further verify the nature of the in-situ exsolved nanoparticles as bimetallic Fe-Ni alloys, XPS was employed to analyse the materials' surface chemistry (Figure 6.3.g-j). Based on analysing the XPS spectra, the peak located at the binding energy (BE) ~707 eV in Figure 6.3.k is attributed to metallic iron (Fe^0) (Biesinger *et al.*, 2011). The peak position at ~709 eV and ~723 eV represents a doublet of Fe $2p_{3/2}$ and $2p_{1/2}$ orbital and the precise positioning of the satellite peaks associated with these Fe peaks is highly sensitive to oxidation states. The satellite peak of Fe $2p_{3/2}$ suggests a Fe^{3+} oxidation state for the iron in the materials (Yamashita and Hayes, 2008). The higher peak of the Fe $2p_{3/2}$ as compared to the Fe $2p_{1/2}$ peak arises due to spin-orbit coupling. XPS also confirmed the presence of Ni (see peak at ~852.6 eV Figure 6.3.j), corresponding to the Ni $2p_{3/2}$ orbital of metallic Ni (Wan *et al.*, 2019). However, the peak intensity is relatively low due to the limited concentration of the dopant and the even lower % of Ni exsolving overall. Interestingly, a slight shift in these BE was observed as compared to the non-Ni doped samples as seen in Figure 6.3 i-j. Specifically, for the Ni-doped samples, a shift of the whole Fe spectra towards higher values is observed. This suggests a potential electronic interaction between these neighbouring atoms involving a partial charge transfer ($Fe^{3+} \rightarrow Ni^{2+}$). This bimetallic interaction could imply the formation of the Fe-Ni alloy nanoparticles (Liu, Liu and Luo, 2016; Gupta *et al.*, 2024). The Fe-Ni alloy nanoparticle size distribution for both the samples is quite wide, ranging from 40-80 nm for the Sm sample and 40-100 nm for the Pr sample (Figure 6.3e and f). This behaviour is characteristic of the reversible type of exsolution that happens when A-site stochiometric samples are used (Neagu et al., 2013)."

6.6. Catalytic activity of the new catalysts in rWGS

CO_2 conversion results are depicted in Figure 6.4. As expected, higher CO_2 conversion was achieved at higher temperatures with the four studied catalysts Figure 6.6.a-b. *r*-SBFO achieved the highest conversion values once temperature reached 550 ºC. At T = 700 ºC, maximum CO_2 conversion, 56%, was achieved, and conversion remained very close to the thermodynamic equilibrium when T > 600 ºC. Contrarily to expectations, Ni-doped

catalysts did not exhibit higher reaction rates than the non-doped equivalents. Reactivity trend was *r*-SBFO > *r*-PBFO > *r*-PBFNO > *r*-SBFNO, describing that reduced Ni-doped samples were not as active. One would think that Ni-doping promotes the formation of additional oxygen vacancies that activate CO_2 (Lindenthal *et al.*, 2021). However, this did not occur. The reason for this might be caused by an unbalanced oxygen vacancies formation.

With this type of catalysts, possessing reducible supports, tend to follow a Mars-van Krevelen (MvK) mechanism (Opitz *et al.*, 2020). For this, oxygen vacancies are needed for CO_2 activation providing the lattice with labile oxygen atoms upon the formation of CO. On the other hand, H_2 needs to be activated by a metal (Fe in this case) to react with the labile oxygen released by CO_2, to form H_2. This H_2 activation is believed to be the rate-limiting step of the rWGS process, according to Opitz et al. (2020). The better rates of *r*-SBFO compared to *r*-PBFO can be explained by the larger amount of oxygen vacancies present in the Sm-based one, as described above. It is possible that even though Ni provides an additional amount of oxygen vacancies to the system, its exsolution depletes the material of lattice oxygen, being therefore less active, as also described by Opitz et al. (2020). Both Ni-doped catalysts underwent this trend.

When studying selectivity, at low temperatures (400 ºC < T < 500 ºC), 25% higher CO selectivity increases is noticed for *r*-SBFNO as compared to *r*-SBFO (75% vs 50%, respectively). At this temperature range, CH_4 formation, which is typically favoured, was minimised, reaching even 100% selectivity upon high temperatures. Analogously to Sm-based catalysts, Pr-based and Ni-doped materials showcased a similar trend. CH_4 was minimised, favouring the formation of CO. This high selectivity is indeed due to the formation of the FeNi alloy.

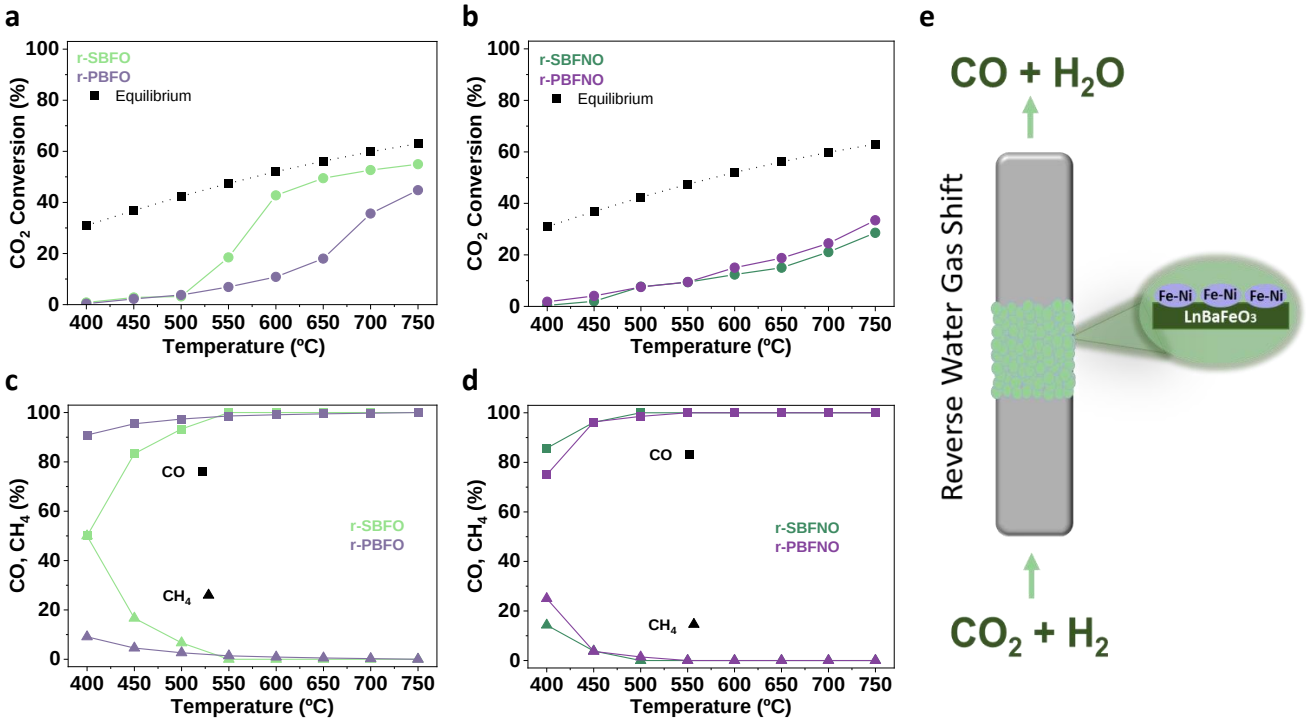

Figure 6.4. Employing the newly prepared ferrites in rWGS. CO_2 conversion with temperature for reduced SBFO and PBFO **a.** and reduced Ni-doped counterparts **b**. Both graphs display an equilibrium curve for the tested temperatures. Products selectivity at different temperature for reduced SBFO and PBFO **c.** and reduced Ni-doped counterparts **d**. CO selectivity is represented with square (■) and CH_4 selectivity is represented with triangle (▲), **e.** Schematic representation of the concept presented here.

6.7. Replenishing the oxygen lattice

To reach an understanding and test the connection between oxygen lattice exhaustion during the exsolution process and Ni-presence, the above catalysts were re-oxidised (600 ºC during 1 h) and subsequently reduced (600 ºC for 30 min). These new conditions were chosen to solely reduce the surface and avoid complete removal of the freshly replenished oxygen lattice. These samples are now *ra*-PBFO, *ra*-PBFNO, *ra*-SBFO and *ra*-SBFNO. Results of both CO_2 conversion and CO selectivity are illustrated in Figure 6.5.a-d. In this case, *ra*-SBFNO displayed the highest activity, doubling the values presented before, going from 28% CO_2 conversion in the reduced state (*r*-SBFNO) to 56% CO_2 conversion when the catalyst was reactivated, *ra*-SBFNO, almost reaching equilibrium values. Similarly occurred with *ra*-PBFNO, which increased CO_2 conversion by 10%, reaching up to 42% conversion at 750 ºC, vs 32% conversion that *r*-PBFNO displayed. Outstandingly, upon reactivation, all catalysts completely avoided CH_4 formation and reached 100% selectivity at T > 550 ºC (Figure 6.5.c-d).

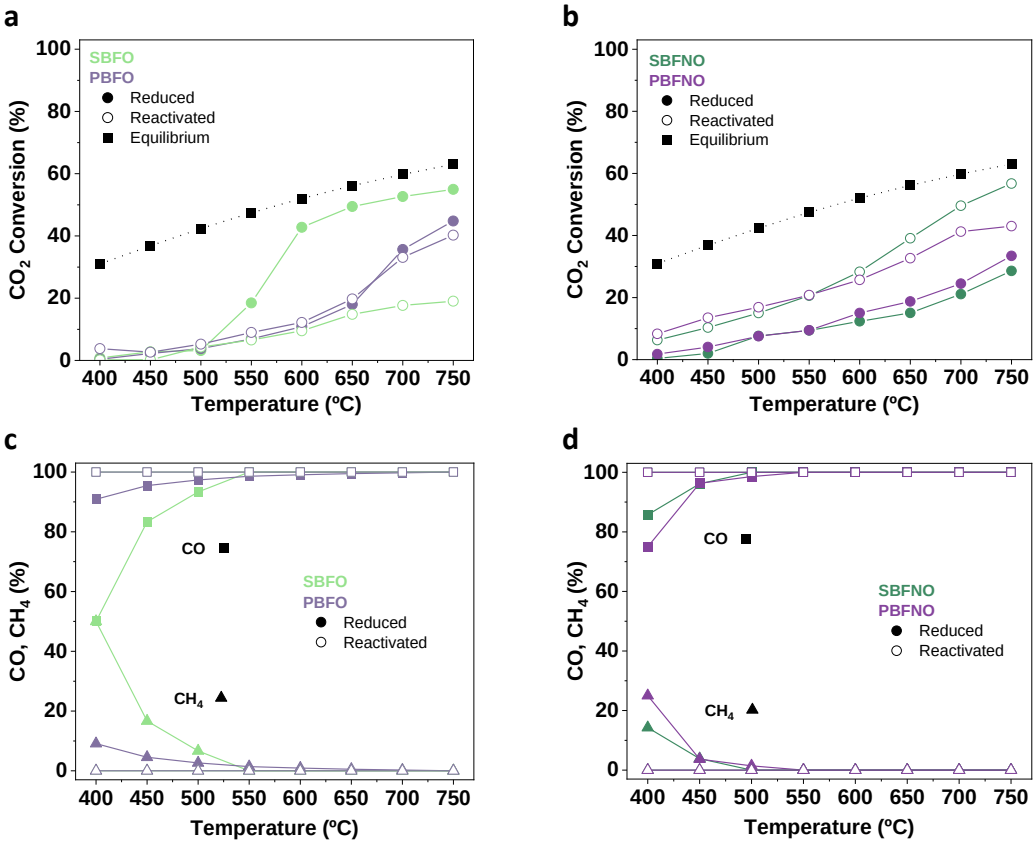

Figure 6.5. Catalytic testing of the reactivated materials. CO_2 conversion with temperature for reduced (●) and reactivated (◌) SBFO and PBFO **a**. and Ni-doped counterparts **b**. Both graphs display an equilibrium curve for the tested temperatures. Products selectivity at different temperatures for reduced (●) and reactivated (◌) SBFO and PBFO **c**. and reduced Ni-doped counterparts **d**. CO selectivity is represented with a square (■) and CH_4 selectivity is represented with a triangle (▲). Selectivity values are identical for the reactivated samples hence they might not be visible in the graphs.

On the other hand, *ra*-SBFO underwent deactivation under this treatment, dropping the conversion rates down to 19% (Figure 6.5.a-b). This could be possibly due to the destruction of the SBFO microstructure upon reoxidation, as shown in. Even though *ra*-SBFNO showcased the highest conversion values, post-test SEM images revealed changes in the microstructure (Figure 6.6.b). These changes are explained by partial decomposition caused by A-site segregation (previously reported by Fu et al. 2023). Pr-based catalysts do not appear to be adversely impacted by the re-oxidation. Figure 6.5.a reveals that *ra*-PBFO conversion remains almost identical as before undergoing re-oxidation and CO_2 conversion increased for *ra*-PBFNO (Figure 6.5.b). Both materials ultimately displayed similar micro/nanostructure as prior reactivation .

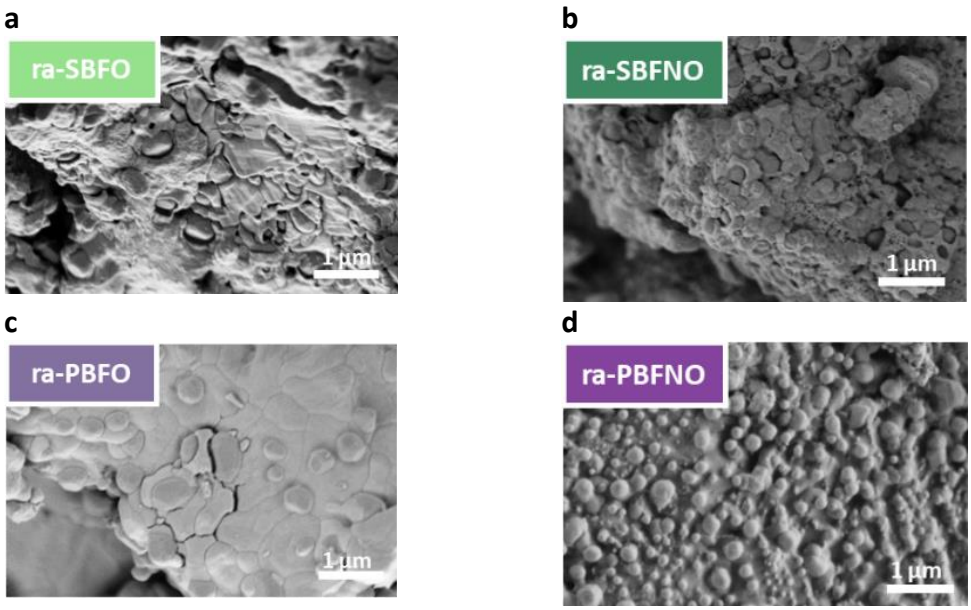

Figure 6.6. Characterisation of reactivated materials SEM images of catalysts after being reduced at 600ºC for 1 h after undergoing exsolution at 900ºC for 10h, subsequent reoxidation at 600ºC for 30 min. In order: *ra*-SBFO, *ra*-SBFNO, *ra*-PBFO, *ra*-PBFNO, **a-d**.

6.8. Summary of Chapter 6

"We have designed a set of four different tailored and exsolved perovskites for the catalytic rWGS. We demonstrate that the substitution of the A-site and doping B-site as well as the concentration of oxygen vacancies are important design principles to consider when designing a material for the conversion of CO_2 to CO. Our results show that A-site doping with Pr appears to produce more stable catalysts when compared to Sm-doped ones, even though the latter tends to be slightly more active. We also show that the existence of lattice oxygen is crucial for this process and has to be taken into consideration for efficient future material design.

For the best catalytic activity, a balance between H_2 activation and CO_2 dissociation should be tailored by the oxygen vacancy concentration. We demonstrate more oxygen vacancies does not always result in better activity. Lastly, the incorporation of a small quantity of Ni on the B-site combined with exsolution results in very high selectivity, with no methane formation, even at low temperatures where methanation conditions are favourable due to the production of Fe-Ni alloys. Although there is still room for improvement for our catalysts regarding their stability and low temperature activity, our results provide a new insight of the significance of oxygen vacancies in CO_2 hydrogenation. These findings imply

the potential of such materials for low temperature rWGS processes that include the production of liquid fuels either downstream or in combination in the same reactors.”

Chapter 7 Conclusions and Future work

7.1. Summary of the thesis

Here, the main results and outcomes of this thesis are discussed. The work has been split in two CL processes: CLWGS and CLSRM. CLWGS needs CO as feedstock, which needs to be generated from other sources, such as CH_4. Therefore, the first process can be understood as a logical continuation of the latter, generating up to 4 mol of H_2 per 1 mol of CH_4 fed to the reactor, as both half-oxidation reactions are conducted with H_2O as oxidising agent to replenish the oxygen lattice.

The principal goal of this PhD thesis was to identify, design and develop oxygen carrier materials with enough OSC to be suitable for H_2 production in CL processes involving both CLWGS and CLSRM. Two oxygen non-stoichiometric materials, $Sm_{0.5}Ba_{0.5}FeO_{3-\delta}$ and $Pr_{0.5}Ba_{0.5}FeO_{3-\delta}$ (SBFO and PBFO), were initially identified and synthesised. These were chosen as the non-stoichiometry was expected to increase the initial activity. The novelty of this study lays on the implementation of these materials in CL processes and the study of their OSC, which has never been reported in previous works.

Their characterisation involved a crystallographic study by PXRD, the deconvolution of its crystalline structure via Rietveld refinement and a microstructural study by SEM. Besides this study, a δ-pO_2 relationship profile was elaborated, and their gradient followed the gradient of the WGS conditions. This indicated that the OCM possessed usable oxygen to be exchanged during the process. Despite displaying a lower amount of initial oxygen vacancies, PBFO exhibited larger reducibility, even though OCM were generally stable under reducing conditions, while still capable of recovering their initial perovskite structure upon reoxidation. Two different regimes were observed for the presented OCM. These regimes were governed by the sole existence of one phase, cubic in this case, or the coexistence of two or more phases, tetragonal and cubic for both samples. SBFO displayed this transition between regimes at $\delta \sim 0.23$, whilst PBFO did it at $\delta \sim 0.29$.

The materials were both tested under CLWGS. Small amounts of material (1 mmol) were used and the creation of an oxygen profile was not expected given the small amount of material used at the equilibrium conditions at 820 ºC, as predicted by Metcalfe et al. (2019) Aiming at observing the long-time stability, short cycles of 1 min were run per half-cycle. Gases flows were 5% CO and 6.5% H_2O. Even though both materials were proven stable

after cycling, as expected PBFO outperformed its analogue SBFO due to its greater reducibility and larger amount of oxygen vacancies, resulting in higher H_2 formation rates. By the end of the cycles, 4.5 mol $H_2 \cdot g^{-1} \cdot min^{-1}$ for PBFO vs ~ 3.6 mol $H_2 \cdot g^{-1} \cdot min^{-1}$ for SBFO were generated, surpassing results from previous studies. An example of these better results is the work by Gao et al. (2022), which obtained a H_2 formation rate of 0.8 mmol $H_2 \cdot g^{-1} \cdot min^{-1}$ by using Fe_2O_3 on different supports. Another work is from Scheffe et al. (2011), where a maximum value of 2.34 mmol $H_2 \cdot g^{-1} \cdot min^{-1}$ when using different Fe-based OCM was obtained.

Due to its larger number of oxygen vacancies and higher H_2 yield in CLWGS, PBFO was chosen for future development. In this case, CLSRM was the studied process. For high CH_4 transformation into syngas whilst avoiding combustion products, highly reducing environments are required. Reactivity of PBFO towards CH_4 was tested. The material displayed activity and no signs of decomposition under 5% CH_4. Results indicated a need for further modifications, which still allowed to keep the core perovskite structure initially developed. By incorporating Ni and inducing A-site deficiency, the material maintained the main perovskite structure, increased its reactivity towards CH_4. This methodology demonstrated how controlled exsolution of metallic nanoparticles from the B-site onto the surface could be achieved. *Operando* synchrotron PXRD shed light into the exsolution mechanism, where the exsolution of Ni nanoparticles was firstly monitored. This exsolution acted as driving force to promote the exsolution of Fe and form a FeNi alloy. Through this same technique, partial redissolution of the formed nanoparticles was observed, demonstrating the reversibility of the process. Eventually, upon reactivation of the system via a new reduction and observation under *operando* synchrotron PXRD, the studied materials exhibited larger oxygen vacancies formation and increased H_2 generation from CH_4 whilst avoiding coke deposition, as a result of CH_4 cracking.

The FeNi exsolved nanoparticles acted as active sites promoting high selectivity and enabling the high selective process at lower temperatures. The typical reaction temperature was decreased, going from 750-800 ºC to an early activation at 690 ºC with the modified material, now PBFNO, which is remarkable for a non-noble metal system. Full syngas selectivity was observed at T ~ 730 ºC and maintained through time. Thereby, this newly modified material demonstrated to be an ideal candidate to be implemented in CLSRM.

Aiming at operating at lower temperatures than usual CSRM (where T > 850 ºC in order to achieve optimal syngas selectivity), initial tests were conducted at lower-than-usual values to find the optimal temperature value to conduct the tests. As expected, as temperature increased, conversion was incremented. However, contrary to observations from preliminary experiments with high syngas selectivity in CH_4 activation, the OCM did not exhibit high conversion or selectivity, regardless of the temperature used. The duration of the CLSRM cycles was set at 1 min, as the best results in terms of syngas and pure H_2 production suggested this.

The amount and quality of produced syngas was not in line with expectations. Since the oxidising potential of H_2O is not as high as others such as oxygen, the aim was to generate larger amounts of nanoparticles through cycling. However, the objective was not achieved. H_2O consistently replenished the surface oxygen vacancies, thereby promoting CH_4 combustion instead of the expected partial oxidation that leads to syngas formation, producing lower H_2 and syngas yields than similar recent studies. Despite the low selectivity achieved, the materials' oxygen capacity was not depleted and displayed a consistent conversion throughout the 400 cycles, highlighting their thermal and redox stability in the long-term.

The implementation of the material in an exsolved state would certainly enhance both the CH_4 activity and selectivity for the mentioned process. However, this would come at the cost of sacrificing some oxygen capacity, as the OCM would have been previously reduced.

These designed and modified materials were tested beyond CL purposes. The tailored oxygen vacancies resulted in an enhanced activation of the CO_2 hydrogenation process for the catalytic rWGS reaction compared to previous findings from the literature. Reduction conditions were applied to induce exsolution of nanoparticles in both systems: Ni-doped and non Ni-doped PBFO and SBFO. The presence of Ni facilitated a more controlled exsolution of nanoparticles through the formation of a FeNi alloy. This alloy significantly enhanced CO selectivity whilst hindering CH_4 formation even at low temperatures.

Pr-based materials, possessing fewer oxygen vacancies than their equivalent Sm-based, resulted in enhanced stability. This observation reveals that a larger amount of initial oxygen vacancies does not always translate into higher product yields.

The thesis has overall satisfied the initial objectives of creating stable materials with high oxygen storage capacity and applicability in CL processes for H_2 production while remaining stable under these conditions after the long-term cycling tests. High H_2 yields have been achieved in CLWGS. Ni-doping and subsequent exsolution conditions have seem to enhance the stability of the material when applied in CLSRM, even though the selectivity achieved was not as high as desired. Beyond their primary use, they have been proven active in catalytic processes such as catalytic rWGS.

7.2. Possible future work

Since the δ-pO_2 relationship of these materials is a novel study from this work and was never explored in the literature, a more detailed δ-pO_2 profile could generate a better understanding of the oxygen variation dynamics of the OCM. The combination of both TGA and coulometric titrations could provide a full oxygen variation profile: the first could be used for the low-pO_2 range, whereas the latter could cover the mid-pO_2 range. Cell variation and its correlation to the oxygen loss or intake could be studied under different buffer gases, simulating CLWGS whilst monitored via *in situ* PXRD. Loading larger amounts of powder in the reactor could assist in constructing a complete oxygen profile while conducting neutron scattering experiments.

Understanding the stability and of OCM in chemical looping processes depends on the precise identification of oxygen vacancies. Although this thesis used methodologies like iodometric titrations and XPS, which yielded insightful results, their limitations highlight the need for more sophisticated approaches in subsequent research. Methods like synchrotron-based X-ray Absorption Near Edge Structure (XANES), Extended X-ray Absorption Fine Structure (EXAFS) and neutron diffraction would provide improved accuracy and the capacity to examine bulk characteristics, offering a more thorough comprehension of oxygen vacancies and their function in material performance in the future. XANES provides insights into electronic structure and local chemical environments, EXAFS reveals atomic distances and coordination numbers, and neutron diffraction offers detailed atomic arrangements, enabling a deeper understanding of oxygen vacancies and their role in material performance.

The formation of oxygen vacancies depends also on the behaviour of elements within the composition. Praseodymium can have multiple oxidation states (+3 and +4), impacting the

material's redox behaviour and oxygen vacancies. Current methods fall short in distinguishing these states. Using advanced techniques like XANES or Electron Energy Loss Spectroscopy (EELS) could address this. EELS offers high-resolution spatial information on Pr oxidation states. These analyses would validate calculated oxygen vacancies and deepen our understanding of Pr role in material stability during CL cycles, potentially optimizing oxygen carrier materials for better performance and stability upon cycles.

However, as mentioned through the different chapters, although CO serves as an ideal gas for laboratory-based studies, its industrial use as feedstock is still limited and must be derived from other sources, such as CH_4. The Ni-doping and implementation of A-site deficiency in these materials opened a new route of exploration for CL and CH_4 conversion applications. Nanoparticle exsolution has significantly decreased the operating temperatures for CH_4 activation. Varying doping ratios and optimisation of the exsolution conditions, would notably impact both CH_4 conversion and products selectivity under different cycling conditions, accordingly.

Typically, CL CH_4 reforming processes involve the use of a third reactor to fully reoxidised the material. In this case, it has not been necessary its implementation as the material underwent the required oxidation (and even beyond) solely with steam. This has been chosen to facilitate the process. Therefore, the CL research with the suggested material is on the right track. Broader research is needed on the reduction conditions to promote the exsolution of both active metals Fe and Ni, either as one alloy or separately. The control of this material treatment combined with the optimised half-cycle duration in CL CH_4 reforming applications will directly promote the selectivity towards the desired products, as it has been demonstrated in the CH_4 activation experiments.

References

Abad, A. *et al.* (2007) 'The use of iron oxide as oxygen carrier in a chemical-looping reactor', *Fuel*, 86(7–8), pp. 1021–1035. Available at: https://doi.org/10.1016/j.fuel.2006.09.021.

Abdalla, A.M. *et al.* (2018) 'Hydrogen production, storage, transportation and key challenges with applications: A review', *Energy Conversion and Management*, 165(April), pp. 602–627. Available at: https://doi.org/10.1016/j.enconman.2018.03.088.

Adanez, J. *et al.* (2012) 'Progress in chemical-looping combustion and reforming technologies', *Progress in Energy and Combustion Science*, 38(2), pp. 215–282. Available at: https://doi.org/10.1016/j.pecs.2011.09.001.

AlHumaidan, F.S. *et al.* (2023) 'Blue hydrogen: Current status and future technologies', *Energy Conversion and Management*, 283(August 2022), p. 116840. Available at: https://doi.org/10.1016/j.enconman.2023.116840.

Allendorf, M.D. *et al.* (2022) 'Challenges to developing materials for the transport and storage of hydrogen', *Nature Chemistry 2022 14:11*, 14(11), pp. 1214–1223. Available at: https://doi.org/10.1038/s41557-022-01056-2.

Amin, A.M., Croiset, E. and Epling, W. (2011) 'Review of methane catalytic cracking for hydrogen production', *International Journal of Hydrogen Energy*, 36(4), pp. 2904–2935. Available at: https://doi.org/10.1016/j.ijhydene.2010.11.035.

Anthony, B. and Patchigolla, K. (no date) *Calcium looping and advanced doping techniques*. Available at: https://www.cranfield.ac.uk/case-studies/research-case-studies/world-and-uk-firsts-in-calcium-looping-and-advanced-doping-techniques.

Araki, W., Miaolong, Q. and Arai, Y. (2017) 'Oxygen non-stoichiometry of $La_{0.6}Sr_{0.4}Co_{0.2}Fe_{0.8}O_{3-\delta}$ under uniaxial compression evaluated by coulometric titration', *Electrochimica Acta*, 253, pp. 339–343. Available at: https://doi.org/10.1016/j.electacta.2017.09.073.

Ban, H. *et al.* (2014) 'Influence of rare-earth elements (La, Ce, Nd and Pr) on the performance of Cu/Zn/Zr catalyst for CH_3OH synthesis from CO_2', *Catalysis Communications*, 54, pp. 50–54. Available at: https://doi.org/10.1016/J.CATCOM.2014.05.014.

Baraj, E., Ciahotný, K. and Hlinčík, T. (2021) 'The water gas shift reaction: Catalysts and reaction mechanism', *Fuel*, 288(June 2020). Available at: https://doi.org/10.1016/j.fuel.2020.119817.

Bayham, S.C. *et al.* (2016) 'Chemical looping technology for energy and chemical production', *Wiley Interdisciplinary Reviews: Energy and Environment*, 5(2), pp. 216–241. Available at: https://doi.org/10.1002/wene.173.

Bian, Z. *et al.* (2020) 'A review on perovskite catalysts for reforming of methane to hydrogen production', *Renewable and Sustainable Energy Reviews*, 134, p. 110291. Available at: https://doi.org/10.1016/J.RSER.2020.110291.

Biesinger, M.C. *et al.* (2011) 'Resolving surface chemical states in XPS analysis of first row transition metals, oxides and hydroxides: Cr, Mn, Fe, Co and Ni', *Applied Surface Science*, 257(7), pp. 2717–2730. Available at: https://doi.org/10.1016/j.apsusc.2010.10.051.

Biswas, S. *et al.* (2023) 'A critical review on cathode materials for steam electrolysis in solid oxide electrolysis', *International Journal of Hydrogen Energy*, 48(34), pp. 12541–12570. Available at: https://doi.org/10.1016/j.ijhydene.2022.11.307.

Bleeker, M.F., Kersten, S.R.A. and Veringa, H.J. (2007) 'Pure hydrogen from pyrolysis oil using the steam-iron process', *Catalysis Today*, 127(1–4), pp. 278–290. Available at: https://doi.org/10.1016/j.cattod.2007.04.011.

Burnat, D. *et al.* (2016) 'Smart material concept: Reversible microstructural self-regeneration for catalytic applications', *Journal of Materials Chemistry A*, 4(30), pp. 11939–11948. Available at: https://doi.org/10.1039/c6ta03417a.

Calì, E. *et al.* (2023) 'Real-time insight into the multistage mechanism of nanoparticle exsolution from a perovskite host surface', *Nature Communications*, 14(1). Available at: https://doi.org/10.1038/s41467-023-37212-6.

Cao, Y., Sit, S.P. and Pan, W.P. (2014) 'Preparation and Characterization of Lanthanum-Promoted Copper-based Oxygen Carriers for Chemical Looping Combustion Process', *Aerosol and Air Quality Research*, 14(2), pp. 572–584. Available at: https://doi.org/10.4209/AAQR.2013.05.0175.

Carpenter, J.I.I. (1965) 'The accuracy of the Winkler method for dissolved Oxygen Analysis', *Limnology and Oceanography*, 10(1), pp. 135–140.

Carrillo, A.J. *et al.* (2020) 'La0.6Sr0.4Cr0.8Co0.2O3Perovskite Decorated with Exsolved Co Nanoparticles for Stable CO2Splitting and Syngas Production', *ACS Applied Energy Materials*, 3(5), pp. 4569–4579. Available at: https://doi.org/10.1021/ACSAEM.0C00249/ASSET/IMAGES/MEDIUM/AE0C00249_M006.GIF.

Carrillo, A.J. *et al.* (2021) 'Boosting methane partial oxidation on ceria through exsolution of robust Ru nanoparticles', *Materials Advances*, 2(9), pp. 2924–2934. Available at: https://doi.org/10.1039/D1MA00044F.

Carvalho, M.D. *et al.* (2006) 'Magnetic studies on $Sr_{0.8}Ce_{0.1}Fe_{0.7}Co_{0.3}O_{3-\delta}$ perovskite', *Solid State Sciences*, 8(5), pp. 444–449. Available at: https://doi.org/10.1016/j.solidstatesciences.2005.12.001.

Cha, J. *et al.* (2021) 'An efficient process for sustainable and scalable hydrogen production from green ammonia', *Renewable and Sustainable Energy Reviews*, 152(September). Available at: https://doi.org/10.1016/j.rser.2021.111562.

Chaubey, R. *et al.* (2013) 'A review on development of industrial processes and emerging techniques for production of hydrogen from renewable and sustainable sources', *Renewable and Sustainable Energy Reviews*, 23, pp. 443–462. Available at: https://doi.org/10.1016/J.RSER.2013.02.019.

Chen, L. *et al.* (2020) 'Catalytic Hydrogen Production from Methane ':

Chen, W.H. *et al.* (2010) 'Thermodynamic analysis of hydrogen production from methane via autothermal reforming and partial oxidation followed by water gas shift reaction', *International Journal of Hydrogen Energy*, 35(21), pp. 11787–11797. Available at: https://doi.org/10.1016/j.ijhydene.2010.08.126.

Cheng, Z. *et al.* (2016) 'Oxygen vacancy promoted methane partial oxidation over iron oxide oxygen carriers in the chemical looping process', *Physical Chemistry Chemical Physics*, 18(47), pp. 32418–32428. Available at: https://doi.org/10.1039/c6cp06264d.

Cho, W.C. *et al.* (2014) 'Continuous operation characteristics of chemical looping hydrogen production system', *Applied Energy*, 113, pp. 1667–1674. Available at: https://doi.org/10.1016/j.apenergy.2013.08.078.

Chung, C. *et al.* (2017) 'Chemically and physically robust, commercially-viable iron-based composite oxygen carriers sustainable over 3000 redox cycles at high temperatures for chemical looping applications', *Energy and Environmental Science*, 10(11), pp. 2318–2323. Available at: https://doi.org/10.1039/c7ee02657a.

Dai, F. *et al.* (2023) 'Recent Progress on Hydrogen-Rich Syngas Production from Coal Gasification', *Processes*, 11(6). Available at: https://doi.org/10.3390/pr11061765.

Damaskinos, C.M. *et al.* (2019) 'The Effect of CeO2 Preparation Method on the Carbon Pathways in the Dry Reforming of Methane on Ni/CeO2 Studied by Transient Techniques', *Catalyst*, 9(621), pp. 1–24.

Das, A., Das, U. and Das, A.K. (2023) 'Relativistic effects on the chemical bonding properties of the heavier elements and their compounds', *Coordination Chemistry Reviews*, 479, p. 215000.

Das, S. *et al.* (2022) 'Hydrogen production using chemical looping technology: A review with emphasis on H_2 yield of various oxygen carriers', *International Journal of Hydrogen Energy*, 47(66), pp. 28322–28352. Available at: https://doi.org/10.1016/j.ijhydene.2022.06.170.

Dass, C. (2007) 'Basics of Mass Spectroscopy', in *Fundamentals of Contemporary Mass Spectrometry*.

Dawood, F., Anda, M. and Shafiullah, G.M. (2020) 'Hydrogen production for energy: An overview', *International Journal of Hydrogen Energy*, 45(7), pp. 3847–3869. Available at: https://doi.org/10.1016/j.ijhydene.2019.12.059.

Delgado-Galicia, B. *et al.* (2024) 'Effects of lanthanide doping on the electrode properties and exsolution behavior of A-site deficient $Sr_{1.9}Fe_{1.3}Ni_{0.2}Mo_{0.5}O_{6-\delta}$ double perovskites', *Solid State Ionics*, 410(March), p. 116532. Available at: https://doi.org/10.1016/j.ssi.2024.116532.

Deml, A.M. *et al.* (2014) 'Oxide enthalpy of formation and band gap energy as accurate descriptors of oxygen vacancy formation energetics', *Energy & Environmental Science*, 7(6), p. 1996. Available at: https://doi.org/10.1039/c3ee43874k.

Denton, A.R. and Ashcroft, N.W. (1991) 'Vegard's "law"', *Physical Review (A)*, 43(6), pp. K117–K118. Available at: https://doi.org/10.1002/pssb.19660180251.

de Diego, L.F. *et al.* (2008) 'Synthesis gas generation by chemical-looping reforming in a batch fluidized bed reactor using Ni-based oxygen carriers', *Chemical Engineering Journal*, 144(2), pp. 289–298. Available at: https://doi.org/10.1016/j.cej.2008.06.004.

Ding, H. *et al.* (2018) 'A novel composite perovskite-based material for chemical-looping steam methane reforming to hydrogen and syngas', *Energy Conversion and Management*, 171(May), pp. 12–19. Available at: https://doi.org/10.1016/j.enconman.2018.05.088.

Ding, S. *et al.* (2020) 'A-site deficient perovskite with nano-socketed Ni-Fe alloy particles as highly active and durable catalyst for high-temperature CO2 electrolysis', *Electrochimica Acta*, 335, p. 135683. Available at: https://doi.org/10.1016/j.electacta.2020.135683.

Du, Z. *et al.* (2016) 'High-Performance Anode Material $Sr_2FeMo_{0.65}Ni_{0.35}O_{6-\delta}$ with in Situ Exsolved Nanoparticle Catalyst', *ACS Nano*, 10(9), pp. 8660–8669. Available at: https://doi.org/10.1021/acsnano.6b03979.

Dueso, C. *et al.* (2012) 'Reduction and oxidation kinetics of nickel-based oxygen-carriers for chemical-looping combustion and chemical-looping reforming', *Chemical Engineering Journal*, 188(x), pp. 142–154. Available at: https://doi.org/10.1016/j.cej.2012.01.124.

Dueso, C., Thompson, C. and Metcalfe, I. (2015) 'High-stability, high-capacity oxygen carriers: Iron oxide-perovskite composite materials for hydrogen production by chemical looping', *Applied Energy*, 157, pp. 382–390. Available at: https://doi.org/10.1016/j.apenergy.2015.05.062.

Elbadawi, A.H. *et al.* (2021) 'Catalytic partial oxidation of methane to syngas: review of perovskite catalysts and membrane reactors', *Catalysis Reviews*, 63(1), pp. 1–67. Available at: https://doi.org/10.1080/01614940.2020.1743420.

Emam, A.S. *et al.* (2024) 'A review on recent trends, challenges, and innovations in alkaline water electrolysis', *International Journal of Hydrogen Energy*, 64(March), pp. 599–625. Available at: https://doi.org/10.1016/j.ijhydene.2024.03.238.

Epp, J. (2016) 'X-Ray diffraction (XRD) techniques for materials characterization', in *Materials Characterization Using Nondestructive Evaluation (NDE) Methods*, pp. 17–43.

ESRF (no date) *Technical Description*. Available at: https://www.esrf.fr/id22/technical-description.

Evans, J.S.O. (2018) '1. The powder diffraction method', *Rietveld Refinement*, pp. 1–15. Available at: https://doi.org/10.1515/9783110461381-001.

Fan, L.S. (2011) *Chemical Looping Systems for Fossil Energy Converson*. John Wiley & Sons, Ltd.

Farias, C.B.B. *et al.* (2022) 'Use of Hydrogen as Fuel: A Trend of the 21st Century', *Energies 2022, Vol. 15, Page 311*, 15(1), p. 311. Available at: https://doi.org/10.3390/EN15010311.

Fitch, A. *et al.* (2023) 'ID22 - the high-resolution powder-diffraction beamline at ESRF', *Journal of Synchrotron Radiation*, 30, pp. 1003–1012. Available at: https://doi.org/10.1107/S1600577523004915.

Fu, C.J. *et al.* (2023) 'Recent Advances in Perovskite Oxides Electrocatalysts: Ordered Perovskites, Cations Segregation and Exsolution', *ChemCatChem*, 15(11), p. e202300389. Available at: https://doi.org/10.1002/CCTC.202300389.

Gao, Z. *et al.* (2022) 'Gd, La co-doped CeO_2 as an active support for Fe_2O_3 to enhance hydrogen generation via chemical looping water gas shift', *International Journal of Hydrogen Energy*, 47(54), pp. 22806–22818. Available at: https://doi.org/10.1016/j.ijhydene.2022.05.112.

García-Labiano, F. *et al.* (2009) 'Effect of fuel gas composition in chemical-looping combustion with ni-based oxygen carriers. 1. fate of sulfur', *Industrial and Engineering Chemistry Research*, 48(5), pp. 2499–2508. Available at: https://doi.org/10.1021/ie801332z.

Ghavam, S. *et al.* (2021) 'Sustainable Ammonia Production Processes', *Frontiers in Energy Research*, 9, p. 580808. Available at: https://doi.org/10.3389/FENRG.2021.580808/BIBTEX.

Go, K.S. *et al.* (2009) 'Hydrogen production from two-step steam methane reforming in a fluidized bed reactor', *International Journal of Hydrogen Energy*, 34(3), pp. 1301–1309. Available at: https://doi.org/10.1016/J.IJHYDENE.2008.11.062.

Goldschmidt, V. (1926) 'Die Gesetze der Krystallochemie', *Naturwissenschaften*, 14, pp. 477–485. Available at: https://doi.org/10.1007/BF01507527.

González-Castaño, M., Dorneanu, B. and Arellano-García, H. (2021) 'The reverse water gas shift reaction: A process systems engineering perspective', *Reaction Chemistry and Engineering*, 6(6), pp. 954–976. Available at: https://doi.org/10.1039/d0re00478b.

Goodenough, J.B. (2004) 'Electronic and ionic transport properties and other physical aspects of perovskites', *Reports on Progress in Physics*, 67(11), pp. 1915–1993. Available at: https://doi.org/10.1088/0034-4885/67/11/R01.

Grigoriev, S.A. *et al.* (2020) 'Current status, research trends, and challenges in water electrolysis science and technology', *International Journal of Hydrogen Energy*, 45(49), pp. 26036–26058. Available at: https://doi.org/10.1016/J.IJHYDENE.2020.03.109.

Gupta, P. *et al.* (2011) 'Chemical Looping Particles', in *Chemical Looping Systems for Fossil Energy Conversions*. John Wiley & Sons, Ltd, pp. 57–135.

Gupta, U. *et al.* (2024) 'FexNiy/SiO2-Al2O3 catalyzed hydrodeoxygenation of biorenewable platform molecules', *Fuel*, 360, p. 130588. Available at: https://doi.org/10.1016/J.FUEL.2023.130588.

Hosseini, D. *et al.* (2019) 'Reversible Exsolution of Dopant Improves the Performance of Ca2Fe2O5 for Chemical Looping Hydrogen Production', *ACS Applied Materials and Interfaces*, 11(20), pp. 18276–18284. Available at: https://doi.org/10.1021/acsami.8b16732.

Hu, Z. *et al.* (2021) 'Nickel-iron modified natural ore oxygen carriers for chemical looping steam methane reforming to produce hydrogen', *International Journal of Hydrogen Energy*, 46(80), pp. 39700–39718. Available at: https://doi.org/10.1016/j.ijhydene.2021.09.242.

Huang, J., Balcombe, P. and Feng, Z. (2023) 'Technical and economic analysis of different colours of producing hydrogen in China', *Fuel*, 337, p. 127227. Available at: https://doi.org/10.1016/J.FUEL.2022.127227.

Iihoshi, M., Goto, M. and Shimakawa, Y. (2024) 'Stabilities of Charge Disproportionated States by Successive Charge Transitions of Mixed and Unusually High Valence Fe $^{3.5+}$ in *Ln* $BaFe_2O_6$ (*Ln* = Pr, Sm)', *Chemistry of Materials*, 36(12), pp. 6047–6052. Available at: https://doi.org/10.1021/acs.chemmater.4c00578.

Irvine, J. *et al.* (2021) 'Roadmap on inorganic perovskites for energy applications', *Journal of Physics: Energy*, 3(3), p. 031502. Available at: https://doi.org/10.1088/2515-7655/ABFF18.

Islam, Q.A. *et al.* (2021) 'Nanoparticle exsolution in perovskite oxide and its sustainable electrochemical energy systems', *Journal of Power Sources*, 492(November 2020), p. 229626. Available at: https://doi.org/10.1016/j.jpowsour.2021.229626.

Iulianelli, A. *et al.* (2016) 'Advances on methane steam reforming to produce hydrogen through membrane reactors technology: A review', *Catalysis Reviews - Science and Engineering*, 58(1), pp. 1–35. Available at: https://doi.org/10.1080/01614940.2015.1099882.

Ivanov, I.L. *et al.* (2022) 'Nonstoichiometry, Defect Chemistry and Oxygen Transport in Fe-Doped Layered Double Perovskite Cobaltite $PrBaCo_{2-x}Fe_xO_{6-\delta}$ (x = 0–0.6) Membrane Materials', *Membranes*, 12(12). Available at: https://doi.org/10.3390/membranes12121200.

Jain, R. *et al.* (2022) 'Bio-hydrogen production through dark fermentation: an overview', *Biomass Conversion and Biorefinery* [Preprint], (0123456789). Available at: https://doi.org/10.1007/s13399-022-03282-7.

Jeong, M.H., Lee, D.H. and Bae, J.W. (2015) 'Reduction and oxidation kinetics of different phases of iron oxides', *International Journal of Hydrogen Energy*, 40(6), pp. 2613–2620. Available at: https://doi.org/10.1016/j.ijhydene.2014.12.099.

Jiang, B. *et al.* (2021) 'Iron–oxygen covalency in perovskites to dominate syngas yield in chemical looping partial oxidation', *Journal of Materials Chemistry A*, 9(22), pp. 13008–13018. Available at: https://doi.org/10.1039/D1TA02103F.

Jiang, K. *et al.* (2020) 'A novel catalytic membrane reactor with homologous exsolution-based perovskite catalyst', *Journal of Membrane Science*, 608, p. 118213. Available at: https://doi.org/10.1016/J.MEMSCI.2020.118213.

Jiang, Q. *et al.* (2020) 'Chemical Looping Combustion over a Lanthanum Nickel Perovskite-Type Oxygen Carrier with Facilitated O2-Transport', *Energy and Fuels*, 34(7), pp. 8732–8739. Available at: https://doi.org/10.1021/acs.energyfuels.0c01038.

Jo, S. *et al.* (2022) 'Exsolution of phase-separated nanoparticles via trigger effect toward reversible solid oxide cell', *Applied Energy*, 323(March), p. 119615. Available at: https://doi.org/10.1016/j.apenergy.2022.119615.

Johansson, M. *et al.* (2008) 'Using continuous and pulse experiments to compare two promising nickel-based oxygen carriers for use in chemical-looping technologies', *Fuel*, 87(6), pp. 988–1001. Available at: https://doi.org/10.1016/J.FUEL.2007.08.010.

Jurković, D.L. *et al.* (2017) 'Effect of Copper-based Catalyst Support on Reverse Water-Gas Shift Reaction (RWGS) Activity for CO_2 Reduction', *Chemical Engineering and Technology*, 40(5), pp. 973–980. Available at: https://doi.org/10.1002/ceat.201600594.

Karen, P. *et al.* (2002) 'Verwey Transition under Oxygen Loading in $RBaFe_2O_{5+w}$ (R=Nd and Sm)', *Journal of Solid State Chemistry*, 167(2), pp. 480–493. Available at: https://doi.org/10.1006/JSSC.2002.9665.

Karen, P. (2021) 'Synthesis and equilibrium oxygen nonstoichiometry of PrBaFe2O5+w', *Journal of Solid State Chemistry*, 299(April). Available at: https://doi.org/10.1016/j.jssc.2021.122147.

Karen, P. and Woodward, P.M. (1999) 'Synthesis and structural investigations of the double perovskites $REBaFe_2O_{(5+w)}$ (RE=Nd, Sm)', *Journal of Materials Chemistry*, 9(3), pp. 789–797. Available at: https://doi.org/10.1039/a809302d.

Katz, M.B. *et al.* (2011) 'Self-regeneration of Pd-$LaFeO_3$ catalysts: New insight from atomic-resolution electron microscopy', *Journal of the American Chemical Society*, 133(45), pp. 18090–18093. Available at: https://doi.org/10.1021/ja2082284.

Khan, M.N. and Shamim, T. (2017) 'Thermodynamic screening of suitable oxygen carriers for a three reactor chemical looping reforming system', *International Journal of Hydrogen Energy*, 42(24), pp. 15745–15760. Available at: https://doi.org/10.1016/J.IJHYDENE.2017.05.037.

Kim, J. *et al.* (2023) 'Electrocatalytic Oxidative Coupling of Methane on NiFe Exsolved Perovskite Anode: Effect of Water', *ChemCatChem*, 15(7). Available at: https://doi.org/10.1002/cctc.202201336.

Kim, Y. *et al.* (2022) 'Carbon dioxide splitting and hydrogen production using a chemical looping concept: A review', *Journal of CO2 Utilization*, 63, p. 102139. Available at: https://doi.org/10.1016/J.JCOU.2022.102139.

Kim, Y. *et al.* (2023) 'Enhanced redox performance of LaFeO3 perovskite through in-situ exsolution of iridium nanoparticles for chemical looping steam methane reforming',

Chemical Engineering Journal, 468, p. 143662. Available at: https://doi.org/10.1016/J.CEJ.2023.143662.

Kim, Y.H. *et al.* (2023) 'Nanoparticle Exsolution on Perovskite Oxides: Insights into Mechanism, Characteristics and Novel Strategies', *Nano-Micro Letters 2023 16:1*, 16(1), pp. 1–35. Available at: https://doi.org/10.1007/S40820-023-01258-4.

Konysheva, E., Suard, E. and Irvine, J.T.S. (2009) 'Effect of oxygen non stoichiometry and oxidation state of transition elements on high-temperature phase transition in a-site deficient La 0.95Ni0.6Fe0.4O3-δ perovskite', *Chemistry of Materials*, 21(21), pp. 5307–5318. Available at: https://doi.org/10.1021/cm902443n.

Kousi, K., Neagu, D., Bekris, L., Papaioannou, E.I., *et al.* (2020) 'Endogenous Nanoparticles Strain Perovskite Host Lattice Providing Oxygen Capacity and Driving Oxygen Exchange and CH4 Conversion to Syngas', *Angewandte Chemie*, 132(6), pp. 2531–2540. Available at: https://doi.org/10.1002/ANGE.201915140.

Kousi, K., Neagu, D., Bekris, L., Calì, E., *et al.* (2020) 'Low temperature methane conversion with perovskite-supported: exo / endo -particles', *Journal of Materials Chemistry A*, 8(25), pp. 12406–12417. Available at: https://doi.org/10.1039/d0ta05122e.

Kousi, K., Neagu, D. and Metcalfe, I.S. (2020) 'Combining Exsolution and Infiltration for Redox, Low Temperature CH4 Conversion to Syngas', *Catalysts 2020, Vol. 10, Page 468*, 10(5), p. 468. Available at: https://doi.org/10.3390/CATAL10050468.

Kousi, Kalliopi *et al.* (2021) 'Emergence and Future of Exsolved Materials', *Small*, 17(21), p. 2006479. Available at: https://doi.org/10.1002/SMLL.202006479.

Kuhn, M. *et al.* (2011) 'Oxygen nonstoichiometry, thermo-chemical stability and lattice expansion of $La_{0.6}Sr_{0.4}FeO_{3-\delta}$', *Solid State Ionics*, 195(1), pp. 7–15. Available at: https://doi.org/10.1016/j.ssi.2011.05.013.

Kuhn, M., Hashimoto, S., *et al.* (2013) 'Oxygen nonstoichiometry and thermo-chemical stability of $La_{0.6}Sr_{0.4}CoO_{3-\delta}$', *Journal of Solid State Chemistry*, 197, pp. 38–45. Available at: https://doi.org/10.1016/J.JSSC.2012.08.001.

Kuhn, M., Fukuda, Y., *et al.* (2013) 'Oxygen Nonstoichiometry and Thermo-Chemical Stability of Perovskite-Type $La_{0.6}Sr_{0.4}Co_{1-y}Fe_yO_{3-\delta}$ (y = 0, 0.2, 0.4, 0.5, 0.6, 0.8, 1) Materials', *Journal of The Electrochemical Society*, 160(1), pp. F34–F42. Available at: https://doi.org/10.1149/2.050301JES/XML.

Kuo, Y.L. *et al.* (2013) 'Assessment of redox behavior of nickel ferrite as oxygen carriers for chemical looping process', *Ceramics International*, 39(5), pp. 5459–5465. Available at: https://doi.org/10.1016/J.CERAMINT.2012.12.055.

Kwon, O. *et al.* (2020) 'Review on exsolution and its driving forces in perovskites', *JPhys Energy*, 2(3). Available at: https://doi.org/10.1088/2515-7655/ab8c1f.

Kyriakou, Vasileios *et al.* (2021) 'Plasma Driven Exsolution for Nanoscale Functionalization of Perovskite Oxides', *Small Methods*, 5(12), p. 2100868. Available at: https://doi.org/10.1002/SMTD.202100868.

Lai, K.Y. and Manthiram, A. (2018) 'Evolution of Exsolved Nanoparticles on a Perovskite Oxide Surface during a Redox Process', *Chemistry of Materials*, 30(8), pp. 2838–2847. Available at: https://doi.org/10.1021/ACS.CHEMMATER.8B01029/SUPPL_FILE/CM8B01029_SI_001.PDF.

de Leeuwe, C. (2019) 'Studies of a fixed bed chemical looping reactor for H_2 production by in-situ and operando X-Ray and neutron diffraction'.

de Leeuwe, C., Hu, W., Evans, J., *et al.* (2021) 'Production of high purity H2 through chemical-looping water–gas shift at reforming temperatures – The importance of non-stoichiometric oxygen carriers', *Chemical Engineering Journal*, 423(April), p. 130174. Available at: https://doi.org/10.1016/j.cej.2021.130174.

de Leeuwe, C., Hu, W., Neagu, D., *et al.* (2021) 'Revisiting the thermal and chemical expansion and stability of $La_{0.6}Sr_{0.4}FeO_{3-\delta}$', *Journal of Solid State Chemistry*, 293, p. 121838. Available at: https://doi.org/10.1016/J.JSSC.2020.121838.

Lein, H.L., Wiik, K. and Grande, T. (2006) 'Kinetic demixing and decomposition of oxygen permeable membranes', *Solid State Ionics*, 177(19-25 SPEC. ISS.), pp. 1587–1590. Available at: https://doi.org/10.1016/j.ssi.2006.03.001.

Levalley, T.L., Richard, A.R. and Fan, M. (2014) 'The progress in water gas shift and steam reforming hydrogen production technologies - A review', *International Journal of Hydrogen Energy*, 39(30), pp. 16983–17000. Available at: https://doi.org/10.1016/j.ijhydene.2014.08.041.

Li, D., Xu, R., Li, X., *et al.* (2020) 'Chemical Looping Conversion of Gaseous and Liquid Fuels for Chemical Production: A Review', *Energy and Fuels*, 34(5), pp. 5381–5413. Available at: https://doi.org/10.1021/acs.energyfuels.0c01006.

Li, D., Xu, R., Gu, Z., *et al.* (2020) 'Chemical-Looping Conversion of Methane: A Review', *Energy Technology*, 8(8), p. 1900925. Available at: https://doi.org/10.1002/ENTE.201900925.

Li, K., Wang, H. and Wei, Y. (2013) 'Syngas Generation from Methane Using a Chemical-Looping Concept A Review of Oxygen.pdf', *Journal of Chemistry*, pp. 1–8.

Li, X. *et al.* (2021) 'A-site perovskite oxides: an emerging functional material for electrocatalysis and photocatalysis', *Journal of Materials Chemistry A*, 9(11), pp. 6650–6670. Available at: https://doi.org/10.1039/d0ta09756j.

Li, X.P. *et al.* (2021) 'Transition metal-based electrocatalysts for overall water splitting', *Chinese Chemical Letters*, 32(9), pp. 2597–2616. Available at: https://doi.org/10.1016/J.CCLET.2021.01.047.

Liang, H. (2015) 'Study on the effect of CeO_2 on $Fe_2O_3/LaNiO_3$ as the oxygen carrier applied in chemical-looping hydrogen generation', *International Journal of Hydrogen Energy*, 40(39), pp. 13338–13343. Available at: https://doi.org/10.1016/J.IJHYDENE.2015.08.013.

Lindenthal, L. *et al.* (2020) 'Modifying the surface structure of perovskite-based catalysts by nanoparticle exsolution', *Catalysts*, 10(3), pp. 1–14. Available at: https://doi.org/10.3390/catal10030268.

Lindenthal, L. *et al.* (2021) 'Novel perovskite catalysts for CO_2 utilization - Exsolution enhanced reverse water-gas shift activity', *Applied Catalysis B: Environmental*, 292, p. 120183. Available at: https://doi.org/10.1016/J.APCATB.2021.120183.

Liu, H.X. *et al.* (2022) 'Partially sintered copper–ceria as excellent catalyst for the high-temperature reverse water gas shift reaction', *Nature Communications*, 13(1), pp. 1–11. Available at: https://doi.org/10.1038/s41467-022-28476-5.

Liu, L. *et al.* (2020) 'Low temperature catalytic reverse water-gas shift reaction over perovskite catalysts in DBD plasma', *Applied Catalysis B: Environmental*, 265(December 2019), p. 118573. Available at: https://doi.org/10.1016/j.apcatb.2019.118573.

Liu, S., Liu, Q. and Luo, J.L. (2016) 'Highly Stable and Efficient Catalyst with in Situ Exsolved Fe-Ni Alloy Nanospheres Socketed on an Oxygen Deficient Perovskite for Direct CO_2 Electrolysis', *ACS Catalysis*, 6(9), pp. 6219–6228. Available at: https://doi.org/10.1021/ACSCATAL.6B01555.

Liu, T. *et al.* (2020) 'Robust redox-reversible perovskite type steam electrolyser electrode decorated with: In situ exsolved metallic nanoparticles', *Journal of Materials Chemistry A*, 8(2), pp. 582–591. Available at: https://doi.org/10.1039/c9ta06309a.

Loiland, J.A. *et al.* (2016) 'Fe/γ-Al_2O_3 and Fe-K/γ-Al_2O_3 as reverse water-gas shift catalysts', *Catalysis Science and Technology*, 6(14), pp. 5267–5279. Available at: https://doi.org/10.1039/c5cy02111a.

Luciani, G. *et al.* (2018) 'Partial substitution of B cation in La0.6Sr0.4MnO3 perovskites: A promising strategy to improve the redox properties useful for solar thermochemical water and carbon dioxide splitting', *Solar Energy*, 171(June), pp. 1–7. Available at: https://doi.org/10.1016/j.solener.2018.06.058.

Luo, M. *et al.* (2018) 'Review of hydrogen production using chemical-looping technology', *Renewable and Sustainable Energy Reviews*, 81(June 2017), pp. 3186–3214. Available at: https://doi.org/10.1016/j.rser.2017.07.007.

Lyngfelt, A. *et al.* (2019) '11,000 h of chemical-looping combustion operation—Where are we and where do we want to go?', *International Journal of Greenhouse Gas Control*, 88(May), pp. 38–56. Available at: https://doi.org/10.1016/j.ijggc.2019.05.023.

Madsen, B.D. *et al.* (2007) 'SOFC Anode Performance Enhancement through Precipitation of Nanoscale Catalysts', *ECS Transactions*, 7(1), pp. 1339–1348. Available at: https://doi.org/10.1149/1.2729237/XML.

Markov, A.A. *et al.* (2016) 'Oxygen non-stoichiometry and mixed conductivity of La0.5Sr0.5Fe1–xMnxO3–δ', *Journal of Solid State Electrochemistry*, 20(1), p. 225. Available at: https://doi.org/10.1007/S10008-015-3027-0.

Martinez Martin, A. *et al.* (2024) 'Tailoring the A and B site of Fe-based perovskites for high selectivity in the reverse water-gas shift reaction', *Journal of CO2 Utilization*, 83(April), p. 102784. Available at: https://doi.org/10.1016/j.jcou.2024.102784.

Mattisson, T. and Lyngfelt, A. (2001) 'Applications of chemical-looping combustion with capture of CO_2', *Control*, (1), pp. 46–51.

Medeiros, R.L.B.A. *et al.* (2017) 'Study of the reactivity by pulse of CH4 over NiO/Fe-doped MgAl2O4 oxygen carriers for hydrogen production', *International Journal of Hydrogen Energy*, 42(39), pp. 24823–24829. Available at: https://doi.org/10.1016/J.IJHYDENE.2017.08.019.

Meloni, E., Martino, M. and Palma, V. (2020) 'A short review on ni based catalysts and related engineering issues for methane steam reforming', *Catalysts*, 10(3). Available at: https://doi.org/10.3390/catal10030352.

Metcalfe, I.S. *et al.* (2019) 'Overcoming chemical equilibrium limitations using a thermodynamically reversible chemical reactor', *Nature Chemistry 2019 11:7*, 11(7), pp. 638–643. Available at: https://doi.org/10.1038/s41557-019-0273-2.

Midilli, A. *et al.* (2021) 'A comprehensive review on hydrogen production from coal gasification: Challenges and Opportunities', *International Journal of Hydrogen Energy*, 46(50), pp. 25385–25412. Available at: https://doi.org/10.1016/J.IJHYDENE.2021.05.088.

Mihai, O., Chen, D. and Holmen, A. (2012) 'Chemical looping methane partial oxidation: The effect of the crystal size and O content of LaFeO3', *Journal of Catalysis*, 293, pp. 175–185. Available at: https://doi.org/10.1016/J.JCAT.2012.06.022.

Mikkelsen, M., Jørgensen, M. and Krebs, F.C. (2010) 'The teraton challenge. A review of fixation and transformation of carbon dioxide', *Energy and Environmental Science*, 3(1), pp. 43–81. Available at: https://doi.org/10.1039/b912904a.

Moltineri, A. (2007) 'Basics of Rietveld Refinement', in, pp. 1–25.

Mondal, K. *et al.* (2004) 'Reduction of iron oxide in carbon monoxide atmosphere - Reaction controlled kinetics', *Fuel Processing Technology*, 86(1), pp. 33–47. Available at: https://doi.org/10.1016/j.fuproc.2003.12.009.

Murugan, A., Thursfield, A. and Metcalfe, I.S. (2011) 'A chemical looping process for hydrogen production using iron-containing perovskites', *Energy & Environmental Science*, 4(11), pp. 4639–4649. Available at: https://doi.org/10.1039/C1EE02142G.

Nalbandian, L., Evdou, A. and Zaspalis, V. (2011) 'La1−xSrxMyFe1−yO3−δ perovskites as oxygen-carrier materials for chemical-looping reforming', *International Journal of Hydrogen Energy*, 36(11), pp. 6657–6670. Available at: https://doi.org/10.1016/J.IJHYDENE.2011.02.146.

Neagu, D. (2012) 'Materials and Microstructures for High Temperature Electrochemical Devices through Control of Perovskite Defect Chemistry', (December), pp. 1–257.

Neagu, D. *et al.* (2013) 'In situ growth of nanoparticles through control of non-stoichiometry', *Nature Chemistry 2013 5:11*, 5(11), pp. 916–923. Available at: https://doi.org/10.1038/nchem.1773.

Neagu, D. *et al.* (2015) 'Nano-socketed nickel particles with enhanced coking resistance grown in situ by redox exsolution', *Nature Communications 2015 6:1*, 6(1), pp. 1–8. Available at: https://doi.org/10.1038/ncomms9120.

Neagu, D. *et al.* (2019) 'In Situ Observation of Nanoparticle Exsolution from Perovskite Oxides: From Atomic Scale Mechanistic Insight to Nanostructure Tailoring', *ACS Nano*, 13(11), pp. 12996–13005. Available at: https://doi.org/10.1021/acsnano.9b05652.

Neagu, D. *et al.* (2023) 'Roadmap on exsolution for energy applications', *Journal of Physics: Energy*, 5(3), p. 031501. Available at: https://doi.org/10.1088/2515-7655/ACD146.

Neagu, D. and Irvine, J.T.S. (2011) 'Enhancing electronic conductivity in strontium titanates through correlated A and B-site doping', *Chemistry of Materials*, 23(6), pp. 1607–1617. Available at: https://doi.org/10.1021/cm103489r.

Nishihata, Y. *et al.* (2002) 'Self-regeneration of a Pd-perovskite catalyst for automotive emissions control', *Nature 2002 418:6894*, 418(6894), pp. 164–167. Available at: https://doi.org/10.1038/nature00893.

Opitz, A.K. *et al.* (2020) 'Understanding electrochemical switchability of perovskite-type exsolution catalysts', *Nature Communications 2020 11:1*, 11(1), pp. 1–10. Available at: https://doi.org/10.1038/s41467-020-18563-w.

Orsini, F. *et al.* (2023) 'Exsolution-enhanced reverse water-gas shift chemical looping activity of Sr2FeMo0.6Ni0.4O6-δ double perovskite', *Chemical Engineering Journal*, 475, p. 146083. Available at: https://doi.org/10.1016/J.CEJ.2023.146083.

Ortiz, M. *et al.* (2012) 'Catalytic activity of ni-based oxygen-carriers for steam methane reforming in chemical-looping processes', *Energy and Fuels*, 26(2), pp. 791–800. Available at: https://doi.org/10.1021/ef2013612.

Osman, A.I. (2020) 'Catalytic Hydrogen Production from Methane Partial Oxidation: Mechanism and Kinetic Study', *Chemical Engineering and Technology*, 43(4), pp. 641–648. Available at: https://doi.org/10.1002/ceat.201900339.

Otsuka, K. *et al.* (2003) 'Chemical storage of hydrogen by modified iron oxides', *Journal of Power Sources*, 122(2), pp. 111–121. Available at: https://doi.org/10.1016/S0378-7753(03)00398-7.

Otto, S.K. *et al.* (2019) 'Exsolved Nickel Nanoparticles Acting as Oxygen Storage Reservoirs and Active Sites for Redox CH4 Conversion', *ACS Applied Energy Materials*, 2(10), pp. 7288–7298. Available at: https://doi.org/10.1021/ACSAEM.9B01267.

Padi, S.P. *et al.* (2020) 'Coke-free methane dry reforming over nano-sized NiO-CeO2 solid solution after exsolution', *Catalysis Communications*, 138, p. 105951. Available at: https://doi.org/10.1016/J.CATCOM.2020.105951.

Pahija, E. *et al.* (2022) 'Experimental and Computational Synergistic Design of Cu and Fe Catalysts for the Reverse Water-Gas Shift: A Review', *ACS Catalysis*, 12, pp. 6887–6905. Available at: https://doi.org/10.1021/acscatal.2c01099.

Papaioannou, E.I. *et al.* (2019) 'Sulfur-Tolerant, Exsolved Fe–Ni Alloy Nanoparticles for CO Oxidation', *Topics in Catalysis*, 62(17–20), pp. 1149–1156. Available at: https://doi.org/10.1007/S11244-018-1053-8/FIGURES/6.

Papargyriou, D., Miller, D.N. and Irvine, J.T.S. (2019) 'Exsolution of Fe–Ni alloy nanoparticles from (La,Sr)(Cr,Fe,Ni)O3 perovskites as potential oxygen transport membrane catalysts for methane reforming', *Journal of Materials Chemistry A*, 7(26), pp. 15812–15822. Available at: https://doi.org/10.1039/C9TA03711J.

Park, S.Y. *et al.* (2017) 'Deactivation characteristics of Ni and Ru catalysts in tar steam reforming', *Renewable Energy*, 105, pp. 76–83. Available at: https://doi.org/10.1016/j.renene.2016.12.045.

Pastor-Pérez, L. *et al.* (2018) 'Improving Fe/$Al2O_3$ Catalysts for the Reverse Water-Gas Shift Reaction: On the Effect of Cs as Activity/Selectivity Promoter', *Catalysts 2018, Vol. 8, Page 608*, 8(12), p. 608. Available at: https://doi.org/10.3390/CATAL8120608.

Peña, M.A. and Fierro, J.L.G. (2001) 'Chemical structures and performance of perovskite oxides', *Chemical Reviews*, 101(7), pp. 1981–2017. Available at: https://doi.org/10.1021/CR980129F/ASSET/IMAGES/LARGE/CR980129FF00014.JPEG.

Protasova, L. and Snijkers, F. (2016) 'Recent developments in oxygen carrier materials for hydrogen production via chemical looping processes', *Fuel*, 181, pp. 75–93. Available at: https://doi.org/10.1016/j.fuel.2016.04.110.

Qasim, M. *et al.* (2021) 'Recent Advances and Development of Various Oxygen Carriers for the Chemical Looping Combustion Process: A Review', *Industrial and Engineering Chemistry Research*, 60(24), pp. 8621–8641. Available at: https://doi.org/10.1021/ACS.IECR.1C01111/ASSET/IMAGES/MEDIUM/IE1C01111_M005.GIF.

Ranganathan, R. V. *et al.* (2019) 'Plasma-catalysis chemical looping CH4 reforming with water splitting using ceria supported Ni based La-perovskite nano-catalyst', *Journal of CO2 Utilization*, 32(December 2018), pp. 11–20. Available at: https://doi.org/10.1016/j.jcou.2019.03.014.

Rydén, M. *et al.* (2008) 'Novel oxygen-carrier materials for chemical-looping combustion and chemical-looping reforming; LaxSr1−xFeyCo1−yO3−δ perovskites and mixed-metal oxides of NiO, Fe2O3 and Mn3O4', *International Journal of Greenhouse Gas Control*, 2(1), pp. 21–36. Available at: https://doi.org/10.1016/S1750-5836(07)00107-7.

le Saché, E. *et al.* (2018) 'Ni stabilised on inorganic complex structures: superior catalysts for chemical CO_2 recycling via dry reforming of methane', *Applied Catalysis B: Environmental*, 236(March), pp. 458–465. Available at: https://doi.org/10.1016/j.apcatb.2018.05.051.

Santaya, M. *et al.* (2022) 'Tracking the nanoparticle exsolution/reoxidation processes of Ni-doped SrTi0.3Fe0.7O3−δ electrodes for intermediate temperature symmetric solid oxide fuel cells', *Journal of Materials Chemistry A*, 10(29), pp. 15554–15568. Available at: https://doi.org/10.1039/d2ta02959f.

Santaya, M. *et al.* (2023) 'Exsolution versus particle segregation on (Ni,Co)-doped and undoped SrTi0.3Fe0.7O3-δ perovskites: Differences and influence of the reduction path on the final system nanostructure', *International Journal of Hydrogen Energy*, 48(98), pp. 38842–38853. Available at: https://doi.org/10.1016/j.ijhydene.2023.06.203.

Scheffe, J.R. *et al.* (2011) 'Hydrogen production via chemical looping redox cycles using atomic layer deposition-synthesized iron oxide and cobalt ferrites', *Chemistry of Materials*, 23(8), pp. 2030–2038. Available at: https://doi.org/10.1021/cm103622e.

Sengodan, S. *et al.* (2015) 'Layered oxygen-deficient double perovskite as an efficient and stable anode for direct hydrocarbon solid oxide fuel cells', *Nature Materials*, 14(2), pp. 205–209. Available at: https://doi.org/10.1038/nmat4166.

Sengodan, S. *et al.* (2018) 'Advances in reforming and partial oxidation of hydrocarbons for hydrogen production and fuel cell applications', *Renewable and Sustainable Energy Reviews*, 82, pp. 761–780. Available at: https://doi.org/10.1016/J.RSER.2017.09.071.

Sengupta, S. *et al.* (2019) 'Catalytic performance of Co and Ni doped Fe-based catalysts for the hydrogenation of CO_2 to CO via reverse water-gas shift reaction', *Journal of Environmental Chemical Engineering*, 7(1), p. 102911. Available at: https://doi.org/10.1016/j.jece.2019.102911.

Shah, V. *et al.* (2021) 'Enhanced methane conversion using Ni-doped calcium ferrite oxygen carriers in chemical looping partial oxidation systems with CO_2 utilization', *Reaction Chemistry and Engineering*, 6(10), pp. 1928–1939. Available at: https://doi.org/10.1039/d1re00150g.

Sharma, R., Delebarre, A. and Alappat, B. (2014) 'Chemical-looping combustion an overview and application of the recirculating', *Intl J of Energy Research*, 38, pp. 1331–1350.

Shen, Y. *et al.* (2019) 'The structure-reactivity relationships of using three-dimensionally ordered macroporous $LaFe_{1-x}NixO3$ perovskites for chemical-looping steam methane reforming', *Journal of the Energy Institute*, 92(2), pp. 239–246. Available at: https://doi.org/10.1016/J.JOEI.2018.01.012.

Shin, T.H. *et al.* (2012) 'Self-Recovery of Pd Nanoparticles That Were Dispersed over LaSrFeMnO3 for Intelligent Oxide Anodes of Solid-Oxide Fuel Cells', *Chemistry - A European Journal*, 18, pp. 11695–11702. Available at: https://doi.org/10.1002/chem.201200536.

Siang, T.J. *et al.* (2020) 'Thermodynamic equilibrium study of altering methane partial oxidation for Fischer–Tropsch synfuel production', *Energy*, 198, p. 117394. Available at: https://doi.org/10.1016/j.energy.2020.117394.

Silvester, L. *et al.* (2015) 'NiO supported on Al2O3 and ZrO2 oxygen carriers for chemical looping steam methane reforming', *International Journal of Hydrogen Energy*, 40(24), pp. 7490–7501. Available at: https://doi.org/10.1016/J.IJHYDENE.2014.12.130.

Simoes, S.G. *et al.* (2021) 'Water availability and water usage solutions for electrolysis in hydrogen production', *Journal of Cleaner Production*, 315(June). Available at: https://doi.org/10.1016/j.jclepro.2021.128124.

Sitte, W., Bucher, E. and Preis, W. (2002) 'Nonstoichiometry and transport properties of strontium-substituted lanthanum cobaltites', *Solid State Ionics*, 154–155, pp. 517–522. Available at: https://doi.org/10.1016/S0167-2738(02)00503-9.

Søgaard, M., Vang Hendriksen, P. and Mogensen, M. (2007) 'Oxygen nonstoichiometry and transport properties of strontium substituted lanthanum ferrite', *Journal of Solid State Chemistry*, 180(4), pp. 1489–1503. Available at: https://doi.org/10.1016/J.JSSC.2007.02.012.

Son, S.R., Go, K.S. and Kim, S.D. (2009) 'Thermogravimetric analysis of copper oxide for chemical-looping hydrogen generation', *Industrial and Engineering Chemistry Research*, 48(1), pp. 380–387. Available at: https://doi.org/10.1021/ie800174c.

Song, J., Ning, D. and Bouwmeester, H.J.M. (2020) 'Influence of alkaline-earth metal substitution on structure, electrical conductivity and oxygen transport properties of perovskite-type oxides La0.6A0.4FeO3−δ(A = Ca, Sr and Ba)', *Physical Chemistry Chemical Physics*, 22(21), pp. 11984–11995. Available at: https://doi.org/10.1039/d0cp00247j.

Sun, F.M. *et al.* (2015) 'Ni/Ce-Zr-O catalyst for high CO_2 conversion during reverse water gas shift reaction (RWGS)', *International Journal of Hydrogen Energy*, 40(46), pp. 15985–15993. Available at: https://doi.org/10.1016/j.ijhydene.2015.10.004.

Sun, Y.F. *et al.* (2015) 'A-site-deficiency facilitated in situ growth of bimetallic Ni–Fe nano-alloys: a novel coking-tolerant fuel cell anode catalyst', *Nanoscale*, 7(25), pp. 11173–11181. Available at: https://doi.org/10.1039/C5NR02518D.

Sun, Zhao *et al.* (2023) 'Recent advances in exsolved perovskite oxide construction: exsolution theory, modulation, challenges, and prospects', *Journal of Materials Chemistry A*, 11(34), pp. 17961–17976. Available at: https://doi.org/10.1039/d3ta03292b.

Swamy, V., Dubrovinskaya, N.A. and Dubrovinsky, L.S. (1999) 'High-temperature powder x-ray diffraction of yttria to melting point', *Journal of Materials Research*, 14(2), pp. 456–459. Available at: https://doi.org/10.1557/JMR.1999.0065.

Swartzendruber, L.J., Itkin, V.P. and Alcock, C.B. (1991) 'The Fe-Ni (iron-nickel) system', *Journal of Phase Equilibria*, 12(3), pp. 288–312. Available at: https://doi.org/10.1007/BF02649918.

Tan, P. *et al.* (2017) 'Recent Advances in Perovskite Oxides as Electrode Materials for Nonaqueous Lithium–Oxygen Batteries', *Advanced Energy Materials*, 7(13), p. 1602674. Available at: https://doi.org/10.1002/AENM.201602674.

Tanaka, H. *et al.* (2004) 'Design of the intelligent catalyst for Japan ULEV standard', *Topics in Catalysis*, 30–31(1), pp. 389–396. Available at: https://doi.org/10.1023/B:TOCA.0000029780.70319.36/METRICS.

Tanaka, H., Taniguchi, M., *et al.* (2006) 'Self-Regenerating Rh- and Pt-Based Perovskite Catalysts for Automotive-Emissions Control', *Angewandte Chemie International Edition*, 45(36), pp. 5998–6002. Available at: https://doi.org/10.1002/ANIE.200503938.

Tanaka, H., Uenishi, M., *et al.* (2006) 'The intelligent catalyst having the self-regenerative function of Pd, Rh and Pt for automotive emissions control', *Catalysis Today*, 117(1–3), pp. 321–328. Available at: https://doi.org/10.1016/j.cattod.2006.05.029.

Tang, C. *et al.* (2021) 'Trends and Prospects of Bimetallic Exsolution', *Chemistry - A European Journal*, 27(22), pp. 6666–6675. Available at: https://doi.org/10.1002/chem.202004950.

Tang, M., Xu, L. and Fan, M. (2015) 'Progress in oxygen carrier development of methane-based chemical-looping reforming: A review', *Applied Energy*, 151, pp. 143–156. Available at: https://doi.org/10.1016/J.APENERGY.2015.04.017.

Theofanidis, S.A. *et al.* (2019) *How Does the Surface Structure of Ni-Fe Nanoalloys Control Carbon Formation During Methane Steam/Dry Reforming?*, *Advanced Nanomaterials for Catalysis and Energy: Synthesis, Characterization and Applications*. Elsevier Inc. Available at: https://doi.org/10.1016/B978-0-12-814807-5.00006-1.

Travis, W. *et al.* (2016) 'On the application of the tolerance factor to inorganic and hybrid halide perovskites: a revised system', *Chemical Science*, 7(7), pp. 4548–4556. Available at: https://doi.org/10.1039/C5SC04845A.

Ungut, M.S. (2022) 'Approaching the design of novel oxygen- carrier materials for hydrogen production via the chemical looping water-gas shift process in a packed bed reactor'.

Vieira, L.H. *et al.* (2023) 'Noble Metals in Recent Developments of Heterogeneous Catalysts for CO_2 Conversion Processes', *ChemCatChem*, 15(14). Available at: https://doi.org/10.1002/cctc.202300493.

Villafán-Vidales, H.I. *et al.* (2017) 'Carbo- and Methanothermal Reduction of Tungsten Trioxide into Metallic Tungsten for Thermochemical Production of Solar Fuels', *Energy Technology*, 5(5), pp. 692–702. Available at: https://doi.org/10.1002/ENTE.201600455.

Voitic, G. and Hacker, V. (2016) 'Recent advancements in chemical looping water splitting for the production of hydrogen', *RSC Advances*, 6(100), pp. 98267–98296. Available at: https://doi.org/10.1039/c6ra21180a.

Volkova, N.E. *et al.* (2019) 'Structure and properties of layered perovskites $Ba1\text{-}xLnxFe_{1-y}Co_yO_{3-\delta}$ (Ln = Pr, Sm, Gd)', *Journal of Alloys and Compounds*, 784, pp. 1297–1302. Available at: https://doi.org/10.1016/j.jallcom.2018.12.391.

Wan, Y. *et al.* (2019) 'Vanadium-Doped Strontium Molybdate with Exsolved Ni Nanoparticles as Anode Material for Solid Oxide Fuel Cells', *ACS Applied Materials and*

Interfaces, 11(45), pp. 42271–42279. Available at: https://doi.org/10.1021/acsami.9b15584.

Wang, L. *et al.* (2013) 'Effect of precipitants on Ni-CeO_2 catalysts prepared by a co-precipitation method for the reverse water-gas shift reaction', *Journal of Rare Earths*, 31(10), pp. 969–974. Available at: https://doi.org/10.1016/S1002-0721(13)60014-9.

Wang, L., Zhang, S. and Liu, Y. (2008) 'Reverse water gas shift reaction over Co-precipitated Ni-CeO2 catalysts', *Journal of Rare Earths*, 26(1), pp. 66–70. Available at: https://doi.org/10.1016/S1002-0721(08)60039-3.

Ward, S. *et al.* (2021) 'Boosting the oxygen evolution activity in non-stoichiometric praseodymium ferrite-based perovskites by A site substitution for alkaline electrolyser anodes', *Sustainable Energy & Fuels*, 5(1), pp. 154–165. Available at: https://doi.org/10.1039/D0SE01278E.

Wei, G. *et al.* (2014a) 'Chemical-Looping Reforming of Methane Using Iron Based Oxygen Carrier Modified with Low Content Nickel', *Chinese Journal of Chemistry*, 32(12), pp. 1271–1280. Available at: https://doi.org/10.1002/CJOC.201400563.

Wei, G. *et al.* (2014b) 'Chemical-looping reforming of methane using iron based oxygen carrier modified with low content nickel', *Chinese Journal of Chemistry*, 32(12), pp. 1271–1280. Available at: https://doi.org/10.1002/cjoc.201400563.

Wenzel, M., Rihko-Struckmann, L. and Sundmacher, K. (2017) 'Thermodynamic Analysis and Optimization of RWGS Processesfor Solar Syngas Production from CO_2', *AIChE Journal*, 63(1), pp. 15–22. Available at: https://doi.org/10.1002/aic.15445.

Wu, C. *et al.* (2021) 'Understanding and Application of Strong Metal-Support Interactions in Conversion of CO_2 to Methanol: A Review', *Energy and Fuels*, 35(23), pp. 19012–19023. Available at: https://doi.org/10.1021/acs.energyfuels.1c02440.

Xu, B., Bhawe, Y. and Davis, M.E. (2012) 'Low-temperature, manganese oxide-based, thermochemical water splitting cycle', *Proceedings of the National Academy of Sciences*, 109(24), pp. 9260–9264. Available at: https://doi.org/10.1073/pnas.1206407109.

Xu, N. *et al.* (2010) 'Dependence of critical radius of the cubic perovskite ABO3 oxides on the radius of A- and B-site cations', *International Journal of Hydrogen Energy*, 35(14), pp. 7295–7301. Available at: https://doi.org/10.1016/j.ijhydene.2010.04.149.

Xu, Q. *et al.* (2021) 'Atomic heterointerface engineering overcomes the activity limitation of electrocatalysts and promises highly-efficient alkaline water splitting', *Energy & Environmental Science*, 14(10), pp. 5228–5259. Available at: https://doi.org/10.1039/D1EE02105B.

Xu, X., Zhou, Q. and Yu, D. (2022) 'The future of hydrogen energy: Bio-hydrogen production technology', *International Journal of Hydrogen Energy*, 47(79), pp. 33677–33698. Available at: https://doi.org/10.1016/J.IJHYDENE.2022.07.261.

Yamashita, T. and Hayes, P. (2008) 'Analysis of XPS spectra of Fe2+ and Fe3+ ions in oxide materials', *Applied Surface Science*, 254(8), pp. 2441–2449. Available at: https://doi.org/10.1016/J.APSUSC.2007.09.063.

Yang, L. *et al.* (2023) 'Effect of Nickel and Cobalt Doping on the Redox Performance of $SrFeO_{3-\delta}$ toward Chemical Looping Dry Reforming of Methane', *Energy and Fuels*, 37(16), pp. 12045–12057. Available at: https://doi.org/10.1021/acs.energyfuels.3c01149.

Yang, T. *et al.* (2024) 'Reversible exsolution of iron from perovskites for highly selective syngas production via chemical looping dry reforming of methane', *Fuel*, 366(March), p. 131386. Available at: https://doi.org/10.1016/j.fuel.2024.131386.

Yin, W.J. *et al.* (2019) 'Oxide perovskites, double perovskites and derivatives for electrocatalysis, photocatalysis, and photovoltaics', *Energy and Environmental Science*, 12(2), pp. 442–462. Available at: https://doi.org/10.1039/c8ee01574k.

Yin, X. *et al.* (2021) 'Perovskite-type $LaMn_{1-x}B_xO_{3+\delta}$ (B = Fe, CO and Ni) as oxygen carriers for chemical looping steam methane reforming', *Chemical Engineering Journal*, 422(2), p. 128751. Available at: https://doi.org/10.1016/j.cej.2021.128751.

Zacharias, R., Bock, S. and Hacker, V. (2020) 'The impact of manufacturing methods on the performance of pelletized, iron-based oxygen carriers for fixed bed chemical looping hydrogen in long term operation', *Fuel Processing Technology*, 208(April), p. 106487. Available at: https://doi.org/10.1016/j.fuproc.2020.106487.

Zafar, Q. *et al.* (2007) 'Reduction and oxidation kinetics of Mn3O4/Mg–ZrO2 oxygen carrier particles for chemical-looping combustion', *Chemical Engineering Science*, 62(23), pp. 6556–6567. Available at: https://doi.org/10.1016/J.CES.2007.07.011.

Zafar, Q., Mattisson, T. and Gevert, B. (2005) 'Integrated hydrogen and power production with CO_2 capture using chemical-looping reforming-redox reactivity of particles of CuO, Mn_2O_3, NiO, and Fe_2O_3 using SiO_2 as a support', *Industrial and Engineering Chemistry Research*, 44(10), pp. 3485–3496. Available at: https://doi.org/10.1021/IE048978I/ASSET/IMAGES/LARGE/IE048978IF00011.JPEG.

Zaidi, A., de Leeuwe, C. and Spallina, V. (2024) 'Bi-metallic Ni–Fe LSF perovskite for chemical looping hydrogen application', *Powder Technology*, 436(January 2024), p. 119510. Available at: https://doi.org/10.1016/j.powtec.2024.119510.

Zeng, Z. *et al.* (2020) 'Rare-earth-containing perovskite nanomaterials: Design, synthesis, properties and applications', *Chemical Society Reviews*, 49(4), pp. 1109–1143. Available at: https://doi.org/10.1039/c9cs00330d.

Zhang, H., Sun, Z. and Hu, Y.H. (2021) 'Steam reforming of methane: Current states of catalyst design and process upgrading', *Renewable and Sustainable Energy Reviews*, 149(May), p. 111330. Available at: https://doi.org/10.1016/j.rser.2021.111330.

Zhang, L. *et al.* (2020) 'Identifying the Role of A-Site Cations in Modulating Oxygen Capacity of Iron-Based Perovskite for Enhanced Chemical Looping Methane-to-Syngas

Conversion', *ACS Catalysis*, 10(16), pp. 9420–9430. Available at: https://doi.org/10.1021/acscatal.0c01811.

Zhang, M. *et al.* (2021) 'Recent development of perovskite oxide-based electrocatalysts and their applications in low to intermediate temperature electrochemical devices', *Materials Today*, 49, pp. 351–377. Available at: https://doi.org/10.1016/J.MATTOD.2021.05.004.

Zhang, X. *et al.* (2017) 'Highly Dispersed Copper over β-Mo_2C as an Efficient and Stable Catalyst for the Reverse Water Gas Shift (RWGS) Reaction', *ACS Catalysis*, 7(1), pp. 912–918. Available at: https://doi.org/10.1021/acscatal.6b02991.

Zhang, X., Su, Y., *et al.* (2020) 'Chemical looping steam reforming of methane over Ce-doped perovskites', *Chemical Engineering Science*, 223, p. 115707. Available at: https://doi.org/10.1016/j.ces.2020.115707.

Zhang, X., Pei, C., *et al.* (2020) 'FeO_6 Octahedral Distortion Activates Lattice Oxygen in Perovskite Ferrite for Methane Partial Oxidation Coupled with CO_2 Splitting', *Journal of the American Chemical Society*, 142(26), pp. 11540–11549. Available at: https://doi.org/10.1021/JACS.0C04643/ASSET/IMAGES/MEDIUM/JA0C04643_M012.GIF.

Zhao, K. *et al.* (2014) 'Three-dimensionally ordered macroporous $LaFeO_3$ perovskites for chemical-looping steam reforming of methane', *International Journal of Hydrogen Energy*, 39(7), pp. 3243–3252. Available at: https://doi.org/10.1016/j.ijhydene.2013.12.046.

Zhao, K. *et al.* (2016) 'CaO/MgO modified perovskite type oxides for chemical-looping steam reforming of methane', *Ranliao Huaxue Xuebao/Journal of Fuel Chemistry and Technology*, 44(6), pp. 680–688. Available at: https://doi.org/10.1016/s1872-5813(16)30032-9.

Zhao, K. *et al.* (2016) 'Perovskite-type oxides LaFe1−xCoxO3 for chemical looping steam methane reforming to syngas and hydrogen co-production', *Applied Energy*, 168, pp. 193–203. Available at: https://doi.org/10.1016/J.APENERGY.2016.01.052.

Zhao, K., Zheng, A., *et al.* (2017) 'Exploration of the mechanism of chemical looping steam methane reforming using double perovskite-type oxides La1.6Sr0.4FeCoO6', *Applied Catalysis B: Environmental*, 219, pp. 672–682. Available at: https://doi.org/10.1016/J.APCATB.2017.08.027.

Zhao, K., Li, L., *et al.* (2017) 'Synergistic improvements in stability and performance of the double perovskite-type oxides La2−xSrxFeCoO6 for chemical looping steam methane reforming', *Applied Energy*, 197, pp. 393–404. Available at: https://doi.org/10.1016/J.APENERGY.2017.04.049.

Zhao, L. *et al.* (2021) 'Oxygen carriers for chemical-looping water splitting to hydrogen production: A critical review', *Carbon Capture Science and Technology*, 1(October), p. 100006. Available at: https://doi.org/10.1016/j.ccst.2021.100006.

Zhao, Y. *et al.* (2023) 'Measurement and control of oxygen non-stoichiometry in praseodymium-cerium oxide thin films by coulometric titration', *Journal of Electroceramics*, 51(1), pp. 28–36. Available at: https://doi.org/10.1007/s10832-023-00309-x.

Zhao, Z. *et al.* (2016a) 'Redox Kinetics Study of Fuel Reduced Ceria for Chemical-Looping Water Splitting', *Journal of Physical Chemistry C*, 120(30), pp. 16271–16289. Available at: https://doi.org/10.1021/acs.jpcc.6b01847.

Zhao, Z. *et al.* (2016b) 'Redox Kinetics Study of Fuel Reduced Ceria for Chemical-Looping Water Splitting', *Journal of Physical Chemistry C*, 120(30), pp. 16271–16289. Available at: https://doi.org/10.1021/acs.jpcc.6b01847.

Zheng, Y. *et al.* (2017) 'Designed oxygen carriers from macroporous LaFeO3 supported CeO2 for chemical-looping reforming of methane', *Applied Catalysis B: Environmental*, 202, pp. 51–63. Available at: https://doi.org/10.1016/J.APCATB.2016.08.024.

Zhong, F. *et al.* (2023) 'Cation-deficient perovskite Sr1-xTi1-yNiyO3-δ anodes with in-situ exsolution of Ni nanoparticles for direct ammonia solid oxide fuel cells', *Chemical Engineering Journal*, 471, p. 144650. Available at: https://doi.org/10.1016/J.CEJ.2023.144650.

Zhou, Jun *et al.* (2023) 'Fabrication of Heterostructural FeNi3-Loaded Perovskite Catalysts by Rapid Plasma for Highly Efficient Photothermal Reverse Water Gas Shift Reaction', *Small*, 2307302, pp. 1–10. Available at: https://doi.org/10.1002/smll.202307302.

Zhou, W. *et al.* (2007) 'Fundamentals of scanning electron microscopy (SEM)', *Scanning Microscopy for Nanotechnology: Techniques and Applications*, pp. 1–40. Available at: https://doi.org/10.1007/978-0-387-39620-0_1.

Zhu, M. *et al.* (2018) 'Effects of supports on reduction activity and carbon deposition of iron oxide for methane chemical looping hydrogen generation', *Applied Energy*, 225(December 2017), pp. 912–921. Available at: https://doi.org/10.1016/j.apenergy.2018.05.082.

Zhu, X. *et al.* (2011) 'Reaction characteristics of chemical-looping steam methane reforming over a Ce–ZrO2 solid solution oxygen carrier', *Mendeleev Communications*, 21(4), pp. 221–223. Available at: https://doi.org/10.1016/J.MENCOM.2011.07.017.

Zhu, X. *et al.* (2013) 'Ce-Fe oxygen carriers for chemical-looping steam methane reforming', *International Journal of Hydrogen Energy*, 38(11), pp. 4492–4501. Available at: https://doi.org/10.1016/j.ijhydene.2013.01.115.

Zhu, X. *et al.* (2014) 'Chemical-looping steam methane reforming over a CeO_2-Fe_2O_3 oxygen carrier: Evolution of its structure and reducibility', *Energy and Fuels*, 28(2), pp. 754–760. Available at: https://doi.org/10.1021/EF402203A/ASSET/IMAGES/LARGE/EF-2013-02203A_0009.JPEG.

Zhu, X. *et al.* (2020) 'Chemical looping beyond combustion-a perspective', *Energy and Environmental Science*, 13(3), pp. 772–804. Available at: https://doi.org/10.1039/c9ee03793d.

Zhu, Y. *et al.* (2018) 'Synergistically enhanced hydrogen evolution electrocatalysis by in situ exsolution of metallic nanoparticles on perovskites', *Journal of Materials Chemistry A*, 6(28), pp. 13582–13587. Available at: https://doi.org/10.1039/c8ta02347f.

Zubenko, D., Singh, S. and Rosen, B.A. (2017) 'Exsolution of Re-alloy catalysts with enhanced stability for methane dry reforming', *Applied Catalysis B: Environmental*, 209, pp. 711–719. Available at: https://doi.org/10.1016/j.apcatb.2017.03.047.